ISSN 1316-7081
ISSN Electrónico 2244-8780

# CIENCIA e INGENIERÍA

Vicerrectorado Administrativo y
Académico
Mérida, Venezuela

**UNIVERSIDAD DE LOS ANDES**
**(ULA)**
**Facultad de Ingeniería**
**Núcleo Universitario**
**«Pedro Rincón Gutiérrez»**
**Mérida - Venezuela**

**Vol. 47** **Agosto – Noviembre 2026** **No 3**

*Artículo de Investigación. Revista Ciencia e Ingeniería. Vol. 47, No. 3 pp. 213-220, agosto-noviembre, 2026.*
*ISSN 1316-7081. ISSN Elect. 2244-8780 Universidad de los Andes (ULA)*

# Optimización del flujo y utilización de recursos en procesos de limpieza y desinfección de contenedores reutilizables mediante DMAIC en sistemas logístico-farmacéuticos

# Optimization of flow and resource utilization in cleaning and disinfection processes of reusable containers using DMAIC in pharmaceutical logistics systems

**Ortiz, Gisela[1]; Medero, Pamela[1]; Olivares, Luis[1]; García, María[1]; Rondón, Jairo[2*]**
[1] Industrial Engineering Department, Universidad Politécnica de Puerto Rico, San Juan, PR 00918, USA
[2] Biomedical & Chemical Engineering Departments, Universidad Politécnica de Puerto Rico, San Juan, PR 00918, USA
*jrondon@pupr.edu

**Resumen**

*Este estudio presenta la optimización de un proceso de limpieza y desinfección de contenedores reutilizables en un entorno logístico del sector farmacéutico mediante la metodología Lean Six Sigma bajo el enfoque DMAIC (Definir, Medir, Analizar, Mejorar y Controlar). El análisis de datos operacionales evidenció que, aunque el sistema cumplía con la demanda promedio de 3.868 unidades diarias, presentaba una alta variabilidad (σ = 732), lo que afectaba la estabilidad del flujo y la eficiencia global. Se integraron análisis de productividad, tiempos de ciclo y capacidad del proceso, determinándose que la principal restricción no era la capacidad instalada, sino el diseño del flujo y la asignación de recursos. Asimismo, se observó que el incremento en la dotación de personal no necesariamente mejora el desempeño, y que la variabilidad en los tiempos de procesamiento constituye un factor crítico en la inestabilidad del sistema. La implementación de mejoras basadas en balance de línea, la estandarización de tareas y la eliminación de actividades sin valor agregado, permitieron reducir el tiempo de ciclo en aproximadamente un 30 % y mejorar la estabilidad del proceso. Adicionalmente, se logró una reducción significativa de los costos operativos. Los resultados demuestran que la eficiencia de los sistemas logísticos depende principalmente de la gestión del flujo y de la variabilidad.*

**Palabras clave:** Lean Six Sigma, variabilidad del proceso, capacidad del proceso, optimización de flujo

**Abstract**

*This study presents the optimization of a cleaning and disinfection process for reusable containers in a pharmaceutical logistics environment using the Lean Six Sigma methodology under the DMAIC framework (Define, Measure, Analyze, Improve, and Control). The analysis of operational data revealed that, although the system met the average demand of 3,868 units per day, it exhibited high variability (σ = 732), affecting flow stability and overall efficiency. Productivity analysis, cycle time evaluation, and process capability assessment were integrated, showing that the main constraint was not the installed capacity, but rather the flow design and resource allocation. It was also observed that increasing workforce size does not necessarily improve performance, and that variability in processing times constitutes a critical factor in system instability. The implementation of improvements based on line balancing, task standardization, and elimination of non-value-added activities allowed a reduction of approximately 30% in cycle time and improved process stability. Additionally, a significant reduction in operational costs was achieved. The results demonstrate that efficiency in logistics systems primarily depends on flow management and variability reduction.*

**Keywords:** Lean Six Sigma, Process variability, Process capability, Flow optimization

## 1 Introducción

La gestión del flujo en sistemas productivos y logísticos constituye un elemento central de la ingeniería industrial, particularmente en entornos en los que la continuidad del suministro depende de la sincronización entre procesos

interdependientes. En estos sistemas, la interacción entre la variabilidad operativa, la capacidad instalada y la asignación de recursos determina la estabilidad del desempeño y la confiabilidad del servicio (Montgomery, 2020; Ivanov, 2021).

En las operaciones de limpieza y desinfección de contenedores reutilizables en las cadenas logísticas del sector farmacéutico, la variabilidad desempeña un papel crítico. Las diferencias en los tiempos de ciclo, la mezcla de productos y la dependencia de actividades manuales pueden generar fluctuaciones significativas en el flujo del sistema. Cuando este flujo no está adecuadamente balanceado, pequeñas variaciones se amplifican a lo largo del proceso, provocando acumulaciones, tiempos de espera y pérdida de eficiencia global, un fenómeno ampliamente descrito en la literatura Lean (Womack y col., 1997; Tortorella y col., 2018).

Diversos estudios han demostrado que la mejora del desempeño en sistemas productivos no depende exclusivamente del incremento de recursos, sino también de la reducción de la variabilidad y de la estandarización del flujo (McDermott y col., 2022; Chiarini y col., 2018).

De manera complementaria, la literatura ha documentado la aplicación de enfoques de calidad, Lean, Six Sigma y Lean Six Sigma en diversos sectores en los que la eficiencia, la reducción de desperdicios y la confiabilidad del proceso son elementos críticos. En la industria de alimentos, Costa y col. (2018) identificaron que estas metodologías se han utilizado para mejorar los procesos productivos, reducir la variabilidad y fortalecer el desempeño operativo.

De forma similar, Henrique y Godinho Filho (2020) reportaron aplicaciones empíricas de Lean y Six Sigma en el sector salud, destacando su contribución a la mejora del flujo de trabajo, la calidad del servicio y la eficiencia de los procesos. Asimismo, desde una perspectiva más amplia de la gestión de la calidad, Psomas y Antony (2017) evidenciaron que los principios de la calidad total también se han aplicado en instituciones de educación superior, lo que refuerza la adaptabilidad de estos enfoques a distintos contextos organizacionales.

En este contexto, la metodología Lean Six Sigma, y particularmente el enfoque DMAIC, proporciona un marco estructurado basado en datos que permite identificar causas raíz, reducir desperdicios y mejorar la capacidad efectiva del sistema (Sreedharan y col., 2020; Tampubolon y col., 2021).

A pesar de ello, en muchos entornos operativos persiste una brecha entre la capacidad instalada y el desempeño real. Es común que los sistemas que cumplen con metas promedio de producción presenten altos niveles de variabilidad que afectan la previsibilidad del flujo y la utilización eficiente de los recursos. Esta condición sugiere que la restricción principal no siempre está asociada a la infraestructura, sino al diseño del flujo y a la forma en que se distribuye el trabajo dentro del sistema.

El estudio se desarrolla en un proceso real de limpieza y desinfección de contenedores reutilizables en una organización del sector logístico-farmacéutico en Puerto Rico. El sistema analizado presenta una producción promedio de 3.868 unidades por día, acompañada de una desviación estándar de 732 unidades, lo que evidencia una variabilidad significativa que compromete la estabilidad del flujo y la confiabilidad del suministro hacia los procesos aguas abajo. Adicionalmente, la asignación de recursos humanos responde a configuraciones históricas, sin una validación formal basada en el análisis de la capacidad y del comportamiento estadístico del proceso.

En este contexto, el objetivo de la investigación es evaluar y optimizar el flujo del proceso mediante la aplicación de la metodología DMAIC, analizando la relación entre los tiempos de ciclo, la variabilidad y la configuración de los recursos. Específicamente, se busca determinar si la capacidad efectiva del sistema permite cumplir de manera consistente con la demanda en distintos escenarios operacionales, así como identificar las condiciones necesarias para convertir la capacidad instalada en un desempeño estable y predecible.

Desde la perspectiva de la ingeniería industrial, este trabajo aporta evidencia empírica basada en datos reales, integrando análisis de capacidad, balance de línea y reducción de desperdicios en un entorno logístico altamente variable. Asimismo, contribuye a la literatura al demostrar que la utilización efectiva de recursos depende fundamentalmente del diseño del flujo, y no únicamente de la cantidad de personal asignado, proporcionando un marco metodológico replicable para sistemas productivos similares.

## 2 Metodologia

### *2.1 Diseño de la investigación*

Corresponde a una investigación aplicada, de enfoque cuantitativo y de tipo de estudio de caso, desarrollada en un entorno operativo real de una organización del sector logístico-farmacéutico en Puerto Rico. El objetivo metodológico fue analizar el desempeño del proceso de limpieza y desinfección de contenedores reutilizables en condiciones reales de operación, sin alterar las restricciones productivas ni regulatorias del sistema.

El horizonte temporal del estudio abarcó múltiples semanas de operación continua, lo que permitió capturar variaciones en la demanda diaria, cambios en la mezcla de contenedores y fluctuaciones en la asignación de recursos humanos. La meta operativa establecida por la organización fue de 3.868 unidades por día, valor utilizado como referencia para el análisis de la capacidad y el desempeño del proceso.

Las variables principales analizadas fueron: (i) tiempo de ciclo por unidad, (ii) productividad por operador (unidades/hora-persona), (iii) variabilidad del proceso (desviación estándar) y (iv) capacidad del sistema en relación con la demanda.

La investigación se estructuró bajo la metodología Lean Six Sigma, mediante el ciclo DMAIC (Define, Measure, Analyze, Improve, Control), que permite abordar problemas complejos con un enfoque sistemático basado en datos (George, 2002; McDermott y col., 2022).

### *2.2 Fase Definir (Define)*

En esta fase se estableció el problema central del estudio, definido como la falta de alineación cuantitativa entre la variabilidad del proceso, la capacidad operativa y la asignación de recursos humanos. Aunque el sistema lograba cumplir con la producción promedio requerida, no existía evidencia que validara si la configuración de personal era óptima para mantener el desempeño en escenarios de variabilidad.

Se identificó como cliente principal el área de despacho, cuya necesidad crítica es contar con contenedores desinfectados disponibles de manera continua y confiable. A partir de esta necesidad, se definieron características críticas de calidad (CTQ), que incluyen el cumplimiento de la meta diaria, la estabilidad del tiempo de ciclo y la reducción de las interrupciones en el flujo.

Adicionalmente, se delimitó el alcance del estudio desde la recepción de contenedores sucios hasta el paletizado del producto desinfectado, sin considerar modificaciones en la infraestructura física ni en los requisitos regulatorios del proceso.

### *2.3 Fase Medir (Measure)*

La fase Medir tuvo como propósito caracterizar el desempeño actual del proceso mediante la recolección y el análisis de datos operacionales. Se utilizaron registros históricos de producción diaria, datos de dotación de personal por turno y mediciones directas de tiempos de ciclo en planta.

Se construyeron indicadores clave, entre ellos la producción diaria, la productividad por operador y la distribución de los tiempos de ciclo. El análisis permitió identificar una producción promedio de 3.868 unidades diarias, con una desviación estándar de 732 unidades, lo que evidencia una variabilidad significativa en el sistema.

Asimismo, se evaluó la relación entre el número de operadores y la productividad individual, observándose un comportamiento inverso: el incremento del personal reducía la productividad por operador, lo que sugiere la presencia de interferencias operativas y un desequilibrio en la distribución del trabajo.

Se realizó, además, un estudio de tiempos, diferenciando entre tipos de contenedor e identificando diferencias significativas tanto en los promedios como en la dispersión, lo que permitió establecer el tipo de contenedor como una variable crítica del proceso.

### *2.4 Fase Analizar (Analyze)*

En la fase Analizar se integraron herramientas de ingeniería industrial y de Lean Six Sigma para identificar las causas raíz de la variabilidad e ineficiencia del sistema. Se utilizó el mapeo de procesos para distinguir actividades de valor agregado (VA) y no de valor agregado (NVA), lo que evidenció una alta proporción de actividades asociadas al transporte, la espera y la inspección.

Se aplicaron la metodología de los “5 Why’s” y el análisis causa–efecto, identificando como causa raíz principal la ausencia de un sistema estructurado de medición y análisis que vincule la variabilidad del proceso con la asignación de recursos.

Adicionalmente, se realizó un análisis de capacidad del proceso, estimando la capacidad teórica del sistema en función de los cuellos de botella identificados. Los resultados mostraron índices de capacidad superiores a la unidad, lo que indicaba que la infraestructura disponible era suficiente para satisfacer la demanda y que la limitación principal se debía al diseño del flujo.

Como parte del análisis de riesgos, se implementó un análisis FMEA (Failure Mode and Effects Analysis), que permitió priorizar las fallas potenciales asociadas a actividades críticas del proceso, en particular las relacionadas con el registro, la manipulación y la continuidad operativa. Este análisis permitió identificar los puntos de intervención de mayor impacto en la estabilidad del sistema.

### *2.5 Fase Mejorar (Improve)*

La fase Mejorar se centró en intervenir en las causas raíz identificadas mediante el rediseño del flujo operativo y la optimización de la asignación de recursos. Las acciones implementadas incluyeron:

(i) balance de línea para mejorar la continuidad del flujo, (ii) redefinición de roles operacionales con asignación fija en estaciones críticas, (iii) reducción de interrupciones mediante la automatización de microoperaciones y (iv) eliminación de actividades sin valor agregado.

La efectividad de las mejoras se evaluó mediante pruebas piloto en distintas configuraciones de personal. Se comparó el desempeño del sistema antes y después de la intervención, observándose mejoras significativas en el tiempo de ciclo promedio, una reducción de la variabilidad y una mayor estabilidad del flujo con una menor dotación de operadores.

### *2.6 Fase Control (Control)*

La fase Control tuvo como objetivo asegurar la sostenibilidad de las mejoras implementadas mediante la estandarización del proceso y la definición de indicadores de desempeño.

Se establecieron métricas clave, incluyendo el tiempo de ciclo objetivo, el cumplimiento de la producción diaria y

los límites operacionales de variabilidad. Asimismo, se implementaron rutinas de monitoreo continuo, auditorías operacionales y caminatas Gemba para verificar el cumplimiento del método estandarizado.

Estos mecanismos permiten detectar desviaciones de manera temprana y asegurar que el sistema mantenga un desempeño estable a lo largo del tiempo, alineando la capacidad operativa con la demanda del proceso.

En conjunto, la aplicación estructurada de la metodología DMAIC permitió transformar datos operacionales en decisiones basadas en evidencia, identificar oportunidades de mejora y validar configuraciones de recursos que optimizan el desempeño del sistema en condiciones reales de variabilidad.

## 3 Discusión y resultados

### *3.1 Comportamiento de la producción y variabilidad del sistema*

El análisis de la producción diaria evidenció que el sistema opera con un promedio de 3.868 unidades por día, acompañado de una desviación estándar de 732 unidades, lo que representa aproximadamente un 19 % de variación relativa. Este nivel de dispersión indica que, aunque el proceso cumple la meta promedio, presenta una inestabilidad significativa en su desempeño.

Como se muestra en la Figura 1, la producción diaria presenta fluctuaciones recurrentes alrededor del valor objetivo, lo que evidencia una alta dispersión en el sistema.

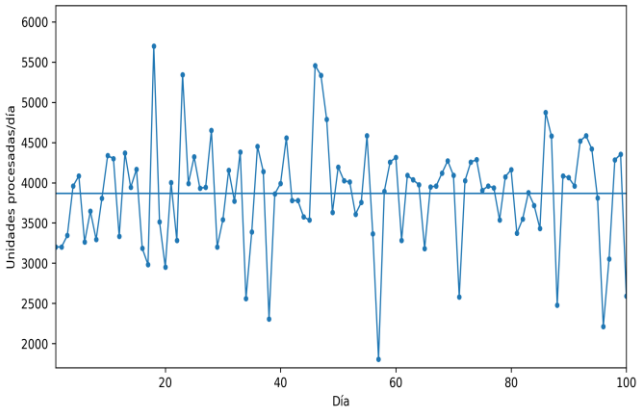


**Fig. 1.** Producción diaria del proceso de limpieza y desinfección, comparada con la meta operativa (3.868 unidades/día), lo que evidencia la variabilidad del sistema.

Desde la perspectiva del control estadístico de procesos, esta variabilidad sugiere la presencia de causas comunes y, potencialmente, de causas especiales que afectan la consistencia del flujo (Montgomery, 2020). Este comportamiento es consistente con lo reportado en sistemas logísticos bajo condiciones de incertidumbre, donde la variabilidad de las entradas y de los tiempos de procesamiento impacta directamente en la confiabilidad del sistema (Ivanov, 2021).

La presencia de múltiples días por debajo de la meta operativa confirma que el cumplimiento promedio no garantiza estabilidad ni capacidad de respuesta ante las fluctuaciones, lo que refuerza la necesidad de analizar el sistema desde una perspectiva de capacidad efectiva y no únicamente del rendimiento medio.

### *3.2 Relación entre dotación de personal y productividad*

El análisis de la productividad por operador reveló una relación inversa entre el número de trabajadores asignados y el rendimiento individual. Con una configuración de cinco operadores, la productividad promedio se situó en aproximadamente 97 unidades por hora por persona; con cuatro operadores aumentó a cerca de 121, y con tres operadores alcanzó valores cercanos a 161 unidades por hora por persona. La Figura 2 muestra claramente la relación inversa entre el número de operadores y la productividad individual del sistema.

Este comportamiento indica la presencia de ineficiencias asociadas a interferencias operativas, tiempos de espera y desequilibrios en la distribución del trabajo. Desde la perspectiva Lean, este fenómeno puede explicarse por la generación de desperdicios de tipo de espera y de movimiento, así como por la falta de sincronización entre estaciones (Womack y col., 1997; Negrão y col., 2017).

Estos resultados evidencian que el incremento de recursos no necesariamente mejora el desempeño global del sistema, y que, en ausencia de un flujo balanceado, puede incluso deteriorar la utilización efectiva de la mano de obra.

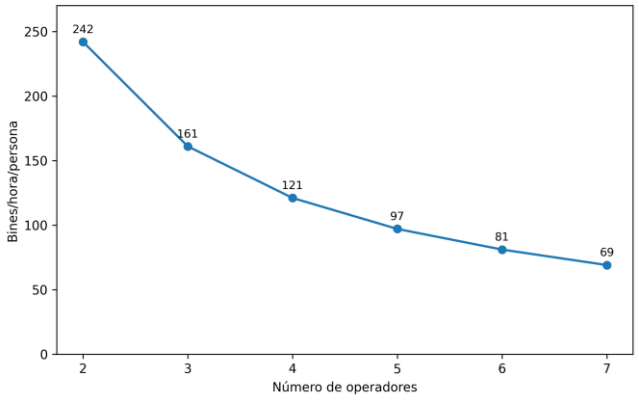


**Fig. 2.** Relación entre el número de operadores y la productividad individual, que muestra un comportamiento inverso asociado a interferencias operativas y al desequilibrio del flujo.

### *3.3 Análisis de tiempos de ciclo y variabilidad por tipo de contenedor*

El estudio de los tiempos de ciclo permitió identificar diferencias significativas entre los tipos de contenedor. Los contenedores de tipo A presentaron un tiempo promedio de procesamiento de aproximadamente 29 segundos, con baja dispersión, mientras que los de Tipo B registraron un promedio de 42 segundos, acompañado de una desviación estándar considerablemente mayor.

Adicionalmente, se identificaron eventos extremos en los contenedores Tipo B, con tiempos superiores a 200 segundos, lo que afecta negativamente la continuidad del flujo y contribuye a la variabilidad global del sistema. La distribución de los tiempos de ciclo se presenta en la Figura 3, donde se observa la mayor dispersión y la presencia de valores extremos en los contenedores Tipo B.

Este comportamiento confirma que la mezcla de productos constituye una fuente crítica de variabilidad, un fenómeno ampliamente documentado en sistemas de producción con heterogeneidad en los tiempos de procesamiento (Katiraee y col., 2023). En este contexto, los contenedores Tipo B actúan como elementos dominantes del flujo, fijan el ritmo del sistema y generan acumulaciones en estaciones críticas.

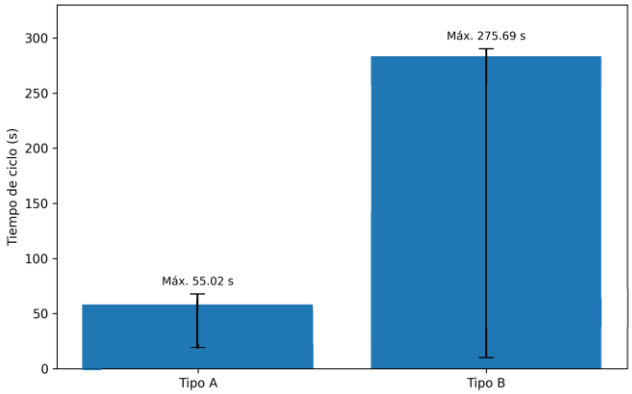


**Fig. 3.** Distribución de tiempos de ciclo por tipo de contenedor, evidenciando mayor variabilidad y presencia de valores extremos en los contenedores Tipo B.

### *3.4 Capacidad del proceso y restricción operativa*

El análisis de capacidad del proceso mostró que la capacidad teórica del sistema supera la demanda diaria. Para los contenedores tipo A se estimó una capacidad aproximada de 4.200 unidades por día, mientras que para los Tipo B se obtuvo una capacidad cercana a 5.040 unidades por día, ambos valores superiores a la meta de 3.868 unidades. La Figura 4 compara la capacidad estimada del proceso con la demanda operativa diaria y evidencia que la capacidad instalada supera los requerimientos del sistema.

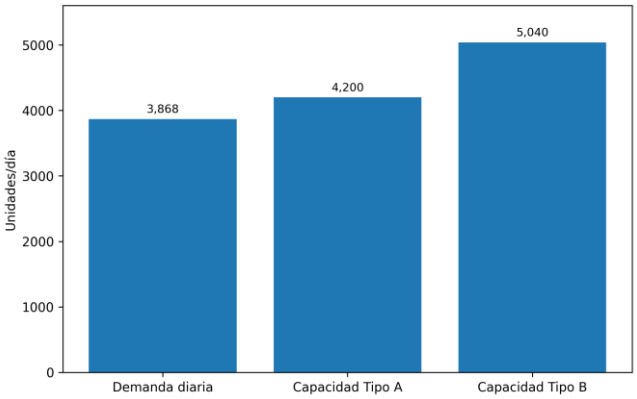


**Fig. 4.** Comparación entre la capacidad del proceso y la demanda operativa.

Estos resultados indican, además, que la restricción principal del sistema no es la infraestructura ni la capacidad instalada, sino el diseño del flujo y la forma en que se gestionan las interacciones entre actividades. Este hallazgo es consistente con estudios recientes que destacan que la viabilidad operativa depende no solo de la capacidad nominal, sino también de la capacidad efectiva bajo condiciones de variabilidad **(**Dolgui y col., 2019).

### *3.5 Evaluación del piloto sin rediseño del flujo*

Durante un piloto inicial en el que se redujo la dotación de cinco a cuatro operadores sin modificar el método de trabajo, se observó un incremento significativo en el tiempo de ciclo de los contenedores Tipo B, que alcanzó valores cercanos a 55 segundos.

El impacto de la reducción de operadores, sin rediseño del flujo, en el tiempo de ciclo se muestra en la figura 5.

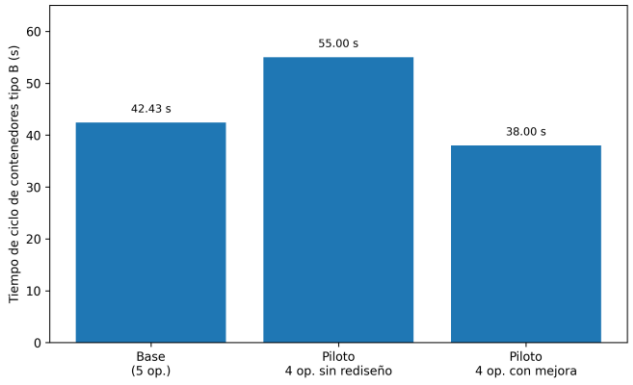


**Fig. 5.** Impacto de la reducción de operadores, sin rediseño del flujo, en el tiempo de ciclo, evidenciando un aumento de la variabilidad y una pérdida de estabilidad del proceso.

Este resultado evidencia que la reducción de recursos, sin intervención en el diseño del flujo, amplifica la variabilidad y desplaza los cuellos de botella hacia las actividades más sensibles del proceso. Aunque el sistema logró cumplir con la producción diaria en términos absolutos, el comportamiento observado mostró una alta dispersión e inestabilidad, lo que indicaba que el desempeño no era sostenible.

Este hallazgo confirma que la eficiencia operativa no puede lograrse únicamente mediante la reducción de recursos, sino que requiere una reconfiguración estructural del sistema (McDermott y col., 2022).

### *3.6 Impacto de las mejoras en el desempeño del sistema*

Tras la implementación de mejoras basadas en balance de línea, redefinición de roles, reducción de interrupciones y eliminación de actividades sin valor agregado, se llevó a cabo un segundo piloto bajo la misma dotación de cuatro operadores.

Los resultados mostraron una reducción del tiempo de ciclo promedio de los contenedores Tipo B a aproximadamente 38 segundos, lo que representa una mejora cercana al 30 %. La Figura 6 ilustra la evolución del tiempo de ciclo en distintos escenarios operativos. Adicionalmente, se observó una disminución de la dispersión de los tiempos y una mayor estabilidad del flujo.

Estos resultados demuestran que la estabilidad del sistema depende principalmente del diseño del flujo y no de la cantidad de recursos disponibles. La estandarización de roles y la eliminación de interferencias operativas permitieron transformar la capacidad potencial en desempeño efectivo, alineando el sistema con los principios del flujo continuo y de la mejora Lean (Chiarini y col., 2018).

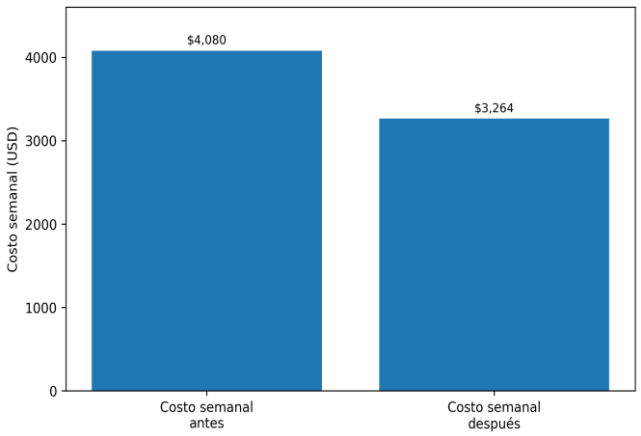


**Fig. 6.** Evolución del tiempo de ciclo bajo diferentes configuraciones operativas, mostrando la mejora obtenida mediante el balance de línea y la estandarización del flujo.

### *3.7 Análisis económico de la mejora*

Desde el punto de vista económico, la optimización del proceso permitió reducir el costo operativo semanal asociado a la mano de obra, generando un ahorro aproximado de $816 por semana, equivalente a $42.432 al año.

La inversión requerida para implementar las mejoras se recuperó en menos de un mes, lo que evidencia la viabilidad financiera de la intervención. Este resultado refuerza la premisa de que las mejoras basadas en el rediseño del flujo pueden generar beneficios significativos sin requerir inversiones sustanciales en infraestructura.

### *3.8 Discusión general*

Los resultados obtenidos demuestran que el desempeño del sistema está determinado por la interacción entre la variabilidad, el flujo y la asignación de recursos, más que por la capacidad instalada en sí misma. En este sentido, el estudio aporta evidencia empírica que refuerza la importancia de abordar los problemas de eficiencia desde una perspectiva sistémica.

A diferencia de enfoques tradicionales que asocian mejoras en la productividad con incrementos de recursos, este trabajo demuestra que la reducción de personal es viable únicamente cuando el flujo ya se ha estabilizado. Este hallazgo contribuye a la literatura al evidenciar que la capacidad efectiva depende del diseño del sistema y de la gestión de la variabilidad.

En conjunto, los resultados confirman que la aplicación estructurada de DMAIC permite transformar sistemas operacionales con alta variabilidad en procesos estables, predecibles y económicamente sostenibles y proporciona un marco replicable para optimizar procesos en entornos logísticos y productivos.

## 4 Conclusion

El presente estudio demostró que la aplicación estructurada de la metodología DMAIC permitió transformar un sistema logístico de alta variabilidad en un proceso más estable, eficiente y económicamente viable. A partir del análisis integrado de producción, tiempos de ciclo y capacidad, se evidenció que el desempeño del sistema no estaba limitado por la capacidad instalada, sino por la configuración del flujo operativo y la gestión de la variabilidad.

Los resultados mostraron que, aunque el proceso cumplía con la demanda promedio, presentaba una dispersión significativa que comprometía su estabilidad. Este hallazgo confirma que el cumplimiento de metas operativas no constituye un indicador suficiente de eficiencia, por lo que es necesario evaluar la capacidad del sistema en condiciones

reales de variabilidad.

Asimismo, se comprobó que el incremento de la dotación de personal no garantiza mejoras en la productividad. Por el contrario, en ausencia de un flujo equilibrado, puede generar interferencias operativas que reduzcan el rendimiento individual y afecten el desempeño global. Este resultado refuerza la importancia del balance de línea y de la estandarización de tareas como elementos críticos para la optimización de procesos.

El análisis de tiempos de ciclo evidenció que la variabilidad en los tipos de contenedor constituye una fuente dominante de inestabilidad, particularmente en los de mayor dispersión y presencia de valores extremos. En este sentido, la mezcla operativa y la heterogeneidad del trabajo deben considerarse variables clave en el diseño de sistemas productivos.

Uno de los aportes más relevantes del estudio es la demostración de que la reducción de recursos es viable únicamente cuando va acompañada de un rediseño del flujo. La implementación de mejoras basadas en el balance de línea, la eliminación de actividades sin valor agregado y la reducción de interrupciones permitieron disminuir el tiempo de ciclo y estabilizar el sistema, lo que validó la hipótesis de que la eficiencia operativa depende principalmente del diseño del proceso y no de la cantidad de recursos disponibles.

Desde el punto de vista económico, las mejoras implementadas generaron una reducción significativa de los costos operativos, con un periodo de recuperación corto, lo que confirma la viabilidad financiera de intervenciones basadas en el rediseño del flujo sin necesidad de inversiones en infraestructura.

En términos de contribución, este trabajo aporta evidencia empírica sobre la relación entre variabilidad, capacidad y flujo en sistemas logísticos y propone un enfoque integrado que combina Lean Six Sigma con el análisis de capacidad para evaluar el desempeño real de los procesos. Este enfoque es replicable en entornos industriales y de servicios, donde la variabilidad y la asignación de recursos inciden directamente en la eficiencia operativa.

Como líneas futuras de investigación, se recomienda incorporar modelos predictivos que permitan anticipar la variabilidad del sistema, así como integrar herramientas de simulación y análisis en tiempo real para fortalecer la toma de decisiones operativas. Asimismo, la inclusión de indicadores de desempeño dinámicos podría contribuir a una gestión más robusta y adaptativa de procesos complejos.

## References

McDermott, O., Antony, J., Bhat, S., Jayaraman, R., Rosa, A., Marolla, G., & Parida, R. (2022). Lean six sigma in healthcare: a systematic literature review on motivations and benefits. *Processes*, *10*(10), 1910. https://doi.org/10.3390/pr10101910

Chiarini, A., Baccarani, C., & Mascherpa, V. (2018). Lean production, Toyota Production System and Kaizen philosophy: A conceptual analysis from the perspective of Zen Buddhism. *The TQM Journal*, *30*(4), 425-438. https://doi.org/10.1108/TQM-12-2017-0178

Costa, L. B. M., Godinho Filho, M., Fredendall, L. D., & Paredes, F. J. G. (2018). Lean, six sigma and lean six sigma in the food industry: A systematic literature review. *Trends in Food Science & Technology*, *82*, 122-133. https://doi.org/10.1016/j.tifs.2018.10.002

Dolgui, A., Ivanov, D., Sethi, S. P., & Sokolov, B. (2019). Scheduling in production, supply chain and Industry 4.0 systems by optimal control: fundamentals, state-of-the-art and applications. *International journal of production research*, *57*(2), 411-432. https://doi.org/10.1080/00207543.2018.1442948

George, M. L. (2002). *Lean Six Sigma: Combining Six Sigma quality with Lean speed*. McGraw-Hill.

Henrique, D. B., & Godinho Filho, M. (2020). A systematic literature review of empirical research in Lean and Six Sigma in healthcare. *Total Quality Management & Business Excellence*, *31*(3-4), 429-449. https://doi.org/10.1080/14783363.2018.1429259

Ivanov, D. (2021). Supply chain viability and the COVID-19 pandemic: A conceptual and formal generalisation of four major adaptation strategies. *International Journal of Production Research*, *59*(12), 3535–3552. https://doi.org/10.1080/00207543.2021.1890852

Katiraee, N., Calzavara, M., Finco, S., Battaïa, O., & Battini, D. (2023). Assembly line balancing and worker assignment considering workers' expertise and perceived physical effort. *International Journal of Production Research*, *61*(20), 6939-6959. https://doi.org/10.1080/00207543.2022.2140219

Montgomery, D. C. (2020). *Introduction to statistical quality control*. John wiley & sons.

Negrão, L. L. L., Godinho Filho, M., & Marodin, G. (2017). Lean practices and their effect on performance: a literature review. *Production Planning & Control*, *28*(1), 33-56. https://doi.org/10.1080/09537287.2016.1231853

Psomas, E., & Antony, J. (2017). Total quality management elements and results in higher education institutions: The Greek case. *Quality Assurance in Education*, *25*(2), 206-223.

Tampubolon, S., & Purba, H. H. (2021). Lean six sigma implementation, a systematic literature review. *International Journal of Production Management and Engineering*, *9*(2), 125-139. https://doi.org/10.4995/ijpme.2021.14561

Sreedharan, V. R., Pattusamy, M., Mohan, S., & Persis, D. J. (2020). A systematic literature review of Lean Six Sigma in financial services: key finding and analysis. *International Journal of Business Excel-*

*lence*, *21*(3), 331-358. https://doi.org/10.1504/IJBEX.2020.108207

Tortorella, G. L., de Castro Fettermann, D., Frank, A., & Marodin, G. (2018). Lean manufacturing implementation: leadership styles and contextual variables. *International Journal of Operations & Production Management*, *38*(5), 1205-1227. https://doi.org/10.1108/IJOPM-08-2016-0453

Womack, J. P., & Jones, D. T. (1997). Lean thinking—banish waste and create wealth in your corporation. *Journal of the operational research society*, *48*(11), 1148-1148.

***Recibido:*** *26 de febrero de 2026*

**Aceptado:** 6 de junio de 2026

***Ortiz, Gisela:*** *BSc. in Industrial Engineering, 2026, Universidad Politécnica de Puerto Rico, San Juan, PR, USA. Email: ortiz_131760@students.pupr.edu*
*https://orcid.org/0009-0007-8355-7689*
***Medero, Pamela:*** *BSc. in Industrial Engineering, 2026, Universidad Politécnica de Puerto Rico. San Juan, PR, USA. E-mail: medero_132378@students.pupr.edu*
*https://orcid.org/0009-0008-6341-5859*

***Olivares Lugo, Luis:*** *M.E., in Systems Management, mention: Artificial Intelligence, 1999, Universidad de Puerto Rico. Professor for the Industrial and Systems Engineering Department, at the Polytechnic University of Puerto Rico. San Juan, PR-USA. E-mail: LOlivares@pupr.edu*
*https://orcid.org/0009-0009-2283-5862*

***Garcia, Maria:*** *Ph.D. in Education, 2012, Ana G. Méndez University. Department Head, and Professor of Industrial Engineering Department, at the Universidad Politécnica de Puerto Rico. San Juan, PR, USA. E-mail: margarcia@pupr.edu*
*https://orcid.org/0000-0002-7134-3057*

***Rondón Contreras, Jairo****: Ph.D. in Applied Chemistry, mention: Materials Study, 2015, Universidad de Los Andes. Professor of Biomedical & Chemical Engineering Departments, at the Polytechnic University of Puerto Rico. San Juan, PR-USA.*
*https://orcid.org/0000-0002-9738-966X*

*Artículo de Investigación. Revista Ciencia e Ingeniería. Vol. 47, No. 3 pp. 221-228, agosto-noviembre, 2026.*
*ISSN 1316-7081. ISSN Elect. 2244-8780 Universidad de los Andes (ULA)*

# Generalized mutual exclusion: Petri nets for resource allocation with choice in manufacturing

# Exclusión mutua generalizada: redes de Petri para la asignación de recursos con elección en manufactura

**Rosales-Moret, José-René[1]*; Mata-Díaz, Guelvis[1]; Ferrer-Guillén, María[2] ; Mantilla Morales, Gisella[3]; Coello-Vera, Adalberto-Antonio[4]; Pérez-Pirela, Maribel[3]**
[1] Faculty of Sciences, Department of Mathematics, University of Los Andes, Mérida, Venezuela.
[2] Faculty of Engineering, Department of Calculating, University of Los Andes, Mérida, Venezuela.
[3] Technical University of Manabí, Ecuador.
[4] Technical University of the State of Quevedo, Ecuador.
*joserene@ula.ve

**Abstract**

*This paper presents a definition of generalized mutual exclusion, along with an application in a manufacturing context. This includes a methodology for developing the most relevant concepts in this class of systems. More precisely, our general problem is stated as follows: given the specifications or conditions in a Manufacturing System, where a shared resource is channeled to carry out operations with choice, to construct a Petri Net-based model containing the aforementioned exclusion, whose structure and initial marking guarantee boundedness, deadlock-freeness, and reversibility.*

**Keywords:** discrete event systems; Petri nets; generalized mutual exclusion; manufacturing systems.

**Resumen**

*En este trabajo se presenta una definición de la exclusión mutua generalizada, junto con una aplicación en un contexto de manufactura, esto incluye una metodología para el desarrollo de los conceptos más relevantes en dicha clase de sistemas. Más precisamente, nuestro problema general es establecido como sigue: dadas las especificaciones o condiciones en un Sistema de Manufactura, donde un recurso compartido es canalizado para llevar a cabo operaciones con elección, construir un modelo basado en Redes de Petri conteniendo una exclusión como la mencionada, cuya estructura y marcación inicial garanticen acotamiento, no bloqueo y reiniciabilidad*.

**Palabras clave:** sistemas de eventos discretos; redes de Petri; exclusión mutua generalizada; sistemas de manufactura.

## 1 Introduction

The evolution toward flexible manufacturing and modern industry has exponentially increased the complexity of Discrete Event Systems (DES), as discussed in (Zhou, 1990). In these automated environments, the optimization of shared resources and conflict prevention are fundamental challenges (Li et al., 2012). When two or more independent processes compete for a shared and indivisible resource, the classic mutual exclusion problem arises; for a precise discussion on this, refer to (Mata et al., 2016).

In its conventional or simple form, mutual exclusion dictates that when a resource is used by multiple processes, it is allocated to one of them, used in a predefined sequence, and subsequently released. To illustrate this, consider an Articulated Robotic Crane shared by three independent processes in a manufacturing cell: Assembly, Inspection, and Cooling. Under the simple mutual exclusion scheme, if the crane serves the Assembly process, it executes a fixed and strict sequence of movements (pick up part, transfer, release) and then becomes free. The same occurs if it serves Inspection or Cooling; the start and end actions have no ambiguity and do not involve decision-making (they are modeled with a single pair of start and end transitions per process).

Modern industrial reality demands flexibility (Coello et

al., 2022; De Souza & Loreiro, 2018). What happens if the system requires operations with choice? Suppose that, upon finishing the Inspection process, the crane must decide the destination of the part: if the part is acceptable, the crane transfers it to the Cooling phase; but if it has defects, it chooses a different route to deposit it at a rework station. Or, in the Loading stage, the crane could choose between different conveyor belts depending on their availability. This scenario of alternative routes and decision-making completely breaks the simple mutual exclusion paradigm, generating the unavoidable need to formulate a generalized mutual exclusion.

The objective of this paper is to establish a formal framework based on Petri Nets (PN) that supports this theoretical generalization and demonstrates its practical feasibility. The paper is organized as follows: Section 2 presents the basic definitions of PN and their qualitative properties; Section 3 details the modeling methodology; Section 4 formally defines simple mutual exclusion and generalized mutual exclusion, demonstrating the preservation of their qualitative properties; Section 5 presents an application that implements the proposed approach; and finally, Section 6 presents the conclusions.

## 2 Basic definitions of Petri Nets and qualitative properties

To unambiguously represent manufacturing systems, we rely on Petri Net theory. Mathematically, these nets are built upon sets that model the system's conditions (places) and the events that alter these conditions (transitions). The system's dynamics—that is, how its state evolves over time due to the occurrence of discrete events—are governed by a token distribution (marking) and strict enabling and firing rules. These fundamental concepts are formalized below.

**Definition 1 (Petri Net).** A Petri Net (**PN**) is a quadruple $R = (L, T, E, S)$, where $L = \{l_1, l_2, ..., l_n\}$ is a finite set of places, $T = \{t_1, t_2, ..., t_k\}$ is a finite set of transitions, $L \cap T = \emptyset$, $E: T \to L^{\infty}$ is an input function such that $E(t)$ is the multiset of input places for $t$; and $S: T \to L^{\infty}$ is an output function such that $S(t)$ is the multiset of output places for $t$.

**Definition 2 (Marked Petri Net).** A marked **PN** is a pair $M = (R, m_0)$, where $R$ is a **PN** and $m_0: L \to \mathbb{N}$ is an initial marking function. For each $l_i \in L$, $m_0(l_i) \in \mathbb{N}$ determines the number of tokens in place $l_i$.

**Observation 1.** Marked **PN** can be represented by bipartite directed graphs, where places are represented by circles and transitions by bars. If $l_i$ and $l_j$ are entry and exit places respectively for a transition t, then there are $\#(l_i, E(t))$ directed arcs from the corresponding circle to the corresponding bar and $\#(l_j, S(t))$ directed arcs from the corresponding bar to the corresponding circle. Finally, the tokens are represented by points inside the circle and, consequently, the marking function is represented by the number of points at the entrances of the **n-**tuple.

**Definition 3 (Enabled Transition).** A transition $t \in T$ in a marked **PN M** is called enabled if $m(l_i) \geq \#(l_i, E(t))$ for all places $l_i \in L$. The set of enabled transitions at marking m is given by $\mathcal{E}(m) = \{t \in T: m(l_i) \geq \#(l_i, E(t)), \forall\, l_i \in L\}$.

**Definition 4 (Marking Change Function).** Given a marked **PN**, the partial marking change function $\delta: \mathbb{N}^{|L|} \times T \to \mathbb{N}^{|L|}$ is defined for $(m, t)$ if and only if $t \in \mathcal{E}(m)$. The resulting marking $m' = \delta(m, t)$ is given by $m'(l_i) = m(l_i) - \#(l_i, E(t)) + \#(l_i, S(t))$.

**Definition 5 (Reachability Set).** Given a marked **PN** $M = (R, m_0)$, a marking m is reachable from $m_0$ if there exists a firing sequence $\sigma$ such that $\delta(m_0, \sigma) = m$. The reachability set is defined as $A(R, m_0) = \{m \in \mathbb{N}^{|L|}: \exists\, \sigma, \delta(m_0, \sigma) = m\}$.

The validation of a model in engineering depends not only on correctly representing the sequence of operations, but also on ensuring that the physical system will operate without failures. This entails ensuring that physical resources are not overloaded (boundedness), that the system does not stall (deadlock-freeness), and that it can return to an idle state to initiate new cycles. To this end, the following qualitative properties are analyzed:

**Definition 6 (Boundedness and Safeness).** A place $l \in L$ is **k-**bounded if there exists $k \in \mathbb{N}$ such that $m(l) \leq k$ for all $m \in A(R, m_0)$. If all places are k-bounded, the net is **k-**bounded. In particular, if the net is **1-**bounded, it is called safe.

**Definition 7 (Non-blocking).** A marked **PN M** is called non-blocking if, for every marking $m \in A(R, m_0)$ and every transition $t_i \in T$, there exists a marking $m' \in A(R, m)$ such that $t_i \in \mathcal{E}(m')$.

**Definition 8 (Reversibility).** A marked **PN M** is called reversible if the initial marking $m_0 \in A(R, m)$ for every marking $m \in A(R, m_0)$.

## 3 Manufacturing Systems and Methodology

A manufacturing system can be described as a pair of sets: a set of activities and a set of resources. These interact to produce a product; thus, it is established that resources are utilized to carry out the pre-established activities within a system, according to a given schedule (admissible sequences).

Based on the aforementioned description, a methodol-

ogy capable of establishing precedence relations in manufacturing systems is considered. To this end, a construction process based on the interpretation of places and transitions is initiated as follows:

1. The resources and activities required for the production of a product are established;

2. The activities are ordered hierarchically based on precedence relations, as dictated by the schedule;

3. For each activity, a place is created to represent its current state. Subsequently, an activity-start transition is created, and an arc from the transition to the place is included. Next, a transition corresponding to the activity's completion is created, including an arc from the place to the transition. Conventionally, the completion transitions of current activities serve as the start transitions for subsequent activities. A token present in a place corresponding to an activity indicates that said activity is being executed; conversely, the absence of tokens in the place indicates that it is not being executed;

4. For each activity, a place is created for every resource required to start the aforementioned activity. These places are connected to the activity's start transition via directed arcs from the places to the start transition. Subsequently, an arc is created from the activity's completion transition to any resource place that becomes available upon completion of the activity. If a place represents a resource condition, the number of tokens in the place indicates the availability of that resource; the absence of tokens indicates that the resource is unavailable;

5. An initial marking is established.

To formalize mutual exclusion, a classification of the places within a **PN** corresponding to manufacturing systems is assumed; that is, a partition of the set of places $L = L_o \cup L_f \cup L_v$, where $L_o$ denotes operations places, $L_f$ denotes fixed-quantity resource places, and $L_v$ denotes variable-quantity resource places.

**Definition 9 (o-path).** Let $y, x \in (L \cup T) \setminus L_o$. An **o-**path between $x$ and $y$ is any elementary path $x_1x_2...x_k$ (sequence of nodes) such that $x_1 = x$, $x_k = y$, and $x_i \in L_o \cup T$ for each $i$ with $2 \leq i \leq k-1$.

To model rigorously, the net must comply with two fundamental design conditions:

**Definition 10 (Condition CL).** Let $M = (R, m_0)$ with $L = L_o \cup L_f \cup L_v$ being a partition of $L$. $M$ has condition **CL** if, given $l' \in (L_f \cup L_v) \cap E(t)$ such that $m_0(l') = 0$, and for every $l \in L$ with $l \neq l'$, the following holds:

$$m_o(l) = \begin{cases} 0, & \text{if } l \in L_o \\ \geq 1, & \text{if } l \in (L_f \cup L_v) \end{cases}$$

$$\Rightarrow t \notin E(m), \text{ for all } m \in A(R, m_o).$$

This condition ensures that a resource in $L_f \cup L_v$ cannot be converted into a different resource. Any released resource must retain its nature.

**Definition 11 (Condition S).** A marked **PN** $M = (R, m_0)$ with $R = (L_0 \cup L_f \cup L_v, T, E, S)$ has condition **S** if for each pair $l, l' \in L_f \cup L_v$ with $l \neq l'$, and for every $t \in T$ and **o-**paths $c(l, t)$ and $c(l', t)$, if they exist, the first encounter between the **o**-paths occurs at a transition.

This condition ensures that, if there are resource tokens from resources of different natures exist, their interaction (synchronization) must occur exclusively through a shared transition, never in a place.

## 4 Mutual Exclusion in Manufacturing and its Generalization

Mutual exclusion occurs when independent processes compete for a common indivisible resource. In the classical modeling of manufacturing systems, if a resource is shared by $k$ distinct processes and each process executes a single routine with no alternatives, the use of said resource can be delimited by an exact pair of events. Formally, the **i-**th process acquires the resource through a specific transition $t_{\alpha i}$ and releases it through another transition $t_{\beta i}$, while the shared resource is modeled by a place $l_E$. This strict dynamics gives rise to the formal definition of simple mutual exclusion, from which important conservation properties for the net are derived.

**Definition 12 (Simple k-mutual exclusion).** Given $M = (R, m_0)$, $R = (L_o \cup L_f \cup L_v, T, E, S)$. A **k-**mutual exclusion **(k-EM)** for $M$ is a pair $(l_E, \varphi)$ such that:

1. $l_E \in L_f$, $m_0(l_E) = 1$ and $\varphi = \{(t_{\alpha 1}, t_{\beta 1}), ..., (t_{\alpha k}, t_{\beta k})\}$, $k \geq 1$, is a finite set of transition pairs that satisfy the following conditions:

   (a) If $i \neq j$, $1 \leq i, j \leq k$, then $t_{\alpha i} \neq t_{\beta j}$, $t_{\alpha i} \neq t_{\alpha j}$ and $t_{\beta i} \neq t_{\beta j}$;

   (b) If $t_{\alpha i} \neq t_{\beta i}$ y $1 \leq i \leq k$, then $\#(l_E, E(t_{\alpha i})) = \#(l_E, S(t_{\beta i})) = 1$ and $\#(l_E, S(t_{\alpha i})) = \#(l_E, E(t_{\beta i})) = 0$. Furthermore, If $t \notin T_\alpha \cup T_\beta$ with $T_\alpha = \{t_{\alpha i} : 1 \leq$

$i \leq k\}$ and $T_\beta = \{t_{\beta i} : 1 \leq i \leq k\}$, then $\#(l_E, E(t)) = \#(l_E, S(t)) = 0$;

(c) If $1 \leq i \leq k$, $l \in L_v$ y $l \in c(t_{\alpha i})$, then $t_{\beta i} \in c(t_{\alpha i})$;

(d) If $1 \leq i \leq k$ and $c(t_{\alpha i}) \cap (L_f \cup L_f) = \{l_E\}$, then $t_{\beta i} \in c(t_{\alpha i})$;

(e) If $1 \leq i \leq k$, $t \in T$ y $t \in c(t_{\alpha i}, t_{\beta i})$, then $t \in c(t_{\alpha i}, t_{\beta i}) = o$-path.

2. If $L_f \cup L_v$ satisfy the conditions **C**L and **S**, $t \in T_\beta$ and $t' \in T_\alpha$, then $\nexists\, c(t, t') = o$-path;

3. There exists a marking $m_1$ and a two-stop sequence of transitions $\sigma$ that contains no transitions in $T_\alpha$ such that $t \in \mathcal{E}(\delta(m_1, \sigma))$, for all $t \in T_\alpha$.

4. For every marking $m_1$, if $t_{\alpha j}$ is fired at $m \in A(R, m_1)$ then for every $t \in T$ such that $c(t_{\alpha j}, t) \neq \emptyset$ and $t_{\beta j} \notin c(t_{\alpha j}, t)$, it follows that $t$ is allowed, and for every sequence of firing transitions $\sigma_j$ that does not contain $t_{\beta j}$ there exists $h_j$ such that $t_{\beta j} \in \mathcal{E}(\delta(m, t_{\alpha j}\, \sigma_j\, h_j))$, moreover, if $m(l_E) = 1$ and $t \in \mathcal{E}(m)$, then $t \notin T_\beta$.

**Lemma 1.** Given $M'$ containing a $k$-EM $(l_E, \varphi)$. If there is a sequence $\sigma$ that does not contain $t_{\beta i}$ such that $t_{\alpha i}\, \sigma\, t_{\beta i}$ is fireable from $m \in A(R', m_0')$, then $\sigma$ does not contain $t_{\alpha j}$ for all $j \neq i$.

**Proof:** Upon firing $t_{\alpha i} \in \mathcal{E}(m)$, $m'(l_E) = 0$. Therefore, the resource is consumed and any $t_{\alpha j}$ with $(1 \leq j \leq k)$ cannot be enabled during $\sigma$. ■

**Lemma 2.** If $M'$ contains a $k$-EM, then $l_E$ is a safe place.

**Proof:** By **Definition 12**, no transition requiring $l_E$ is enabled if $m(l_E)=0$, and release transitions are not fired if $m(l_E)=1$. Thus, $m(l_E) \leq 1$. ■

Let $M$ be a subnet of $M'$ where the resource place $l_E$ is removed, and where the marking is $m=\mu$ whenever $m' = (\mu, m'(l_E))$.

**Theorem 1.** If $M$ is bounded, then $M'$ is bounded.

**Proof:** Every marking $m \in A(R', m_0')$ implies that the sub-marking $\mu$ (without $m(l_E)$) is reachable in $A(R, m_0)$. Since $A(R, m_0)$ is bounded, $\mu$ is bounded. By **Lemma 2**, $m(l_E) \leq 1$. Hence, $M'$ is bounded. ■

**Theorem 2.** If $M$ is non-blocking, then $M'$ is non-blocking.

**Proof:** By induction on $k$. For $k=1$, since $M$ is non-blocking, if the resource is occupied $(m(l_E)=0)$, the net $M$ guarantees that $t_{\beta 1}$ is eventually fired, releasing it. For $k=n+1$, processes compete for $l_E$. Given that $M$ is non-blocking and $l_E$ is cyclically released, there will always be a sequence enabling any $t_{\alpha(n+1)}$. Thus, $M'$ is non-blocking. ■

**Theorem 3.** If $M$ is reversible, then $M'$ is reversible.

**Proof:** Analogous to **Theorem 2**, ensuring that the resource can always be released and the base system can return to its initial state. ■

In many practical cases of modern industry, the behavior of resources is non-linear. A shared resource, such as the aforementioned Articulated Robotic Crane, frequently faces operations with choice. Upon picking up a part, the crane could deposit it at different stations (e.g., Cooling or Rework) depending on the result of an inspection. This flexibility precludes defining the exclusion with a single pair of transitions $(t_\alpha, t_\beta)$ per process. To model this reality without losing mathematical rigor, it is necessary to expand the concept by using a pair of transition sets $(T_\alpha, T_\beta)$ that encompass all possible acquisition and release actions of the resource associated with a process, thereby giving rise to the definition of generalized mutual exclusion.

**Definition 13 (Generalized $k$-mutual exclusion).** A generalized $k$-mutual exclusion for $M'$ is a pair $(l_E, \varphi)$ such that:

1. $l_E \in L_f$, $m_0(l_E) = 1$ and $\varphi = \{(t_{\alpha 1}, t_{\beta 1}), ..., (t_{\alpha k}, t_{\beta k})\}$, $k \geq 1$, is a finite set of pairs of sets that satisfy the following conditions:

   (a) If $i \neq j$, $1 \leq i, j \leq k$, then $T_{\alpha i}, T_{\beta i} \subset T$, $T_{\alpha i} \cap T_{\beta j} = \emptyset$, $T_{\alpha i} \cap T_{\alpha j} = \emptyset$ and $T_{\beta i} \cap T_{\beta j} = \emptyset$;

   (b) If $t \in T_\alpha$, $t' \in T_\beta$ and $t^* \notin T_\alpha \cup T_\beta$, then $\#(l_E, E(t)) = \#(l_E, S(t')) = 1$ and $\#(l_E, S(t^*)) = \#(l_E, E(t^*)) = 0$, where $T_\alpha = T_{\alpha 1} \cup T_{\alpha 2} \cup ... \cup T_{\alpha k}$ and $T_\beta = T_{\beta 1} \cup T_{\beta 2} \cup ... \cup T_{\beta k}$;

   (c) If $t \in T_{\alpha i}$ and $t' \in T_{\beta i}$, then $c(t, t') \neq \emptyset$;

   (d) If $t \in T_{\alpha i}$, $l \in L_v$ and $l \in c(t)$, then there exists $t' \in T_{\beta i}$ such that $t' \in c(t)$;

   (e) If $t \in T_{\alpha i}$ and $c(t) \cap (L_f \cup L_v) = l_E$, then there exists $t' \in T_{\beta i}$ such that $t' \in c(t)$;

   (f) If $t'' \in c(t, t')$, then $t''$ is on an $o$-path $c(t_{\alpha i})$, where $t \in T_{\alpha i}$, $t' \in T_{\beta i}$ with $1 \leq i \leq k$.

2. If $L_f \cup L_v$ satisfy the conditions **CL** and **S**, $t \in T_\beta$ and $t' \in T_\alpha$, then $\nexists\, c(t, t') = o$-path;

3. There exists a marking $m_1$ for a set of transitions $\{t_{\alpha 1}, ..., t_{\alpha k}\}$ where $t_{\alpha i} \in T_{\alpha j}$ and there exists a sequence of transitions $\sigma$ that does not contain any transition in $T_\alpha \setminus \{t_{\alpha 1}, ..., t_{\alpha k}\}$ such that the marking resulting from firing $\sigma$ at $m_1$ enables $t_{\alpha i}$ with $1 \leq i \leq k$.

4. For every marking $m_1$, if $t' \in T_{\alpha j}$ is triggered at $m \in A(R, m_1)$ then for every $t \in T$ such that $c(t', t) \neq \emptyset$ and $T_{\beta j} \cap c(t', t) = \emptyset$, it follows that $t$ can be enabled and for every sequence of triggerable transitions $\sigma_j$ that does not contain $T_{\beta j}$ there exists $h_j$ and $t'' \in T_{\beta j}$ such that the marking reached by the triggering of $t'\sigma_j h_j$ enables $t''$; furthermore, if $m(l_E) = 1$ and $t^*$ is enabled, then $t^* \notin T_\beta$.

**Theorem 4.** Let **M** be a base subnet (without the shared resource) and **M'** the extended net containing a generalized k-mutual exclusion $(l_E, \varphi)$. If **M** possesses the properties of boundedness, non-blocking, or reversibility, then **M'** integrally preserves these properties.

**Proof:** It is evident from **Definition 13** that if $|t_{\alpha i}| = |t_{\beta i}| = 1$ for all $i$, the generalized structure collapses to the simple $k$-mutual exclusion, in which case the proof is given by **Theorems 1**, **2**, and **3**.

For the general case (cardinalities $> 1$), let us observe the marking of place $l_E$. By hypothesis, $m_0'(l_E)=1$. Because the input and output functions are restricted by **point 2** of **Definition 13**, any firing of a transition $t \in T_{\alpha i}$ will consume the only token in $l_E$ $(m(l_E)=0)$. This immediately blocks the firing of any other transition in the union of all $T_{\alpha j}$ sets, ensuring that $m(l_E)$ fluctuates strictly between $0$ and $1$. Therefore, $l_E$ is a safe place. Since $\mu$ (the marking of subnet **M**) is bounded by hypothesis, it is concluded that the global marking in **M'** is also bounded.

Regarding non-blocking and reversibility, suppose a process $i$ captures the resource $(m(l_E)=0)$. Since subnet **M** intrinsically possesses the properties of non-blocking and cyclic behavior, process $i$ will not stagnate in isolation. The natural evolution of **M** guarantees that, regardless of the choice path taken by the process, a state will inevitably be reached that enables the firing of some transition $t' \in T_{\beta i}$. Upon firing $t'$, the resource is restored $(m(l_E)=1)$, allowing the global system to reenable the acquisition sets $T_\alpha$ or return to its initial marking. Consequently, the generalization of the transitions only introduces restrictions in the temporal interleaving order, without destroying the dynamic properties of **M** ■

## 5 Application

Consider an Articulated Robotic Crane at the center of a manufacturing cell, representing a shared resource. Suppose this Crane is required by three distinct processes: Assembly, Inspection, and Cooling; and the aforementioned resource is not released until the current process is completed.

Next, for modeling purposes, the construction is carried out based on **Observation 1**, the previously proposed methodology, and the interpretations of places and transitions, as follows.

1. The operations or activities are those of holding, scanning, and transporting parts by the Crane from **Input Belts A** and **B** for Assembly, from the **Precision Table** for Inspection, and from **Ovens 1**, **2**, and **3** for Cooling. In the system, the resources are the parts and the Articulated Robotic Crane;

2. The admitted activities in the system are $l_2 =$ The Crane holds, scans, transports, and assembles part **A** or **B**, $l_4 =$ The Crane holds, scans, and transports the part to be inspected, and $l_6 =$ The Crane holds and transports parts **1**, **2**, and **3**. Any of these parts is transported one before the other, where such activities do not preserve a precedence relationship;

3. For a part **A** or **B**, the operation of holding, scanning, transporting, and assembling in **Modules 1** or **2** is given in **Figure 1**. The transitions represent the following: $t^1_{\alpha 1} =$ Start of activity $l_2$ from **Input Belt A**, $t^2_{\alpha 1} =$ Start of activity $l_2$ from **Input Belt B**, $t^1_{\beta 1} =$ End of activity $l_2$ to **Module 1**, $t^2_{\beta 1} =$ End of activity $l_2$ to **Module 2**, and $t^3_{\beta 1} =$ End of activity $l_2$ to the Defect **Rejection Bin**.

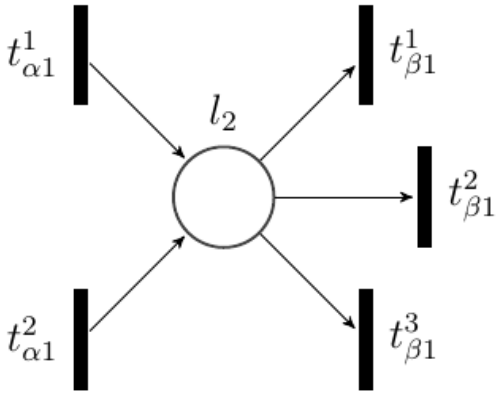


**Figure 1:** A **PN** to model operation $l_2$.

For the **Precision** part, the operation of hold-

ing, scanning, transporting, and inspecting to **Approve** or **Rework** is given in **Figure 2**. The transitions represent the following: $t^1_{\alpha 2}$= Start of activity $l_4$ from the **Precision Table**, $t^1_{\beta 2}$= End of activity $l_4$ to the **Approved Belt**, $t^2_{\beta 2}$= End of activity $l_4$ to the **Rework Table**.

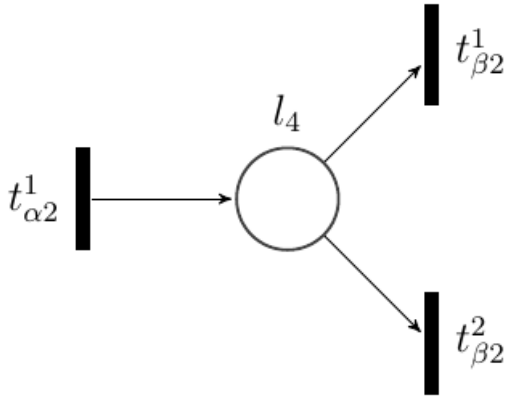


**Figure 2:** A **PN** to model operation $l_4$.

For the **Hot** part, the operation of holding and transporting for **Cooling** is given in **Figure 3**. The transitions represent the following: $t^1_{\alpha 3}$= Start of activity $l_6$ from **Oven 1**, $t^2_{\alpha 3}$= Start of activity $l_6$ from **Oven 2**, $t^3_{\alpha 3}$= Start of activity $l_6$ from **Oven 3**, $t^1_{\beta 3}$= End of activity $l_6$ to the **Drying Belt**.

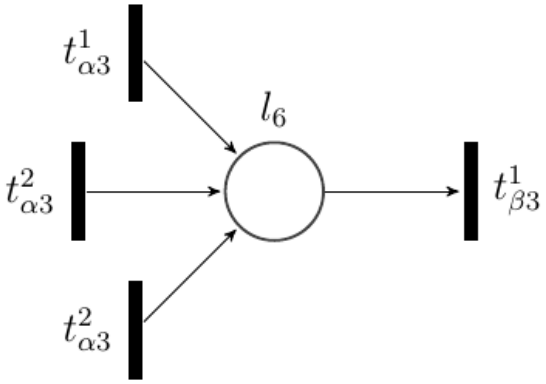


**Figure 3:** A **PN** to model operation $l_6$.

The marking of $l_2, l_4$ and $l_6$ establishes the occurrence of the operation in question;

4. To carry out operations $l_2, l_4$ and $l_6$, the availability of the relevant part and the Articulated Robotic Crane is required. Let $l_1$ = A part **A** or **B** is waiting to be assembled, $l_3$ = A **Precision** part is waiting to be inspected, $l_5$ = A **Hot** part is waiting to be cooled, and $l_E$ = The Articulated Robotic Crane is available to carry out its task. Consequently, places $l_1, l_3$ and $l_5$ are tied to their respective starting transitions, and $l_E$ to all of these without exception; then, $l_1, l_3, l_5$ and $l_E$ become available upon the completion of any activity. Thus, for **Processes 1**, **2**, and **3**, and taking $i=1,3,5$, two directed arcs are constructed from each completion transition to $l_E$ and its respective place $l_i$. This is shown in **Figures 4**, **5**, and **6**. If place $l_i$ is marked with a token, then the part is available; now, if place $l_i$ is not marked, then the respective part is not available. On the other hand, if place $l_E$ is marked, then the Crane is available; otherwise, it is not. Furthermore, if $l_i$ and $l_E$ are marked, then the processes are executable, and in this case, the preconditions for their occurrence are met;

5. Let us consider the initial marking $m_0$= (1,0,1,0,1,0,1), which simultaneously determines the availability of the Crane and the parts to be processed; note that $l_E = l_7$ for our **7**-tuples of marking.

**Observation 2.** The previously described manufacturing system possesses a generalized **3**-mutual exclusion, where $(l_E, \varphi) = (l_E, \{(T_{\alpha 1}, T_{\beta 1}), (T_{\alpha 2}, T_{\beta 2}), (T_{\alpha 3}, T_{\beta 3})\})$, with $T_{\alpha 1}$= $\{t^1_{\alpha 1}, t^2_{\alpha 1}\}$, $T_{\beta 1}$= $\{t^1_{\beta 1}, t^2_{\beta 1}, t^3_{\beta 1}\}$, $T_{\alpha 2}$= $\{t^1_{\alpha 2}\}$, $T_{\beta 2}$ = $\{t^1_{\beta 2}, t^2_{\beta 2}\}$, $T_{\alpha 3}$= $\{t^1_{\alpha 3}, t^2_{\alpha 3}, t^3_{\alpha 3}\}$ y $T_{\beta 3}$= $\{t^1_{\beta 3}\}$. In addition, **L** is partitioned as $L = L_o \cup L_f \cup L_v$, where $L_o$= $\{l_2, l_4, l_6\}$, $L_f$= $\{l_E\}$ and $L_v$= $\{l_1, l_3, l_5\}$. To conclude, the complete **PN** of the system is obtained by coupling the **3** nets to the fixed place $l_E$ from **Figures 4**, **5**, and **6**.

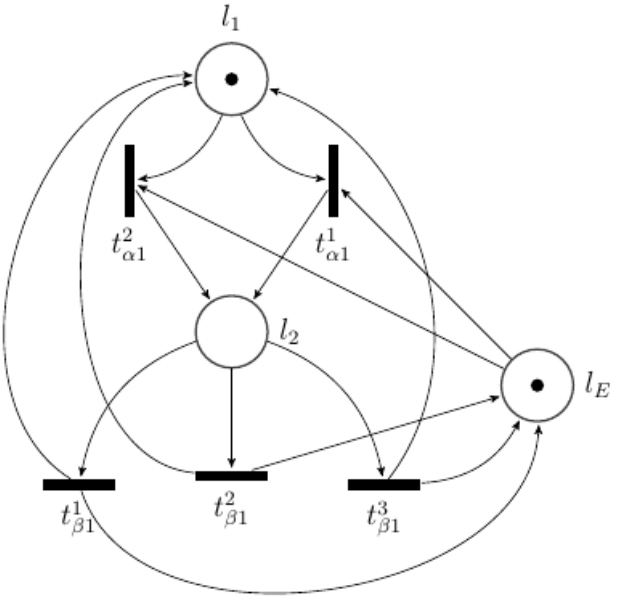


**Figure 4:** A **PN** to model the assembly process.

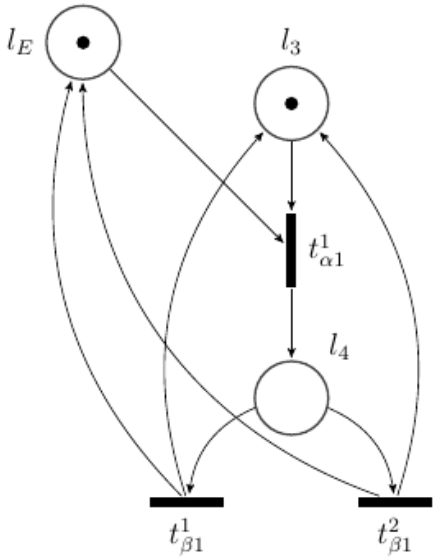


**Figure 5:** A **PN** to model the inspection process.

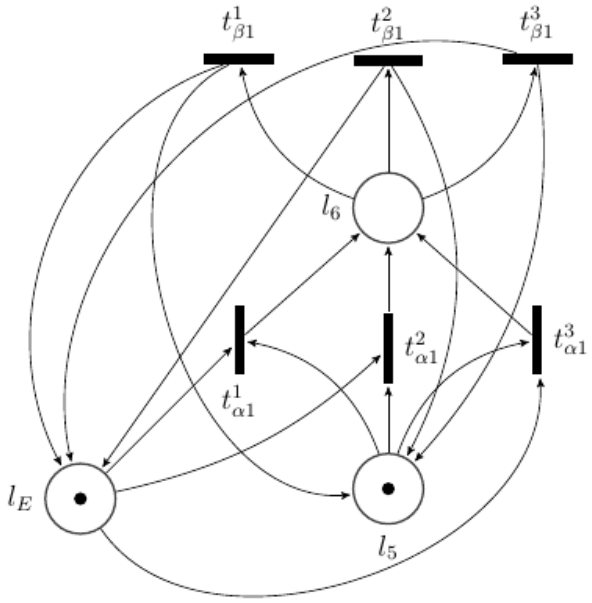


**Figure 6:** A **PN** to model the cooling process.

## 6 Conclusions

The mathematical development of generalized mutual exclusion, transcending the limitations of simple exclusion, responds directly to the demands of modern smart manufacturing.

As demonstrated in **Section 5**, the application of this theory to an Articulated Robotic Crane illustrates how complex and integrated processes—such as Assembly, Inspection, and Cooling—can be successfully modeled, even when shared resources are required to make real-time decisions and select alternative routes.

The formulated preservation theorem (**Theorem 4**) provides an invaluable guarantee: formally certifying that the superposition of this generalized mutual exclusion onto a qualitatively stable process will preserve, without exception, the boundedness, deadlock-freeness, and reversibility of the global system. This synergy between Petri Net algebra and automation allows engineers to directly synthesize—bypassing trial-and-error approaches—supervisory control code that is strictly free from deadlocks and overflows.

## References

Coello, A., & Solé, L. (2022). Generalización de la exclusión mutual en manufactura usando redes de Petri. *Ciencia e Ingeniería*, *43*(2), 129-136.

De Souza, H., & Loreiro, G. (2018). Proposta de um modelo de Planejamento estratégico baseado em engenharia de sistemas. *Revista Espacios*, *39*(13), 10.

Li, Z., Wu, N., & Zhou, M. (2012). Deadlock control of automated manufacturing systems based on Petri nets: A literature review. *IEEE Transactions on Systems, Man, and Cybernetics, Part C (Applications and Reviews)*, *42*(4), 437-462.

Mata, G., Méndez, A., Cardillo, J., & Chacón, E. (2016). Analysis of manufacturing system containing a mutual exclusion in the context of Petri net theory. *Revista Ingeniería UC*, *23*, 30-40.

Zhou, M., & DiCesare, F. A. (1990). Petri net design method for automated manufacturing systems with shared resources. En *Proceedings of the IEEE International Conference on Robotics and Automation*.

***Received:*** *07 de abril 2026*

***Accepted:*** *14 de julio 2026*

***Rosales Moret, José René.*** *Graduate in Mathematics. Master of Science in Mathematics. Active Full Professor. Faculty of Sciences, ULA. Department of Mathematics.*
*https://orcid.org/0009-0006-8265-8181*

**Mata-Diaz, Guelvis E.** *Graduate in Mathematics. Master of Science in Mathematics. PhD in Applied Sciences. Active Full Professor. Faculty of Sciences, ULA. Department of Mathematics. Research area: analysis and control in discrete-event dynamic systems. E-mail: gematad2017@gmail.com*
*https://orcid.org/0000-0001-7147-1422*

***Ferrer-Guillén, María Dolores.*** *Master's degree in Computing. Active Full Professor. Department of Calculation, Faculty of Engineering, ULA. Research area: analysis and control in dynamic systems. E-mail: mariadfg@gmail.com*
*https://orcid.org/0009-0002-8162-233X*

***Mantilla Morales, Gisella.*** *Engineer in Electronics and Telecommunications, Master's degree in Mathematics; full-time professor at the Technical University of Manabí. E-mail: gisella.mantilla@utm.edu.ec*
*https://orcid.org/0000-0002-0826-7741*

***Coello Vera, Adalberto Antonio.*** *Engineer in Agricultural Business Administration, Master's degree in Mathematics; professor at the Technical University of the State of Quevedo. E-mail: adalbertocoellov@hotmail.com*
*https://orcid.org/0000-0001-5985-3532*

**Perez-Pirela, Maribel.** *Chemical engineer. Active Full Professor. Department of Mathematics and Statistics, Faculty of Basic Sciences, Technical University of Manabí. Research area: Mathematics and Statistics. E-mail: maribel.perez@utm.edu.ec*
*https://orcid.org/0000-0002-9687-5471*

*Artículo de Investigación. Revista Ciencia e Ingeniería. Vol. 47, No. 3, pp. 229-242, agosto- noviembre, 2026.*
*ISSN 1316-7081. ISSN Elect. 2244-8780 Universidad de los Andes (ULA)*

# HLB (Balance Hidrofílico-Lipofílico) como novel herramienta para la solubilización de D-limoneno en sistemas de aerosoles

# HLB (Hydrophilic-Lipophilic Balance) as a novel tool for the solubilization of D-limonene in aerosol systems

**Mata-Zabala, Ericson[1,2,3]; Pereira, Juan[1*]**
**[1] Facultad Experimental de Ciencia y Tecnología, Laboratorio de Petróleo, Hidrocarburos y Derivados (PHD), Universidad de Carabobo, Venezuela**
**[2] Corporación Creatón, C.A., Carabobo, Venezuela**
**[3] Suramericana de Aerosoles, C.A., Carabobo, Venezuela**
*jcpereir@uc.edu.ve

**Abstract**

*The primary objective of this study was to employ the well-known colloidal chemistry tool, the HLB (Hydrophilic-Lipophilic Equilibrium) method, for the solubilization of D-limonene in aerosol systems. This was achieved through formulation scans, first in Surfactant-Oil-Water (SOW) systems with an oil phase of heptane + D-limonene (20% to 40%) with a water-to-oil volume ratio (WOR) of 1:1, and then in SOW systems where the heptane in the oil phase was replaced by GLP (A60), and a portion of this, from 20% to 40%, was replaced by D-limonene. Mixtures of non-ionic surfactants (Span© 20, 80 and Tween© 80, 85) were used, and the optimal formulations at phase equilibrium were determined. D-limonene was solubil- ized in the aerosol-sol system at HLB values close to the formulation optimum in HLB scans where the oil phase was hep- tane, to harness the chemical energy of the systems and obtain water-in-oil (O/W) formulations. Thermodynamic stability and micellar aggregate formation were validated by determining the Tyndall effect. The results demonstrate that precise HLB control allows its use as an effective tool for the efficient solubilization of D-limonene in aerosol systems, offering a sustainable technological platform for the potential development of biopesticides, pharmacological agents, other types of products, and delivery systems for molecules that are poorly or insoluble in water.*

**Keywords:** HLB, aerosols, D-limonene, formulation optimum, LPG.

**Resumen**

*Este trabajo tuvo como objetivo central el uso de la muy conocida herramienta de química coloidal, el Método de HLB (Balance Hidrofílico-Lipofílico), para la solubilización de d-limoneno en sistemas de aerosol, mediante barridos de formulación, en primer lugar en sistemas Surfactante-Aceite-Agua (SOW) con fase oleosa heptano+d-limoneno (de 20% al 40% de dicha fase) con una relación volumétrica agua-aceite (WOR) de 1:1 y luego, sistemas SOW donde en la fase oleosa fue sustituido el heptano por GLP (A60) y sustituyó parte de éste, de 20-40% por D-limoneno. Se emplearon mezclas de tensoactivos no iónicos (Span© 20, 80 y Tween© 80, 85), determinando los óptimos de formulación al equilibrio de fases. Luego se realizaron solubilizaciones de d-limoneno en el sistema aerosol, en los valores de HLB parcialmente cercanas al óptimo de formulación en los barridos de HLB donde la fase oleosa era el heptano, para aprovechar la energía química de los sistemas y obtener formulaciones de fase externa agua (O/W). La estabilidad termodinámica y la formación de agregados micelares se validaron mediante la determinación del efecto Tyndall. Los hallazgos demuestran que el control preciso del HLB puede permitir el uso del mismo, como una herramienta efectiva la solubilización eficiente del d-limoneno en sistemas de aerosol, ofreciendo una plataforma tecnológica sostenible, para el posible desarrollo de biopesticidas, agentes farmacológicos, otros tipos de productos y sistemas de liberación de moléculas poco o nada solubles en agua.*

**Palabras claves**: HLB, aerosoles, óptimo de formulación, d-limoneno, GLP.

## 1 Introduction

The HLB (Hydrophilic-Lipophilic Balance) was proposed by William C. Griffin in 1949 as one of the first methods to quantify the hydrophilic and lipophilic balance of surfactants in a SOW (Surfactant-Oil-Water) system. This method assigns a number to each surfactant. However, one of the main weaknesses of this proposal is that it relies on arbitrary assumptions and does not take into account cer- tain trends and variables such as temperature, salinity, and other system characteristics (Griffin, 1949). This initial theoretical-practical approach provided a first formulation scheme called HLB, related to the balance between the hydrophilic and lipophilic (hydrophobic) portions of the molecule. Over time, HLB values have been assigned to many commercial emulsifying agents. In some cases, the HLB number is calculated from the molecule's structure, and in others, it is based on experimental emulsification data (Rosen, 2004).

Griffin proposed a classification of surfactants based on HLB, as shown in Table 1.

Table 2. HLB ranges and surfactant classification

| HLB | Surfactant application |
|---|---|
| 4-6 | EmulsifierW/O |
| 7-9 | Wetting agent |
| 8-18 | Emulsifier O/W |
| 13-15 | Detergents |
| 15-18 | Solubilizer |

In developing an understanding of SOW (Surfactant-Oil-Water) systems, in 1954 Winsor proposed the basic concepts for correlating the phase behavior of SOW sys- tems with the relative interactions of surfactant molecules adsorbed at the oil-water interface. Although Winsor's model simply describes how surfactant, oil, and water interactions affect the physicochemical formulation, its application can be complex in practice. According to the Winsor model, SOW systems can be classified into three types of balanced systems: Winsor I (R = Aco/Acw <1), Winsor II (R = Aco/Acw>1), or Winsor III (R = Aco/Acw = 1), based on the R ratio of affinities of surfactant molecules (C) for oil (O) and water (W), where Aco and Acw are the molecular interactions between the adsorbed surfactant molecule and nearby oil and water molecules (Figure 1). Winsor I sys- tems correspond to an S1-type micellar aggregation of sur- factant molecules, possibly with some oil molecules solubil- ized within, in what is called a swollen micelle. Winsor II systems correspond to S2-type reverse micelles, that is, the opposite structure of surfactant aggregation in the oil phase, eventually with some water solubilization in their core. Winsor III systems, in which the interactions between sur- factant and oil and water are equal, exhibit three-phase be- havior with an intermediate phase that has been represented as a bi- or tricontinuous system of highly complex structures containing fluctuating oil and water domains, resembling an arbitrary “sponge” geometry or other unusual models. Although this phase has been commonly called a “microemulsion,” it should be noted that no emulsion droplets are present (Marquez et al., 2023).

In 1957, Davies introduced a system for the empirical quantification of HLB, taking into account Cassel's work from 1936 and 1938 on Bancroft's rule (the phase in which the stabilizing agent is most soluble will be the continuous phase), the coalescence rate (as the speed of droplet union in a given interfacial film), and the Gibbs free energy of the system. Davies' development of his quantitative theory of emulsion type led him to establish four main conclusions: (i) The emulsion type depends solely on the relative coalescence rates of oil-in-water and water-in-oil systems; (ii) the logarithm of the relative coalescence rates should vary directly with the HLB values for different emulsifiers; (iii) Although Bancroft's rule cannot have a thermodynamic basis, a strict theoretical correlation is established between the relative coalescence rates and the preferential solubility of different emulsifiers in one of the phases, under certain conditions and (iv) the empirical HLB values have a fundamental meaning in terms of free energies, i.e., they must be related to the surfactant distribution between oil and wa- ter under certain conditions (Davies, 1957).

As an evolution of the HLB concept and considering its physicochemical limitations, between the 1970s and 1980s, Salager and his collaborators (1979a, 1979b) intro- duced the HLD concept, which measures the deviation of a SOW system from the optimal formulation state, Windsor type III, where the surfactant's affinity for water or oil be- comes exactly the same and as a result, minimum interfacial tensions are achieved and HLD = 0.

$$HLD = \ln S - kACN - f(CA) + \sigma - \alpha T\,\Delta T$$

Where, S is the salinity of the aqueous phase in % by weight of NaCl; ACN, is the number of carbons (or equivalent) of the alkane used; f(CA), is a function of the concentration of alcohol used as a cosurfactant; σ is a characteristic parameter of the chemical structure of the surfactant used (which increases linearly with the length of the hydrophilic chain); ΔT is the deviation of the temperature from a reference temperature (25 °C) and k and αT are empirical constants (Rosen & Kunjappu, 2012)

On the other hand, limonene is a cyclic monoterpene with the molecular formula $C_{10}H_{16}$ and is an essential oil found in citrus fruits such as lemons, limes, and oranges. It has two optical isomers, with identical chemical properties but different odors. (+)-limonene, or D-limonene, has an orange aroma, while (-)-limonene, or L-limonene, has a pine aroma. The two isomers of limonene are shown in Fig- ure 1 (Royle, 2023).

It is important to highlight that the structural characteristics of D-limonene give it its lipophilic, nonpolar, yet polarizable character due to its double bonds (Figure 2). It has a cyclohexene ring, a chiral center represented by a carbon

atom bonded to four different groups, resulting in the d-(R) and l-(S) enantiomers, represented in Figure 1. Also noteworthy are the two cyclohexene substituents: a methyl group (-$CH_3$) and an isopropenyl group (-$C(CH_3)=CH_2$) at- tached to the ring. Regarding its conformation, the ring is generally shown in a non-planar, chair-like or boat-shaped conformation, making it bent and three-dimensional (IA Gemini, 2025).

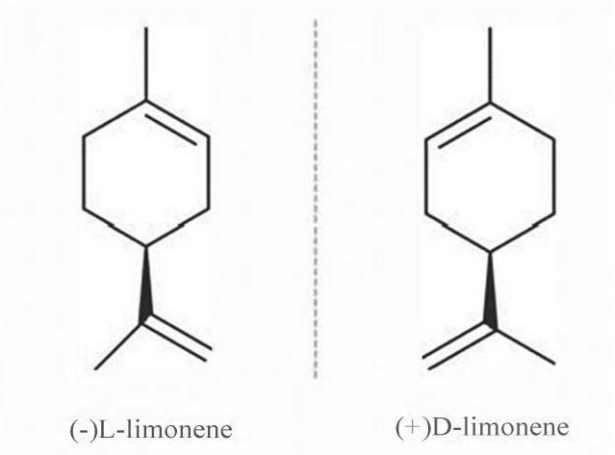


Figure 1.- Optical isomers of Limonene (Royle, 2023)

On the other hand, among the numerous natural compounds, limonene, due to its wide presence in the essential oils of various plants, such as Citrus bergamia, Citrus deliciosa, Montanoa quadrangularis, Juniperus oxycedrus, Citrus unshiu and Bursera graveolens and its excellent bioactivity, has been considered by researchers as a versatile sustainable natural active compound (Lin et al, 2024).

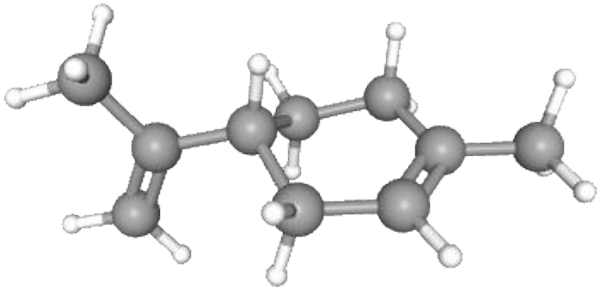

Figure 2. 3D representation of D-limonene.39 CC BY 4.0 License. National Center for Biotechnology Information (2026)

*General Applications of D-limonene*

While studies on the antibacterial7 and antifungal13 activity of D-limonene have been described, a body of knowledge on its mechanisms of action is still being built. Its bioactivity, related to its anthelmintic and pharmacologi- cal activity, potential uses, and, of course, the elucidation of its mechanisms of action and the enhancement of its biolog- ical activity through techniques such as nano- or microencapsulation are also being investigated. There is extensive literature on the antibacterial and antifungal power of D-limonene, as well as its anthelmintic, insecticidal, pharmacological, and antiviral activity (Lin et al., 2024).

*Pharmacological Applications*

Limonene demonstrates remarkable anti-inflammatory effects by modulating pro-inflammatory cytokines and oxidative stress pathways, leading to its inclusion in formulations targeting chronic inflammatory diseases. In oncology, preclinical studies have shown that monoterpenes such as D-limonene have demonstrated the potential to induce apoptosis and inhibit tumor proliferation in combination with metformin (Salim et al., 2024). Furthermore, D- limonene nanoemulsions have been reported to exhibit a strong anti-oral cancer effect by reducing cell viability and cell cycle arrest, making these nanoemulsions a promising alternative therapeutic strategy for the treatment of oral can- cer (Manmuan et al., 2025).

In neuropharmacology, components of essential oils such as linalool, borneol, and α-pinene have been found to modulate the central nervous system, exhibiting sedative, anxiolytic, and neuroprotective effects, which has implications for the treatment of disorders such as anxiety, depression, and neurodegeneration (Kaspute et al, 2025).

*Applications as a biopesticide*

D-limonene, in addition to being an effective insect repellent for direct application to skin and textiles,28 could inhibit the growth of various fungal pathogens, including Pyricularia oryzae (rice blight), Rhizoctonia solani (rice sheath blight), Colletotrichum gloeosporioides (pepper anthracnose), and Phomopsis amygdali (peach bud blight). Notably, the formulation of stable and effective nanoemulsions containing D-limonene offers a practical solution for controlling agricultural crop diseases, complying with FAO regulations, and providing sustainable and environmentally friendly formulations (Ebru et al., 2025).

*Applications in electronics.*

D-limonene has been used as a non-aromatic, non-chlorinated solvent in the electronics industry, specifically for the solution processing of polymers (polyfluorene and copolymers) and conjugated molecules for applications in optoelectronic devices (Zhu et al., 2015).

*Micro- and Nano-emulsification of D-limonene*

To improve the stability and bioavailability of essential oils, and especially those containing D-limonene, various innovative delivery/release systems have been developed. Micro- and nano-emulsification involves solubilizing/encapsulating essential oils or their derived components in protective matrices, preserving their aromatic profiles and therapeutic properties while allowing for controlled re- lease. For example, liposome technology improves the bioavailability of essential oils by encapsulating hydrophilic and hydrophobic compounds, ensuring targeted delivery and sustained release in cosmetic formulations. Self- emulsifying systems further enhance the solubility and ab-

sorption of essential oils, enabling their incorporation into diverse formulations. Overall, essential oils represent a promising and underutilized class of bioactive natural products with considerable potential in modern pharmacotherapy. Their versatility and biocompatibility make them attractive candidates for the development of new therapeutic agents and delivery systems (Kaspute et al., 2025). Based on nanoemulsions, insect repellents have been developed that have demonstrated great potential for controlled release in malaria control, in light of the very worrying reality of insect resistance to pyrethroids (Mapossa et al, 2023). D- limonene microemulsions have also been used for im- proved crude oil recovery, with promising results (Royle, 2023).

Currently, numerous studies focus on the use of essential oils and their micro- or nano-emulsified components as drug delivery systems for oral, parenteral, ocular, pulmo- nary, and topical administration. New herbal formulations based on nanoemulsions and microemulsions can signifi- cantly contribute to the economic growth of the cosmetic, nutraceutical, and pharmaceutical industries. In the future, to overcome the application limitations of essential oils, research could focus on combining different nanocarriers, such as gel systems based on nanoemulsions and nanoemul- sions loaded with nanoparticles. Likewise, essential oils and their micro- or nano-emulsified components have promising prospects in the food industry, as they offer effective methods for improving food safety, performance, and preservation by inhibiting microbial growth. In other words, these micro- and nano-emulsified formulations can serve as natural preservatives, extending the shelf life of food while maintaining its nutritional value and sensory appeal. Furthermore, they can improve the absorption of vital nutrients and antioxidants by encapsulating bioactive substances, thus increasing the value of functional foods. However, alongside these potential advantages and benefits (Figure 3), the optimization of large-scale production techniques, ensuring the stability of the formulations under diverse storage conditions, and regulatory issues are some of the drawbacks that must be addressed for their widespread use (Bolgen et al., 2025).

It is necessary to consider that aerosols, in this work, are understood, beyond their classic definition, not as a suspension of minute particles (from nanometric to micrometric in scale) of solids or liquids dispersed in air or another gas, but as all products packaged under pressure in a metal- lic or non-metallic container, from which various contents are dispensed like a spray by activating a simple valve with the tip of a finger (Yule, 2003). As shown in Figure 4, a typical aerosol container (normally pressurized to 4 or 5 bar, using a liquefied gas), that is, the propellant gas, is a low-boiling-point fluid such as mixtures of hydrocarbons, fluorocarbons, and inert gases like N2, CO2, and even de- hydrated compressed air.

It is important to note that the term aerosol also describes the industry that manufactures such products, which generates considerable confusion, especially given the rigor required by scientific definitions. As a relevant fact, in the early days of the industry, most products were indeed aerosols—liquid insecticides with nanometric particle sizes. Later, products such as shaving foams, which strictly speaking are not aerosols, entered the market. Currently, only some products are aerosols, but most are not (Reed, 1968).

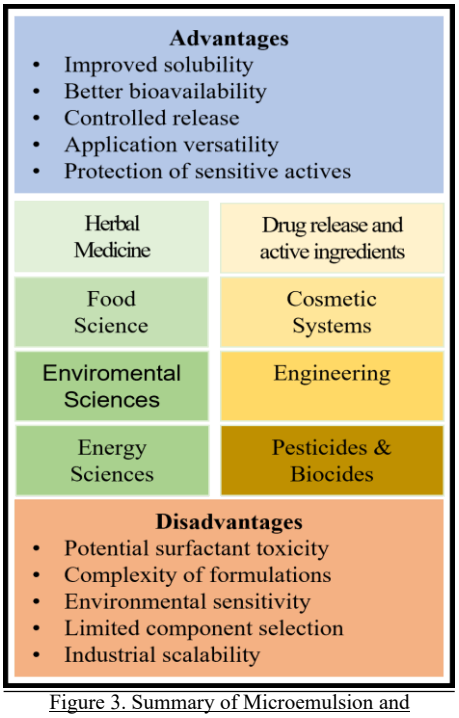


Figure 3. Summary of Microemulsion and Nanoemulsion Applications

It is also necessary to clarify that in English, "spray" is used interchangeably with "aerosol," which always causes confusion. In contrast, in Spanish, "espray" or "spray" is distinct from "aerosol," since "spray" refers to a mechanical pumping system (spraying) and "aerosol" to an application or dispensing system containing a gaseous propellant.

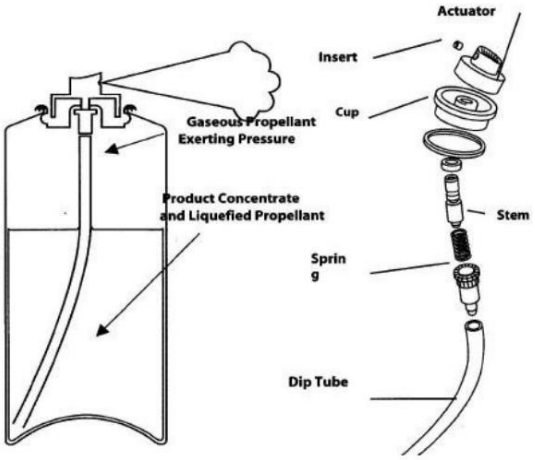


Figure 4. Basic diagram of an aerosol (BAMA, 2022).

Having made the above clarification, it can be said, according to historical records, that the development of aerosol tech-

nology began with U.S. patent 34894, granted on April 8, 1862, to John D. Lynde, a technologist from Philadelphia, USA. He called it a "bottle faucet," and the patent referred to it as an "Improved Bottle for Aerated Liquids" (Lynde, 1862).

In 1899, inventors Heinrich Helbing and Gustave Pertsch received patent US628463A for the development of a system for preparing and applying insulating and coating materials using a propellant such as alkyl chlorides (primarily ethyl and methyl) with or without the addition of alcohol (Helbing & Pertsch, 1899).

However, it wasn't until 1931, in terms of technical and, above all, commercial feasibility, that Erik Rotheim (a Norwegian chemical engineer) received patent US1800156A, entitled "PROCEDURE AND MEANS FOR THE ATOMIZATION OR DISTRIBUTION OF LIQUID OR SEMI-LIQUID MATERIALS," which he had introduced in 1927. According to the patent, the material to be dispensed is packaged in a pressure-resistant (metallic) container along with dimethyl ether, under sufficient pressure to cause the dimethyl ether propellant to liquefy through condensation. The patent description adds that when an outlet is opened in the container holding the material and the condensed dimethyl ether, the material will be expelled under the pressure prevailing in the container. The propellant, which is discharged simultaneously, will evaporate immediately. This patent expands the use of aerosols to atomize or distribute liquids, semi-liquids, or solid substances of any kind (Rotheim, 1931).

Continuing in the vein of evolution and innovation, Julian Kahn received patent US2170531A in 1939 for his APPARATUS FOR MIXING A LIQUID WITH A GAS. This invention is a household appliance for mixing a liquid with a gas, and more specifically, for whipping cream—that is, the mixture of cream and propellant gas—to be dispensed through the appliance's orifice. This appliance was refillable, possessed a protective device or safety valve to prevent excess pressure inside the appliance, and also simplified filling and dispensing, since the valve serves to charge the container with gas and then, by its design, facilitates the formation of cream and gas foam when the contents are dispensed. Another objective of the invention was to greatly simplify the apparatus by using a single valve for two purposes: first, as an inlet valve when filling the container with gas, and second, as a narrow, somewhat labyrinthine passage to induce foaming of the cream and gas mixture (Kahn, 1939).

However, it wasn't until 1941, motivated by military reasons (the need for a product to reduce malaria infections among U.S. military personnel in Southeast Asia), that the research of American inventor and entomologist Lyle Goodhue and entomologist and military officer William Sullivan gave a definitive boost to the development of aerosol technology. Goodhue was a research chemist of lacquer formulations at DuPont Chemical laboratories in 1929, but it was at the U.S. Agricultural Research Center in Maryland, where he developed with Sullivan, his research on an insecticide called "bug bomb", where they used a mixture of pyrethrum, sesame oil and freon 12 (dichlorodifluoromethane). Goodhue and Sullivan applied for the patent in 1941, receiving it in 1943, with the number US2331117A andin whose description it is reported that the invention relates to a dispensing apparatus, and one of the objectives thereof is the provision, in combination with a container adapted to hold a pressurized liquid and a spray device for dispensing the liquid, of means for dosing a predetermined amount of liquid into thecontainer and expelling with the aid of the spray device a predetermined amount or dose, in such a way that each dose dispensed is exactly the same (Goodhue & Sullivan, 1943).

The portability of the Goodhue and Sullivan container, along with its refillable nature, definitively opened up a whole new horizon for aerosols after the end of World War II. But one link remained in the chain of aerosol innovations, and that was, paradoxically, a valve to prevent or facilitate their release. The solution to this technological crux is owed to Robert H. Abplanalp, an American inventor and mechanical engineer, who developed the modern aerosol valve, as It´s knowed it today. His patent, filed in 1949, was granted in 1953 under number US2631814A, VALVE MECHANISM FOR DOSING GASES AND LIQUIDS UNDER PRESSURE31. The facsimile of this patent describes the invention as improvements in valve mechanisms, highlighting that the design is particularly adapted for use with aerosol dispensers, which utilize the principle of mixing a liquefied gas with an active liquid in a container under sufficient pressure to dispense minute particles that can be directed onto an object to form a film, as in the case of paints, waxes, lotions, and others, or for insecticide applications. Germicidals, nasal solutions, and other products where the dispensed active ingredient needs to remain airborne. The Abplanalp design was also adapted for use with either of the two known types of aerosol cans/containers prevalent in the 1950s. One of the many advantages of the Abplanalp design was ensuring the airtightness of the can-valve assembly with a mechanical sealing procedure called "crimping," which prevents propellant leakage and eliminates the need for welding. Another notable advantage was the inclusion of sealing gaskets compatible with the formulations. The design also conformed to the consensus among most contai- ner manufacturers of having a neck with a one-inch diameter (Abplanalp, 1953).

In 1974, a globally significant scientific event occurred when Mexican chemical engineer and postdoctoral student José Mario Molina Pasquel y Henríquez and his advisor, American chemist Frank Sherwood Rowland, presented to the United States Congress the results of their research, "Stratospheric Sink of Chlorofluoromethanes-Atomic Chlorine-Catalyzed Ozone Destruction" (Contreras Nuño et al., 2015). These results, previously published in the scientific journal Nature, revealed that the use of chlorofluorocarbons (CFCs) from the manufacture and operation of refrigeration equipment, and to a lesser extent, from their use as propellants in the aerosol industry (Reed, 1968), contributed to the destruction of the planet's ozone layer. This work earned them both the 1985 Nobel Prize in Chemistry and also triggered a technological leap in the industry. Aerosols, based on scientific evidence and negative opinions about aerosol products, initially slowed their development. However, the industry then replaced freons (CFCs - Chlorofluorocarbons) with fluorocarbons, and from 1989 onwards, the aerosol industry voluntarily eliminated CFCs from its products, except for specific applications such as medical inhalers. Despite this change, flammable

liquefied gases with high VOCs persist as propellants. However, they are often replaced by compressed gases such as nitrogen, carbon dioxide, or even compressed air, which are inert gases that not only have a lower environmental impact but are also more stable (Niemiec et al., 2021). Unlike petroleum gases, however, they experience a pressure drop in the container during dispensing, since they are in a gaseous state.

However, the development of aerosols is a multifaceted one, given the complexity of the system in terms of container type, propellants, valves, and other aspects. This technology fac- es immense challenges because, according to data from the European Commission report "Evaluation of Directive 75/324/EC on Aerosol Dispensers," demand for aerosol products was expected to exceed 18 billion units by 2020. This visible quantitative increase in the aerosol products market simultaneously indicates the need for innovation in this industry segment. The main driver of innovation in this technology is the environment and the requirements of regional and global environmental bodies. Manufacturers of metal containers (tinplate and aluminum), as well as those of plastic containers, are focused on finding innovative solutions in their respective fields. Aluminum and stainless-steel containers have limitations related to the specific properties of the material. The advantages of using plastic as a packaging material include: elimination of corrosion and oxidation, reduced container weight, more flexible delivery times, and, importantly, the lower carbon footprint of modern plastics compared to metals. Ongoing developments in Bag-on-Valve(BOV) technology should also be noted. This technology not only has a less negative environmental impact by using air and nitrogen as propellants, but also offers consumer benefits by reducing the use of preservatives, extending product shelf life, and simplify- ing formula application (Niemiec et al., 2018).

The aim of this research work was to apply the HLB technique for the solubilization of different percentages of D-limonene in the aerosol system.

## 2. Experimental Procedure

### *2.1 Surfactants*

The surfactants used are commercial surfactants, purchased from suppliers that provide the corresponding Certificates of Analysis for the batches purchased, as shown in Table 1.

### *2.2 Reagents*

The reagents used were reagent grade and USP grade, except where otherwise indicated, and were purchased from various suppliers. The only salt used in the different HLB scans was sodium chloride. In the HLB scans, heptane was used as the oil phase; this heptane was distilled at the PHD Laboratory, and D-limonene was used as a substitute in different percentages (20, 25, 30, and 40). In the aerosols, deodorized liquefied petroleum gas (LPG-A60), supplied by UNI-GAS, C.A., was used as the oil phase, along with D-limonene in the same substitution proportions.

For all tests, deionized water with low conductivity (2-3 µS/cm) and pH between 6.8-7 was used, obtained by ion exchange or distillation.

Table 1. Surfactants used for HLB scans

| Surfac-tantType | Commonsurfactantnames | Scan type |
|---|---|---|
| Noóónico | • Span20-SorbitanMonolaurate [2-[(2R,3R,4S)-3,4-dihydroxyoxolan-2-yl]-2-hydroxyethyl] dodecanoate<br>• Span80-Mono-sorbitanoleate (2R)-2-[(2R,3R,4S)-3,4-dihydroxyoxolan-2-yl]-2-hydroxyethyl (9Z)-Octadec-9-enoate<br>• Tween80-Polysorbate80. Polyoxyethylene(20)sorbitanmonooleate<br>• Tween85-Polysorbate85. Polyoxyethylene(20)sorbitantrioleate | HLB |

### *2.3 Equipment and materials*

HLB scans: graduated 15 mL test tubes, burettes, volumetric pipettes, volumetric flasks, and test tube racks were used. An analytical balance with ±0.0001 g precision was used to prepare surfactant stock solutions and salt.

Solubilization of D-limonene in the aerosol-sol system: Safety aerosol test tubes with an average volume of 110 mL, ungraduated, were used with an average pressure of 8.17 atmospheres and aerosol filling machine, fabricated by AILED.

To verify the presence of surfactants and determine the Tyndall effect, both in HLB scans and in the solubilization of aerosol systems, a 640-680 nm laser with a power of 3 mW was used in each phase of the formulated tubes after reaching equilibrium. For photographic documentation of the initial and equilibrium states of each formulated system, natural light was used against a non-glare black back- ground, and an iPhone 8 was used, recording at 4K resolu- tion at 60 fps.

### *2.4 Experimental Methodologies*

HLB scans: Formulation scans were performed, oil-water-surfactant scans where the formulation variable is the HLB (Hydrophilic-Lipophilic Balance) of a mixture of non-ionic surfactants, in our case Span 80, Span 20, Tween 85 and Tween 80, whose individual HLB values are respective- ly: 4.3; 8.6; 11 and 15, with the minimum HLB being 4.3 and the maximum 15. Mixtures of the surfactants are made in different proportions to obtain an HLB scale and the sa- linity (1%), the hydrocarbon (heptane) and D-limonene (its substitute part in the percentages 20, 25, 30 and 40% of the oil phase) and the 2:1 mixture of sec-butanol/pentanol are kept constant. The objective was to evaluate for each percentage of substitution of D-limonene, in what proportion of surfactants or HLB, the optimal formulation is obtained, whose characteristics are indicated above.

In each formulation tube, the SOW (surfactant-water-oil) systems contained a water:oil volume ratio of 1:1, i.e.,

WOR=1. Each phase contained a volume of 5 mL, to obtain a total volume of 10 mL in each analyzed tube.

The tubes were prepared by adding the components in the following order: a) low HLB surfactant, Span 80, and then the mixtures for each previously calculated HLB, b) water and sodium chloride solution, c) high HLB surfactant, d) oil (heptane), and e) the alcohol mixture. The tubes were gently shaken by hand three times.

The tubes were left to stand to allow the systems to reach phase equilibrium, defined as the state where no changes occur in the visible configuration of the system. Once in equilibrium, the presence of surfactants in each phase of the formulated tubes was verified using a laser to determine the existence of micellar formations or micro- emulsions. Photographic records were made of the systems at the beginning and when they reached equilibrium.

The tube with the optimal formulation was designated as the tube where a three-phase system is formed, with similar volumes (Pereira, 2009; Salager et al, 1979b). In cases where the optimum is not obtained, the changes in HLB values are refined, usually by 0.1. This scale refinement is called the HLB scan zoom.

D-limonene solubilization by HLB: The previous formulation scans performed with the heptane oil phase, formulated according to the HLB criteria of a mixture of non-ionic surfactants, in our case Tween 85 and Tween 80, whose individual HLB values are 11 and 15 respectively, served as the basis for this part of the experimentation. In each formulation tube, the surfactant/water/oil systems con- tained a water:oil volume ratio of 1:1, i.e., WOR=1. Each phase contained a volume of 20 mL, to obtain a total vol- ume of 40 mL in each analyzed tube.

Four D-limonene solubilization systems were studied, at 20%, 25%, 30%, and 40% of the oil phase. The selected HLB values are listed in Table 2.

Table 2. HLB for the solubilization of different % of D-limonene

| Sistema | %de D-limonenobde afaseoleosa | HLB óptimo | HLB,regiónhidrofílica(>opt) | | | |
|---|---|---|---|---|---|---|
| | | | T1 | T2 | T3 | T4 |
| 1 | 20 | 10,7 | 11,1 | 11,6 | 12,1 | 12,6 |
| 2 | 25 | 11,2 | 11,6 | 12,1 | 12,6 | 13,1 |
| 3 | 30 | 10,9 | 11,3 | 11,8 | 12,3 | 12,8 |
| 4 | 40 | 11,1 | 11,5 | 11,9 | 12,4 | 12,9 |

The premises for selecting the solubilization HLB values were as follows:

1. Heptane, in the reference HLB scans, was replaced with liquefied petroleum gas (LPG) A60 as the oil phase.

2. For all systems, HLB values close to the optimum were chosen, excluding those where three-phase systems (pseudo-optimums) formed, starting at the first point with an HLB value 0.4 points above the optimum.

3. Aerosol packaging was developed only in the hydrophilic region (>opt) with HLB values increasing by 0.5 points after the initial tube (T1). This criterion is linked to the general objective of this doctoral thesis, which refers to the study of SOW systems with an exter- nal water phase in aerosol applications, that is, O/W emulsification systems.

4.-The lowest HLB value is 11.1 and the highest HLB value is 13.1

The tubes were left to stand to allow the systems to reach phase equilibrium, defined as the state where no changes occur in the visible configuration of the system. Once in equilibrium, the presence of surfactants in each phase of the formulated tubes was verified using a laser to determine the existence of micellar formations or microemulsions. Photographic records were made of the systems at the beginning and when they reached equilibrium. Two tubes were selected from each system, result- ing in a total of eight. These were selected based on the criteria of greatest solubilization of D-limonene and microemulsion formation. The contents of these tubes were collected in glass bottles, allowing them to degas (the oily phase of LPG—liquefied petroleum gas) and were then identified.3 Discusión y Resultados

*3.1 HLB scans with heptane and D-limonene*.

As initially stated, the process of examining the phase behavior of SOW systems was carried out using commercially available surfactants widely used in industry, such as Span 20, Span 80, Tween 80, and Tween 85. It is worth mentioning that the scan technique and the preferred surfactants were chosen based on two technical criteria: first, these surfactants tend to have low foamability in aerosol formulations, and second, the wide- spread acceptance of the SPAN and TWEEN series (CRODA trademarks) as additives in food, cosmetics, pharmaceuticals, and other industries. The HLB scan, unlike the salinity scan, leaves the salinity fixed and through mixtures of non-ionic surfactants in different proportions, it is possible to obtain a scale of HLB values which, in the case of this project, was from 4.3 to 15.

*Initial scan 0% D-limonene (System 1)*

As shown in Figure 5 (System 1), the HLB formula- tion for the Surfactant-Heptane-Water system, with 0% D-limonene, resulted in its triphasic HLB being 11.5. This HLB point is important because, in subsequent systems, It can be observed how the incorporation of a lipophile such as D-limonene affects/shifts the optimum.

Figure 5. Reference HLB scan with fixed concentration of 1% w/v NaCl.

*Scan with 20% replacement of the oil phase with D-limonene (System 2)*

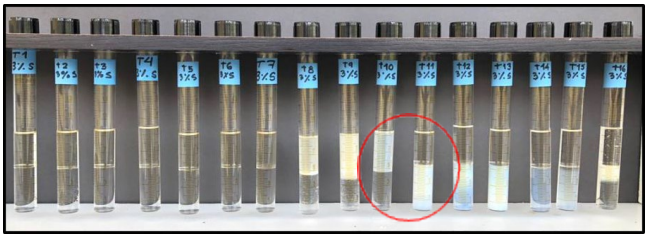

Figure 6. HLB scan (4.3 to 15) with fixed concentration of 1% w/v NaCl.

As can be seen in this scan (Figure 6), a change in the surfactant's location is observed between tubes 10 and 11. That is, in tube 10 the system was a 2 up system (surfactant located in the oil phase or Winsor II) and in tube 11 it was a 2 down system (surfactant located in the aqueous phase, Winsor I), which means that the optimum formulation (Winsor III) is between HLB values of 10.5 and 11. Therefore, a zoom of 10 tubes was performed, with HLB=0.1 graduation, which is described below.

*Zoom of the scan with 20% replacement of the oil phase with D-limonene (System 2)*

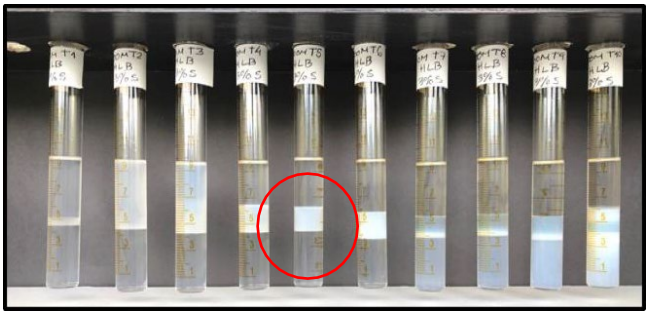

Figure 7. Zoom scan of HLB (T1=10.3 to T10=11.5) with fixed concentration of 1% w/v NaCl. 20% D-limonene in the oil phase

As can be seen in the HLB zoom of system 2 (Figure 7), the formulation optimum (Winsor III) was formed in tube 5 correspondig to HLB=10.7.

*Scan with 25% replacement of the oil phase with D-limonene (System 3)*

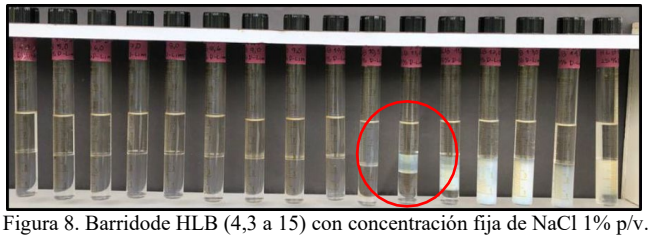

Figure 8. Barridode HLB (4,3 a 15) con concentración fija de NaCl 1% p/v.

In this scan, the amount of D-limonene was increased to 25% (Figure 8) of the oil phase, and the formulation optimum was formed in tube 11 with an HLB value of 11. To determine if this was the true optimum (Winsor III), a zoomed HLB scan was performed between HLB=10.5 and HLB=11.5 with a graduation of 0.1. The results are described in Figure 9.

*Zoom of the scan with 25% replacement of the oil phase with D-limonene (System 3)*

In the zoom of system 3 (Figure 9) it can be observed that in the formulation optimum (Winsor III) it was formed in tube 8 which corresponds to the value of HLB=11.2.

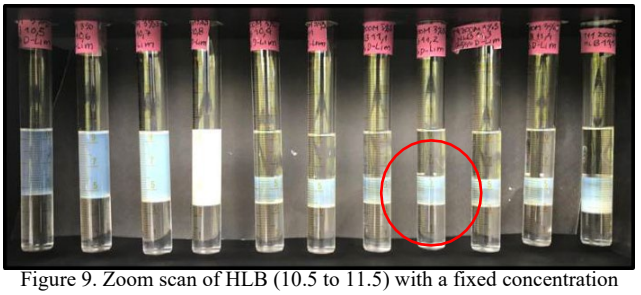

Figure 9. Zoom scan of HLB (10.5 to 11.5) with a fixed concentration of 1% w/v NaCl.

*Scan with 30% replacement of the oil phase with D-limonene (System 4)*

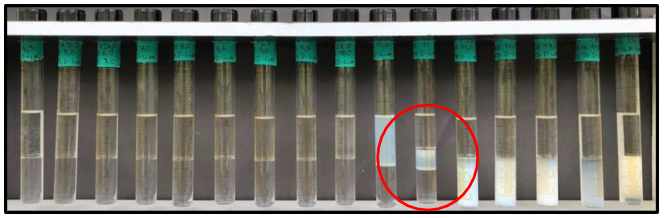

Figure 10. HLB scan (4.3 to 15) with fixed concentration of 1% w/v NaCl.

In this scan, the amount of D-limonene was increased to 30% (Figure 10) of the oil phase, and the formulation optimum (Winsor III) was formed in tube 11 with an HLB value of 11. To determineif this was the true optimum, a zoomed HLB scan was performed between HLB=10.5 and HLB=11 with a graduation of 0.1. The results are described in Figure 11.

*Zoom of the scan with 30% replacement of the oil phase with D-limonene (System*

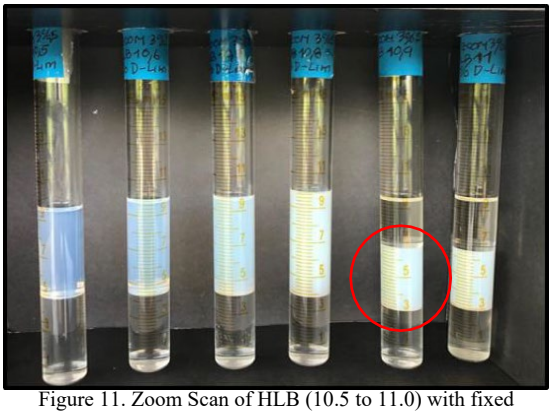

Figure 11. Zoom Scan of HLB (10.5 to 11.0) with fixed concentration of 1% w/v NaCl.

In this zoom it can be observed that the formulation optimum (Winsor III) was formed in the tube 5 which corresponds to the value of HLB=10.9.

*Scan with 40% replacement of the oil phase with D-limonene (System 5)*

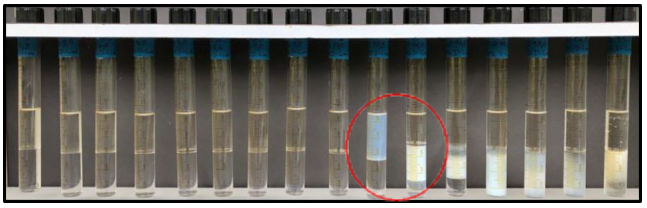

Figure 12. HLB scan (4.3 to 15) with fixed concentration of NaCl 1% w/v.

As can be seen in Figure 12, between tubes 10 and 11 there is a change in the surfactant's location (from Winsor II to Winsor I). That is, in tube 10 the system was a 2 up system (surfactant located in the oil phase, Winsor II) and in tube 11 it was a 2 down system (surfactant located in the aqueous phase, Winsor I), which means that the optimum formulation (Winsor III) is between HLB values of 10.5 and 11. Therefore, a zoom of 10 tubes was performed, with HLB graduation of 0.1, which is described in Figure 13.

*Zoom of the scan with 40% replacement of the oil phase with D-limonene (System 5)*

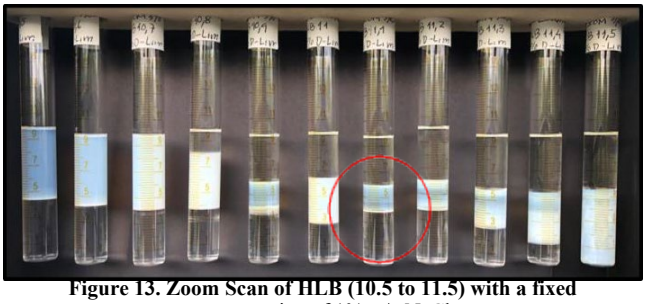

**Figure 13. Zoom Scan of HLB (10.5 to 11.5) with a fixed** concentration of 1% w/v NaCl.

In the zoom of system 5 (Figure 13) it can be observed that the formulation optimum (Winsor III) was formed in tube 7, which corresponds to the value of HLB=11.1.

Table 3 consolidates the data of the optimal HLB values, corresponding to the 5 systems studied, with D-limonene concentrations from 0 to 40% of the oil phase.

The slight reduction in the HLB value could be due to increased segregation of limonene at the interface and a possible change in the surfactant conformation at the interface, considering that heptane, the solvent used in the experiments, is a linear alkyl hydrocarbon and D-limonene is a lipophilic solvent. It has been reported that the dynamic structure of the surfactant monolayer is strongly affected if the packing of the surfactant or its system decreases, causing the system as a whole to incorporate less water and affecting, as in this case, the HLB and therefore the hydrophilicity of the system (Papadimitriou et al., 2008).

Table 3. HLB optims for the solubilization of D-limonene from 0 to 40% of the oil phase.

| System | % D-limonene oil phase | HLB opt |
|---|---|---|
| 1 | 0 | 11,5 |
| 2 | 20 | 10,7 |
| 3 | 25 | 11,2 |
| 4 | 30 | 10,9 |
| 5 | 40 | 11,1 |

*3.2 Solubilization of D-limonene in the aerosol System*

In this experiment, the heptane in the initial HLB scans was replaced with liquefied petroleum gas (LPG) A60, which represents a technological and scientific novelty, since most of the scientific literature refers to formulation scans at atmospheric pressure (Márquez et al., 2023; Salager et al., 1979a; Salager et al., 1979b) and not at 8.16 atmospheres, as is the average of the systems presented below.

As initially stated, the solubilization process was carried out using the formation of SOW systems with the HLB technique. Commercial surfactants, Tween 80 and Tween 85, widely used in industry, were employed. This was cho- sen because it aligns with the overall objective about to ana- lyze SOW systems with an aqueous continuous phase in or- der to reduce VOC. Therefore, solubilization was performed in the hydrophilic region, to which these two surfactants be- long. It is worth mentioning that, in the solubilization tech- nique, the surfactants were selected based on two technical criteria: first, these surfactants tend to have low foamability in aerosol formulations; and second, the Tween series is widely accepted as a food, cosmetic, and pharmaceutical additive. Furthermore, the figures shown represent the equi- librium state of all the solubilization systems performed, thus omitting the initial states.

As can be seen in Figure 14, tubes 2 (HLB: 11.6) and 3 (HLB: 12.1) exhibit the highest amount of solubilized D-limonene. These tubes present two-phase systems, with the lower phase being isotropic and bluish, where the D-limonene is solubilized. It is important to mention that a

three-phase system, which could be called "pseudo- optimal," formed in tube 1. This system was discarded be- cause it violates premise 2 of the solubilization criteria us- ing the HLB scan technique.

*Final State FO System 2-20% D-limonene*

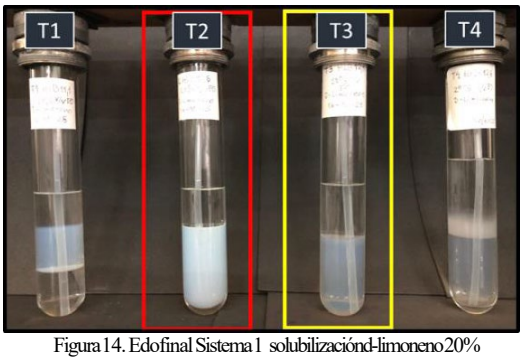


Figura 14. Edofinal Sistema 1 solubilizacióndd-limoneno 20% delafaseoleosa.HLB: T1-11,1/ T2-11,6/ T3-12,1/ T4-12,6, concentración fija de NaCl 1%p/v.

*Tyndall Effect Verification System 2. Selected Tubes (T2 and T3)*

As can be seen in Figure 15, when the red laser is applied to the solubilized phase, the Tyndall effect is confirmed, which is an indication of the formation of ordered solubilization structures, of nanometric order, since they do not cause scattering of the coherent lightbeam.

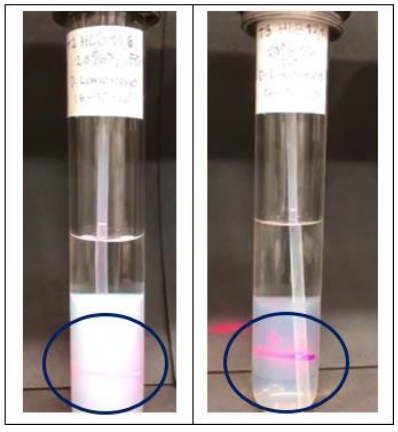

Figure 15. Verification of Tyndall effect, in the selected tubes T2 HLB 11.6 (left) and T3 HLB 12.1 (right) 640 nm red laser.

*Final State FO System 3-25% D-limonene*

As can be seen in Figure 16, tubes 1 (HLB: 11.6) and 2 (HLB: 12.1) exhibit the highest amounts of solubilized D-limonene. As detailed, these tubes present three-phase systems with the solubilized D-limonene in the lower portion, but with two distinct solubilization patterns: one pattern with the formation of a macroemulsion, characterized by its white color, and an aqueous phase in the lower portion, characterized by its isotropic and bluish appearance. It is important to note that in tube 2, the amount of emulsified D-limonene is greater than the amount of D-limonene in the aqueous phase.

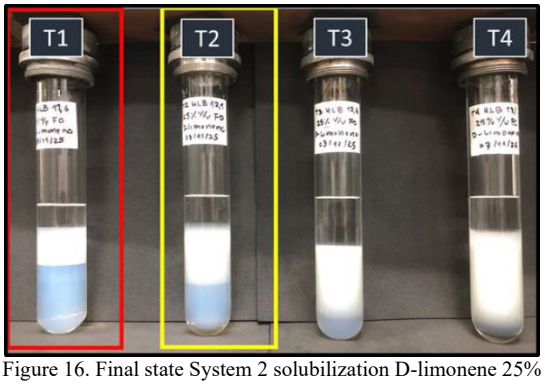


Figure 16. Final state System 2 solubilization D-limonene 25% of the oil phase.HLB: T1-11.6 / T2-12.1 / T3-12.6 / T4-13.1 fixed concentration of NaCl 1% w/v.

It is important to mention that, in tube 4 of figure 16, D-limonene is completely solubilized in an emulsion (white appearance and high light scattering).

*Tyndall Effect Verification System 3. Selected Tubes (T1 and T2)*

As can be seen in Figure 17, when the red laser is applied to the solubilized phase, the Tyndall effect is confirmed, which is an indication of the formation of ordered solubilization structures, of nanometric order, since they do not cause scattering of the coherent light beam.

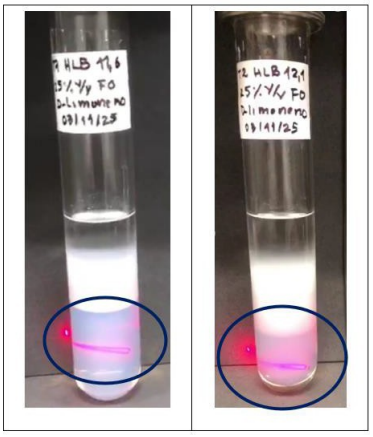

Figure 17. Verification of the Tyndall effect in the selected tubes T1 HLB 11.6 (left) and T2 HLB 12.1 (right) 640 nm red laser

*Final State FO System 4-30% D-limonene*

As can be seen in Figure 18, tubes 1 (HLB: 11.3) and 2 (HLB: 11.8) show the highest amount of solubilized D-limonene. As detailed, the tubes exhibit biphasic systems, with the lower phase being isotropic and bluish, where the D-limonene is solubilized.

It is important to note that, although in tubes 3 and 4

D-limonene is solubilized via aqueous phase, it is done in a smaller quantity, with the presence of a higher phase of solubilization in emulsion (tube 3).

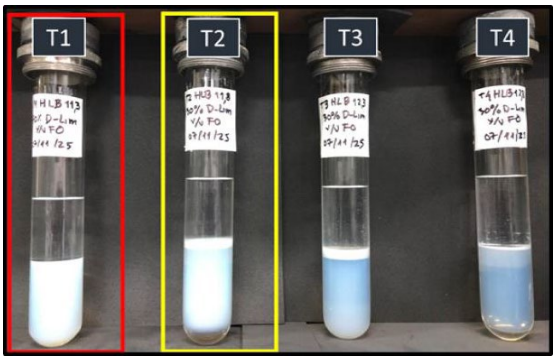


Figure 18. Final state System 3 solubilization D-limonene 30% of the oil phase.HLB: T1- 11.3 / T2-11.8 / T3-12.3 / T4-12.8, fixed concentration of NaCl 1% w/v.

*Verification of the Tyndall Effect in System 4. Selected Tubes (T1 and T2).*

As can be seen in Figure 19, applying the red laser to the solubilized phase of both tubes (1 and 2) confirms the Tyndall effect, which indicates the formation of ordered solubilization structures of nanometric order, since they do not cause scattering of the coherent light beam.

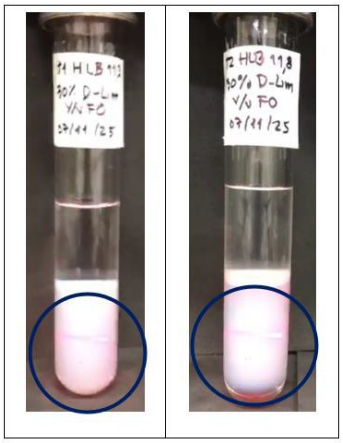

Figure 19. Verification of the Tyndall effect in the Selected tubes T1 HLB 11.3 (left) and T2 HLB 11.8 (right) 640 nm red laser

*Final State FO System 5-40% D-limonene*

As can be seen in Figure 20, tubes 2 (HLB: 11.9) and 3 (HLB: 12.4) exhibit the highest amounts of solubilized D-limonene. As detailed, these tubes exhibit biphasic systems, with the lower phase being isotropic and bluish, where the D-limonene is solubilized.

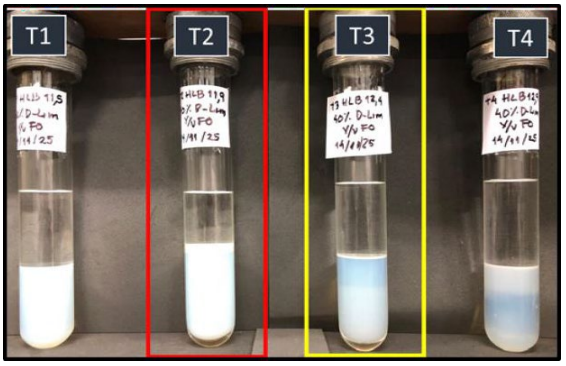


Figure 20. Final state System 4 solubilization D-limonene 40% of the oil phase.HLB: T1-11.5 / T2-11.9 / T3-12.4 / T4-12.9, fixed concentration of NaCl 1% w/v.

*Verification of Tyndall Effect in System 5. Selected Tubes (T2 and T3).*

Como se puede observar en la Figura 21, al aplicar el láser rojo en la fase del solubilizado ambos tubos (2 y 3) se corrobora el efecto Tyndall, lo cual es indicio de la formación de estructuras ordenadas de solubilización, de orden nanométrico, puesto que no causan esparcimiento del haz de luz coherente.

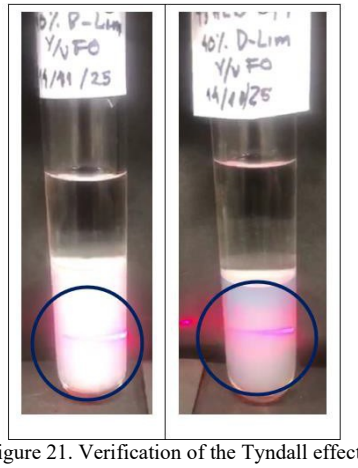

Figure 21. Verification of the Tyndall effect in the selected tubes T2 HLB 11.9 (left) and T2 HLB 12.4 (right) 640 nm red laser

However, the solubilization of D-limonene in SOW systems containing non-ionic surfactants, such as those described above, cannot be explained solely by the chemical affinity of the species. Intermolecular forces also play a role in these systems, and therefore the following premises will be considered to explain them: structural analysis and structural affinity of the components; lipophilic (hydrophobic) phase interactions; hydrophilic phase interactions and the stabilization mechanism by steric effect (Rosen, 2004; Salager et al., 1979b; McClements, 2004; Israelachvili, 2011).

Let's begin with the structural analysis and structural affinity of the components, to understand the forces, based first on the molecular geometries, namely: The Dispersed Phase is made up of D-limonene (from 20% to 40% of the oil phase) and this, as already mentioned, is a cyclic monoterpene (C10H16), with lipophilic, non-polar character, but polarizable due to its double bonds (π electrons) and the aerosol propellant, which is a mixture of low

molecular weight alkanes, such as propane ($C_3H_8$), butane and isobutane ($C_4H_{10}$), which are lipophilic and non-polar.

Among the surfactants are Tween 80 and 85, both non-ionic surfactants of low molecular weight, but with remarkably different characteristics. Tween 80 has a lipophilic tail (oleic acid residue, C18:1) and in this tail, it has a cis unsaturation that creates a "knee" or bend in the chain. The head of Tween 80 is a highly hydrophilic head, due to the polyoxyethylene (POE) groups attached to a sorbitan ring; it is therefore a bulky and highly hydratable head, hence the HLB of Tween 85 is 15. In contrast, Tween 85 has three lipophilic tails, two of which have a cis unsaturation that creates "knees" or bends in the chain, and a shorter tail than the previous ones, which also has an unsaturation, but does not cause the tail to bend. The head of Tween 85 is a less hydrophilic head than that of Tween 80, due to the insertion of the tails in the OH groups, attached to a sorbitan ring, although the head is bulky and is less hydratable and hence Tween 85 has an HLB of 11, that is, less hydrophilic than its counterpart, Tween 80.

Secondly, there are interactions in the oily (lipophilic) phase, which occur in the tails of Tween 80 and 85 and D-limonene. At the internal interface of the droplet, the surfactant tails anchor to limonene, with greater power for Tween 85 and less for Tween 80. Furthermore, quantitatively in the solubilization experiments, for the lowest chosen HLB (11.3), the composition and percentage mixing ratio Tween85:Tween80 is 93:7, and for the highest chosen HLB (12.4), the composition and percentage mixing ratio Tween85:Tween80 is 52:48. Given these characteristics, the following forces govern these systems:

London Dispersion Forces (Van der Waals), as the primary interaction, since D-limonene lacks strong polar functional groups, the attraction is based on fluctuating induced instantaneous dipoles. The long alkyl chains of Tween 80 and 85 maximize the contact points with the terpene ring.

π-π interactions ("weak stacking"): D-limonene has a cyclohexene ring and a vinyl group (double bonds), and the tails of Tween 80 and Tween 85 also have double bonds. According to the principles of supramolecular chemistry, there is a weak, stabilizing interaction in the orbitals between these unsaturated systems (D-limonene-surfactant tails), which improves solubilization compared to saturated-chain surfactants (such as Tween 40 or 60).

Steric Affinity (Geometry): The "curved" structure of the Tween 80 tail and the two Tween 85 tails (due to cis bonds) prevents the formation of rigid crystalline structures at the interface. This favors mixing with D-limonene, which is a spatially bulky and nonlinear molecule (Figure 3).

Thirdly, there are interactions in the aqueous phase, occurring in the head region of Tween 80 and 85 with water. The hydrophilic parts of surfactants extend into the continuous medium through the following intermolecular forces, namely:

Hydrogen bonds occur due to the polyoxyethylene ($-OCH_2CH_2-$) head groups of both surfactants, which contain oxygen ether atoms with lone pairs of electrons. These electron pairs act as hydrogen bond acceptors with water molecules in the medium. Additionally, a fixed amount of electrolyte (NaCl) has been added to the solubilization systems, reducing the repulsion between the head groups.

Dipolar Hydration: A robust "hydration sphere" forms around the surfactant heads, as the water in the systems becomes strongly bound to the Tween polymer network, creating a structured physical water barrier.

Likewise, there is a stabilization mechanism, via steric repulsion, that occurs in the "drop-to-drop" zone. Unlike ionic surfactants such as SDS (sodium dodecylsulfonate), where electrostatic repulsion forces governed by Coulomb's Law act, in the D-limonene/Tween 80 and 85 solubilization system, these systems are stabilized by steric repulsion. In effect, when two emulsion drops approach each other due to Brownian motion, the following physical phenomena occur:

1. Osmotic compression, where the polyoxyethylene heads of both drops begin to overlap, locally increasing the polymer concentration in the contact zone.

2. Thermodynamic Response, where the solvent (water) tends to diffuse toward the high-concentration area to dilute the polymer (Osmotic Pressure), thus separating the droplets again.

3. Entropic Constraint (Excluded Volume Effect), which occurs when the Tween 80 and 85 chains are compressed. These chains lose conformational degrees of freedom (entropy decreases, $\Delta S<0$), and since thermodynamics favors disorder, the system resists this compression, generating an elastic repulsive force.

It is crucial to highlight that, in the case of D-limonene, the hydrophobic effect plays a significant role. This effect is not, in itself, an attractive force for lipophilic molecules, but rather a consequence of the entropy caused by water's ability to form hydrogen bonds. From a classical perspective, this means that when D-limonene is introduced into the system, water is forced to organize itself into clathrate-like structures around the oil phase, resulting in a reduction of entropy. To minimize this entropy loss, the D-limonene molecules and the alkanes in the liquefied petroleum gas aggregate, reducing the surface contact area with water. This aggregation is achieved through the Brownian motion of the solute and solvent: once the hydrophobic molecules aggregate, it is unfavorable for them to redissolve (Google, 2025; González et al., 2011). This theory was formulated by Frank and Evans and is called the "iceberg theory" due to the hypothetical layer of constricted, ice-like water molecules surrounding the hydrophobic molecule. Whether the surface area of the hydrophobic solute is the best measure of the hydrophobic effect is still debated (Norvaišas et al., 2012). Furthermore, the hydrophobic tails of surfactants enhance the solubilizing effect of D-limonene and alkanes. The latter modify the curvature of the interface and thus the solubilizing capacity, because alkanes behave as co-solvents by penetrating these tails, unlike D-limonene, which is a bulky cyclic molecule. In most cases, one of the synergistic effects of this SOW system is a reduction in the viscosity and flexibility of the interface via a decrease in the radius of curvature (Google. 2025; González et al,2011).

Based on the above description, the SOW systems studied are a promising method for aerosol design, where D-limonene can be a nanoencapsulator or nanocarrier of poorly or not at all soluble molecules, in O/W type micro-emulsification systems.

## 4 Conclusions

It is possible to solubilize D-limonene in the studied range (0-40%) and obtain in all cases, systems where formulation optima (triphasic) are observed, that is, with ultra-low interfacial tensions.

The formulation optima obtained are useful for developing formulations using the HLB technique partially outside of these optimal values, in the hydrophilic zone (tentatively at HLB > 11.3), in aerosol systems.

The D-limonene solubilization experiments do not drastically change the HLB and could be used in future work for the solubilization of molecules or active ingredi- ents similar to D-limonene, with the aim of encapsulation and controlled release of these molecules from the oil phase.

Under the given conditions, heptane from the atmospheric HLB scans was successfully replaced by GLP-A60 in the aerosol system solubilizations (pressure of 8.16 atmospheres).

For an HLB value of 11.1 in system 1 (20% D- limonene solubilization), a three-phase Winsor III reac- tion was obtained, with a Tyndall effect in its middle phase. It is possible to solubilize D-limonene (20 to 40%) using the HLB methodology, taking advantage of the system's chemi- cal energy, within the HLB range of 11.3 to 12.4. This re- sults in systems where microemulsions form, and when sub- jected to laser beam testing, the Tyndall effect is observed.

The presence of the Tween 85 and 80 combination is significant for D-limonene solubilization due to the complex and complex interactions between the surfactants, D-limonene, the electrolyte, water, and the propellant gas (the oil phase of aerosol systems).

It remains to evaluate the qualities of the structures of the solubilized materials. For this purpose, 2 solubilizations were chosen for each system, for a total of 8, which will be packaged in aerosol, and their performance will be evaluated under different conditions (different valves and actuators).

## References


Abplanalp, R. (1953) Valve mechanism for dispensing gases and liquids under pressure (Patente de EE.UU, Nº US2631814A) US Patents: https://patents.google.com/patent/US2631814A/en Consulta:3-01-2023.

Bolgen, U. M. G., Kayiran, S. D., Ozogul, Y., & Ozogul, F. (2025). Essential oil-based nanoemulsions with current knowledge Formulation, characterization, and applications in food and pharmaceuticals. Industrial Crops. https://doi.org/10.1016/j.indcrop.2025.121411

British Aerosol Manufactures´ Association (BAMA). Página web. https://bama.co.uk/library. Consulta: 30- 12-2022.

Contreras Nuño, J., Jiménez Álvarez, D. y Pichardo Corpus, J. (2015). Mario Molina y la sagadelozono: ejemplo de vinculación ciencia sociedad., Andamios, 12(2.),15-32. http:/www.scielo.org.mx/scielo.php?script=sci_artext&pid=S1870-06320150003000 15&lng=es&tlng=es. Consulta:21-02-2023.

Davies, J. T. (1957). A quantitative kinetic theory of emulsion type, I. Physical chemistry of the emulsifying agent. In Gas/Liquid and Liquid/Liquid Interface. Proceedings of the International Congress of Surface Activity (Vol. 1, pp. 426-438). https://www.semanticscholar.org/paper/A-QUANTITATIVE-KINETIC-THEORY-OF-EMULSION-TYPE-.-I-Davies/3247eead9a12ee37c1216fd7ab95ebd863823c88

Ebru, T. A., Gamze, D. T., Seyda, K., & Buket, A. G. (2025). Development of insect repellent textiles via treating with microcapsules containing Citrus aurantium L. peel essential oil. Industria Textila, 76(1),62-72. DOI:10.35530/IT.076.01.2024112

Griffin, W.C. (1949). Classification of Surface-Active Agents by 'HLB'. Journal of the Society of Cosmetic Chemists, 1 (5): 311–26. Pdf en línea. Consulta:28-04-2024

Goodhue, L. y Sullivan, W. (1943) Dispensing apparatus (Patente de EE.UU, número US2331117A) US Patents. https://patents.google.com/patent/US2331117A/en Consulta: 3-01-2023.

González, H. H. R., Moroyoqui, P. G., Fernández, I. M., & Cortes, J. D. J. B (2011). Aplicación de Tween 80 y D-Limoneno en la biorremediación de suelo contaminado con hidrocarburos. Ide@s CONCYTEG, 6 (71), pp. 572-584.

Google. (2025). Gemini (standard version) [Hydrophobic effect of D-limonene in microemulsions formed with non-ionic surfactants (Tween 80) and short-chain alkanes]. https://gemini.google.com/

Google. (2025). Gemini (standard version) [Intermolecular forces in a D-limonene system with non-ionic surfactants such as Tween 80]. https://gemini.google.com/

Helbing, H. y Pertsch, G. (1899) Collodion mixture (Patente de EE.UU, número US628463A) US Patents. https://patents.google.com/patent/US628463A/en. Consulta: 2-01-2023.

Israelachvili, J. N. (2011). Intermolecular and surface forces. Academic press. DOI:10.1016/b978-0-12-391927-4.10024-6

Kahn, J. (1939) Apparatus for mixing a liquid with a gas. (Patente de EE.UU, número US2170531A) US Patents

Lynde, J. (1862). Aerosol Dispenser, U.S. Patent #39894," House Divided: The Civil War Research Engine at Dickinson College, https://hd.housedivided.dickinson.edu/node/39026. Consulta: 30-12-22.

Manmuan, S., Weerapol, Y., Chuenbarn, T., Limmatvapirat, S., Limmatvapirat, C., & Tubtimsri, S. (2025). Development of D-limonene nanoemulsions for oral cancer inhibition: investigating the role of ostwald ripening inhibitors and cell death mechanisms. International Journal of Molecular Sciences, 26(11), 5279. https://doi.org/10.3390/ijms26115279

Mapossa, A. B., & Sitoe, A. (2023). Nanoemulsion as a promising carrier of plant-derived repellents for mosquito-borne malaria control: Nanotechnology aspects. In Natural Products in Vector-Borne Disease Management (pp. 499-516). Academic Press. https://doi.org/10.1016/B978-0-323-91942-5.00001-X

Márquez, R., Ontiveros. J.F., Barrios, N., Tolosa, L., Palazzo, G., Nardello-Rataj, V., y Salager, J.L. (2023). Advantages and limitations of different methods to determine the optimum. J Surfact Deterg. 2023;1–32, doi:10.1002/jsde.12703

Norvaišas, P., Petrauskas, V., & Matulis, D. (2012). Thermodynamics of

cationicandanionicsurfactantinteraction.TheJournalof Physical Chemistry B, 116(7), 2138-2144. https://doi.org/10.1021/jp2095888Riojas H. H.,

McClements, DJ (2004). Emulsiones alimentarias: principios, prácticas y técnicas. CRC Press. https://doi.org/10.1201/9781420039436

National Center for Biotechnology Information (2026). PubChem Compound Summary for CID 440917, (+)-Limonene. Retrieved January 10, 2026 from https://pubchem.ncbi.nlm.nih.gov/compound/4R_-1-methyl-4-prop-1-en 2-ylcyclohexene,CCBY 4.0

Niemiec, K., Fitrzyk, A. y Grabowik, C. (2018) Technological solutions and innovations within aerosol packaging. IOP Conference Series: Materials Science and Engineering, Volume 400, Issue 2, doi:10.1088/1757-899X/400/2/022040

Niemiec, K., Fitrzyk, A y Grabowik, C. (2021). The circular economy aspects and recycling of materials in the aerosol industry. International Journal of Manufacturing Economics and Management, Vol.I, No.1 / 2021.

Papadimitriou, V., Pispas, S., Syriou, S., Pournara, A., Zoumpanioti, M., Sotiroudis, T. G., & Xenakis, A. (2008). Biocompatible microemulsionsbased on limonene: formulation, structure, and applications. Langmuir, 24(7), 3380-3386. https://doi.org/10.1021/la703682c

Pereira, A., Juan C. (2009). Fenómenos de ruptura e inversión de emulsiones: aspectos fisicoquímicos y cinéticos. Tesis Doctoral. Universidadde LosAndes.

Reed, F. T. (1968). Aerosol Industry Literature. Literature of Chemical Technology, 632–635.doi:10.1021/ba-1968-0078.ch038

Rosen, M. (2004) Surfactants and interfacial phenomena / Milton J. Rosen. John Wiley & Sons, Inc. 3 ra ed. Cap 4 y 8.

Rosen, M. J., & Kunjappu, J. T. (2012). Surfactants and interfacial phenomena.JohnWiley&Sons.4th Ed.

Rotheim, E. (1931) Method and means for the atomizing or distribution of liquid or semiliquid materials. (Patente de EE.UU, número US1800156A) US Patents. https://patents.google.com/patent/US1800156A/en Consulta: 2-01-2023. 23.

Royle, M. (2023). Physical Chemistry of Limonene Microemulsions and their Interaction with Oil (Doctoral dissertation, Durham University).

Salager J L, Morgan J C, Schechter R S, Wade W H, Vásquez. (1979a) Optimum Formulation of Surfactant/Water/Oil Systems for Mini- mum Interfacial Tension or Phase Behavior. SPE J. 19: 107–115. https://doi.org/10.2118/7054-PA

Salager, J. L., Bourrel, M., Schechter, R. S., & Wade, W. H. (1979b). Mixing rules for optimum phase-behavior formulations of surfactant/oil/water systems. Society of Petroleum Engineers Journal, 19(05),271-278. https://doi.org/10.2118/7584-PA

Salim, E. I., Alabasy, M. M., Nashar, E. M. E., Al-Zahrani, N. S., Alzahrani, M. A., Guo, Z., & Shahen, M. (2024). Molecularinteractionsbetween metformin and D-limoneneinhibit proliferationand promote apoptosis in breast and liver cancer cells. BMC Complementary Medicine and Therapies, 24(1), 185. https://doi.org/10.1186/s12906-024-04453-x

Yule, A. (2003)The household aerosol:presentand future of theworld's largest market for spray technology. Conference: ICLASS 2003At: Hilton Sorrento, Organisers University of Naples, Italy Volume: Invited Paper, Proc Pub Begell House NY USA. Documento en línea: https://www.researchgate.net/publication/266472050_The_household_aerosol_pre sent_and_future_of_the_world's_largest_market_for_spray_technologyConsultado:6-7-2023

Zhu, Y., Chen, Z., Yang, Y., Cai, P., Chen, J., Li, Y., ... & Cao, Y. (2015). Using D-limonene as the non-aromatic and non-chlorinated solvent for the fabrications of highperformance polymer light-emitting diodes and field-effect transistors. Organic Electronics, 23, 193-198. https://doi.org/10.1016/j.orgel.2015.05.004

***Received:*** *february 28, 2026*

***Accepted:*** *july 13, 2026*

***Mata-Zabala, Ericson L.:*** *MSc in Engineering and Specialist in Higher Education. Executive Director of the Technology Consulting Firm Corporación CREATON, C.A. and Project Director of Suramericana de Aerosoles, C.A.*
*Email: emata1@uc.edu.ve*
***https://orcid.org/0009-0002-7811-8765***

***Pereira Antique, Juan Carlos:*** *PhD in Applied Sciences (ULA). Director at Laborato-ry of Petroleum, Hydrocarbons and Derivatives (PHD). Full Professor, Department of Chemistry at Faculty of Ex-perimental Sciences and Technology, University of Cara-bobo, Carabobo, Venezuela. Industrial Consultant in Inter-facial Phenomena. Email: jcpereir@uc.edu.ve*
***https://orcid.org/0000-0003-4600-726X***

*Research Article. Science and Engineering Journal. Vol. 47, No. 3, pp. 243–250, august–november 2026.*
*ISSN 1316-7081. ISSN Elect. 2244-8780 Universidad de los Andes (ULA)*

# Effect of *Curcuma longa* L. on the antioxidant capacity of three fractions of palm oil.

# Efecto de la *Curcuma longa* L. sobre la capacidad antioxidante de tres fracciones de aceite de palma

**Moreno-Romero, Wilmer[1*], Velásquez, Ingrid[2,3]**

[1] Bioprocessing Laboratory, Simón Rodríguez National Experimental University, Canoabo Campus, Carabobo, Venezuela
[2] Center for Chemical Research, University of Carabobo, Carabobo, Venezuela
[3] Soil and Environmental Research and Technology Laboratory, University of Carabobo, Carabobo, Venezuela
email: wjmr2023@gmail.com

**Abstract**

*Enrichment through maceration or infusion facilitates the extraction of fat-soluble active ingredients that act as a kind of organic solvent. Turmeric is one of the most important spices due to its active biochemical activities. Anti-inflammatory, antioxidant, antibacterial and hypoglycemic qualities have been discovered in curcumin. The composition of the oil plays an important role, this research used three fractions of palm oil, resulting in that for crude oil and olein there was an increase in volatile compounds and a decrease in the peroxide index, while superolein behaved inversely. In terms of phenolic content and antioxidant capacity, the fraction that was the best was palm olein; however, superolein is favored with the inclusion of curcuminoids, given that it is the fraction most susceptible to oxidation. Therefore, the inclusion of this type of extract favored all the fractions studied.*

**Keywords:** Turmeric, enriched oil, palm oil, antioxidant capacity.

**Resumen**

*El enriquecimiento mediante maceración o infusión facilita la extracción de ingredientes activos liposoluble que actúa como una especie de disolvente orgánico. La cúrcuma es una de las especias más importantes debido a sus activas actividades bioquímicas. Se han descubierto en la curcumina cualidades antiinflamatorias, antioxidantes, antibacterianas e hipoglucemiantes. La composición del aceite juega un rol importante, esta investigación empleo tres fracciones de aceite de palma, obteniendo como resultado que para el aceite crudo y la oleína hubo un incremento de los compuestos volátiles y una disminución del índice de peróxido, mientras la superoleina se comportó de manera inversa. En cuanto a contenido de fenoles y la capacidad antioxidante la fracción que resulto mejor fue la oleína de palma, sin embargo, la superoleina se ve favorecida con la inclusión de los curcuminoides, dado que es la fracción más susceptible a la oxidación. Por tanto, la inclusión de este tipo de extracto favoreció a todas las fracciones estudiadas*

***Palabras clave:*** *Curcuma, aceite enriquecido, aceite de palma, capacidad antioxidante*

## 1. Introduction

Among the solvents industrially used for extracting non-polar edible natural products such as colorants, flavors, fragrances, or lipids, hexane is the most widely utilized, forming part of the list of extraction solvents permitted in the manufacture of food products or food ingredients. However, this substance is also known to be toxic (Cravotto et al., 2022), and substantial scientific evidence highlights the adverse effects associated with solvents like n-hexane. Another vital aspect to consider when implementing an extraction technique is economic viability, particularly when scaling up to an industrial level. A techno-economic cost-benefit analysis must include byproduct valorization and the added value derived from enhanced oil quality through the co-extraction of secondary compounds (Rodríguez-Blázquez et al., 2025).

Plant secondary metabolites are commonly extracted using conventional techniques such as maceration, hydrodistillation, Soxhlet extraction, and heat-reflux. Despite their efficiency, these methods carry the risk of degrading target compounds due to high temperatures and prolonged extraction times. Efforts to overcome the drawbacks of conventional extraction methods have led to the implementation of 'green technologies'. These approaches offer multiple processing advantages while minimizing environmental impact by significantly reducing or entirely replacing organic solvents with green alternatives (Wong-Paz et al., 2020).

Vegetable oils serve as ecological alternatives to petroleum-derived solvents like hexane due to their excellent solvating properties. They represent a versatile class of substances in the chemical industry, and their utilization as solvents, co-solvents, or raw materials for derivative compounds is highly valuable within the field of Green Chemistry. Economically, they are readily available and low-cost. From a biosecurity standpoint, they are non-toxic and safe for small- and large-scale operations. Their application as solvents is gaining increasing traction in the pharmaceutical, cosmetic, and food industries, where they have been successfully employed in drug delivery formulations (Cheikhyoussef & Cheikhyoussef, 2021). These non-polar substances offer the distinct advantage of being non-toxic, non-volatile, and non-irritating, ensuring that endogenous micronutrients—such as phospholipids, sterols, monoglycerides, and diglycerides—do not impede food, cosmetic, or nutraceutical applications (Yara et al., 2017). Consequently, edible oils can be effectively regarded as 'green' solvents for compound extraction.

Curcuma longa, commonly known as turmeric, is an annual herb featuring a short stem, large oblong leaves, and yellowish-brown oval, elliptical, or pear-shaped rhizomes that are occasionally branched. It is widely recognized as a panacea in herbal medicine due to its broad spectrum of pharmacological effects (Jyotirmayee & Mahalik, 2022). Contemporary research confirms that turmeric contains diverse active ingredients, including diarylheptanoids, terpenoids, aromatics, steroids, fatty acids, minerals, and nucleosides. Furthermore, it contains various macro- and microelements, such as K, Mg, Ca, Na, Al, Cr, Cu, Mn, Rb, Sr, and Zn (Tian et al., 2025). Whether administered as a powder, extract, or isolated compound, turmeric demonstrates extensive pharmacological activity with minimal adverse effects. The methoxy group of curcumin on the phenyl ring, alongside its phenolic and 1,3-diketone systems, plays a crucial role in its diverse pharmacological actions. Numerous curcumin- or turmeric-enriched products addressing various health conditions are available in both domestic and international markets. Unlike other phytoantioxidants, curcumin is safe, non-toxic, and acts as a potent natural component (Jyotirmayee & Mahalik, 2022).

Curcumin rapidly degrades via autoxidative transformation into various chemical species, a mechanism suggested to be driven by oxidative stress induction (reactive oxygen species, ROS). The stability of these compounds is closely linked to the solvent medium. In this regard, edible vegetable oils have proven to be promising green solvents for extraction and have gained popularity for isolating bioactive compounds. These oils are renewable and non-toxic resources, as their fatty acid esters do not emit volatile organic compounds (VOCs) and offer technical performance comparable to organic solvents used in extracting biocompounds from plant matrices (Cardoso et al., 2024).

This research investigates the incorporation of bioactive compounds present in Curcuma longa L. using three palm oil fractions as extraction solvents: crude palm oil (CPO), palm olein (PO), and palm superolein (SOP), evaluating their subsequent effect on antioxidant capacity. The resulting products can be defined as flavored or gourmet oils, depending on the botanical source of the extracted compound.

## 2. Experimental procedure

### 2.1. Treatment of turmeric rhizomes

Turmeric rhizomes were manually washed to remove all soil traces, then drained and dried at room temperature for six (6) hours. Subsequently, they were sliced into approximately 4 mm thick flakes and dried in a convection oven at 45 °C until reaching a constant weight. The dried flakes were milled and sieved using an 8" x 2" stainless steel ASTM N° 80 sieve (180 µm mesh opening) and

stored at room temperature in airtight polyethylene bags. A proximate analysis of the resulting turmeric powder was performed using Near-Infrared Spectroscopy (NIR).

### 2.2. Characterization of palm oil fractions

The three palm oil fractions (crude palm oil, palm olein, and palm superolein) were characterized by determining their relative density using pycnometry at 20 °C (COVENIN 703, 1996); the iodine value using the Wijs method (COVENIN 324, 1996); free acidity by volumetric titration with 0.1 N KOH, expressed as oleic acid (COVENIN 325, 1996); the peroxide value by volumetric titration of the released iodine with 0.01 N $Na_2S_2O_3$ in a mixture of acetic acid and chloroform (COVENIN 508, 1997); the refractive index, measured directly at 15 °C with a refractometer (COVENIN 702, 1996); the saponification index by volumetric titration with 0.5 N HCl following saponification with 0.5 N methanolic KOH (COVENIN 323, 1981); and the unsaponifiable matter according to COVENIN 326 (1997).

### 2.3. Extraction of bioactive compounds using vegetable oils as solvents

The extraction was carried out by maceration, placing the turmeric powder in contact with the different palm oil fractions at a sample-to-solvent ratio of 3:17 (w/w). Maceration was conducted at room temperature for 48 hours. Following extraction, the mixtures were centrifuged at 2,000 rpm to separate the solid residue from the enriched vegetable oil. The resulting oils were bottled in amber glass containers and stored at 8 °C until subsequent analysis. The bioactive-enriched oils were characterized by determining the percentage of volatile compounds and total phenolic content using the Folin-Ciocalteu colorimetric method, with results expressed as milligrams of gallic acid equivalents per gram of sample (mg GAE/g). All assays were performed in triplicate, and antioxidant capacity was determined using the DPPH radical scavenging assay.

## 3. Results and Discussion

Curcumin is a natural polyphenolic compound and a potent hydrophobic bioactive compound. It is a yellow dye found in the rhizome of turmeric (Curcuma longa). Turmeric contains between 3% and 5% curcuminoids, which include curcumin (77%), demethoxylation (17%), demethoxylation (3%), and a negligible amount of cyclocurcumin. Often, the term 'curcumin' is used interchangeably with the term curcuminoids (Sabet et al., 2021).

### 3.1. Proximate analysis of turmeric powder

Table 1 shows the results of the proximal analysis of powder obtained from turmeric rhizomes. Moulick et al. (2023) reported a moisture content of 8.68% and fat of 7.27% in turmeric rhizomes. Meanwhile, a more recent study shows that the moisture, protein, fiber, fat, ash, and carbohydrate content are 5.59, 8.73, 7.06, 5.61, 5.06, and 67.95%, respectively (Olayinka, 2024), with fat and ash values close to those found in this sample, while the latter is richer in fiber. However, the chemical composition closely depends on the soil conditions where it is grown.

**Table 1.** Proximate analysis of *Curcuma longa* powder

| Parameter | % |
|---|---|
| Moisture | 2.07 |
| Protein | 12.00 |
| Fat | 4.78 |
| Ash | 8.84 |
| Crude Fiber | 29.67 |
| Carbohydrates | 42.64 |

### 3.2. Physicochemical characterization of palm oil fractions

Table 2 shows the physicochemical characteristics of the different fractions of palm oil. The acidity and peroxide index for crude palm oil indicate that it is prone to degradation. Peroxides are free radicals that can oxidize and affect the bioactive compounds that you want to extract. In the case of olein and superolein, the values are low, making them good candidates as extraction solvents, ensuring chemical stability and no alteration of the compound to be extracted.

**Table 2.** Physicochemical characterization of the different palm oil fractions.

| Parameter | Crude Palm Oil | Palm Olein | Palm Superolein |
|---|---|---|---|
| Relative density at 20 ºC | 0.899 ± 0.006 | 0.913 ± 0.004 | 0.901 ± 0.001 |
| Refractive index at 40 ºC | 1.451 ± 0.002 | 1.457 ± 0.003 | 1.464 ± 0.002 |
| Iodine value (g $I_2$/100g) | 55.68 ± 0.97 | 58.30 ± 0.28 | 64.83 ± 0.03 |
| Free acidity (% oleic acid) | 0.074 ± 0.001 | 0.045 ± 0.000 | 0.015 ± 0.001 |
| Peroxide value (meq $O_2$/kg) | 0.141 ± 0.022 | 0.000 ± 0.000 | 0.000 ± 0.000 |
| Acidity index (mg KOH/g oil) | 3.460 ± 0.080 | 0.425 ± 0.035 | 0.355 ± 0.007 |
| Volatile compounds (%) | 0.059 ± 0.001 | 0.049 ± 0.001 | 0.355 ± 0.001 |

Palm oil is a complex mixture of palmitic acid (saturated) and oleic acid (monounsaturated). Fractionation into liquid (olein) and solid (stearin) components yields products with different optical properties. The Codex Alimentarius has reported refractive index values for crude/refined palm oil ranging

from 1.4550 to 1.4590, for olein from 1.458 to 1.4600, and for superolein from 1.463 to 1.461. Meanwhile, Azad et al. (2021) reported refractive indices of 1.474 and 1.479 for olein and superolein, respectively, correlating these values with the degree of unsaturation in the oils. They also reported iodine values for the olein and superolein fractions of 187.41 mg/g and 205.46 mg/g, respectively—values close to those found in this study.

The reported values (Table 2) show that the vegetable oils are of good quality and can therefore be used as solvents for the extraction of bioactive compounds. The use of edible vegetable oils as solvents has also been considered for the extraction of volatile aromatic compounds, due to their excellent extractability properties for such compounds (Nevado et al., 2012; Li et al., 2014; Sousa et al., 2014; Karoui et al., 2016; Heinrich et al., 2017). Edible vegetable oils used in the green extraction of bioactive compounds offer significant advantages over organic solvents, as they are non-toxic and have minimal impacts on the environment and human health; furthermore, the resulting extracts do not require additional purification steps, since they are already suitable for human consumption or use (Cardoso et al., 2024).

According to other studies, palm oil contains nearly equal amounts of saturated fatty acids (primarily palmitic acid, 44–45%) and unsaturated fatty acids (oleic acid, 39–40%, and linoleic acid, 10–11%). High-quality palm oil used in the edible oil industry contains a large amount of neutral triglycerides. Superolein, on the other hand, is produced by fractionating palm olein, and its content of oleic and linoleic fatty acids is higher than that of palm olein. As the fractionation process progresses, the oil's iodine value increases (Birsen et al., 2021). Palm superolein has a higher content of volatile compounds than palm olein; this is related to the chemical structure and composition of each fraction.

### 3.3. Characterization of bioactive-enriched oils

Enrichment through maceration or infusion facilitates the extraction of fat-soluble active ingredients simply by incorporating and mixing plant extracts into a fatty substance (the oil used for enrichment), which acts as a type of organic solvent (Oubannin et al., 2024). Curcuminoids tend to dissolve in oil due to affinity, which allows them to remain stable in a food matrix.

One of the main bioactive components of turmeric rhizome extract is curcumin, a yellow, hydrophobic polyphenol. It has also been shown to possess therapeutic potential, as well as antioxidant, anticancer, antimicrobial, anti-inflammatory, hypoglycemic, hepatoprotective, and neuroprotective properties, among others. Curcumin's non-toxic nature makes it an ideal therapeutic agent, but its limited bioavailability is a major concern in its application (Sohn et al., 2021).

Table 3 shows the values for the oils enriched with turmeric. In the case of crude palm oil, it can be seen that its peroxide value decreases after being enriched with turmeric; the phenolic compounds present may be responsible for the observed activity. Djikeng et al. (2025) found that supplementation with an antioxidant reduced the peroxide value; this antioxidant contains various compounds such as calebin-A, vanillic acid, vanillin, quercetin, etc., which eliminate free radicals, increase the activity of antioxidant enzymes, and inhibit lipid peroxidation; it exhibits strong free-radical scavenging activity.

**Table 3.** Properties of turmeric-enriched palm oil fractions.

| Parameter | Crude Palm Oil | Palm Olein | Palm Superolein |
|---|---|---|---|
| Peroxide value (meq $O_2$/kg) | 0.087 ± 0.006 | 0.000 ± 0.000 | 0.000 ± 0.000 |
| Volatile compounds (%) | 0.24 ± 0.02 | 0.20 ± 0.02 | 0.18 ± 0.02 |
| Phenolic compounds (mg GAE/g) | 56.70 ± 0.01 | 58.80 ± 0.01 | 39.30 ± 0.01 |
| Antioxidant capacity (%) | 62.76 ± 0.01 | 64.74 ± 0.01 | 53.26 ± 0.01 |

As for volatile compounds, the levels in crude palm oil and olein increased. This increase in volatile compounds is associated with their transformation and a decrease in the peroxide value. This value is a measure of the oxygen content chemically absorbed as lipid hydroperoxides (LOOH), which are considered the primary oxidation products. This implies that the rapid weight gain due to oxygen absorption occurs almost simultaneously with the dramatic decomposition of LOOH into volatile secondary oxidation products (Pashaei & Farhoosh, 2025).

On the other hand, superolein is more susceptible to oxidation; however, the addition of natural antioxidants interferes with the oxidation of its lipid portion, thereby reducing the volatile secondary compounds (Table 3). The most common approach to preventing or delaying lipid oxidation is the addition of natural or synthetic antioxidants to food products. Antioxidants can be defined as any substance capable of delaying or inhibiting substrate oxidation, even at low concentrations (De Oliveira et al., 2025).

The results show that the phenolic compound levels are similar to those reported by Djikeng et al. (2025), who reported a total phenolic content of 40.97 mg EAE/100 g in turmeric extracted with palm oil. Meanwhile, Array et al. (2018) demonstrated that the total phenolic content of the ethanolic turmeric extract was 40.80 mg EAE/100 g. The higher activity of curcumin can be attributed to its

purity. The slight variations in the total phenolic content of turmeric extract compared to the literature can be attributed to the plant's region of origin, its climatic maturity, soil characteristics, genetic factors, etc. The phenolic content may increase with the addition of turmeric and its incorporation into the lipid matrix.

The phenolic compounds in turmeric are known for their antioxidant properties and ability to scavenge free radicals. According to the literature, the oxidative stability of various oils enriched with plant extracts is associated with their polyphenol composition and antioxidant potency (De Oliveira et al., 2025).

The best oxidative stability was observed in the palm olein fraction, which not only had a high content of phenolic compounds but also greater antioxidant potential, resulting in greater stability compared to the other palm oil fractions. The antioxidant capacity of olein (56.19%) and superolein (67.27%) has been reported (Djikeng et al., 2025). Crude oil contains higher amounts of antioxidants (carotenoids and tocotrienols) that provide a protective effect.

The palm oil fractions obtained have different chemical compositions (particularly in terms of triacylglycerol composition and diacylglycerol levels), so their thermal properties can significantly affect the physical quality (especially thermal behavior and sensory characteristics) of the final products. In addition, it is a source of valuable micronutrients, such as sterols, tocopherol, and carotene, which are key factors influencing the product's oxidative stability or shelf life (Jin et al., 2018).

Therefore, adding natural antioxidants to enrich an oil provides greater benefits; in the case of olein, these antioxidants could improve its chemical properties, as curcuminoids donate electrons to free radicals, thereby reducing the peroxide value. In superolein—the fraction most susceptible to oxidative changes—these compounds act as protectors of the double bonds in oleic and linoleic acids, reducing the formation of volatile compounds. Likewise, enriching oils with curcuminoids transforms them into nutraceutical foods with anti-inflammatory, antibacterial, and antioxidant effects, among others.

## 4. Conclusión

The composition of the oil plays an important role; this study used three palm oil fractions and found that, for crude oil and olein, there was an increase in volatile compounds and a decrease in the peroxide value, while superolein exhibited the opposite behavior. In terms of phenolic content and antioxidant capacity, the best-performing fraction was palm olein; however, superolein benefits from the inclusion of curcuminoids, as it is the fraction most susceptible to oxidation. Therefore, the inclusion of this type of extract helps control free radicals.

## Conflict of Interest:

The authors declare that there is no conflict of interest.

## Referencias

Array E. J, Djikeng T. F, Kingne K. F, Kinge E. E. and Womeni H (2018). Effect of different extraction solvents on the phenolic content and antioxidant activity of turmeric (*Curcuma longa*) from South-West Region, Cameroon Food Research 3 (1): 86 - 90 https://doi.org/ 10.26656/fr.2017.3(1).227.

Azad M, Nadeem M, Gulzar N, Imran M. (2021). Impact of fractionation on fatty acids composition, phenolic compounds, antioxidant characteristics of olein and super olein fractions of flaxseed oil. J Food Process Preserv.45: e15369. https://doi.org/10.1111/jfpp.15369

Birsen Yılmaz, Duygu Ağagündüz (2021). Fractionated palm oils: emerging roles in the food industry and possible cardiovascular effects . Critical Reviews in Food Science and Nutrition, 62(7):1990-1998. https://doi.org/10.1080/ 10408398.2020.1869694.

Cardoso R. V, da Silva D. V. T, Santos-Sodré S. d. J. L, Pereira P. R, Freitas C. S, Moterle D, Kanis L. A, Silva L. H. M. d, Rodrigues A. M. d. C, & Paschoalin V. M. F. (2024). Extracción asistida por ultrasonidos verdes de compuestos bioactivos de pimientos Cumari-Do-Pará (*Capsicum Chinense* Jacq.) Emplear aceites vegetales como disolventes. Food 13 (17) 2765. https://doi.org/10.3390/foods13172765

Cravotto C, Fabiano-Tixier A.-S, Claux O, Abert-Vian M, Tabasso S, Cravotto G, Chemat F. (2022). Towards substitution of hexane as extraction solvent of food products and ingredients with no regrets. Alimentos 11: 3412. https://doi.org /10.3390/foods11213412

Cheikhyoussef N, Cheikhyoussef A, (2021). Green sustainable process for chemical and environmental engineering and science. Chapter 1: Vegetable oils as green solvents in the pharmaceutical industry. Solvents for the Pharmaceutical Industry. Pp. 1-11.

De OliveiraSegantini K.C, de Oliveira Santos Junior O, Garcia V.A.D.S, Raspe D.T, da Silva C. (2025) Sunflower Seed Oil Enrichedwith Compounds from the Turmeric Rhizome: Extraction, Characterization and Cell Viability. Separations,

12, 121. https://doi.org/10.3390/ separations12050121

Djikeng, F.T., Ndikum, B.S., Tincho, B.M., Zemoh Sylvia Ninying, V.-T. and Womeni, H.M. (2025), Effect of turmeric root extract on the oxidative stability of palm oil, African walnut oil and their 50:50 and 60:40 blends during accelerated storage. Food Biomacromolecules, 2: 106-121. https://doi.org/10.1002/fob2.70003

Heinrich M, Vikuk V, Daniels R, Stintzing F, Kammerer D, (2017). Characterization of Hypericum perforatum L. (St. John's wort) macerates prepared with different fatty oils upon processing and storage. Phytochemistry Letters. 20, 470–480. http://dx.doi.org/10.1016/j.phytol.2017. 01.004.

Jin J, Jie, L, Zheng L, Cheng M, Xie D, Jin Q, & Wang X. (2018). Características de las fracciones medias de la palma producidas a partir de diferentes caminos de fraccionamiento y sus posibles usos. International Journal of Food Properties, 21(1), 58–69. https://doi.org/ 10.1080/10942912.2018.1437632

Jyotirmayee B. & Mahalik G. (2022). A review on selected pharmacological activities of *Curcuma longa* L. International Journal of Food Properties, 25(1), 1377–1398. https://doi.org/10.1080/10942912.2022.2082464

Karoui I, Msaada K, Abderrabba M, Marzouk B, (2016). Bioactive compounds and antioxidant activities of thyme enriched refined corn oil. J. Agric. Sci. Technol. 18, 79 91.

Li Y, Fabiano-Tixier A.S, Ginies C, Chemat F. (2014). Extracción directa de compuestos aromáticos volátiles en verde utilizando aceites vegetales como disolventes: estudio teórico y experimental de solubilidad. LWT—Tecnología de Ciencia de la Alimentación; 59:724–731. https://doi.org/ 10.1016/j.lwt.2014.05.064.

Moulick S, Jahan F, Badrul MD, Al Bashera M, Sabbir Hasan, Islam J, Ahmed S, Karmakar D, et al. (2023). Nutritional characteristics and antiradical activity of turmeric (*Curcuma longa* L.), beetroot (*Beta vulgaris* L.), and carrot (*Daucus carota* L.) grown in Bangladesh. Heliyon 9(11), e21495 https://doi.org/10.1016/ j.heliyon.2023.e21495

Olayinka I. O. (2024). Proximate, mineral composition and phytochemical analyses of turmeric (*Curcuma longa*) powder. Nigerian Journal of Animal Production, 874–878. https://doi.org/10.51791/njap.vi.6063

Oubannin S, Laila Bijla Youssef El Kharrassi, Moussa Nid Ahmed, Krishna Devkota, Mohamed Ibourki, Abdelhakim Bouyahya, Filippo Maggi Giovanni Caprioli, El Hassan Sakar f, Said Gharby. (2024). Recent advances in the extraction of bioactive compounds from plant matrices and their use as potential antioxidants for vegetable oils enrichment. Journal of Food Composition and Analysis 128, 105995. doi.org/10.1016/j.jfca.2024.105995

Pashaei H, & Farhoosh R. (2025). A New Insight into the Weight Gain Method to Monitor and Evaluate Lipid Peroxidation. Foods, 14(4), 700. https://doi.org/10.3390/ foods14040700

Rodríguez-Blázquez S, Gómez-Mejía E, Rosales-Conrado N, León-González M.E. (2025). Recent Insights into Eco-Friendly Extraction Techniques for Obtaining Bioactive Compounds from Fruit Seed Oils. Foods 14, 2271. https://doi.org /10.3390/foods14132271

Sabet S, Rashidinejad A, Melton L.D, McGillivray D. (2021). Recent advances to improve curcumin oral bioavailability. Trends in Food Science & Technology, 110:253-266. https://doi.org/10.1016/j.tifs.2021.02.006

Sohn S.-I, Priya A, Balasubramaniam B, Muthuramalingam P, Sivasankar C, Selvaraj A, Valliammai A, Jothi R, & Pandian S. (2021). Aplicaciones biomédicas y biodisponibilidad de la curcumina—Una visión general actualizada. Farmacéuticas, 13(12), 2102. https://doi.org/10.3390/pharmaceutics13122102

Sousa A, Casal S, Malheiro R, Lamas H, Bento A, Pereira J, (2015). Aromatized olive oils: Influence of flavouring in quality, composition, stability, antioxidants, and antiradical potential. LWT - Food Science and Technology. 60(1), 22–28 https://doi.org/10.1016/j.lwt. 2014.08.026.

Tian W, Liu L, Chen P. et al. (2025). *Curcuma Longa* (cúrcuma): desde aplicaciones tradicionales hasta focos de investigación en medicina vegetal moderna. Chin Med 20, 76. https://doi.org/10.1186/s13020-025-01115-z

Wong-Paz Jorge Enrique, Aguilar-Zárate Pedro, Veana Fabiola, & Muñiz-Márquez Diana Beatriz. (2021). Impacto de las tecnologías de extracción verdes para la obtención de compuestos bioactivos de los residuos de frutos cítricos. TIP. Revista especializada en ciencias químico-biológicas, 23, e20200255. https://doi.org /10.22201/fesz.23958723e.2020.0.255

Yara-Varón E, Li Y, Balcells M, Canela-Garayoa R, Fabiano-Tixier A, Chemat F, 2017, Vegetable oils as alternative solvents for green oleo-extraction, purification and formulation of food and natural products. Molecules, 22(9), 1474. https://doi.org/10.3390/molecules22091474.

***Received:*** *january 15, 2026*

***Accepted:*** *may 26, 2026*

***Wilmer Moreno:*** *Food Engineer, Master's in Food Biotechnology, Ph.D. in Human Development Ecology, Ph.D. candidate in the Technological Chemistry Program at the Experimental Faculty of Science and Technology of the University of Carabobo, with more than 5 years of research experience. Full-time instructor at the "Simón Rodríguez" National Experimental University.*
**https://orcid.org/0000-0001-8778-7800**

***Ingrid Velásquez:*** *Food Engineer, Master's in Statistics, Ph.D. in Engineering. Full Professor at the Faculty of Engineering, University of Carabobo, with over 15 years of research experience. Industrial consultant in the fields of food science, statistical design of experiments, and interfacial phenomena with applications in agri-food products, hydrocolloids, cosmetics, and petroleum.*
*Email: ingvelasn@gmail.com*
**https://orcid.org/0000-0002-5522-0161**

*Artículo de Investigación. Revista Ciencia e Ingeniería. Vol. 47, No. 3 pp. 251-258, agosto-noviembre, 2026.*
*ISSN 1316-7081. ISSN Elect. 2244-8780 Universidad de Los Andes (ULA)*

# Thermal mineralized waters and active neotectonics in the Mérida terrace, Venezuela: hydrogeochemical and isotopic evidence.

# Aguas termomineralizadas y neotectónica activa en la meseta de Mérida, Venezuela: evidencias hidrogeoquímicas e isotópicas.

**Santiago, Ricardo[1]*; Guerrero, Omar[2]; Molina, Germán[3], Toro, Rosibeth[4], Alarcón, Nayeska[5]**
[1]Faculty of Engineering. School of Geological Engineering ULA,
[2]Faculty of Engineering. School of Geological Engineering ULA,
[3]Faculty of Engineering. School of Geological Engineering ULA,
[4]University of Zaragoza, Department of Internal Geodynamics,
[5]Faculty of Engineering. School of Geological Engineering ULA,
*ricardo.santiago.geol@gmail.com

**Abstract**

*This research evaluates the origin and relationship with neotectonics of the thermomineral waters at the base of the Mérida terrace, Venezuela, by integrating hydrogeochemical, isotopic, and geophysical methods. The main objective was to determine whether these waters, together with La Rosa lagoon, constitute evidence of active faulting associated with the Boconó Fault System. The methodology included in-situ analysis of physicochemical parameters, measurement of stable isotopes ($\delta^2H$ and $\delta^{18}O$) in 14 water samples to trace their origin, the execution of vertical electrical soundings (VES) to identify water tables, and a bathymetric and sedimentological study of the lagoon. The results indicate that all waters are of meteoric origin, with emergence temperatures ranging between 27 °C and 43.5 °C, confirming their thermal nature. Two geochemical affinities were established based on isotopic composition, linking recharge areas (Albarregas River, streams, and La Rosa lagoon itself) with thermal discharge points. The VES revealed shallow and deep water tables that facilitate fluid circulation. Bathymetry of La Rosa lagoon showed a maximum depth of 3.55 m in its northwestern sector, with evidence of active subsidence which, together with its elongated triangular morphology and the presence of microfractures in the sediments, confirms it as a fault sag pond. In conclusion, the hydrothermal system is directly controlled by the neotectonic activity of the Boconó Fault, which acts as a conduit for deep water circulation and generates surface deformation, demonstrating the usefulness of these techniques for mapping active faults.*

**Keywords:** thermal waters, stable isotopes, neotectonics, Boconó Fault, hydrogeochemistry, Mérida terrace.

**Resumen**

*Esta investigación evalúa el origen y la relación con la neotectónica de las aguas termomineralizadas en la base de la meseta de Mérida, Venezuela, integrando métodos hidrogeoquímicos, isotópicos y geofísicos. El objetivo principal fue determinar si estas aguas, junto con la laguna La Rosa, son evidencia de fallamiento activo asociado al Sistema de Falla de Boconó. La metodología incluyó el análisis in situ de parámetros fisicoquímicos, la medición de isótopos estables ($\delta^2H$ y $\delta^{18}O$) en 14 muestras de agua para trazar su origen, la realización de sondeos eléctricos verticales (SEV) para identificar niveles freáticos y un estudio batimétrico y sedimentológico de la laguna. Los resultados indican que todas las aguas son de origen meteórico, con temperaturas de surgencia entre 27 °C y 43,5 °C, lo que confirma su carácter termal. Se establecieron dos afinidades geoquímicas basadas en la composición isotópica, vinculando áreas de recarga (río Albarregas, quebradas y la propia laguna La Rosa) con los puntos de descarga termal. Los SEV revelaron niveles freáticos someros y profundos que facilitan la circulación de fluidos. La batimetría de la laguna La Rosa mostró una profundidad máxima de 3,55 m en su sector noroeste, con evidencia de subsidencia activa que, junto con su morfología triangular alargada y la presencia de microfracturas en los sedimentos, la confirman como una ciénaga de falla. En conclusión, el sistema hidrotermal está directamente controlado por la actividad neotectónica de la Falla de Boconó, que actúa como conducto para la circulación de aguas profundas y genera deformación en superficie, demostrando la utilidad de estas técnicas para la cartografía de fallas activas.*

**Palabras clave**: aguas termominerales, isótopos estables, neotectónica, Falla de Boconó, hidrogeoquímica, meseta de Mérida

## 1 Introduction

The Mérida terrace, located in western Venezuela, is traversed by the Boconó Fault System, one of the most important tectonic structures in the country, widely studied for its seismic activity and influence on regional geomorphology (Alvarado et al., 2021; Schubert & Vivas, 1993). At the base of the natural slope of the terrace, several thermomineralized water springs are found, whose origin and relationship with active tectonics had not yet been studied in detail.

Thermomineralized waters result from the infiltration of meteoric water that circulates at depth, increasing its temperature due to the geothermal gradient and emerging through permeable structures such as faults or fractures (Pinagua, 1992). Their chemical composition is defined by interaction with the geological materials traversed and is usually associated with areas of active tectonics and physicochemical characteristics (salt content, temperature, conductivity, etc.) that can be highly variable and frequently associated with zones of active tectonics (Burguera et al., 1980). These waters can be classified according to their geological origin, predominant chemical composition, and temperature range, allowing distinction between telluric and magmatic systems, different hydrochemical types (for example, chlorinated, sulfated, bicarbonated, or sulfurous), and thermal categories from cold to hyperthermal (Castany, 1971; Clark & Fritz, 1997; Hidromed, 2025).

From a structural point of view, neotectonics studies recent tectonic processes, including active tectonics, responsible for the generation of faults that have experienced movements in the Quaternary and retain reactivation potential (Wallace, 1986; Winslow, 1986). Geomorphological features associated with active faults include linear valleys, scarps, sag ponds, thermal springs, and landslides (Audemard et al., 2007). The Boconó Fault System, a dextral strike-slip structure approximately 500 km in length, crosses the Venezuelan Andes with active segments in the Mérida terrace, including La Rosa Fault, which is located in the study area (Alvarado et al., 2021).

In this context, the present work aims to determine the origin of the thermomineralized waters located at the foot of the Mérida terrace slope, their geochemical evolution, and their relationship with active neotectonics, through the integrated analysis of hydrogeochemical parameters, stable water isotopes, vertical electrical soundings, and the morphometric study of La Rosa lagoon.

## 2 Geological Context

The Mérida Cordillera is one of the most prominent geological and morphological units in western Venezuela; it extends approximately 350 km in a southwest-northeast direction, with a maximum width of nearly 100 km, and is formed by mountain chains associated with reverse, normal, and strike-slip faults controlled by the Boconó Fault System, which accommodates the interaction between the Maracaibo block and the South American plate (Audemard, 2003; Taboada et al., 2000). The basement, of Precambrian–Paleozoic age, includes the Caparo Block, composed of ancient metamorphic rocks covered by Ordovician–Silurian sediments (La Marca, 1997), upon which a complex tectonic evolution is superimposed, encompassing the Hercynian Orogeny and Mesozoic extensional episodes linked to the rifting of the northern margin of South America (Castrillo, 1998).

During the Quaternary, the region was affected by the Mérida glaciation, documented for the late Upper Pleistocene and early Holocene (Schubert, 1976), and the current Mérida terrace functioned as a floodplain filled with fluvial sediments from the Chama, Mucujún, and Albarregas rivers, subsequently incised by fluvial downcutting and tectonic uplift. The Boconó Fault, with NE strike and dextral transcurrent character, divides the cordillera into the Sierra Norte and Sierra Nevada blocks and, together with the Serranía del Escorial, controls the diversion of the Albarregas River and the compartmentalization of the terrace where the city of Mérida is located, characterized by gentle slopes (<5°) on the terraced surface and deeply incised valleys, especially that of the Chama River (Cabello, 1966; Nava, 2009). The local structural geology is dominated by the Boconó–Morón–El Pilar segment of the Venezuelan Fault System, with N45°E strike, 1–5 km width, and length of approximately 500 km (Dávila & Pacheco, 2009), along with active faults in the Mérida terrace, such as Albarregas, La Hechicera, Mucujún, and Jají, which juxtapose Paleozoic, Mesozoic, and Tertiary units and generate intense fracturing, a condition that controls both the geomorphology and the presence of La Rosa lagoon and the associated thermal springs (Google, 2022).

## 3 Methodology

The area is located within the metropolitan area of the city of Mérida, Venezuela, defined through a polygon of approximately 3.5 km² that encompasses the El Carrizal, Las Tapias, and El Chama sectors, summarized in Figure 1.

For its configuration, an analysis of recent aerial photographs and satellite images was conducted (Google, 2022), along with the UTM coordinates of known thermal springs. This was supported by an exhaustive and systematic state-of-the-art investigation, which included the compilation of undergraduate theses, scientific articles, maps, and institutional reports from FUNVISIS, INGEOMIN, and ULA related to the neotectonics of the Boconó Fault, the thermal springs of Mérida State, and the geomorphology of the Mérida terrace. Complementarily, photogeological reconnaissance allowed the identification of straight lineaments, triangular scarps, aligned valleys, and elongated depressions, which are indicative evidence of active fault structures.

Fieldwork was structured in four parallel and key research lines, described as follows:

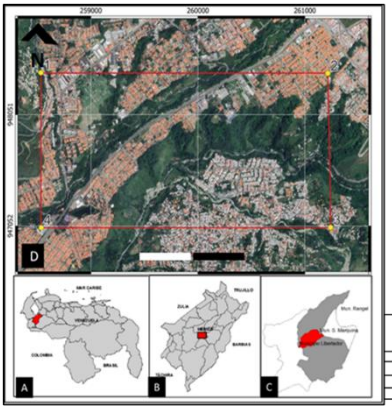


| Punto | Este (m) UTM | Norte (m) UTM |
|---|---|---|
| 1 | 258533 | 948428 |
| 2 | 258533 | 948425 |
| 3 | 258533 | 947032 |
| 4 | 258547 | 947032 |

**Figure 1**. Location of the study area. A: national. B: regional. C: local. D: study area polygon.

**Line 1. Photogeological Analysis and Field Reconnaissance.** During the fieldwork, a structural geological mapping was carried out at a scale of 1:5,000, with systematic recording of strikes and dips of the main discontinuities (fractures, fault planes, and stratification). Additionally, an in situ photogeological analysis was conducted, allowing the correlation of field observations with the main structures recognized in aerial images. Measurements and observations were performed using a geological compass, metric scales, measuring tape, and photographic camera for the recording and documentation of structures. In this context, and with the support of local residents, it was possible to identify more thermal water points than initially planned. A total of four main thermal manifestations were studied, distributed in two zones: three of them located in the El Chama sector and one in the El Chamita sector. At each study point, at least two thermal sub-springs were identified, located very close to each other, forming small groups of closely spatially associated emergences (Figure 2).

**Line 2. Geophysical Characterization.** With the purpose of identifying phreatic levels and characterizing the shallow stratigraphy, two vertical electrical soundings (VES) were carried out (Figure 3), using the Schlumberger array, with a maximum electrode separation AB/2 of 100 m. The measurements were performed using a 270 DAGAN resistivity meter, copper electrodes, and measuring tape for distance control.

The results obtained are presented in Figure 4, where the resistivity variations associated with the different subsurface geological units are observed.

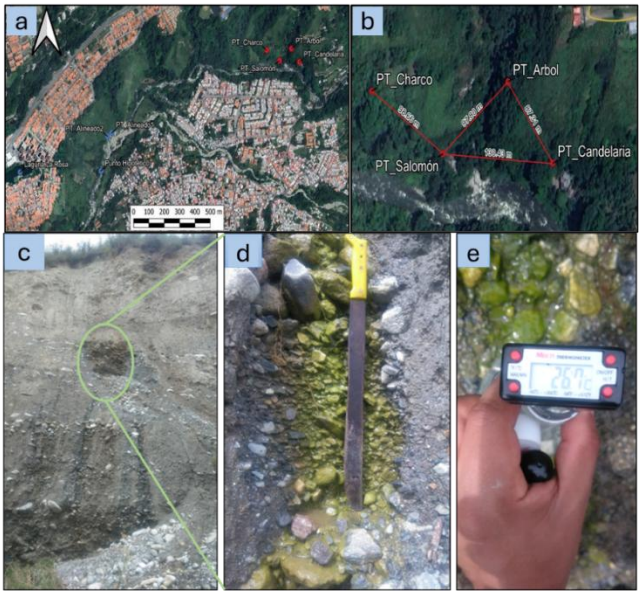


**Figure 2.** A "aligned" thermal spring is presented: the satellite image (a) shows the thermal springs located in the El Galerón sector (El Chamita), while in the close-up (b) the El Chama springs are detailed with their respective distances. In (c), the main scarp of the landslide through which the waters emerge is observed, and in (d) the characteristic green/yellow trail of the microbial mat, formed by thermophilic bacterial pigments. Finally, in (e) the temperature recorded in the hypothermal spring is specified.


**Figure 3.** Location of the electrical line arrays in the execution of the vertical electrical soundings.

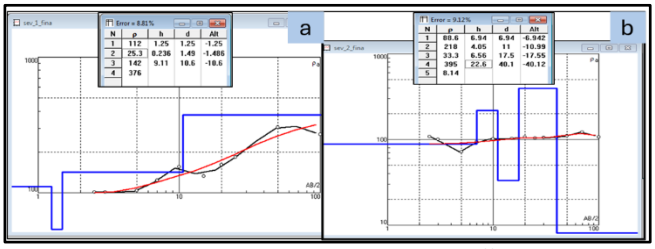


**Figure 4.** Resistivity variations associated with the different geological units encountered. a. VES-1. b. VES-2

**Line 3. Bathymetric Survey and Sediment Sampling.** To characterize the internal morphometry and sedimentary structure of La Rosa lagoon, a bathymetric survey was conducted complemented with sediment core extraction. For bathymetry, a metal raft with barrels at its base was used, which ensured buoyancy during measurement transects (Figure 5a). The survey was performed using the sounding method, appropriate for shallow water bodies, consisting of determining the depth from the vertical distance between the water surface and the lagoon bed. Previously, a navigation grid and a lagoon perimeter line were defined from a vector data model generated in a geographic information system (GIS), upon which several transverse profiles and one longitudinal profile were traced (Figure 5b). In the field, the planimetric position (X, Y) of each measurement point was recorded using a GPS receiver, while the depth elevation (Z) was obtained by lowering a plumb line until contact with the bottom at each station, covering both internal transects and the perimeter of the water body. Positioning was carried out with a global positioning system (GPS) based on the NAVSTAR constellation, which allowed continuous coverage for two-dimensional navigation and georeferencing of sounding points with a 10 m grid.

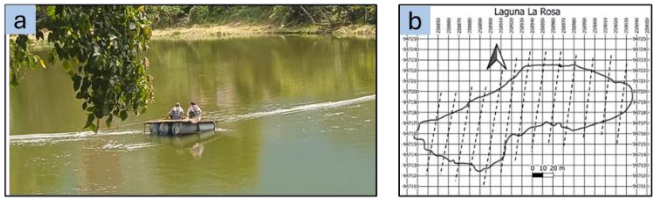


**Figure 5.** a. Image of the metal raft with barrels at its base. b. Sketch of longitudinal and transverse navigation lines, georeferenced with a grid every 10 meters.

The altimetric determination was carried out using a sounding lead consisting of a truncated conical weight suspended from a marked and calibrated sounding line, a technique suitable for water bodies with little wave action such as La Rosa lagoon and in accordance with the objectives of this study.

Complementarily, three sediment cores were extracted (Figure 6), using 3-inch diameter PVC pipes, reaching maximum depths of 1.6 m. Each core was described in detail in terms of lithology, color, texture, and sedimentary structures, using a PVC corer, a 10 kg mallet, spatula, and photographic camera, which allowed preserving the integrity of the material and documenting its characteristics in situ.

**Line 4. Isotopic Analysis.** With the purpose of establishing the origin of the water and its hydrogeochemical evolution, stable isotopes $\delta^{18}O$ and $\delta^{2}H$ were analyzed in 14 water samples (thermomineral waters, surface waters from the Albarregas River, streams, La Rosa lagoon, runoff, and municipal network). The samples were collected with a 24-hour interval post-rainfall in order to avoid the direct influence of recent precipitation on the isotopic composition, using 15 mL PE bottles rinsed X3, sealed with parafilm to prevent evaporation. The analysis was performed at the Water and Soils Laboratory of the Inter-American Center for Environmental and Territorial Development Research (CIDIAT-ULA); using a DLT-100 laser spectrometer (cavity ring-down spectroscopy), precision ±0.3‰ ($\delta^{18}O$) and ±2‰ ($\delta^{2}H$) vs VSMOW. Along with these samples, five of them were additionally destined for physicochemical characterization (temperature, pH, electrical conductivity, and major ions), using a WTW multiparametric probe for the in situ measurement of basic parameters.

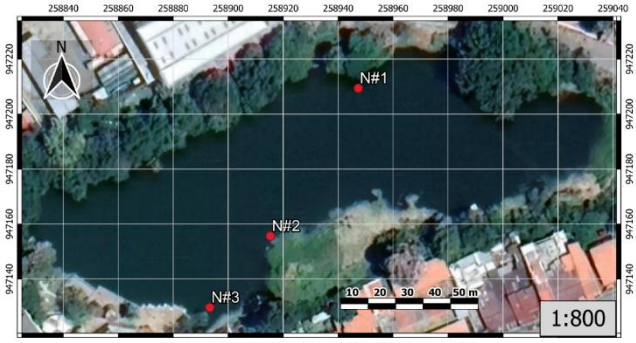


Puntos de Muestreo de Núcleos en la Laguna La Rosa

| ID | Nombre | Norte UTM | Este UTM | Longitud | Punto de Referencia |
|---|---|---|---|---|---|
| N#1 | Núcleo 1 | 947209.7 | 258947.1 | 1.5 m | Entrada principal de aporte de agua de escorrentía |
| N#2 | Núcleo 2 | 947155.3 | 258915.7 | 3.0 m | Más próximo al centro de la Laguna |
| N#3 | Núcleo 3 | 947129.4 | 258893.2 | 1.5 m | Única salida de Agua |

**Figure 6.** Sediment Core Sampling Points of La Rosa Lagoon

## 4 Results and Discussions

This section presents the results derived from the integration of geological, geophysical, geochemical, and isotopic information obtained in previous stages.

First, the geophysical results from the vertical electrical soundings (VES) are presented, which allowed obtaining 1D models with resistivities for 4–5 differentiated layers, revealing the presence of well-contrasted geoelectric units, from shallow levels of low resistivity associated with saturated fine materials to deeper strata of higher resistivity. Additionally, two phreatic levels were identified in the Mérida terrace: one shallow (1.25–11 m) and one deep (>40 m), both with variable resistivities (8–395 Ω·m) reflecting a heterogeneous stratigraphy composed of clays, silts, sands, and gravels. This configuration confirms that basement fractures act as preferential pathways for thermal water circulation, connecting superficial recharge (Albarregas River and streams) with discharge points located at the foot of the slope (Figures 7 and 8).

Regarding La Rosa lagoon, the processing of 347 georeferenced bathymetric points allowed constructing a detailed model of its internal morphometry. The contour lines show an asymmetric basin, with a deeper northwest sector and shallow marginal zones delineating an elongated contour, which evidences variable sediment thicknesses and an axis of maximum depth aligned with the fault trace (Figure 9). The morphometric parameters derived from this model indicate a surface area of 10,367 m², an estimated volume of

13,319 m³, and a maximum depth of 3.55 m in the northwest sector, where active tectonic subsidence is observed (current depths of 3–4 m compared to 1.5 m historically). The shoreline development index (DL = 1.45) and the length/width ratio (3.52) confirm an elongated triangular morphology, characteristic of a fault sag pond structurally controlled by the Boconó Fault.

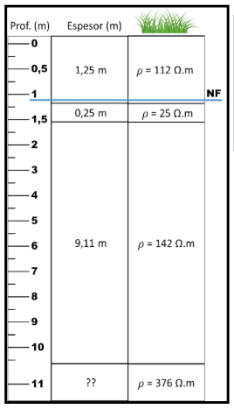


| Resistividad (Ωm) | Espesor (m) | Profundidad (m) | Tipo de Curva |
|---|---|---|---|
| 112 | 1.25 | 1.25 | HA |
| 25 | 0.236 | 1.49 | |
| 142 | 9.11 | 10.6 | |
| 376 | Indefinido | > 10.6 | |

**Figure 7.** Vertical Electrical Sounding No. 1 (UTM coordinates E258817.44 and N947250.52).

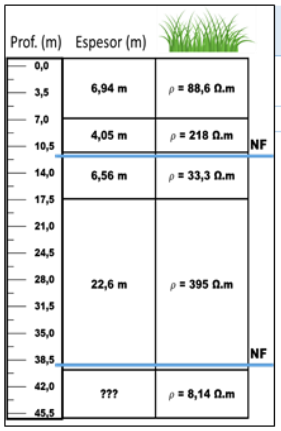


| Resistividad (Ωm) | Espesor (m) | Profundidad (m) | Tipo de Curva |
|---|---|---|---|
| 88.6 | 6.94 | 6.94 | KHK |
| 218 | 4.05 | 11 | |
| 33.3 | 6.56 | 17.5 | |
| 395 | 22.6 | 40.1 | |
| 8.14 | Indefinido | >40.1 | |

**Figure 8.** Vertical Electrical Sounding No. 2 (UTM coordinates E260370.94 and N948270.73).

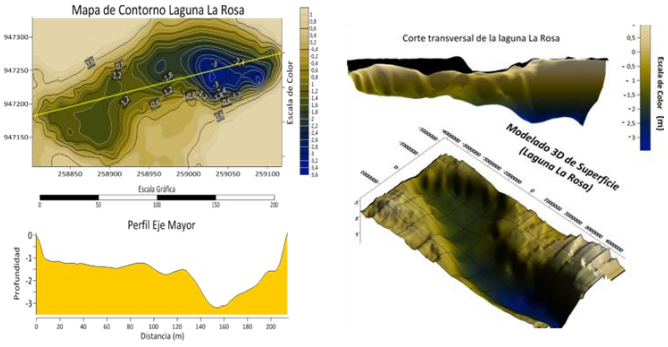


**Figure 9.** Morphometry and summary of the morphometric parameters studied in La Rosa lagoon.

From the cores it was possible to obtain that in core #1 (10a), taken near the main inflow of runoff waters into La Rosa lagoon, it is observed that sediment supply from the basin exceeds lacustrine redistribution, with clayey intervals rich in organic matter in the middle part that would correspond to periods of lower flow and dominance of proper lagoon sedimentation, and a prograding grain-size selection at the top from medium sands to fine gravels. Core #2, extracted at the edge of the wetland over an area previously occupied by the lagoon, reflects a filled environment with abundant soil and organic matter associated with the rooting of aquatic and semi-aquatic vegetation, reducing the water surface area, and shows at its base the beginning of the fine sediment bed. Core #3, located near the water outlet of the lagoon, presents various sedimentary structures that indicate changes in the depositional regime and, at the base, a possible biogenic structure or fluid escape that could be related to the seismicity of the area.

The physicochemical and isotopic analyses of 14 samples discriminate between the hydrogeological processes of the system. The thermomineral waters of El Chama and El Chamita present temperatures of 26.8–43.5 °C, elevated conductivities (up to 793 µS/cm), hardness of 172–397 mg $CaCO_3$/L, and ionic composition dominated by $Ca^{2+}$, $Cl^-$, and $SO_4^{2-}$, classifying as sodium-sulfated (Na–Ca–$SO_4$–$HCO_3$).

Their enriched $\delta^{18}O$ and $\delta^2H$ signatures, together with positive $\delta^{18}O$-$Cl^-$ correlation, indicate deep circulation and progressive mineralization towards the NE.

Surface waters (Albarregas River, streams, runoff) align with the Local Meteoric Line, showing low conductivity and very soft hardness.

La Rosa lagoon exhibits isotopic displacement towards more positive values (intense evaporation) and diluted composition. Municipal network water occupies an intermediate position.

This suggests an affinity that can be summarized as follows: Affinity 1 ($\delta^{18}O$ < -8.5 ‰): Albarregas River, "Árbol" stream, La Rosa lagoon (center/outlet). Recharge from high sectors with dominant meteoric influence. Affinity 2 ($\delta^{18}O$ > -7.5 ‰): Runoff inflows to lagoon, El Chamita springs, Candelaria/Salomón thermal springs (El Chama). Underground flows with superficial evaporation and local recharge. Affinity 3: Municipal network water. No relation with thermal systems or lagoons.

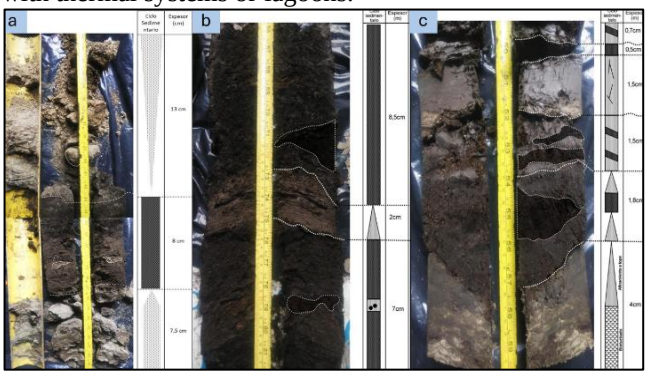


**Figure 10.** Image of extracted cores: a) #1, b) #2, and c) #3

All samples plot on the Global Meteoric Water Line ($\delta^{18}O$: -7.30 to -10.08 ‰; $\delta^2H$: -46.57 to -63.75 ‰),

confirming a primary meteoric origin. The decrease in $Ca^{2+}$, $Mg^{2+}$, $Cl^{-}$, and temperature compared to historical data supports meteoric recharge through fractures into deep circulation.

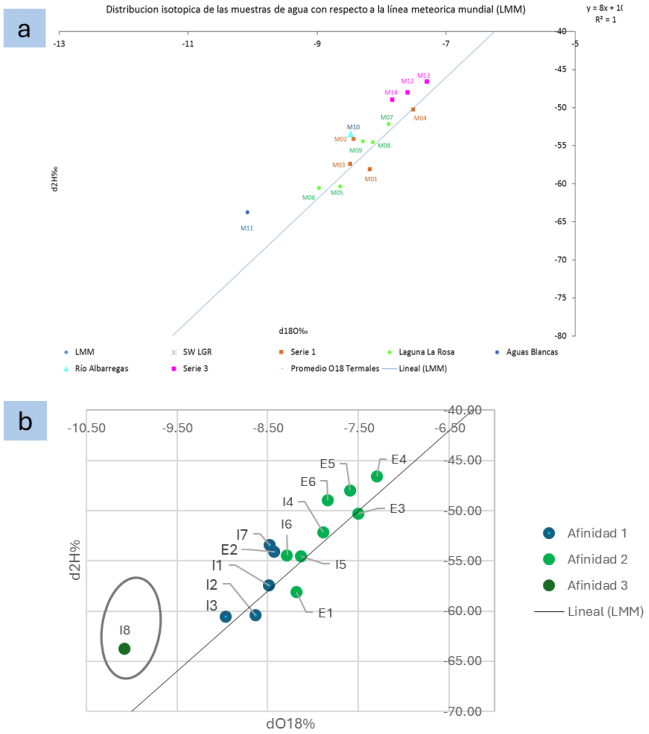


**Figure 11.** a. Isotopic Results. Sample names correspond to the ID in the tables. b. Chemical affinities plotted on the isotopic concentration graph.

The unification of geophysical and isotopic results allowed clarifying the hydrological connections of the thermal system of the Mérida terrace (Figure 12a). The VES faced urban limitations in Mérida, requiring cleared areas of 200 linear meters. VES-2 (Las Tapias, AB/2 = 100 m) identified two phreatic levels: one superficial at 11 m (thickness 6.56 m) and one deep at 40.1 m (undefined thickness) (Figure 12b). VES-1 (Av. Andrés Bello) detected a superficial aquifer at 1.25 m, consistent with the proximity of La Rosa wetland, suggesting favorable conditions for recharge of lower levels (Figure 13).

Isotopic integration evidence that contributions to La Rosa lagoon (I4, I5, I6) share geochemical affinity with outflows from El Chamita (E4, E5, E6) and low thermal springs of El Chama (E1, E3), explained by runoff channels, post-rainfall infiltration, and isotopic homogenization at the end of the rainy season. The Albarregas River maintains affinity with the "Árbol" thermal spring (higher altitude), indicating infiltration in terrace sediments that recharges deep aquifers emerging as thermal waters at the foot of the slope.

The unnamed stream (I1) also potentially feeds the "Árbol" and "Salomón" points (E1), confirming interaction between superficial and thermal systems through fractures and alluvial sediments of the terrace.

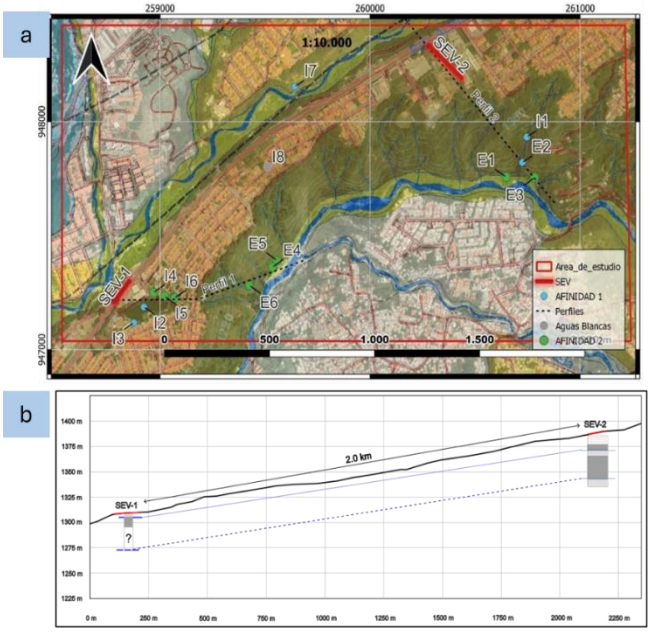


**Figure 12**. **a.** Location results of the affinities. **b.** Correlation of geophysical data on the elevation profile of the Mérida terrace.

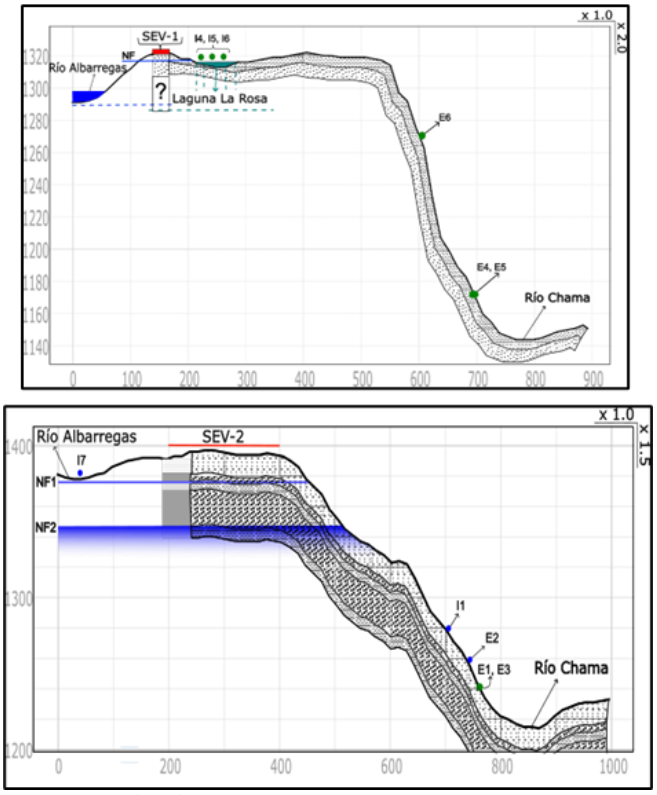


**Figure 13.** Profiles from VES-1 and VES-2 towards the discharge points in El Chamita.

## 5 Conclusion

The thermomineral waters of the Mérida terrace are of meteoric origin, infiltrate through basement fractures

(controlled by the Boconó Fault), are heated by the geothermal gradient, and emerge at the foot of the slope with temperatures of up to 43.5 °C. Recharge comes from the Albarregas River, streams, and La Rosa lagoon, forming an active hydrothermal system linked to regional neotectonics.

The Boconó fault trace generates differential subsidence in the northwest of La Rosa lagoon, confirming its nature as a fault sag pond. The VES and bathymetry evidence variable sediment thicknesses and multiple phreatic levels, validating the active fault model in the Las Tapias-El Carrizal sector.

**El Chama Sector (NE):** waters are hyperthermal (41–43 °C), of high mineralization ($SO_4$-Na-Ca), and greater circulation depth.

**El Chamita Sector (SW):** waters are hypothermal (27 °C), of low mineralization, mixed with shallow waters, shorter ascending path or different fractures. Active landslides in El Chamita are hydrogeologically controlled by the emergence of thermal waters, which increases geomorphological risk. Water-rock interaction and the presence of deep $CO_2$ (inferred from high alkalinity) weaken the slope, accelerating mass removal processes.

The integration of hydrogeochemistry, stable isotopes, geophysics (VES), and bathymetry allowed delimiting recharge zones, mapping active faults, and characterizing thermal reservoirs, laying the groundwork for seismic risk studies and water resource management in the Metropolitan Area of Mérida.

## References


Alvarado, M., Aranguren, R., Ramírez, N., Audemard, F., & Laffaille, J. (2021). Active fault mapping in the metropolitan area of Mérida for seismic microzonification purposes. *Boletín Geominas*, *48*(81), 19–25.

Audemard, F. A. (2003). Neotectonics of the Andean region of Venezuela. In A. Singer & M. A. Lorente (Eds.), *Geology of the Venezuelan Andean Cordillera* (pp. 737–778). Instituto Geográfico de Venezuela Simón Bolívar.

Audemard, F. A., Beck, C., Carrillo, E., & Vásquez, J. F. (2007). Holocene and historical earthquakes on the Boconó Fault system, southern Venezuelan Andes: Trench confirmation. *Journal of Geophysical Research: Solid Earth*, *112*(B1), B01302. https://doi.org/10.1029/2006JB004665

Burguera, M., Millan, F., García, R., Odreman, O., & Sampol, M. (1980). *Study of thermal springs in Mérida State*. Facultad de Ciencias, Universidad de Los Andes.

Cabello, O. (1966). *Geomorphological study of Mérida and its surroundings* [Unpublished undergraduate thesis]. Universidad de Los Andes.

Castany, G. (1971). *Practical treatise on groundwater*. Omega.

Castrillo, D. (1998). Geological-environmental risks derived from mining exploitation in the Tapias-Bailadores region, Mérida State, Venezuelan Andes. In *VI Meeting of the Iberoamerican Association of Higher Education in Mining (AIESMIN)*. Oviedo, Spain.

Clark, I., & Fritz, P. (1997). *Environmental isotopes in hydrogeology*. Lewis Publishers.

Dávila, J., & Pacheco, A. (2009). *Neotectonic mapping of the area between Ejido and Tabay, Mérida, Mérida State* [Unpublished undergraduate thesis]. Universidad de Los Andes.

Google. (2022). *[Satellite image of the Mérida terrace, Venezuela, approximate coordinates 8.5983° N, 71.1442° W]* [Satellite image]. Google Earth. https://earth.google.com/web/ (Map data: Airbus, Maxar Technologies, CNES/Airbus)

Hidromed. (2025). *Water*. https://www.hidromed.org/hm/index.php/el-agua

La Marca, E. (1997). Origin and geological evolution of the Mérida Cordillera, Andes of Venezuela. *Cuadernos de la Escuela de Geografía, Nueva Época*, (1), 1–110.

Nava, R. (2009). *Estimation of sediment thickness from gravimetric modeling for seismic microzonification purposes: Metropolitan area of the city of Mérida* [Unpublished undergraduate thesis]. Universidad de los Andes.

Pinagua, J. (1992). *Hydrothermal infrastructure*. Instituto Tecnológico Geominero de España.

Schubert, C. (1976). Neotectonic research in Venezuela: Objectives and results. *Interciencia*, *1*(3), 32–38.

Schubert, C., & Vivas, L. (1993). *The Quaternary of the Mérida Cordillera*. Universidad de Los Andes.

Taboada, A., Rivera, L. A., Fuenzalida, A., Cisternas, A., Philip, H., Bijwaard, H., Olaya, J., & Rivera, C. (2000). Geodynamics of the northern Andes: Subductions and intracontinental deformation (Colombia). *Tectonics*, *19*(5), 787–813. https://doi.org/10.1029/2000TC900004

Wallace, R. E. (1986). *Active tectonics: Studies in geophysics*. National Academy Press. https://doi.org/10.17226/624

Winslow, M. (1986). Neotectonics: Concepts, definitions and significance. In *Active tectonics: Studies in geophysics* (pp. 1–5). National Academy Press. https://doi.org/10.17226/624


***Received:*** *March 30th, 2026*

***Accepted:*** *June 30th, 2026*

**Santiago Peña, Ricardo de Jesús:** Geological Engineer. Graduate of the University of Los Andes (ULA), Venezuela.
*https://orcid.org/0009-0002-5792-6683*

***Guerrero, Omar Antonio:*** *MSc in Geological Sciences. Professor at the University of Los Andes (ULA), Venezuela. Email: oguerre@ula.ve*
*https://orcid.org/0000-0002-8859-2906*

***Molina Becerra, Germán:*** *Geological Engineer. Professor at the University of Los Andes (ULA), Venezuela. Master's student in Water Resources Planning and Development. Email: gmolinab@ula.ve*
*https://orcid.org/0009-0003-7684-5835*

***Toro Mora, Rosibeth Karina:*** *PhD in Geological Sciences. University of Zaragoza, Department of Internal Geodynamics, Spain. Email: rosibeth@ula.ve*
*https://orcid.org/0000-0002-1252-3584*

***Alarcón Soto, Nayeska Paola:*** *Geological Engineer. Professor at the University of Los Andes (ULA), Venezuela. Email: nayeska@ula.ve*
*https://orcid.org/0009-0006-0283-4668*

*Artículo de Investigación. Revista Ciencia e Ingeniería. Vol. 47, No. 3, pp. 259-266, agosto-noviembre, 2026.*
*ISSN 1316-7081. ISSN Elect. 2244-8780. Universidad de Los Andes (ULA)*

# Control del estado incoherente en redes neuronales

# Control of incoherent state in neural networks

**Tucci, Kay**[*1,2]**; Echeverría, Carlos**[1]**; Uzcátegui, Mayerlin**[1,2]**; Condor, Claudio**[2]
[1]SUMA. Facultad de Ciencias
**Universidad de Los Andes**. Mérida, Venezuela
[2]CeSiMo. Facultad de Ingeniería
**Universidad de Los Andes**. Mérida, Venezuela
[*]kay@ula.ve

**Resumen**

*Uno de los fenómenos que se observa en las redes neuronales naturales o artificiales es el de sincronización. Ocurre cuando las neuronas ajustan su ritmo y su frecuencia entre sí. Clínicamente este fenómeno está relacionado con enfermedades de carácter neurológico tales como la epilepsia y el parkinson. Por medio de un modelo neuronal basado en un mapa caótico, se recrea el fenómeno de sincronización neuronal en redes plásticas. Se determina la posibilidad de mantener la red de neuronas desincronizada mediante aplicación de perturbaciones externas a los elementos de la red siguiendo cuatro estrategias de selección espacial y temporal. Para todas las estrategias se construye el diagrama de fases en el espacio de los parámetros de control, encontrándose que en todas ellas existen regiones en la que se logra controlar significativamente la aparición de este fenómeno de sincronización.*

**Palabras clave**: Sincronización, Neuronas, Control, Redes, Epilepsia.

**Abstract**

*One of the phenomena observed in natural or artificial neural networks is synchronization. It happens when neurons adjust their rhythm and frequency to each other. Clinically, this phenomenon is related to neurological diseases such as epilepsy and Parkinson's. By means of a neuronal model based on a chaotic map, the phenomenon of neuronal synchronization in plastic networks is recreated. The possibility of keeping the network of neurons out of sync by applying external perturbations to the elements of the network is determined by following four spatial and temporal selection strategies. For all the strategies the diagram of phases in the space of the control parameters is constructed, finding that in all of them there are regions in which it is possible to control significantly the appearance of this phenomenon of synchronization.*

**Key words**: Synchronization, Neurons, Control, Networks, Epilepsy.

## 1 Introducción

El surgimiento de dinámicas colectivas y sincronizadas de elementos acoplados se ha estudiado desde finales del siglo pasado en diferentes contextos y en una variedad de campos, que van desde la física (Strogatz, 2000) con láseres y circuitos electrónicos, pasando por la sociología, las comunicaciones (Manrubia y Mikhailov, 2004), la música en todas sus expresiones y manifestaciones, y llegando hasta la biología y la medicina (Pykovsky, Rosemblum, y Kurths, 2001).

Ya a mediados de los años 60, A. Winfree elaboró la primera modelación matemática de la sincronización (Winfree, 1967), luego de observar el comportamiento cooperativo en una gran población de osciladores biológicos con ciclos límite y frecuencias intrínsecas distribuidas alrededor de un valor promedio. Indicando que este fenómeno ocurre cuando un grupo de osciladores autónomos se coordina y ajusta sus ritmos, volviéndose cada vez más similares debido a la presencia de una interacción entre ellos. Este comportamiento descrito por Winfree, captó el interés de Kuramoto (1975), quien comenzó a estudiarlo mediante un modelo conocido actualmente como el Modelo de Kuramoto. Este modelo ha sido utilizado para describir el fenómeno de sincronización de grandes grupos de osciladores acoplados (Strogatz, 2000). Casi de inmediato, se comenzó a estudiar ampliamente el fenómeno de la sincronización caótica en redes dinámicas

(Pecora y Carroll, 1990; Boccaletti, Kurths, Osipov, Valladares, y Zhou, 2002; Strogatz, 2004) sobre diferentes topologías de redes: no dirigidas (Zhou, Motter, y Kurths, 2006; Alvarez-Llamoza, Tucci, Cosenza, y Pineda, 2007), dirigidas (Alvarez-Llamoza y Cosenza, 2010; Bauer, Atay, y Jost, 2010; DeCastro y Tucci, 2010) y complejas (Arenas, Díaz-Guilera, Kurths, Moreno, y Zhou, 2008; Márquez-Rodríguez, Tucci, y Cosenza, 2024); y con dinámicas locales caóticas continuas (Rosenblum, Pikovsky, y Kurths, 1996; Agiza y Yassen, 2001) y discretas (Jost y Joy, 2001; Sinha, 2002), logrando determinar que el comportamiento colectivo de un sistema no sólo depende de las características de los osciladores, sino que también depende de las propiedades del sustrato sobre el que se desarrolla la dinámica (Tucci, 2002; Belykh, Hasler, Lauret, y Nijmeijer, 2005; Atay, Bıyıkoğlu, y Jost, 2006).

Estos modelos son frecuentemente usados para investigar y caracterizar el comportamiento de fenómenos críticos en sistemas naturales muy diversos, como el comportamiento de: tejido cardíaco (Karma, 2013; Keener y Sneyd, 2026), incendios forestales (Bak y Chen, 1991; Clar, Drossel, y Schwabl, 1996), la propagación de enfermedades y rumores (Pastor-Satorras y Vespignani, 2001; Moreno, Nekovee, y Pacheco, 2004), la formación estelar (Shore, 1981; Gerola y Seiden, 1978), algunas reacciones químicas (Zhabotinsky, 1991; Epstein y Pojman, 1998), comunicación entre luciérnagas (Buck, 1988; Strogatz, 2004), floración sincronizada (Satake y Iwasa, 2000), entre otros; siendo muy relevantes para comprender, por ejemplo, la unificación de la actividad cerebral y la emergencia de nuestra conciencia (Buzsáki y Draguhn, 2004) o en la aparición de algunas enfermedades como la epilepsia, la esquizofrenia y el parkinson; que surgen como resultado de la sincronización repentina o indeseable de un gran número de neuronas (Glass, 2001; Cumin y Unswort, 2007; Escalona Morán, Guillén, Cosenza, y Coutin, 2011).

En la mayoría de estos trabajos se parte de sistemas cuyas dinámicas son espontáneamente incoherentes, buscando las condiciones bajo las cuales emerge un comportamiento coherente, es decir, la sincronización. En cambio, el objetivo de este trabajo es estudiar cómo estabilizar el estado incoherente o desincronizado partiendo de un sistema que espontáneamente tiende a la sincronización. Para ello, se construye una red de osciladores neuronales idénticos, con dinámicas excitables caóticas, acoplados mediante una red plástica que sigue un proceso o regla de aprendizaje hebbiano, a la cual se le aplican perturbaciones externas con la finalidad de mantenerlas desincronizadas.

## 2 Método

Para el estudio de la sincronización en sistemas de osciladores caóticos excitables sometidos a perturbaciones consideremos, en primer lugar, que es absolutamente necesario partir de un modelo que permita un estudio amplio de sincronización caótica en redes formadas por modelos activos de neuronas que cumplan con las condiciones mínimas necesarias para la aparición del fenómeno de sincronización caótica en sistemas complejos (Cosenza y González, 1998). Además, dicho fenómeno requiere la presencia de una relación funcional diferente a la identidad entre los elementos que componen la red, la cual ha de ser establecida entre el subsistema de forzamiento y el subsistema de respuesta (Rulkov, Sushchick, Tsimring, y Abarbanel, 1995). Uno de los modelos de oscilador neuronal que cumple con estos requerimientos es el mapa propuesto por Chialvo (1995),

$$x_{t+1} = f_x(x_t, y_t) = x_t^2 e^{y_t - x_t} + k \tag{1}$$

$$y_{t+1} = f_y(x_t, y_t) = a y_t - b x_t + c \tag{2}$$

en el que $x_t$ y $y_t$ representan los estados de activación y recuperación del oscilador, respectivamente, en el instante de tiempo discreto $t$. El comportamiento del oscilador se ajusta mediante 4 parámetros: $k$, que representa una entrada constante o incluso puede representar una perturbación aditiva que no depende del tiempo; $a$, que es la constante de recuperación; $b$, que establece la dependencia de activación en el proceso de recuperación, y $c$, que es el valor de offset. En este trabajo, los parámetros del oscilador neuronal se fijaron en $a = 0.89, b = 0.18, c = 0.28$ y $k = 0.03$ que aseguran que su dinámica sea caótica y excitable.

Por otra parte, Kaneko (1993) propone el uso de redes de mapas acoplados (RMA) como una manera eficiente de realizar el estudio numérico de un sistema complejo y, en particular, de una red neuronal. Una RMA consiste en una simplificación del sistema en la que se construye un modelo compuesto por elementos con dinámica local capaces de interactuar entre sí. Siguiendo esta metodología, nuestro modelo base, sin perturbaciones, lo conforma una red de mapas acoplados con enlaces ponderados, compuesta por $N$ osciladores neuronales caóticos excitables que representan las neuronas y cuya dinámica viene dada por:

$$x_{t+1}^i = (1-\epsilon) f_x(x_t^i, y_t^i) + \frac{\epsilon}{N-1} \sum_{j \neq i} w_t^{ij} f_x(x_t^j, y_t^j) \tag{3}$$

$$y_{t+1}^i = f_y(x_t^i, y_t^i) + c \tag{4}$$

donde $x_t^i$ y $y_t^i$ representan las variables de estado de la neurona $i = 1, 2, \cdots, N$; en el instante de tiempo $t$; $\epsilon \in (0, 1)$ es un parámetro que controla la intensidad del acoplamiento y $w_t^{ij}$ es el elemento de la matriz de adyacencia $\mathbf{W}$ que representa el peso con el que la neurona $j$ influye en la neurona $i$ en el instante $t$.

Por su parte, la evolución de los pesos sigue el mecanismo de plasticidad homeostática (Alvarez-Silva, Alvarez-Rodríguez, Pérez-Echeverría, y Alvarez-Silva, 2006) y viene dada por:

$$w_{t+1}^{ij} = \frac{(1 + \delta g(x_t^i, x_t^j)) w_t^{ij}}{\sum_j (1 + \delta g(x_t^i, x_t^j)) w_t^{ij}} \tag{5}$$

donde $\delta \in (0,1)$ representa el grado de plasticidad de la red y el denominador de la expresión actúa como normalizador de los pesos para que estos se mantengan en el intervalo $[0,1]$. Aquí, la función $g(x_t^i, x_t^j)$ representa el "proceso o regla de aprendizaje" (Ito y Kaneko, 2000; Hebb, 2005) de la red que viene dada por:

$$g(x_t^i, x_t^j) = \begin{cases} \cos\left(\frac{x_t^j - x_t^i}{\Omega}\right) & \text{si} \quad |x_t^j - x_t^i| \leq 4 \\ 0 & \text{en otros casos} \end{cases} \tag{6}$$

donde $\Omega = 1.25$.

Con el fin de cuantificar el grado de sincronización de las neuronas, calculamos la varianza promedio en $T$ iteraciones,

$$\sigma^2 = \frac{1}{T}\sum_{t=1}^{T} \sigma_t^2 \tag{7}$$

a partir de $\sigma_t^2$, que es la varianza instantánea de los estados de los elementos del sistema,

$$\sigma_t^2 = \frac{1}{N-1}\sum_{i=1}^{N} \left(x_t^i - \overline{x_t}\right)^2 + \left(y_t^i - \overline{y_t}\right)^2 \tag{8}$$

donde $\overline{x_t}$ e $\overline{y_t}$ son los promedios instantáneos de las variables de estado de las $N$ neuronas de la red en la iteración $t$.

Se propone introducir cuatro estrategias para perturbar el sistema con la finalidad de estabilizar un estado incoherente, es decir, desincronizar el sistema. La primera estrategia es la más agresiva porque introduce una perturbación constante que afecta a todos los elementos del sistema en todas las iteraciones. Para ello, sumamos la perturbación a la ecuación (3), obteniendo

$$\begin{aligned} x_{t+1}^i = {} & (1-\epsilon) f_x(x_t^i, y_t^i) \\ & + \frac{\epsilon}{N-1}\sum_{j\neq i} w_t^{ij} f_x(x_t^j, y_t^j) + B \end{aligned} \tag{9}$$

donde $B$ es la magnitud de la perturbación que se aplica a cada elemento $x_t^i$ de la red en todo instante de tiempo $t$.

La segunda estrategia busca disminuir la agresividad al reducir la frecuencia con la que se aplica la perturbación. Para ello, se introduce la función aleatoria

$$\Theta_t(p) = \begin{cases} 1 & \text{con probabilidad} \quad p \\ 0 & \text{con probabilidad} \quad 1-p \end{cases} \tag{10}$$

donde $p_1$ es la probabilidad con la que la perturbación se aplica en el instante de tiempo $t$, modificando la ecuación (3) de la forma:

$$\begin{aligned} x_{t+1}^i = {} & (1-\epsilon) f_x(x_t^i, y_t^i) \\ & + \frac{\epsilon}{N-1}\sum_{j\neq i} w_t^{ij} f_x(x_t^j, y_t^j) + \Theta_t(p_1) B \end{aligned} \tag{11}$$

Nótese que la probabilidad $p_1$ actúa como un modulador de la agresividad de la estrategia, ya que la perturbación $B$ solamente se suma al estado $x_{t+1}^i$ cuando $\Theta_t(p_1) = 1$.

Al igual que la estrategia anterior, la tercera estrategia también busca moderar la agresividad de la primera. Esto lo logra reduciendo la cantidad de elementos a los que se aplica la perturbación mediante la función aleatoria

$$\Theta^i(q) = \begin{cases} 1 & \text{con probabilidad} \quad q \\ 0 & \text{con probabilidad} \quad 1-q \end{cases} \tag{12}$$

donde $q$ representa la probabilidad de que la perturbación se aplique al elemento $i$. En esta estrategia, la ecuación (3) del modelo sin perturbaciones se modifica de la siguiente forma

$$\begin{aligned} x_{t+1}^i = {} & (1-\epsilon) f_x(x_t^i, y_t^i) \\ & + \frac{\epsilon}{N-1}\sum_{j\neq i} w_t^{ij} f_x(x_t^j, y_t^j) + \Theta^i(q) B \end{aligned} \tag{13}$$

Finalmente, la cuarta estrategia combina las dos estrategias anteriores, aplicando una perturbación externa a algunos elementos en algunas ocasiones. En este caso, modificamos la ecuación (3) de la siguiente forma:

$$\begin{aligned} x_{t+1}^i = {} & (1-\epsilon) f_x(x_t^i, y_t^i) \\ & + \epsilon \sum_{j} w_t^{ij} f_x(x_t^j, y_t^j) + \Theta_t(p_1)\Theta^i(q) B \end{aligned} \tag{14}$$

donde la perturbación se aplica en el instante de tiempo $t$ con probabilidad $p_1$ al elemento $i$ con probabilidad $q$.

## 3 Resultados.

Las simulaciones del modelo se llevaron a cabo sobre una red de $N = 1000$ osciladores neuronales descrita en las ecuaciones (1-2) con condiciones iniciales aleatorias uniformemente distribuidas: $x_o^i \in (0.1, 5.0)$ e $y_o^i \in (0.8, 2.3)$, que garantizan que todos los osciladores están en un estado caótico y excitable. El valor inicial de los pesos se estableció en

$$w_o^{ij} = \begin{cases} \frac{1}{N-1} & i \neq j, \\ 0 & i = j \end{cases}$$

La figura 1 muestra la evolución temporal de 10 elementos de la red durante 300 iteraciones para dos valores diferentes de la intensidad de acoplamientos, $\epsilon = 0.15$ a la izquierda y $\epsilon = 0.25$ a la derecha. En la gráfica de la izquierda

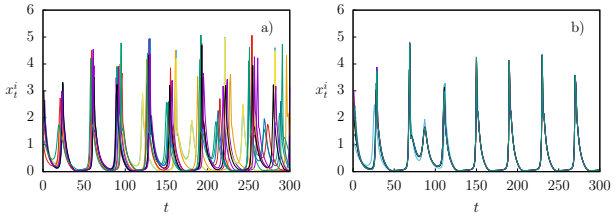


**Fig. 1:** Evolución temporal de la variable de activación $x_t^i$ para 10 elementos de la red con plasticidad $\delta = 0.5$. **a)** Comportamiento incoherente con $\epsilon = 0.15$. **b)** Comportamiento sincronizado con $\epsilon = 0.25$.

se aprecia que cuando el acoplamiento no es suficientemente

intenso ($\epsilon = 0.15$) el comportamiento de las neuronas de la red es incoherente. Por su parte, en la gráfica de la derecha de la figura 1 tenemos la evolución de estos mismos 10 elementos para un acoplamiento mayor ($\epsilon = 0.25$). Allí vemos claramente que la red alcanza un estado sincronizado en muy pocas iteraciones ($t < 100$).

Teniendo en cuenta esto, con el fin de eliminar el efecto de las condiciones iniciales, en los resultados siguientes se descartan aproximadamente $10^3$ iteraciones antes de aplicar la perturbación y calcular los promedios temporales de la ecuación (7). Además, para su cálculo se estableció que $T = 10^3$ iteraciones.

La figura 2 muestra el diagrama de fase del modelo en el espacio de parámetros $(\epsilon, \delta)$ antes de aplicar ninguna perturbación (Ecs. (3-5)). Como es de esperarse, para

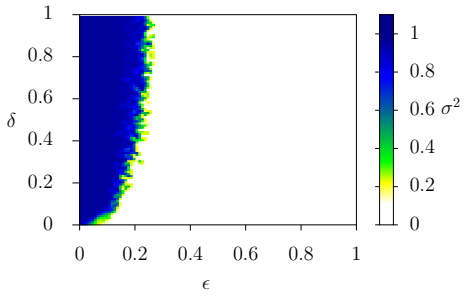


**Fig. 2:** Diagrama de fases de la red sin perturbaciones en el espacio de parámetros $(\epsilon, \delta)$. En negro se muestra la región de incoherente y en blanco la región sincronizada.

valores pequeños de la intensidad de los acoplamientos $\epsilon$ el comportamiento del sistema es incoherente ($\sigma^2 \approx 1$) y al aumentarla se llega a un punto en el que el sistema se sincroniza ($\sigma^2 \approx 0$). Además, se aprecia que los valores de $\epsilon$ para los que ocurre la transición aumentan al incrementar el valor de la plasticidad de la red $\delta$.

Para estudiar los efectos del forzamiento en el sistema con cada una de las cuatro estrategias, se eligió una intensidad del acoplamiento de $\epsilon = 0.30$ y una plasticidad de la red de $\delta = 0.50$. De esta forma se asegura que el modelo sin forzamiento se encuentre en la fase sincronizada, pero suficientemente cerca de la transición a la fase incoherente.

La figura 3 muestra el comportamiento de la varianza, $\sigma^2$ en función de la intensidad de la perturbación, $B$, con la primera estrategia (Ec. (9)), que consiste en aplicar siempre una perturbación externa a todas las neuronas de la red.

Nótese que para para $B = 0$, es decir, cuando no se aplica ninguna perturbación, el sistema se encuentra sincronizado ($\sigma^2 = 0$). También se aprecia que si la intensidad de la perturbación $B < -0.20$ la varianza $\sigma^2$ alcanza valores que indican que el sistema se encuentra en un estado incoherente. En otras palabras, encontramos que partiendo de un sistema que espontáneamente ($B = 0$) se sincroniza es posible mantener al sistema en su fase incoherente aplicando una

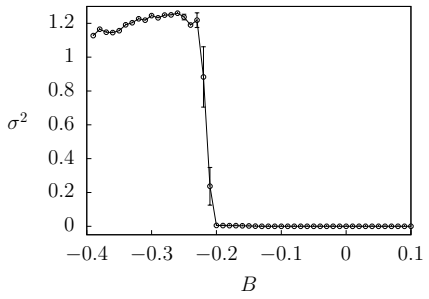


**Fig. 3:** Comportamiento de $\sigma^2$ en función de $B$ con la primera estrategia. Las barras de error indican desviaciones estándar típicas sobre los valores medios de $\sigma^2$ obtenidos en 10 realizaciones para cada valor de $B$.

perturbación ($B < -0.20$) a todos los osciladores todo el tiempo.

Buscando ser menos agresivo con la aplicación de la perturbación, la figura 4 muestra el comportamiento del sistema al aplicar la segunda estrategia, planteada en las ecuaciones (10)–(11). En el diagrama de fase, Fig. 4a, se aprecia

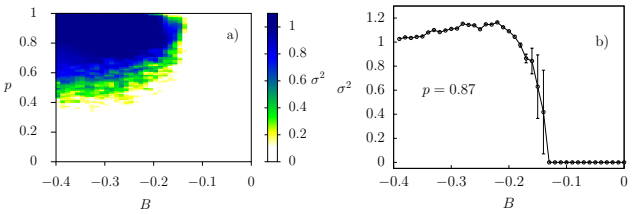


**Fig. 4:** Varianza $\sigma^2$ al aplicar la segunda estrategia, es decir, aplicar la perturbación $B$ a todos los elementos con probabilidad $p$. **a)** Diagrama de fases en el espacio de parámetros $(B, p)$. **b)** Valores de $\sigma^2$ en función de $B$ para $p = 0.87$. Las barras de error indican desviaciones estándar típicas sobre los valores medios de $\sigma^2$ obtenidos en 10 realizaciones para cada valor de $B$.

en azul la región en la que al aplicar la perturbación $B$ a todos los elementos con probabilidad $p$ se logra mantener al sistema en un estado incoherente. Nótese que con esta estrategia existen valores de $p < 1$ para los cuales el sistema alcanza el régimen incoherente, incluso con cuando la magnitud de la perturbación $B$ es menor que la requerida si se aplicara todo el tiempo, esto es con $p = 1$ (primera estrategia). En particular, para $p = 0.87$ se tiene que el comportamiento del sistema es incoherente para valores de la intensidad de la perturbación $B < -0.15$ como lo muestra a la izquierda la figura 4b.

Otra forma de reducir la agresividad de la perturbación es aplicar la tercera estrategia (Ecs. (12)–(13)), que consiste en perturbar con intensidad $B$ siempre, pero escogiendo aleatoriamente los elementos a los que se les perturba con probabilidad $q$. Al aplicarla se obtiene el diagrama de fase en el espacio de parámetros $(B, q)$ que se muestra en la figura 5a. Allí se observa que el régimen sincronizado de los elementos de la red se pierde para valores de la magnitud de $B > -0.2$, considerablemente más cercanos a cero

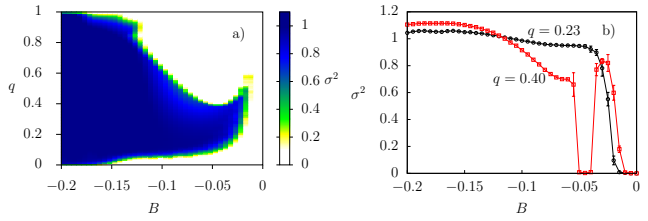


**Fig. 5:** Varianza $\sigma^2$ al aplicar la tercera estrategia. **a)** Diagrama de fases en el espacio de parámetros $(B, q)$. **b)** Valores de $\sigma^2$ en función de $B$ para $q = 0.23$ (círculos negros) y $q = 0.40$ (cuadrados rojos). Las barras de error indican desviaciones estándar típicas sobre los valores medios de $\sigma^2$ obtenidos en 10 realizaciones para cada valor de $B$.

en comparación con lo que ocurre al aplicar la primera o segunda estrategia, (Figs. 3 y 4). Por su parte, la figura 5b, muestra el comportamiento de la varianza $\sigma^2$ para dos valores de la probabilidad $q$. Cuando $q = 0.23$ (círculos negros) vemos que existe una única transición de la fase sincronizada a la incoherente para valores de la intensidad de la perturbación $-0.03 \leq B \leq -0.02$. En cambio, cuando $q = 0.40$ (cuadrados rojos) se aprecian tres transiciones entre las dos fases. Este comportamiento evidencia la complejidad en el comportamiento que pueden llegar a presentar este tipo de sistemas.

Finalmente, al combinar las dos estrategias anteriores para la aplicación de la perturbación externa, se tiene la cuarta estrategia representada por las ecuaciones (10), (12) y (14). En esta estrategia hay tres parámetros que controlan al sistema, $B$, $p$ y $q$. La figura 6 muestra el comportamiento del sistema al fijar uno de los tres parámetros y variar los otros dos. Las probabilidades $p = 0.87$ y $q = 0.23$, que se

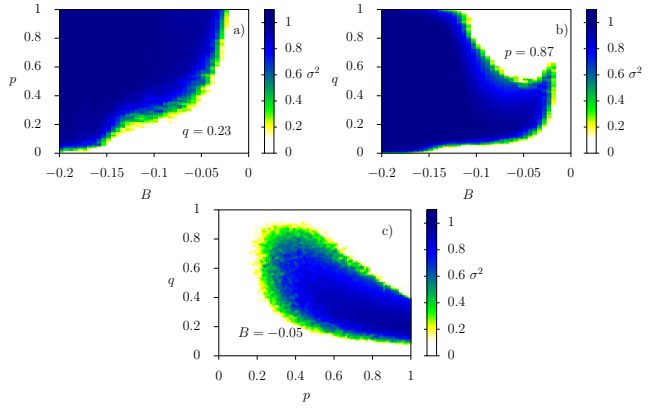


**Fig. 6:** Varianza $\sigma^2$ al aplicar la cuarta estrategia. **a)** Diagrama de fase en el espacio de parámetros $(B, p)$ para $q = 0.23$. **b)** Diagrama de fase en el espacio de parámetros $(B, q)$ para $p = 0.87$. **c)** Diagrama de fase en el espacio de parámetros $(p, q)$ para $B = -0.05$.

usaron en la figura, corresponden respectivamente a los valores mínimos para los cuales la segunda y tercera estrategia lograron que el sistema se mantuviese en su fase incoherente. Por su parte, la intensidad $B = -0.05$ se seleccionó porque en la tercera estrategia el sistema presenta un cambio de comportamiento en ese valor.

Al comparar las figuras 4a y 6a se puede observar que al disminuir la probabilidad de seleccionar un elemento para aplicar la perturbación de $q = 1$ a $q = 0.23$ aumenta el área de la fase incoherente, ampliando significativamente el rango tanto de la probabilidad $p$ como de la intensidad de la perturbación $B$. Del mismo modo, al comparar las figuras 5a y 6b se puede observar que al disminuir la probabilidad de aplicar la perturbación en cada iteración de $p = 1$ a $p = 0.87$ el área de la fase incoherente aumenta, aunque en este caso el cambio no es tan marcado como en el caso anterior. Por último, la figura 6c muestra que existen varias combinaciones para las probabilidades $p$ y $q$ que logran mantener el sistema en su fase incoherente para una intensidad de la perturbación relativamente baja $B = -0.05$, menos de un cuarto de la magnitud mínima si se aplicara la primera estrategia (Fig. 3), esto es aplicar la perturbación siempre y a todos los elementos.

## 4 Discusión y conclusiones.

Para estudiar el efecto que tiene un campo externo de magnitud constante sobre sistema de elementos excitables sincronizado, se sometió a una red neuronal con dinámica caótica a una perturbación siguiendo cuatro estrategias. En la primera estrategia se aplicó la perturbación a todos los elementos de la red en cada iteración. Con esta estrategia se determinó que es posible inducir un comportamiento incoherente de los elementos de la red manteniendo el carácter caótico y excitable de cada elemento de la red, como se muestra en la figura 3.

Aunque la primera estrategia logra el objetivo de estabilizar el comportamiento incoherente en el sistema, en algunos sistemas reales puede ser muy agresiva. Por ejemplo, en el caso de un ataque epiléptico la aplicación de una perturbación relativamente grande a todos los elementos todo el tiempo implicaría someter a todas las neuronas del cerebro a un choque eléctrico continuamente. Es por esto que con las otras tres estrategias se buscó disminuir la agresividad al intervenir menos en el sistema. Nótese que la segunda y tercera estrategia buscan reducir respectivamente la frecuencia y la cantidad de elementos sobre los que se interviene, mientras que la cuarta estrategia es el producto de combinar las dos anteriores.

En la figura 4 se observa que en el caso de la segunda estrategia, con la que se somete la red neuronal a una perturbación que afecta a todos los elementos con cierta probabilidad, es posible estabilizar el estado incoherente sin necesidad de aplicar la perturbación en todo momento. Además, para ciertos valores de la probabilidad de aplicar la perturbación, como por ejemplo $p = 0.87$, se aprecia que la estabilización de la fase incoherente se logra con magnitudes de la intensidad de la perturbación menor que lo observado con la primera estrategia.

En cambio, con la tercera estrategia se busca reducir la agresividad disminuyendo la cantidad de elementos que se perturban. Para ello, en cada iteración, se seleccionan los elementos que son sometidos a la perturbación con cierta probabilidad $q$. En este caso, al igual que ocurrió con la segunda estrategia, se encontró que es posible estabilizar la fase incoherente sin necesidad de afectar a todos sus elementos, logrando también una reducción del valor de la magnitud de la perturbación para algunos valores de probabilidad como por ejemplo $q = 0.23$, como se muestra en la figura 5. Además, se encontró que para algunos valores de la probabilidad, por ejemplo $q = 0.40$, al variar la intensidad de la perturbación ocurren tres transiciones entre las fases sincronizada e incoherente. Estudiar el origen y la naturaleza de estas transiciones escapa del alcance de este trabajo, pero podría ser un tema de interés para futuras investigaciones.

Finalmente, con la cuarta estrategia se busca disminuir aún más la agresividad combinando las dos estrategias anteriores, es decir, perturbar a algunos elementos a veces. Los resultados de aplicar esta estrategia se muestran en la figura 6. En la figura se aprecia que existe un amplio rango para los valores de las probabilidades $p$ y $q$, y de la intensidad de la perturbación $B$ donde se logra el objetivo de estabilizar el comportamiento incoherente del sistema Nótese además que esto puede lograrse para valores combinados de los parámetros $p$, $q$ y $|B|$ inferiores a los mínimos obtenidos usando las primeras tres estrategias.

## Referencias


Agiza, H., y Yassen, M. (2001). Synchronization of rossler and chen chaotic dynamical systems using active control. *Physics Letters A*, *278*(4), 191–197.

Alvarez-Llamoza, O., y Cosenza, M. G. (2010). Synchronization induced by intermittent versus partial drives in chaotic systems. *International Journal of Bifurcation and Chaos*, *20*(02), 323–330.

Alvarez-Llamoza, O., Tucci, K., Cosenza, M., y Pineda, M. (2007). Random global coupling induces synchronization and nontrivial collective behavior in networks of chaotic maps. *The European Physical Journal Special Topics*, *143*(1), 245–247.

Alvarez-Silva, S., Alvarez-Rodríguez, J., Pérez-Echeverría, M., y Alvarez-Silva, I. (2006). Panic and epilepsy. *Journal of anxiety disorders*, *20*(3), 353–362.

Arenas, A., Díaz-Guilera, A., Kurths, J., Moreno, Y., y Zhou, C. (2008). Synchronization in complex networks. *Physics reports*, *469*(3), 93–153.

Atay, F. M., Bıyıkoğlu, T., y Jost, J. (2006). Network synchronization: Spectral versus statistical properties. *Physica D: Nonlinear Phenomena*, *224*(1-2), 35–41.

Bak, P., y Chen, K. (1991). Self-organized criticality. *Scientific American*, *264*(1), 46–53.

Bauer, F., Atay, F. M., y Jost, J. (2010). Synchronized chaos in networks of simple units. *Europhysics Letters*, *89*(2), 20002.

Belykh, I., Hasler, M., Lauret, M., y Nijmeijer, H. (2005). Synchronization and graph topology. *International Journal of Bifurcation and Chaos*, *15*(11), 3423–3433.

Boccaletti, S., Kurths, J., Osipov, G., Valladares, D., y Zhou, C. (2002). The synchronization of chaotic systems. *Physics reports*, *366*(1-2), 1–101.

Buck, J. (1988). Synchronous rhythmic flashing of fireflies. ii. *The Quarterly review of biology*, *63*(3), 265–289.

Buzsáki, G., y Draguhn, A. (2004). Neuronal oscillations in cortical networks. *Science*, *304*(5679), 1926-9. doi: doi:10.1126/science.1099745

Chialvo, D. (1995). Generic excitable dynamics on a two-dimensional map. *Chaos, Solitons & Fractals*, *5*(5), 461–479.

Clar, S., Drossel, B., y Schwabl, F. (1996). Forest fires and other examples of self-organized criticality. *Journal of Physics: Condensed Matter*, *8*(37), 6803–6824.

Cosenza, M. G., y González, J. (1998). Synchronization and collective behavior in globally coupled logarithmic maps. *Progress of Theoretical Physics*, *100*(1), 21–38.

Cumin, D., y Unswort, C. (2007). Generalizing the kuramoto model for the study of neuronal synchronization in the brain. *Physica D: Nonlinear Phenomena*, *226*(2), 181–196.

DeCastro, D., y Tucci, K. (2010). Chaotic synchronization on directed networks. En *Journal of physics: Conference series* (Vol. 246, p. 012010).

Epstein, I. R., y Pojman, J. A. (1998). *An introduction to nonlinear chemical dynamics.* New York: Oxford Univ. Press.

Escalona Morán, M., Guillén, P., Cosenza, M., y Coutin, P. (2011). Análisis de la sincronización de señales eeg usando dinámica no lineal. *Ciencia*, *13*(4).

Gerola, H., y Seiden, P. E. (1978). Stochastic star formation and spiral structure of galaxies. *Astrophysical Journal, Part 1, vol. 223, July 1, 1978, p. 129-135, 137, 139.*, *223*, 129–135.

Glass, L. (2001). Synchronization and rhythmic processes in physiology. *Nature*, *410*(6825), 277-84. doi: doi:10.1038/35065745

Hebb, D. (2005). *The organization of behavior: A neuropsychological theory* (reprint ed.). New York: Psychology Press.

Ito, J., y Kaneko, K. (2000). Self-organized hierarchical structure in a plastic network of chaotic units. *Neural Networks*, *13*(3), 275–281.

Jost, J., y Joy, M. P. (2001). Spectral properties and synchronization in coupled map lattices. *Physical Review E*, *65*(1), 016201.

Kaneko, K. (1993). *Theory and applications of coupled map lattices* (Vol. 12). John Wiley & Son Ltd.

Karma, A. (2013). Physics of cardiac arrhythmogenesis. *Annu. Rev. Condens. Matter Phys.*, *4*(1), 313–337.

Keener, J., y Sneyd, J. (2026). Neuroendocrine cells. En *Mathematical physiology* (pp. 467–502). Springer.

Kuramoto, Y. (1975). Self-entrainment of a population of coupled non-linear oscillators. En *International symposium on mathematical problems in theoretical physics* (pp. 420–422). Springer.

Manrubia, S. C., y Mikhailov, A. S. (2004). *Emergence of dynamical order: synchronization phenomena in complex systems*. World Scientific.

Márquez-Rodríguez, V., Tucci, K., y Cosenza, M. (2024). Chimera states and information transfer in interacting populations of map-based neurons. *Neural Computing and Applications*, *36*(29), 18151–18159.

Moreno, Y., Nekovee, M., y Pacheco, A. F. (2004). Dynamics of rumor spreading in complex networks. *Physical Review E—Statistical, Nonlinear, and Soft Matter Physics*, *69*(6), 066130.

Pastor-Satorras, R., y Vespignani, A. (2001). Epidemic spreading in scale-free networks. *Physical review letters*, *86*(14), 3200.

Pecora, L. M., y Carroll, T. L. (1990). Synchronization in chaotic systems. *Physical review letters*, *64*(8), 821.

Pykovsky, A., Rosemblum, M., y Kurths, J. (2001). Synchronization: A universal concept in nonlinear science. *Cambridge Univ. Press*.

Rosenblum, M. G., Pikovsky, A. S., y Kurths, J. (1996). Phase synchronization of chaotic oscillators. *Physical review letters*, *76*(11), 1804.

Rulkov, N., Sushchick, M., Tsimring, L., y Abarbanel, H. (1995). Generalized synchronization of chaos in directionally coupled chaotic systems. *Physical Review E*, *51*(2), 980.

Satake, A., y Iwasa, Y. (2000). Pollen coupling and synchronous flowering: a theoretical study of resource-budget models. *Journal of Theoretical Biology*, *203*(1), 63–79.

Shore, S. N. (1981). Star formation as a critical phenomenon. *The Astrophysical Journal*, *249*, 93–105.

Sinha, S. (2002). Random coupling of chaotic maps leads to spatiotemporal synchronisation. *arXiv preprint nlin/0205008*.

Strogatz, S. (2000). From kuramoto to crawford: exploring the onset of synchronization in populations of coupled oscillators. *Physica D: Nonlinear Phenomena*, *143*(1), 1–20.

Strogatz, S. (2004). *Sync: The emerging science of spontaneous order*. Penguin UK.

Tucci, K. (2002). *Procesos dinámicos espaciotemporales en redes inhomogéneas* (Tesis Doctoral no publicada). Postgrado de Física Fundamentel, Universidad de Los Andes, Mérida.

Winfree, A. (1967). Biological rhythms and the behavior of populations of coupled oscillators. *Journal of theoretical biology*, *16*(1), 15–42.

Zhabotinsky, A. M. (1991). Self-oscillating chemical reactions. En *Selected topics in chemical physics.* Elsevier / North-Holland.

Zhou, C., Motter, A. E., y Kurths, J. (2006). Universality in the synchronization of weighted random networks. *Physical review letters*, *96*(3), 034101.

***Recibido**: 26 de mayo de 2026*

***Aceptado**: 05 de julio de 2026*

***Tucci, Kay:*** *Ingeniero de Sistemas ULA 1993, Doctor en Física Fundamental ULA 2002. Profesor Titular en la Facultad de Ciencias de la Universidad de Los Andes, Mérida. Venezuela*
https://orcid.org/0000-0002-7628-7752

***Echeverría, Carlos:*** *Licenciado en Química 1995, Magister en Física Fundamental ULA 1999, Doctor en Física Fundamental ULA 2008. Profesor Titular en la Facultad de Ingeniería de la Universidad de Los Andes, Mérida. Venezuela*
*Correo electrónico: cecheve@ula.ve*
https://orcid.org/0000-0003-4114-7845

***Uzcátegui, Mayerlin:*** *Ingeniero de Sistemas ULA 1993, Magister Scientiae en Computación ULA 2002. Candidato al grado de Doctor en Ciencias Aplicadas ULA. Profesor Titular en la Facultad de Ciencias de la Universidad de Los Andes, Mérida. Venezuela*
*Correo electrónico: maye@ula.ve*
https://orcid.org/0009-0007-1449-2690

*Artículo de Investigación. Revista Ciencia e Ingeniería. Vol. 47, No. 3 pp. 267-276, agosto-noviembre, 2026.*
*ISSN 1316-7081. ISSN Elect. 2244-8780 Universidad de los Andes (ULA)*

# Hidrazonas 2,4-dinitrofenilhidrazínicas: Síntesis, Caracterización Espectroscópica y Evaluación *in vitro* frente a *Escherichia coli*

# 2,4-Dinitrophenylhydrazone Derivatives: Synthesis, Spectroscopic Characterization, and *in vitro* Evaluation against *Escherichia coli*

**Rodríguez, Fabio[1]*; Vizcaya, Marietta[1]; Pérez, Patricia[1]; Chacón, Zarack[2]; Lugo, Claudio[3]**
[1]Laboratorio de Polímeros, Departamento de Química, Facultad de Ciencias, Universidad de Los Andes, Venezuela.
[2] Laboratorio Microbiología Molecular y Biotecnología, Departamento de Biología, Facultad de Ciencias, ULA, Venezuela.
[3]Laboratorio de Cinética y Catálisis, Departamento de Química, Facultad de Ciencias, Universidad de Los Andes, Venezuela.
*fabiorod95@gmail.com

**Resumen**

Se sintetizaron una serie de nuevos derivados de 2,4-dinitrofenilhidrazonas (P1–P4) mediante la reacción de condensación ácido-catalizada entre 2,4-dinitrofenilhidrazina (2,4-DNPH) y cuatro cetonas diferentes (R1–R4) en etanol bajo reflujo, utilizando proporciones estequiométricas equimolares. Las cetonas empleadas fueron 2-bromo-1-(4-fenilfenil) etanona (R1), 2-cloro-1-feniletanona (R2), 2-bromo-1-(4-clorofenil) etanona (R3) y 1-(4-metoxifenil) etanona (R4). Las hidrazonas correspondientes se obtuvieron con buenos rendimientos y se caracterizaron completamente mediante técnicas espectroscópicas. La elucidación estructural confirmó la formación exitosa de los compuestos esperados. Los espectros FT-IR mostraron la banda de absorción característica del grupo imino (C=N) junto con la desaparición de la vibración de tensión del carbonilo (C=O) de las cetonas de partida. En los espectros de RMN-$^1$H, desaparecieron las señales correspondientes a los protones de la amina primaria ($–NH_3$) de la 2,4-DNPH, mientras que se observó un desplazamiento a campo bajo característico del protón azometino (=N–NH–). La espectroscopia UV-Vis reveló un marcado efecto batocrómico en la banda de absorción asociada al sistema hidrazónico, consistente con una extensión significativa del sistema π-conjugado. Además, los datos de punto de fusión y solubilidad fueron consistentes con las estructuras propuestas. La actividad antibacteriana *in vitro* de las hidrazonas sintetizadas se evaluó frente a *Escherichia coli* mediante una modificación del método de difusión en disco de *Kirby-Bauer*. Ninguno de los compuestos (P1–P4) exhibió actividad bacteriostática en las condiciones ensayadas.

**Palabras claves:** Hidrazonas, 2,4-DNPH, Condensación, *Escherichia coli.*

**Abstract**

A series of novel 2,4-dinitrophenylhydrazone derivatives (P1–P4) were synthesized through an acid-catalyzed condensation reaction between 2,4-dinitrophenylhydrazine (2,4-DNPH) and four different ketones (R1–R4) in ethanol under reflux conditions, employing equimolar stoichiometric ratios. The ketones used were 2-bromo-1-(4-phenylphenyl)ethan-1-one (R1), 2-chloro-1-phenylethan-1-one (R2), 2-bromo-1-(4-chlorophenyl)ethan-1-one (R3), and 1-(4-methoxyphenyl)ethan-1-one (R4). The corresponding hydrazones were obtained in good yields and fully characterized by spectroscopic techniques. Structural elucidation confirmed the successful formation of the expected compounds. FT-IR spectra showed the characteristic absorption band of the imine group (C=N) along with the disappearance of the carbonyl (C=O) stretching vibration of the starting ketones. In the $^1$H-NMR spectra, the signals of the primary amine protons ($–NH_3$) of 2,4-DNPH disappeared, while a characteristic downfield shift was observed for the azomethine proton (=N–NH–). UV-Vis spectroscopy revealed a significant bathochromic shift in the absorption band associated with the hydrazone moiety, consistent with an extended π-conjugated system. Additionally, melting point and solubility data were consistent with the proposed structures. The in vitro antibacterial activity of the synthesized hydrazones was evaluated against *Escherichia coli* using a modified Kirby-Bauer disk diffusion method. None of the compounds (P1–P4) exhibited bacteriostatic activity under the tested conditions.

**Keywords:** Hidrazones, *2,4*-DNPH, Condensation, *Escherichia coli.*

## 1 Introducción

La síntesis orgánica ha constituido uno de los pilares fundamentales del progreso científico y tecnológico, evolucionando continuamente para satisfacer la demanda de nuevas moléculas con propiedades funcionales específicas (Bosch y Rosich, 2008). Este desarrollo se ha caracterizado por la implementación de metodologías cada vez más eficientes, selectivas y sostenibles, adaptadas a las necesidades de la sociedad moderna. Un hito trascendental en esta trayectoria fue el enfoque racional introducido por Paul Ehrlich, quien estableció un protocolo sistemático basado en la síntesis de una amplia serie de análogos estructurales a partir de una molécula base, seguido de su evaluación biológica *in vitro* e *in vivo*. Este método, que culminó con el descubrimiento del Salvarsán®, representó el nacimiento de la química medicinal moderna al sustituir el descubrimiento empírico por una estrategia deliberada de diseño, síntesis y optimización de propiedades farmacológicas (Bosch y Rosich, 2008).

Dentro de las diversas familias de compuestos nitrogenados, las hidrazonas ocupan un lugar destacado debido a su accesibilidad sintética y a la versatilidad estructural que ofrece el grupo funcional imino (C=N). Su preparación convencional, mediante condensación entre hidrazinas o hidrazidas y carbonilos en medio alcohólico acidificado bajo reflujo, suele proceder con buenos rendimientos y permite una fácil incorporación de diversos fragmentos moleculares (Popiołek, 2021; Barqi y col., 2023).

En el ámbito farmacéutico, varios medicamentos derivados de hidrazina han alcanzado relevancia clínica. Entre ellos destacan la procarbazina, utilizada en el tratamiento del linfoma de Hodgkin y tumores cerebrales; la fenelzina, un inhibidor de la monoaminooxidasa (MAO) con actividad antidepresiva; y la hidralazina, un vasodilatador empleado en el manejo de la hipertensión arterial (Guillou y col., 2024).

La 2,4-dinitrofenilhidrazina (2,4-DNPH), comúnmente conocida como reactivo de Brady, constituye uno de los derivados más importantes de la hidrazina en química orgánica analítica y sintética; se emplea ampliamente para la identificación y caracterización de aldehídos y cetonas, ya que reacciona con ellos formando 2,4-dinitrofenilhidrazonas cristalinas, estables y con puntos de fusión característicos que facilitan su aislamiento y purificación (Brady, 1931).

Estructuralmente, la 2,4-DNPH consiste en un anillo bencénico sustituido con un grupo hidrazino en posición 1 y dos grupos nitro en posiciones 2 y 4. Se trata de un sólido de color anaranjado, sensible a impactos y fricción, por lo que se comercializa habitualmente en forma hidratada para mejorar su estabilidad (Allen, 1930). Es un reactivo ideal para la obtención de hidrazonas cristalinas con buenos rendimientos, lo cual resulta particularmente útil tanto en la identificación cualitativa de carbonilos como en la preparación de derivados para estudios estructurales y biológicos posteriores.

Por otra parte, la alta multifuncionalidad de compuestos como las hidrazonas, junto con la posibilidad de introducir diversos sustituyentes en ambos extremos de la molécula, explica la amplia variedad de actividades biológicas reportadas para esta familia de compuestos y el sostenido interés de la comunidad científica en su síntesis con fines farmacológicos (Vivas y col., 2017; De la Cruz Argüello y col., 2022). En el ámbito terapéutico, diversas hidrazonas han alcanzado uso clínico como agentes antibacterianos. Entre los ejemplos más relevantes se encuentran la nitrofurazona, la furazolidona y la nitrofurantoína, compuestos que continúan empleándose en el tratamiento de diversas infecciones (Celik y col., 2020).

En los últimos años, esta clase de compuestos ha sido objeto de intensa investigación, particularmente en el ámbito de la actividad antimicrobiana. Puskullu y colaboradores en el año 2020 reportaron la síntesis de hidrazonas derivadas de quinolina-2-carbaldehído que exhibieron actividad inhibitoria frente a varios microorganismos (Puskullu y col., 2020). De manera similar, en 2022 Sahib y colaboradores obtuvieron derivados que incorporaban fragmentos de sulfonamida y amida, demostrando actividad antimicrobiana moderada contra bacterias Gram-positivas y Gram-negativas, con un compuesto que alcanzó un desempeño comparable al de la amoxicilina frente a *Staphylococcus epidermidis* (Sahib y col., 2022). Por otra parte, en 2020 Ade y colaboradores prepararon una serie de 2,4-dinitrofenilhidrazonas que mostró actividad débil a moderada contra *E. coli*, *P. aeruginosa*, *K. pneumoniae*, *S. aureus y S. pneumoniae*, incluyendo efectos moduladores de resistencia antibiótica. (Ade y col., 2020).

Estudios posteriores, como los de Babalola y colaboradores en 2022 (Babalola y col., 2022) y Popiołek y colaboradores en 2023 (Popiołek y col., 2023), han subrayado la influencia significativa de los sustituyentes aromáticos (particularmente halógenos y grupos metoxi), sobre la actividad antibacteriana y antifúngica de estas moléculas. Asimismo, en Venezuela recientemente se sintetizaron 2,4-dinitrofenilhidrazonas derivadas de naftoquinonas, destacando su potencial como plataformas para futuros estudios biológicos (Barrios y col., 2021). Sin embargo, el interés en las hidrazonas trasciende su potencial antimicrobiano. Diversos trabajos han explorado su aplicación en otras áreas terapéuticas relevantes. Recientemente se incorporaron núcleos de quinolina en el diseño de hidrazonas con el objetivo de evaluar su actividad citotóxica, inspirados en la eficacia demostrada de derivados quinólicos en terapias antitumorales (Katariya y col., 2020).

De igual manera se sintetizaron derivados de hidralazina que mostraron notables efectos antinociceptivos y antiinflamatorios en modelos *in vivo*. Por otra parte, en esta década de importantes avances de síntesis de hidrazonas se reportaron 2-tiazolilhidrazonas con prometedora capacidad antioxidante, alcanzando en algunos casos una neutralización

del radical DPPH• comparable a la de la curcumina. (Maltarollo y col., 2018). La notable versatilidad biológica de las hidrazonas se atribuye a la combinación de su relativa simplicidad sintética, la reactividad inherente del grupo imino y la facilidad para modular su estructura mediante la introducción de diferentes sustituyentes. Estos atributos las convierten en plataformas atractivas para el desarrollo de nuevas entidades químicas.

En el presente estudio, se sintetizaron cuatro nuevas hidrazonas derivadas de 2,4-dinitrofenilhidrazina mediante reacción de condensación ácido-catalizada con diferentes cetonas. Los productos obtenidos (P1–P4) fueron caracterizados en detalle mediante técnicas espectroscópicas (FT-IR, RMN-$^1$H y UV-Vis), confirmando la formación del grupo imino y la extensión del sistema π-conjugado. Adicionalmente, se evaluó su actividad bacteriostática *in vitro* frente a *Escherichia coli* mediante una modificación del método de difusión en disco de Kirby-Bauer. Este trabajo contribuye al conocimiento estructural y biológico de esta importante familia de compuestos, sentando las bases para futuras optimizaciones dirigidas al diseño de moléculas con mayor potencial terapéutico.

## 2 Procedimiento Experimental

### 2.1 Metodología y Materiales

#### *2.1.1 Síntesis Química de hidrazonas*

Las cetonas de partida (R1–R4) fueron seleccionadas con el propósito de evaluar el efecto de diferentes sustituyentes en el núcleo carbonílico sobre las propiedades estructurales y espectroscópicas de las hidrazonas resultantes. Las estructuras de los reactivos empleados y los productos obtenidos se muestran en la Figura 1.

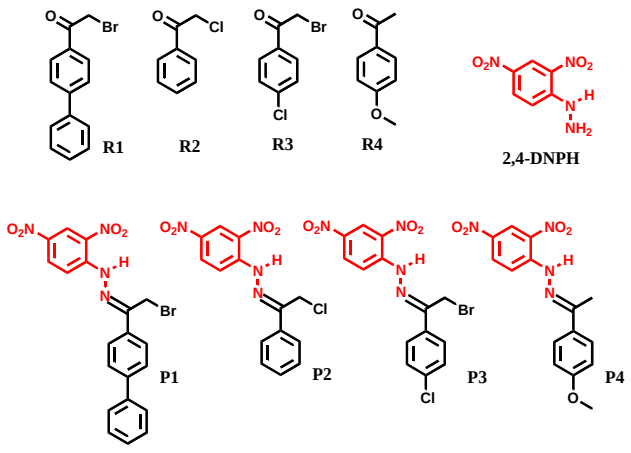


**Fig. 1.** Estructuras de las cetonas de partida (R1–R4), la 2,4-dinitrofenilhidrazina (2,4-DNPH) y las hidrazonas correspondientes (P1–P4).

La síntesis de las hidrazonas P1–P4 se llevó a cabo disolviendo cantidades equimolares (1 *mmol*) de 2,4-dinitrofenilhidrazina (2,4-DNPH) y la cetona correspondiente de Merck® sin purificación previa [2-bromo-1-(4-fenilfenil)etanona (R1), 2-cloro-1-feniletanona (R2), 2-bromo-1-(4-clorofenil)etanona (R3) o 1-(4-metoxifenil)etanona (R4)] en 15 *mL* de etanol de grado analítico. A la mezcla se añadió 0,05 *mL* de ácido sulfúrico concentrado como catalizador. La reacción se mantuvo bajo reflujo con agitación magnética constante durante unas 3 horas, hasta la aparición de un precipitado insoluble que indicaba la formación del producto. El progreso de la reacción se monitoreó mediante cromatografía de capa fina (TLC).

Una vez completada la reacción, los sólidos obtenidos fueron aislados por filtración al vacío y lavados sucesivamente con porciones de agua destilada y etanol frío para eliminar impurezas y reactivos no consumidos. La purificación final de las hidrazonas se realizó mediante recristalización en etanol. Los productos P1–P4 se obtuvieron como sólidos cristalinos de colores característicos y se secaron a temperatura ambiente.

### 2.2 Caracterización

#### *2.2.1 Caracterización Espectroscópica*

Los espectros de absorción electrónica se registraron en el rango 190–1100 *nm* en un espectrofotómetro UV-Vis *Thermo Scientific Evolution* 300, utilizando soluciones de las hidrazonas y reactivos de partida en diclorometano a concentraciones entre $1{,}0\times10^{-7}$ y $1{,}0\times10^{-6}$ $molL^{-1}$. Se efectuó un análisis comparativo de los espectros correspondientes a la triada cetona–hidrazina–hidrazona.

Los espectros infrarrojos con transformada de Fourier (FT-IR) se obtuvieron en el intervalo entre 4000–400 $cm^{-1}$ empleando un espectrofotómetro Perkin-Elmer Lambda 3 y pastillas de KBr al 1 % p/p (100 *mg* de KBr por muestra).

Los espectros de $^1$H-NMR se adquirieron en un espectrómetro Bruker Avance de 300 MHz. Las muestras se prepararon en $CDCl_3$ o DMSO-$d_6$ a una concentración de 7 *mM*, utilizando tetrametilsilano (TMS) como referencia interna.

#### *2.2.2 Evaluación de la actividad bacteriostática*

La actividad antibacteriana de las hidrazonas sintetizadas (P1–P4) se evaluó cualitativamente mediante una modificación del método de difusión en agar (Kirby-Bauer), utilizando la cepa estándar Escherichia coli ATCC 25922; como control positivo se empleó Estreptomicina (Sigma-Aldrich®) y como control negativo dimetilsulfóxido (DMSO) grado analítico (Sigma-Aldrich®). El medio de cultivo utilizado fue agar Müeller-Hinton (Sigma-Aldrich®),

preparado según las especificaciones del método estándar (Baüer y Kirby, 1966).

La cepa bacteriana se cultivó previamente durante 24 h a 37 °C en caldo Luria-Bertani. Las placas de Petri se esterilizaron por autoclave a 15 psi y 121 °C durante 15 *min*. Una vez enfriado el medio en ~ 60 °C, se vertió en placas de Petri hasta alcanzar un espesor uniforme. Tras solidificación, las placas se inocularon con 100 $\mu L$ de suspensión bacteriana ajustada, distribuyéndola homogéneamente con un esparcidor estéril. (Cavalieri y col., 2005).

Como modificación al método convencional, se aplicaron directamente 10 $\mu L$ de las soluciones de las hidrazonas (300 $\mu g/mL$ en DMSO) sobre puntos marcados en la superficie del agar. Las placas se incubaron a 37 °C durante 24 horas. Posteriormente, se midieron los diámetros de las zonas de inhibición alrededor de los puntos de aplicación. Todos los ensayos se realizaron por triplicado.

## 3 Discusión y Resultados

Los puntos de fusión de las hidrazonas P1–P4 se incrementaron notablemente respecto a las cetonas de partida (R1-R4), ver Tabla 1, lo que es consistente con la formación de estructuras planas y rígidas que favorecen un empaquetamiento cristalino más eficiente. La solubilidad también cambió de forma significativa: mientras las cetonas iniciales son más solubles en solventes polares, las hidrazonas muestran mayor afinidad por solventes de polaridad intermedia (Tabla 1), debido al aumento del carácter hidrofóbico tras la condensación con la 2,4-DNPH.

**Tabla 1.** Rendimiento, punto de fusión y solubilidad de las 2,4-dinitrofenilhidrazonas sintetizadas (P1–P4) y sus cetonas de partida (R1–R4).

| Caracterización física de las Hidrazonas sintetizadas | | | |
|---|---|---|---|
| **Compuesto** | **Rendimiento (%)** | **PF (°C)** | **(Solubilidad) 100mg/mL** |
| P1 | 86 | 228 | Acetona/$CH_2Cl_2$/ THF y $CHCl_3$ |
| P2 | 72 | 206 | |
| P3 | 69 | 212 | |
| P4 | 93 | 209 | |
| R1 | - | 125 | Etanol/Agua |
| R2 | - | 59 | |
| R3 | - | 97 | |
| R4 | - | 38 | |

### *3.1 Espectroscopia UV-visible*

La comparación de los espectros UV-Vis de la 2,4-dinitrofenilhidrazina (2,4-DNPH), la cetona de partida y la hidrazona correspondiente permitió observar un desplazamiento batocrómico en la banda de mayor longitud de onda, atribuible a la extensión del sistema π conjugado generado por la formación del grupo hidrazona.

En la Figura 2 se muestra la triada representativa para el compuesto P1 (2,4-dinitrofenilhidrazona de 2-bromo-1-(4-fenilfenil)etanona), junto con sus precursores 2,4-DNPH y R1. Se observa claramente el desplazamiento batocrómico de la banda de absorción de mayor longitud de onda (388 *nm*) en la hidrazona, ausente en los reactivos iniciales. Este comportamiento es consistente con la conjugación extendida mediada por el orbital $sp^3$ del nitrógeno, que permite la deslocalización del par electrónico no enlazante hacia el sistema π (Kamlet y col., 1971; Pavia y col., 2001).

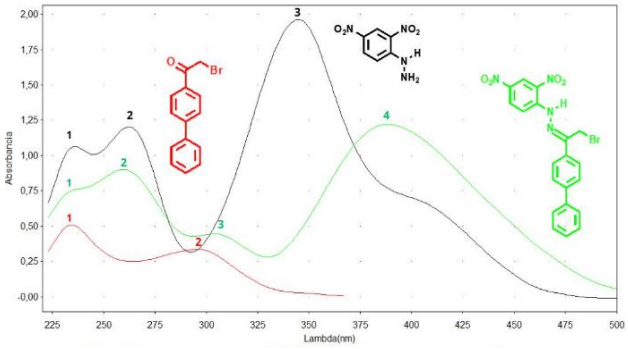


**Fig. 2**. Espectro UV-Vis de R1, 2,4-DNPH y P1

Los valores de $\lambda_{máx}$ de todos los productos sintetizados se encuentran resumidos en la Tabla 2. En esta tabla se aprecia que las hidrazonas P1–P4 presentan una banda característica entre 377 y 389 *nm*, resultado de la extensión de la conjugación π.

**Tabla 2.** Longitudes de onda de absorción máxima ($\lambda máx$) de las bandas UV-Vis de la 2,4-DNPH, las cetonas de partida (R1-R4) y las hidrazonas sintetizadas (P1–P4).

| Longitudes de onda de absorción máxima ($\lambda_{máx}$) | | | | |
|---|---|---|---|---|
| **Compuesto** | **1** | **2** | **3** | **4** |
| 2,4-DNPH | 232 | 263 | 346 | - |
| R1 | 232 | 295 | - | - |
| R2 | 247 | 280 | - | - |
| R3 | 268 | - | | |
| R4 | 275 | - | | |
| P1 | 232 | 261 | 305 | 388 |
| P2 | 233 | 377 | - | - |
| P3 | 233 | 380 | - | - |
| P4 | 232 | 389 | - | - |

En la Figura 3 se comparan los espectros UV-Vis de las cuatro hidrazonas P1–P4. Se observa que todos los productos exhiben la misma banda característica alrededor de 380 *nm*, confirmando la formación exitosa de las 2,4-dinitrofenilhidrazonas. Esta banda es coherente con lo reportado en la literatura para compuestos análogos (Koivusalmi, 2001). Además, se mantiene en todos los casos la banda a ~232 *nm* correspondiente al núcleo 2,4-DNPH, lo que indica que este fragmento estructural se conserva intacto tras la reacción de condensación.

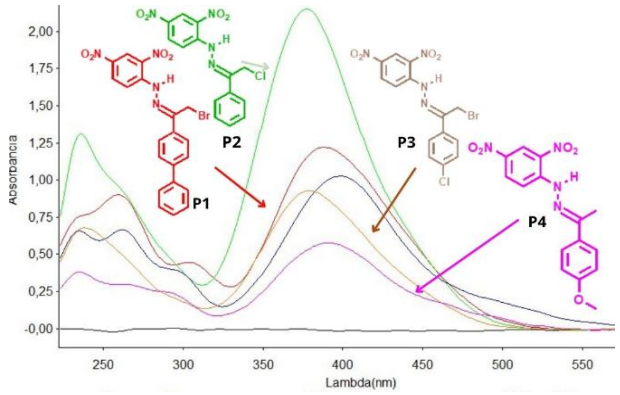


**Fig. 3.** Espectros UV-Vis superpuestos de las 2,4-dinitrofenilhidrazonas P1–P4.

La aparición sistemática del desplazamiento batocrómico y de la banda alrededor de 380 *nm* en todos los productos sintetizados demuestra la extensión del sistema cromóforo como fenómeno general en la formación de las 2,4-dinitrofenilhidrazonas.

### *3.2 Espectroscopia infrarroja, FT-IR*

La espectroscopia infrarroja (FT-IR) confirmó la formación de las 2,4-dinitrofenilhidrazonas mediante la desaparición de las bandas características del grupo carbonilo (C=O) de las cetonas de partida y de la amina primaria (–$NH_2$) de la 2,4-DNPH, así como la aparición de la banda de tensión del enlace C=N y la persistencia de la amina secundaria.

La Figura 4 muestra los espectros FT-IR superpuestos de la triada representativa: 2,4-DNPH, cetona R1 y la hidrazona P1. En el espectro de R1 se observa la banda C=O a 1687,9 $cm^{-1}$ (desplazada hacia frecuencias más bajas por conjugación aromática). El espectro de la 2,4-DNPH muestra las bandas de tensión N-H primaria y secundaria. En P1 desaparecen las señales de amina primaria y carbonilo, apareciendo la banda característica C=N a 1615,3 $cm^{-1}$ junto con la amina secundaria. Todas las asignaciones se detallan en la Tabla 3.

**Tabla 3.** Correlación de bandas FT-IR características en los espectros de 2,4-DNPH, R1 y P1.

| Bandas FT-IR. Espectros de 2,4-DNPH, R1 y P1 ($cm^{-1}$) | | | | |
|---|---|---|---|---|
| **Asignación** | **Señal** | **2,4-DNPH** | **R1** | **P1** |
| U N-H (1°) | A | 3326 | - | - |
| U N-H (2°) | B | 3285,7 | - | 3278,3 |
| U =C-H | C | 3103,8 | 3050,6 | 3046,3 |
| U C=O | E | - | 1687,9 | - |
| U C=N | F | - | - | 1615,3 |
| U C=C | G | 1645 | 1601,7 | 1590 |
| U $NO_2$ | H | 1517,9 | - | 1496,1 |
| U NO2 | I | 1319.4 | - | 1331,1 |

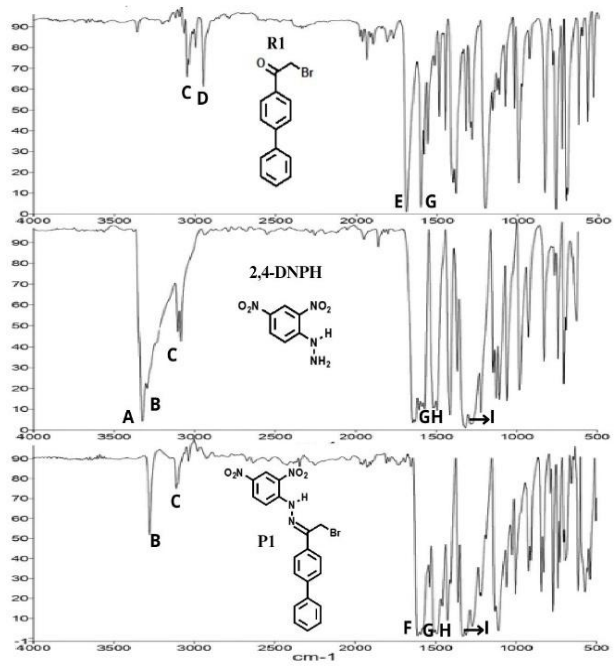


**Fig. 4.** Espectros FT-IR superpuestos de las 2,4-dinitrofenilhidrazonas P1 y R1.

De manera análoga, los espectros FT-IR de las hidrazonas P2, P3 y P4 presentaron un comportamiento espectral idéntico al de P1. Este patrón consistente se resume en la Tabla 4, donde se recopilan las bandas características de los cuatro productos.

**Tabla 4.** Correlación de bandas FT-IR características en los espectros de 2,4-DNPH, R1 y P1.

| Bandas FT-IR de las 2,4-dinitrofenilhidrazonas sintetizadas (P1–P4) ($cm^{-1}$) | | | | |
|---|---|---|---|---|
| **Asignación** | **P1** | **P2** | **P3** | **P4** |
| U N-H (2°) | 3278,3 | 3285,3 | 3292,3 | 3292,3 |
| U C=N | 1615,3 | 1615,5 | 1610,6 | 1610,6 |
| U C=C | 1590 | 1580 | 1590,1 | 1590,1 |
| U NO2 | 1496,1 | 1517,2 | 1495 | 1495 |
| U NO2 | 1331,1 | 1332 | 1336,6 | 1333,6 |
| U C-O-C | - | - | - | 1251,9 |
| U C-O-C | - | - | - | 1025 |

### *3.3 Espectroscopia RMN-$^1$H*

La espectroscopia RMN-$^1$H confirmó de manera inequívoca la formación de las 2,4-dinitrofenilhidrazonas mediante la desaparición de la señal característica de la amina primaria (–$NH_2$) de la 2,4-DNPH, el notable desplazamiento hacia campos más bajos del protón –NH– y la retención de los patrones alifáticos y aromáticos de los precursores, todo ello consistente con la creación del sistema conjugado C=N–NH–.

En la Figura 5 se muestran los espectros RMN-$^1$H superpuestos de la triada representativa: 2,4-dinitrofenilhidrazina (2,4-DNPH), cetona R1 y la hidrazona P1. La Tabla 5 recopila las señales observadas.

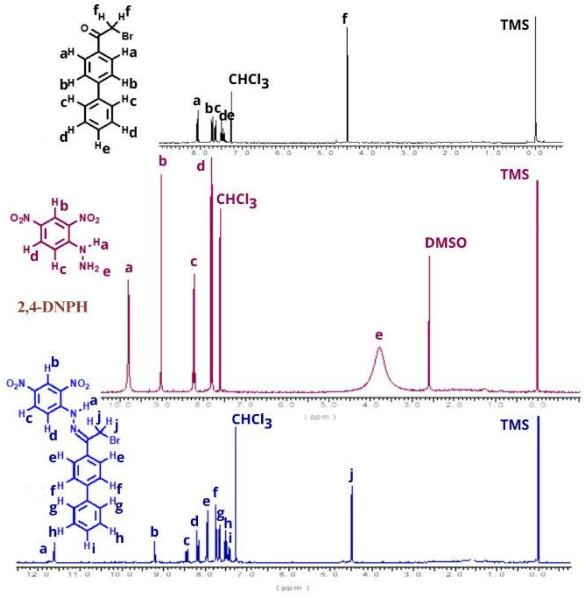


**Fig. 5.** Espectros RMN-$^1$H superpuestos de las 2,4-dinitrofenilhidrazonas P1 y R1.

**Tabla 5.** Señales RMN-$^1$H características de 2,4-DNPH, R1 y P1.

| Compuesto | Señal | δ(ppm) | Multipl. | Integral |
|---|---|---|---|---|
| 2,4-DNPH | a | 9,801 | s | 1 |
| 2,4-DNPH | b | 9,019 | s | 1 |
| 2,4-DNPH | c | 8,231 | d | 1 |
| 2,4-DNPH | d | 7,803 | d | 1 |
| 2,4-DNPH | a | 3,800 | s (ancha) | 2 |
| R1 | - | 8,090 | d | 2 |
| R1 | a, b, c, d, e | 7,720-7,440 | m | 9 |
| R1 | f | 4,491 | s | 2 |
| P1 | a | 11,621 | s | 1 |
| P1 | b, c, d, e, f, g, h | 9,204-7,425 | m | 12 |
| P1 | j | 4,475 | s | 2 |

*s= singlete, d=doblete y m=multiplete*

En el espectro de P1 desaparece por completo la señal ancha a 3.80 *ppm* (2H, –$NH_2$) de la 2,4-DNPH, mientras que el protón –NH– sufre un fuerte desplazamiento deshieldado hasta 11.621 *ppm*. Este efecto se debe al aumento del carácter s del nitrógeno $sp^2$ en el sistema conjugado C=N–NH–, al efecto anisotrópico del anillo dinitrofenílico y a la atracción electrónica de los grupos nitro, todo lo cual reduce la densidad electrónica sobre el protón. La señal –$CH_2Br$ permanece prácticamente inalterada (4.476 *ppm*), y los protones aromáticos muestran los desplazamientos esperados por la extensión de la conjugación. Estos cambios constituyen evidencia espectral directa y concluyente de la formación de la hidrazona.

Los espectros RMN-$^1$H de las hidrazonas P2, P3 y P4 presentaron un patrón idéntico al de P1, con las mismas asignaciones diagnósticas. Las señales clave de los cuatro productos se resumen de forma condensada a continuación (Tabla 6):

**Tabla 6.** Señales claves en RMN-$^1$H de los productos (P1-P4).

| P1 | | P2 | |
|---|---|---|---|
| **δ(ppm)** | **Asignación** | **δ(ppm)** | **Asignación** |
| 11.621 | (s, 1H, NH) | 11.581 | (s, 1H, NH) |
| 9.204 | (s, 1H, Ar–H) | 9.056 | (s, 1H, Ar–H) |
| 8.432 | (d, 1H, Ar–H) | 8.448 | (d, 1H, Ar–H) |
| 8.173 | (d, 1H, Ar–H) | 8.173 | (d, 1H, Ar–H) |
| 7.943–7.425 | (m, 9H, Ar–H) | 7.953–7.497 | (m, 4H, Ar–H) |
| 4.476 | (s, 2H, $CH_2Br$) | 4.851 | (s, 2H, $CH_2Cl$) |
| **P3** | | **P4** | |
| **δ(ppm)** | **Asignación** | **δ(ppm)** | **Asignación** |
| 11.579 | (s, 1H, NH) | 11.355 | (s, 1H, NH) |
| 9.193 | (s, 1H, Ar–H) | 9.167 | (s, 1H, Ar–H) |
| 8.426 | (d, 1H, Ar–H) | 8.350 | (d, 1H, Ar–H) |
| 8.118 | (d, 1H, Ar–H) | 8.110 | (d, 1H, Ar–H) |
| 7.803–7.477 | (m, 4H, Ar–H) | 7.832 | (d, 2H, Ar–H) |
| --- | --- | 6.974 | (d, 2H, Ar–H) |
| 4.409 | (s, 2H, $CH_2Br$) | 3.879 | (s, 3H, $OCH_3$) |
| --- | --- | 2.440 | (s, 3H, C=N–$CH_3$) |

La superposición de los espectros de las cuatro hidrazonas P1–P4 junto con la 2,4-DNPH se muestra en la Figura 6; se aprecia de forma clara el desplazamiento sistemático del protón –NH– y la ausencia de la señal –$NH_2$ en todos los productos.

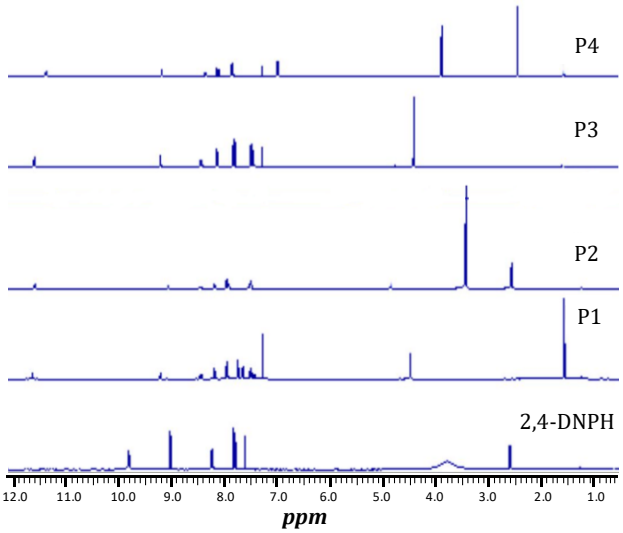


**Fig. 6.** Espectros RMN-$^1$H superpuestos de las 2,4-dinitrofenilhidrazonas P1-P4

Estos datos, combinados con la retención de los patrones alifáticos y aromáticos de cada cetona de partida,

validan por completo la estructura de las hidrazonas sintetizadas y la selectividad de la reacción de condensación.

### *3.4 Actividad antibacteriana*

La actividad antibacteriana de las hidrazonas sintetizadas (P1–P4) se evaluó mediante una modificación del método de difusión en agar frente a *Escherichia coli* ATCC 25922. Tras 24 h de incubación a 37 °C, ninguna de las hidrazonas produjo zona de inhibición visible alrededor del punto de aplicación (Figura 7). En contraste, el control positivo (estreptomicina) generó un claro halo de inhibición de 29 ± 1 *mm*, mientras que el control negativo (DMSO) no mostró efecto alguno (Tabla 7).

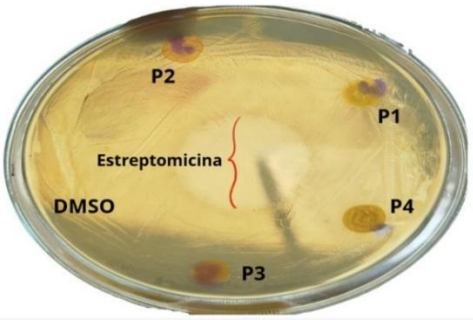


**Fig. 7.** Placa de Petri después de 24 h de incubación con las muestras a ensayar y los grupos controles

La ausencia de actividad bacteriostática observada puede atribuirse, al menos parcialmente, a la limitada difusión de los compuestos en el medio sólido Müeller-Hinton. Como se aprecia en la Figura 7, la coloración característica de las hidrazonas permaneció localizada en el sitio de aplicación, sin evidenciar una migración significativa a través del agar. Este comportamiento sugiere una posible adsorción de las moléculas sobre la superficie del medio de cultivo o una baja solubilidad en las condiciones ensayadas, lo que impediría alcanzar concentraciones efectivas en las proximidades de la bacteria (Celik y col., 2020).

**Tabla 7**. Zonas de inhibición (mm) de las hidrazonas (P1–P4) y controles frente a *E. coli* ATCC 25922.

| Compuesto | Zona de Inhibición ± 1mm |
|---|---|
| P1 | --- |
| P2 | --- |
| P3 | --- |
| P4 | --- |
| DMSO | --- |
| Estreptomicina | 29 |
| (-) Ausencia de Halo de Inhibición | |

Es importante destacar que la concentración empleada (300 $\mu g/mL$) fue comparable a la utilizada en estudios previos donde hidrazonas derivadas de aldehídos mostraron actividad moderada contra *E. coli* (Sahib et al., 2022). Por lo tanto, la naturaleza del núcleo carbonílico (cetonas α-sustituidas versus aldehídos aromáticos) podría influir en las propiedades fisicoquímicas y, consecuentemente, en la bioactividad observada.

Estos resultados preliminares indican que, bajo las condiciones del método de difusión en agar, las hidrazonas P1–P4 no exhibieron actividad bacteriostática detectable frente a *E. coli* ATCC 25922. Se recomienda realizar ensayos complementarios mediante métodos de microdilución en caldo, los cuales permitirían determinar la concentración mínima inhibitoria (CMI), superar posibles limitaciones de difusión y obtener una evaluación más precisa del potencial antimicrobiano de esta serie de compuestos.

## 4 Conclusiones

Se sintetizaron con éxito cuatro nuevas hidrazonas derivadas de 2,4-dinitrofenilhidrazina (P1–P4) mediante reacción de condensación ácido-catalizada entre 2,4-DNPH y las cetonas correspondientes (R1–R4) en etanol bajo reflujo. Los compuestos se obtuvieron con buenos rendimientos (69 y 93%) y presentaron las propiedades físicas esperadas, tales como color característico, valores de Rf y puntos de fusión definidos.

La elucidación estructural de los productos se realizó mediante técnicas espectroscópicas complementarias. Los espectros UV-Vis mostraron bandas de absorción en el rango de 346–398 *nm*, atribuibles a transiciones $\pi \rightarrow \pi^*$ del sistema conjugado extendido característico de las hidrazonas. Los espectros de FT-IR confirmaron la formación del grupo imino mediante la desaparición de la banda de tensión del carbonilo (C=O) de las cetonas precursoras y la aparición de la señal característica de tensión C=N alrededor de 1615 $cm^{-1}$. Por su parte, los espectros de $^1$H NMR evidenciaron la desaparición de las señales correspondientes a los protones de la amina primaria de la 2,4-DNPH y el desplazamiento químico característico del protón azometino (=N–NH–), confirmando la estructura propuesta para las hidrazonas sintetizadas.

La evaluación de la actividad bacteriostática *in vitro* frente a *Escherichia coli* ATCC 25922, realizada mediante una modificación del método de difusión en agar (Kirby-Bauer) en medio Müeller-Hinton, reveló que ninguna de las hidrazonas sintetizadas (P1–P4) produjo zona de inhibición detectable bajo las condiciones ensayadas. El control positivo (estreptomicina) mostró un claro halo de inhibición, confirmando la sensibilidad de la cepa bacteriana. Estos resultados contribuyen al conocimiento estructural de hidrazonas 2,4-dinitrofenilhidrazínicas derivadas de cetonas y destacan la importancia de considerar las propiedades fisicoquímicas al evaluar el potencial biológico de esta clase de compuestos.

**Agradecimientos**

Los autores expresan su sincero agradecimiento al Dr. Carlos Ayala del Laboratorio de Espectroscopía Molecular de la Facultad de Ciencias, Universidad de Los Andes, por permitir el acceso a su laboratorio y facilitar la realización de los espectros UV-Visible.

Asimismo, agradecen a la MSc. Marlin Villaroel del Laboratorio de Cinética y Catálisis de la Facultad de Ciencias, Universidad de Los Andes, por su valiosa colaboración en el procesamiento y obtención de los espectros infrarrojo (FT-IR).

Finalmente, se agradece especialmente al Dr. Antxon Martínez de Ilarduya de la Universidad Politécnica de Cataluña por su generoso apoyo y asistencia en la adquisición y análisis de los espectros de resonancia magnética nuclear de protón ($^1$H -NMR).

**Referencias**

Ade A., Amengor C., Brobbey A., Ayensu I., Harley B., Boakye Y., (**2020**). Synthesis and Antimicrobial Resistant Modulatory Activity of 2, 4-Dinitrophenylhydrazone Derivatives as Agents against Some ESKAPE Human Pathogens, *Journal of Chemistry*, Vol. 2020(1), pp. 1-9.

Allen C., (**1930**). The identification of carbonyl compounds by use of 2, 4-dinitrophenylhydrazine, *Journal of the American Chemical Society*, Vol. 52(7), pp. 2955-2959.

Babalola S., Igie N., Idris A., Hamza A., Sanni Y., Muhammad H., Erumiseli O., Bakare L., (**2022**). Antimicrobial activities of hydrazones with a 2, 4-dichloro moiety, *Drug Discovery*, Vol. 16(37), pp. 53-62.

Barqi M., Ashar A., Bhutta Z., Javed M., Abdellah I., Eletmany M., (**2023**). Comprehensive Investigation of the Potential of Hydrazine and its Derivatives for the Synthesis of Various Molecules with Biological Activity, *International journal of chemical and biochemical sciences*, Vol. 24(4), pp. 369-385.

Barrios J., Vizcaya M., Carrillo F., Delgado G., (**2021**). Síntesis y caracterización de hidrazonas obtenidas a partir de 1, 2 y 1, 4-naftoquinona con 2, 4-dinitrofenilhidracina, *Avances en Química*, Vol. 16(2), pp. 31-37.

Bauer A.W., Kirby W.M., Sherris J.C., Turck M., (**1966**). Antibiotic Susceptibility Testing by a Standardized Single Disk Method, *American Journal of Clinical Pathology*, Vol. 45(4), 493-496.

Bosch F., Rosich L., (**2008**). The contributions of Paul Ehrlich to pharmacology: a tribute on the occasion of the centenary of his Nobel Prize, *Pharmacology*, Vol. 82(3), pp. 171-179.

Brady O., (**1931**). The use of 2: 4-dinitrophenylhydrazine as a reagent for carbonyl compounds, *Journal of the Chemical Society (Resumed)*, issue 0, 756-759.

Cavalieri S., Rankin I., Harbeck R., Sautter R., McCarter Y., Sharp S., Ortez, J., Spiegel C., (**2005**). Manual de pruebas de susceptibilidad antimicrobiana, *American Society for Microbiology*, 1-248.

Celik I., Erol M., Puskullu M., Uzunhisarcikli E., Ince U., Kuyucuklu G., Suzen S., (**2022**). In vitro and *in silico* studies of quinoline-2-carbaldehyde hydrazone derivatives as potent antimicrobial agents, *Polycyclic Aromatic Compounds*, Vol. 42(4), pp. 1942-1958.

De la Cruz Argüello B., Gálvez B., Díaz G., Morán A., (**2022**). Síntesis y evaluación de la actividad antifúngica de hidrazonas aromáticas, *Revista Ingeniería Investigación y Desarrollo: I2+ D*, Vol. 22, pp.6-15.

Guillou A., Peyrottes S., Vasseur J., Mathé C., Smietana M., (**2024**). The hydrazine moiety in the synthesis of modified nucleosides and nucleotides, *ChemMedChem*, Vol. 19(20), pp. 1-20.

Kamlet M.J., Eastes J.W., Aldridge M.H., Minesinger R.R., (**1971**). Hybridization on amine nitrogens and pKa values of some N-(4-nitrophenyl) polymethylenimines, *The Journal of Organic Chemistry*, Vol. 36(25), 3847-3851.

Katariya K., Shah S., Reddy D., (**2020**). Anticancer, antimicrobial activities of quinoline based hydrazone analogues: Synthesis, characterization and molecular docking, *Bioorganic chemistry*, Vol. 94, pp. 103406.

Koivusalmi E., (**2001**). Characterisation and analysis of synthesis mixtures of hydroxy aldehydes, hydroxy carboxylic acids and polyols (Doctoral dissertation, Helsingin yliopisto).

Maltarollo V., de Resende M., Kronenberger T., Lino C., Sampaio M., da Rocha Pitta M., de Melo Rego M., Labanca R., de Oliveira R., (**2018**). In vitro and in silico studies of antioxidant activity of 2-thiazolylhydrazone derivatives, *Journal of Molecular Graphics and Modelling*, Vol. 86, pp. 106-112.

Pavia D.L., Lampman G.M., Kriz G.S., Vyvyan J.R., (**2001**). Introduction to spectroscopy. Belmont, USA, 13.

Popiołek Ł., (**2021**). Updated information on antimicrobial activity of hydrazide–hydrazones, *International Journal of Molecular Sciences*, Vol. 22 (17), pp. 9389.

Popiołek Ł., Gawrońska-Grzywacz M., Dziduch A., Biernasiuk A., Piątkowska-Chmiel I., Herbet M., (**2023**). Design, Synthesis, and In Vitro and In Vivo Bioactivity Studies of Hydrazide–Hydrazones of 2, 4-Dihydroxybenzoic Acid, *International Journal of Molecular Sciences*, Vol. 24(24), pp. 17481.

Puskullu M., Celik I., Erol M., Fatullayev H., Uzunhisarcikli E., Kuyucuklu G., (**2020**). Antimicrobial and antiproliferative activity studies of some new quinoline-

3-carbaldehyde hydrazone derivatives, *Bioorganic Chemistry*, Vol. 101, pp. 104014.

Sahib H., Hadi M., Abdulkadir M., (**2022**). Synthesis, and Antimicrobial Evaluation of New hydrazone Derivatives of (2, 4-dinitrophenyl) hydrazine, *Research Journal of Pharmacy and Technology*, Vol. 15(4), pp. 1743-1748.

Vivas B., Balbuena L., López I., (**2017**). Síntesis verde de una hidrazona aromática con estructura nueva / New structure aromatic hydrazone green synthesis. *CIBA, Revista Iberoamericana de las Ciencias Biológicas y Agropecuarias*, Vol. 6(12), pp. 17-32.

***Recibido:*** *13 de mayo de 2026*

***Aceptado:*** *22 de julio de 2026*

***Rodríguez, Fabio:*** *Licenciado en Química 2025, Departamento de Química (Laboratorio de Polímeros) Facultad de Ciencias, Universidad de Los Andes, Mérida, Venezuela.*
***https://orcid.org/0009-0009-2108-629X***

***Vizcaya, Marietta:*** *PhD. en Química de Medicamentos, 2014, Instituto de Investigaciones Científicas, Facultad de Farmacia y Bioanálisis, Universidad de Los Andes; Profesora del Departamento de Química (Laboratorio de Polímeros), Facultad de Ciencias, ULA. Mérida, Venezuela. Correo electrónico: marietta@ula.ve*
***https://orcid.org/ 0000-0002-2064-4175***

***Pérez Dávila, Patricia:*** *PhD. en Química de Medicamentos, 2017, Instituto de Investigaciones Científicas, Facultad de Farmacia y Bioanálisis, Universidad de Los Andes; Profesora del Departamento de Química (Laboratorio de Polímeros), Facultad de Ciencias, ULA. Mérida, Venezuela. Correo electrónico: perezdpatricia@gmail.com*
***https://orcid.org/0000-0003-0591-2351***

***Chacón, Zarack:*** *MSc. en Biotecnología de Microorganismos (2002). Maestría en Biotecnología de Microorganismos, Facultad de Ciencias, Universidad de los Andes; Profesor del Laboratorio de Microbiología Molecular y Biotecnología, Facultad de Ciencias, ULA. Mérida, Venezuela.* ***Correo electrónico****: zarack5272@gmail.com*
***https://orcid.org/ 0009-0008-0728-8824***

***Lugo González, Claudio Antonio:*** *PhD. en Química Aplicada, mención: Estudio de Materiales, PiQA, 2017, Universidad de Los Andes; MSc. en Química Aplicada, mención: Estudio de Materiales, PiQA, 2009, Universidad de Los Andes; Profesor Titular del Departamento de Química (adscrito al Laboratorio de Cinética y Catálisis), Facultad de Ciencias, ULA. Mérida, Venezuela. Correo electrónico: claudiolugo@ula.ve*
***https://orcid.org/0000-0001-8003-0354***

*Artículo de Investigación. Revista Ciencia e Ingeniería. Vol. 47, No. 3 pp. 277-282, agosto-noviembre, 2026.*
*ISSN 1316-7081. ISSN Elect. 2244-8780 Universidad de los Andes (ULA)*

# Factores personales y organizacionales en fallas por error humano: análisis en procesos críticos de minería aurífera venezolana

# Personal and organizational factors in human error failures: analysis in critical processes of Venezuelan gold mining

**Varela, Andrónico[1]*; Labrador, Rafael[2]**
[1]Universidad Nacional Experimental del Táchira,
San Cristóbal, Táchira, Venezuela.
[2]Universidad de Los Andes,
San Cristóbal, Táchira, Venezuela.
*avarelac01@gmail.com

**Resumen**

*La evolución de los procesos industriales ha traído consigo un aumento en sus niveles de productividad y calidad, pero también ha generado nuevas exigencias operacionales y riesgos que pueden afectar el cumplimiento de metas cada vez más exigentes, así como la seguridad de personas, instalaciones y medio ambiente. Esto se pone de manifiesto en las empresas de minería aurífera ubicadas en el Arco Minero del Orinoco, un entorno caracterizado por procesos con bajos niveles de automatización, altos riesgos operativos y condiciones laborales retadoras. La investigación desarrollada se centró en el estudio de los factores personales y organizacionales asociados a las fallas por error humano ocurridas en los procesos críticos de las empresas mineras de la zona. La metodología, enmarcada en el paradigma positivista, bajo un enfoque cuantitativo con diseño bibliográfico de tipo documental descriptivo, partió del análisis de las fallas documentadas en los registros del área de operaciones de la planta, para determinar los puestos de trabajo críticos, las fallas de mayor impacto y las causas raíz asociadas a errores humanos, las cuales se categorizaron y analizaron bajo el marco de la neurociencia y la ingeniería. Los resultados indican que los procesos de Extracción Primaria y Molienda son los más críticos, las causas raíz de los errores humanos se concentran en la omisión de instrucciones (48%), la falta de competencias (41%) y la carencia de procedimientos documentados (30%). La investigación concluye que el error humano en el contexto minero no es un evento aislado, sino una propiedad emergente de un diseño sociotécnico precario que afecta la conducta del personal responsable de la operación y el mantenimiento de los procesos en términos de actitud y aptitud, haciéndolos vulnerables a errores por desacoplamiento perceptivo y brechas de competencias.*

**Palabras clave**: factores personales y organizacionales, error humano, empresa minera.

**Abstract**

*The evolution of industrial processes has led to increased levels of productivity and quality; however, it has also generated new operational demands and risks that can jeopardize the achievement of increasingly stringent goals, as well as the safety of personnel, facilities, and the environment. This is particularly evident in gold mining companies located in the Orinoco Mining Arc, an environment characterized by low levels of automation, high operational risks, and challenging labor conditions. The present research focused on studying the personal and organizational factors associated with human error failures occurring in the critical processes of mining companies in the region. The methodology, framed within the positivist paradigm under a quantitative approach with a descriptive documentary-bibliographic design, began with an analysis of documented failures in plant operations records. This allowed for the identification of critical job positions, high-impact failures, and root causes associated with human error, which were categorized and analyzed through the lenses of neuroscience and engineering. The results indicate that Primary Extraction and Grinding are the most critical processes. The root causes of human errors are primarily concentrated in the omission of instructions (48%), lack of competencies (41%), and*

*the absence of documented procedures (30%). The research concludes that human error in the mining context is not an isolated event, but rather an emergent property of a precarious sociotechnical design. This design adversely affects the conduct of personnel responsible for operations and maintenance in terms of attitude and aptitude, making them vulnerable to errors caused by perceptual decoupling and competency gaps.*

**Keywords:** personal and organizational factors, human error, mining company.

## 1 Introducción

Las exigencias a las que están sometidos los procesos industriales en la actualidad demandan la mejora continua de sus sistemas, a fin de alcanzar mayores niveles de confiabilidad, productividad y seguridad. Las instalaciones industriales hoy en día están equipadas con dispositivos y sistemas que permiten la automatización y el control avanzado de los procesos, pero el análisis de accidentes en las organizaciones revela que, para alcanzar mayores niveles de confiabilidad, aún se requiere una amplia mejora en lo que respecta a la seguridad, particularmente en el área de factores humanos y organizacionales (Zarei et al., 2021).

Diversas investigaciones señalan que la confiabilidad de un sistema industrial está afectada directa o indirectamente, entre un 70% y un 90%, por la influencia de las desviaciones en la gestión del ser humano, las cuales surgen como resultado de la interacción entre multiples factores, algunos de naturaleza personal y otros de naturaleza organizacional. Esto es particularmente importante en sectores industriales de alto riesgo, como el minero, donde la mayor parte de los accidentes se relacionan con acciones y decisiones humanas en la cadena operativa, y fallas latentes en la organización (González et al., 2022; Labrador et al., 2012; Leveson, 2020; NASA, 2023; Woods y Hollnagel, 2017).

En Venezuela, la explotación aurífera en el Arco Minero del Orinoco se desarrolla en un contexto de baja automatización y elevada hostilidad ambiental, con espacios de trabajo carentes de condiciones ergonómicas adecuadas, servicios básicos deficientes y personal con escasa formación técnica (Salomón et al., 2018); esto sitúa al recurso humano como el eje central de la confiabilidad. La presente investigación analiza cómo la interacción entre la biología del trabajador y el diseño organizacional precipita el error humano en procesos críticos.

## 2 Marco Teórico

### *2.1 Perspectiva Sociotécnica del Error Humano.*

El error humano no debe conceptualizarse como una causa aislada, sino como un síntoma de problemas sistémicos profundos, en el contexto industrial minero, el éxito y el error provienen de la misma fuente: la capacidad de adaptación ante un sistema impredecible. Siguiendo el modelo de Reason, las fallas latentes (decisiones gerenciales, diseño de procedimientos, características del puesto de trabajo) crean "agujeros" en las defensas de la organización que permiten que el error activo cometido por la persona (por desatención, desconocimiento u omisión) se materialice en una falla del proceso o en un accidente (Reason, 1990; Hollnagel, 2021; Dekker, 2014)

### *2.2 Fundamentos Neurocognitivos del Desempeño.*

La conducta humana es el resultado emergente de circuitos neuronales que procesan información sensorial, motora y asociativa. El sistema de ganglios basales almacena rutinas automáticas que permiten al cerebro ahorrar energía, mientras la corteza prefrontal gestiona la toma de decisiones consciente. El error ocurre cuando el sistema de hábitos toma el control en situaciones que requieren supervisión lógica, cuando las competencias del trabajador se ven superadas por las demandas de las situaciones que enfrenta, o cuando el estrés inunda el cerebro de cortisol, inhibiendo la flexibilidad cognitiva y provocando respuestas rígidas (Labrador et al., 2012; Kandel et al., 1999, 2021, Inzlicht y Schmeichel, 2012; Purves et al., 2018; Duhigg, 2012; Gehring et al., 2012; Posner, 2012).

### *2.3 Motivación, Atención y Error Humano.*

La motivación depende de la vía mesocorticolímbica; niveles óptimos de dopamina energizan la corteza prefrontal para mantener el foco atencional. Sin embargo, un desequilibrio entre el esfuerzo exigido y la recompensa percibida genera una degradación del control cognitivo. Este fenómeno, conocido como "desacoplamiento perceptivo", provoca que el cerebro deje de procesar estímulos externos críticos para priorizar pensamientos internos, debilitando la señal de Negatividad Relacionada al Error (ERN) y precipitando fallas por desatención (Smallwood y Schooler, 2015; Gehring et al., 2012; Labrador et al., 2012)

### *2.4 Competencias y Error Humano.*

La competencia es un constructo multidimensional que articula recursos personales (conocimientos, habilidades y actitudes) con el contexto profesional para resolver problemas

específicos de manera eficaz. El desempeño humano confiable depende de la aptitud (saber y poder), la cual está determinada por el nivel de desarrollo de las competencias requeridas para el desempeño de la función en el medio laboral. Bajo la perspectiva de la neurociencia, la pericia técnica reside en la consolidación de redes neuronales y en la memoria de largo plazo. Cuando existe un déficit aptitudinal, el cerebro del trabajador no ha desarrollado los esquemas mentales necesarios para interpretar señales críticas, lo que genera una "falla de diseño" en el sistema sociotécnico. La falta de formación técnica impide que estas redes neuronales se activen de forma automática y segura, el error humano emerge entonces cuando la demanda de la tarea supera la capacidad biológica y cognitiva del operario debido a la ausencia de herramientas intelectuales para la ejecución (Alles, 2016; Lazzati, 2012; Le Boterf, 2001; Boyatzis, 2008; Tobón, 2013, Dolan, 2007; Bubb, 2005; Labrador et al., 2012; Kandel et al., 1999,2021).

*2.5 Precondiciones Organizacionales y Ergonómicas.*

La ergonomía cognitiva define los límites de la carga mental que una interfaz puede imponer sin superar la capacidad de la memoria de trabajo. En organizaciones con "opacidad sistémica", donde no hay visibilidad clara de los límites operativos, el trabajador es forzado a improvisar. El diseño del puesto de trabajo actúa así como un inductor de variabilidad: si la organización falla en proveer condiciones ergonómicas básicas, procedimientos claros, herramientas aptas; el error humano se convierte en una consecuencia inevitable del diseño y no solo en una falla individual (Cañas, 2011; Dekker, 2014; API770, 2001)

## 3 Metodología

La investigación desarrollada, enmarcada en el paradigma positivista, bajo un enfoque cuantitativo, tiene un diseño bibliográfico de tipo documental descriptivo, donde las fallas ocurridas en los puestos de trabajo críticos de la empresa se tomaron de los registros de paradas no programadas del proceso durante los dos últimos años, para posteriormente ser analizadas utilizando la técnica del análisis de causa raíz.

La identificación de las fallas que afectan a los procesos de la empresa se llevó a cabo mediante la revisión de datos secundarios contenidos en los registros históricos de fallas, así como en los informes especiales elaborados por el área de operaciones ante la ocurrencia de fallas. Para la jerarquización de los procesos y de las fallas ocurridas se utilizó la técnica del Análisis de Pareto, para la clasificación de los procesos y de sus fallas según su frecuencia e impacto se utilizaron técnicas de jerarquización basadas en el análisis de riesgo, y sobre las fallas de alto impacto identificadas se aplicó la técnica del Análisis de Causa Raíz, a fin de identificar las causas raíz de las fallas, tanto las humanas como las organizacionales.

## 4 Discusión y Resultados

Una vez recopilada la información proveniente de los históricos de fallas del área de operaciones, para jerarquizar la vulnerabilidad del sistema se aplicó el modelo de Criticidad Total por Riesgo CTR (Parra et al., 2021), definido como el producto de la Frecuencia de Fallas (FF) por la Consecuencia (C). La frecuencia se estimó en una escala de 1 a 4 basada en el volumen de fallas del bienio 2023-2024. La consecuencia se calculó mediante la suma ponderada del impacto en la operación, costos de mantenimiento e impacto en seguridad, higiene y ambiente.

Como se observa en la Matriz CTR (Fig. 1), los procesos de Extracción Primaria (FF: 4; C: 17; CTR: 68) y Molienda (FF: 3; C: 18; CTR: 54) resultaron ser los nodos críticos. Estos procesos concentran la mayor carga cognitiva y presentan una baja predictibilidad tecnológica, lo que incrementa la probabilidad de error inducido por el entorno.

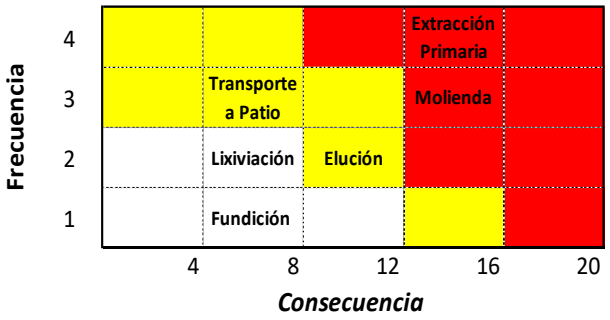


**Fig. 1.** Matriz CTR.

Tras definir los procesos críticos, se revisaron los registros históricos para identificar los equipos con mayor incidencia en la indisponibilidad operativa. Se determinó que, para la Extracción Primaria, los cargadores frontales acumularon la mayor cantidad de eventos. Para la Molienda, el molino de bolas y la bomba de pulpa fueron los equipos más afectados. Se seleccionaron nueve fallas recurrentes que acumulaban entre el 83% y el 87% del tiempo fuera de servicio en sus respectivos equipos (Tabla 1) para la aplicación del análisis profundo.

**Tabla 1.** Fallas de alto impacto en sistemas críticos.

| Procesos Críticos | Equipos Críticos | Fallas de alto impacto | % del tiempo total de falla del equipo |
|---|---|---|---|
| Extracción Primaria | Cargador frontal | Equipo no enciende<br>Pérdida de potencia en pala<br>Pérdida de potencia desplazamiento | 84% |
| Molienda | Molino de bolas | Reducción de capacidad de molienda<br>Tamaño de grano fuera de especificación<br>Molino no enciende | 87% |
| | Bomba de pulpa | Bomba no levanta presión<br>Bomba no enciende<br>Fuga de pasta | 83% |

El ACR fue ejecutado por un equipo multidisciplinarioempleando el método de validación de hipótesis. Por

ejemplo, para el evento "cargador frontal no enciende", se formularon hipótesis de primer nivel (bomba de aceite, sistema eléctrico, combustible) que fueron aceptadas o descartadas mediante evidencia física y registros de mantenimiento. Este proceso iterativo permitió rastrear el evento hasta encontrar las causas humanas y latentes, como se ilustra en el diagrama para la falla en la bomba de aceite del cargador frontal.

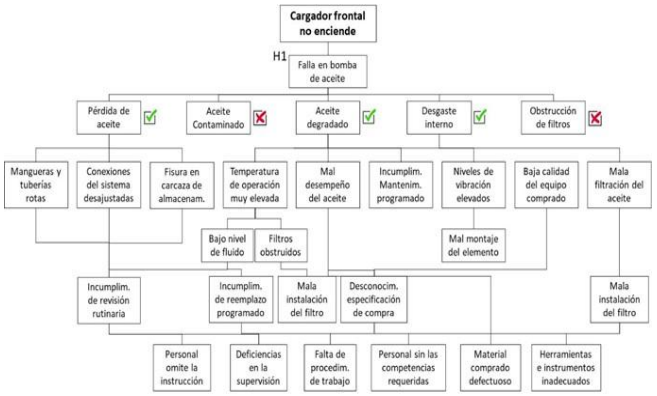


**Fig. 2.** Análisis causa raíz para falla en bomba de aceite.

Los resultados del ACR se procesaron estadísticamente para identificar los patrones de ocurrencia, luego las causas se agruparon en una taxonomía de tres categorías basadas en su origen: la Motivacional-Actitudinal (el "querer"), que incluye la omisión de instrucciones y la falta de atención, presente en el 48% y el 25% de las fallas respectivamente; la Ergonómica-Cognitiva (relacionada con el "saber" y el "poder") referida a la falta de competencias técnicas y la opacidad y condiciones de sobrecarga del sistema que impide la aplicación de las competencias del personal, presente en el 41% de las fallas. Finalmente está la categoría Organizacional-Laboral, que incorpora al diseño organizacional como inductor de variabilidad en el desempeño laboral, lo cual se traduce en fallas por ausencia de procedimientos de trabajo, presente en el 30% de los eventos, las condiciones ergonómicas no adecuadas, presente en el 28% de las fallas, y la supervisión deficiente, presente en el 22%. La clasificación de las causas raíz se presenta a continuación en la Tabla 2.

Este agrupamiento evidencia que el error activo cometido por la persona, disparado por una desconexión con la realidad del puesto de trabajo por bajos niveles de motivación (actitud) y falta de formación (aptitud), no es contenido por las barreras organizacionales que la empresa debe proveer en términos de procedimientos de ejecución documentados, dotación de equipos y materiales adecuados para la ejecución de las actividades, supervisión efectiva, por lo que la acción humana incorrecta pasa las ventanas de contención organizacional generando una falla con consecuencias significativas que pueden afectar la producción, la calidad, los costos, la seguridad de personas, instalaciones, comunidades y medio ambiente.

**Tabla 2.** Clasificación de las causas raíz.

| | Tipo de causa raíz | | Causa raíz | % de fallas en las que se encuentra presente | Nivel de Impacto |
|---|---|---|---|---|---|
| 1 | Conductual | Actitud | Personal no sigue las instrucciones o no cumple los procedimientos | 48% | |
| 2 | Conductual | Aptitud | Personal no tiene las competencias requeridas para ejecutar las actividades | 41% | A |
| 3 | Organizacional | Documentación de procesos | Ausencia de procedimientos y estándares de trabajo documentados | 30% | |
| 4 | Organizacional | Ergonomía | Condiciones ergonómicas no adecuadas para ejecutar las actividades | 28% | |
| 5 | Conductual | Actitud | Falta de atención en el personal que ejecuta la actividad | 25% | |
| 6 | Organizacional | Supervisión | Deficiencias en la supervisión del personal ejecutor | 22% | M |
| 7 | Organizacional | Recursos | Herramientas, instrumentos y equipos inadecuados o no disponibles | 19% | |
| 8 | Organizacional | Comunicación | Líneas de autoridad y comunicación poco claras | 10% | |
| 9 | Externo | Social | Interrupcion de actividades por conflictos en la zona (externos) | 5% | |
| 10 | Organizacional | Recursos | Personal insuficiente para los requerimientos de la actividad | 4% | B |
| 11 | Externo | Medio Ambiente | Interrupción de la operación por condiciones ambientales | 4% | |
| 12 | Externo | Materiales | Material defectuoso | 2% | |

## 5 Conclusiones

La investigación permite concluir que la vulnerabilidad que presentan las personas que laboran en los procesos críticos de la minería aurífera no es un fenómeno estocástico, sino una propiedad emergente de un diseño sociotécnico precario sumergido en un entorno hostil. En este contexto el error humano puede definirse como una acción que afecta el desempeño de los procesos críticos de las empresas de minería aurífera, y a su vez como una respuesta adaptativa fallida ante la variabilidad de un sistema minero impredecible, donde la acción u omisión del individuo es inducida por factores como la degradación del control cognitivo por problemas de motivación y atención (actitudinal), por un vacío del conocimiento del personal debido a una falta de capacitación para desarrollar los esquemas mentales que le permitan interpretar correctamente señales críticas y tomar decisiones acertadas (aptitudinal), y por un entorno laboral con fallas latentes que no ofrece guías de acción claras ni condiciones ergonómicas adecuadas (organizacional).

El error humano representa un drenaje patrimonial crítico, con pérdidas directas de USD 488.130 anuales en procesos críticos y un déficit productivo de 45,6 Kg de metal al año. Esta "entropía organizacional" consume los recursos que deberían invertirse en la propia mitigación del error, creando un bucle de retroalimentación negativa.

La gestión de la confiabilidad en este sector debe enfocarse en la creación de sistemas resilientes que reconozcan los límites neurocognitivos del ser humano y mitiguen las fallas latentes del entorno organizacional. La seguridad y la productividad no son variables contrapuestas, sino el resultado emergente de un sistema sociotécnico en equilibr

**Referencias**


Alles, M. (2016). *Diccionario de Competencias. La Trilogía Tomo I*. Buenos Aires: Granica S.A.

Andrade, M., Chong, M., Cobo, E. (2021). Importancia de la motivación en los entornos laborales de las empresas. *Revista Tecnológica, Ciencias y Educación Edwards Deming*, 5(2), 101-115.

Acquah, A., Kwabena, T., Naa, E., Otoo, B. (2021). Literature review on theories of motivation. *International Journal of Economic and Business Review*, 9(5), 25-29.

API Publication 770 (2001). *A Manager's Guide to Reducing Human Errors Improving Human Performance in the Process Industries*. USA: American Petroleum Institute.

Boyatzis, R. (2008). Competencies in the 21st century. *Journal of Management Development*, 27(1), 5–12.

Bubb, H. (2005). Human reliability: A key to improved quality in manufacturing. *Human Factors and Ergonomics in Manufacturing & Service Industries*, 15(4), 353-368.

Cañas, J. (2011). *Ergonomía cognitiva*. Bogotá: Editorial Médica Panamericana.

Dekker, S. (2014). *The field guide to understanding 'human error'*. (3.ª ed.). USA: Routledge.

Díaz, A., Benítez, R., Del Castillo, A., Cabrera, J., Villar, L., Rodríguez, A. (2021). Formulación de un nuevo concepto de confiabilidad operacional. Ingeniare Revista Chilena de Ingeniería, 29(1).

Dolan, S., Valle, R., Jackson, S., Schuler, R. (2007). *La gestión de los recursos humanos: Preparando profesionales para el siglo XXI* (3.ª ed.). México: McGraw-Hill Interamericana.

Gehring, W., Liu, Y., Orr, J., Carp, J. (2012). *The error-related negativity*. En S. J. Luck y E. S. Kappenman (Eds.), *The Oxford handbook of event-related potential components* (pp. 231–292). USA: Oxford University Press.

González E., Cardona, M., Hernández, C. (2019). Condiciones de seguridad y salud en el trabajo, una revisión teórica desde la minería colombiana. *Revista Venezolana de Gerencia* (RVG), 24(87), 884-900.

Hollnagel, E. (2021). *Synesis: The unification of productivity, quality, safety, and reliability*. USA: Routledge Taylor and Francis Group.

Inzlicht, M. Schmeichel, B. (2012). What is ego depletion? Toward a mechanistic revision of the self-control resource model. *Perspectives on Psychological Science*, 7(5), 450–463.

Kandel, E., Koester, J., Mack, S., Siegelbaum, S. (2021). *Principles of neural science* (6th ed.). USA: McGraw-Hill Education.

Kandel, E., Schwartz, J., Jessell, T. (1999). *Neurociencia y Conducta*. Barcelona: Pearson Prentice Hall.

Labrador, R., Fernández, L., Chacón, C., Nava, M., (2012). Confiabilidad humana en los procesos productivos - Un enfoque integrado. http://r2menlinea.com/w3/PT/PT007_Confiabilidad_Humana_Un_Enfoque_Integrado

Lacabana, M. (2012). Impactos socioambientales de la minería del oro en Venezuela. De la apertura económica en los noventa a la renacionalización actual. *Theomai*, 25, 148-156.

Lazzati, S. (2012). *El cambio del comportamiento en el trabajo*. Buenos Aires: Granica

Le Boterf, G. (2001). *Ingeniería de las competencias*. Bercelona: Gestión 2000.

Leveson, N. (2020). *Engineering a safer world: Systems thinking applied to safety*. USA: The MIT Press.

National Aeronautics and Space Administration. (2023). NASA System Safety Handbook (NASA/SP-2023-1010). https://www.nasa.gov/wp-content/uploads/2023/12/20231212-nasa-sp-2023-1010-system-safety-handbook.pdf

Occupational injuries statistics from ILOSTAT. International Labour Organization. https://ilostat.ilo.org/topics/occupational-injuries/

Parra, C., Crespo, A., González-Prida, V., Tino, G. Parra, J., Viveros, P., Rodríguez, F. (2021). Metodología básica de análisis de riesgo para evaluar la criticidad de activos industriales ligeros. *Industria Química*, (94), 64-70.

Raisg y SOS Orinoco. (2023). Venezuela ha perdido más de un millón de hectáreas de bosques y sabanas en solo dos décadas. https://www.raisg.org/es/radar/venezuela-ha-perdido-mas-de-un-millon-de-hectareas-de-bosques-y-sabanas-en-solo-dos-decadas-informe/

Salomón, L., Ortiz, A., Cordero, V. (2018). Productividad del proceso minero, más allá de la producción. *Universidad, Ciencia y Tecnología*, 22(89), 04-16.

Smallwood, J., Schooler, J. (2015). The science of mind wandering: Empirically navigating the stream of consciousness. *Annual Review of Psychology*, 66, 487–518

Tobón, S. (2013). *Formación integral y competencias: Pensamiento complejo, currículo, didáctica y evaluación* (4.ª ed.). Bogotá: Ecoe Ediciones.

Woods, D., Hollnagel, E. (2017). *Resilience Engineering: Concepts and Precepts*. USA: CRC Press.

Zarei, E., Khan, F., Abbassi, R. (2021). Importance of human reliability in process operation: a critical analysis. *Reliability Engineering & System Safety*, 211(1), Julio 2021.

***Recibido:*** *3 de marzo de 2026*

***Aceptado:*** *5 de junio de 2026*

***Varela, Andrónico:*** *MSc Ingeniería Industrial, Esp. Gcia. de Producción, Ingeniero Mecánico, Docente Pregrado y Postgrado, Vicepresidente de Grupo Empresarial con operaciones en Agroindustria, Minería, Petroleo y Servicios: avarel* ***https://orcid.org/ 0000-0001-8823-7739***

***Labrador, Rafael****: MSc, PhD Neurociencias, Médico Cirujano, Docente de Pregrado y Postgrado, Asesor Mayor en Confiabilidad Humana y Neuroeducación, Terapista Cognitivo Conductual. Correo electrónico: rafael.labrador1@gmail.com* ***https://orcid.org/ 0000-0002-4148-1774***

*Artículo de Investigación. Revista Ciencia e Ingeniería. Vol. 47, No. 3 pp. 283-292, agosto-noviembre, 2026.*
*ISSN 1316-7081. ISSN Elect. 2244-8780 Universidad de los Andes (ULA)*

# Activated carbons derived from abundant biomass sources for reversible methane ($CH_4$) adsorption

# Carbones activados derivados de fuentes de biomasa abundantes para la adsorción reversible de metano ($CH_4$).

**Pérez, Patricia[1]*; Prado, Jonas[2]; Vizcaya, Marietta[1]; Rondón, Jairo[3]; Rodríguez, Pedro[2]; Lugo, Claudio[2]**

[1]Laboratorio de Polímeros, Departamento de Química, Facultad de Ciencias, Universidad de Los Andes, Mérida, Venezuela.
[2]Laboratorio de Cinética y Catálisis, Departamento de Química, Facultad de Ciencias, Universidad de Los Andes, Mérida, Venezuela.
[3]Biomedical & Chemical Engineering Departments, Universidad Politécnica de Puerto Rico, San Juan, PR 00918 USA.

*perezdpatricia@gmail.com

**Abstract**

*Carbonaceous materials were synthesized from sugarcane bagasse (BAz), coconut shells (CC), and peach kernels (SD) through carbonization followed by nitric acid activation. The materials were characterized by FTIR, XRD, and SEM analyses. FTIR results revealed functional groups typical of activated carbons, while XRD patterns showed partially amorphous graphitic structures with nanometric domains (<100 nm). SEM micrographs evidenced heterogeneous surfaces with cracks and openings, mainly in the carbons derived from BAz and SD. Finally, methane ($CH_4$) adsorption was evaluated, showing higher performance for activated carbons compared to non-activated carbons at 40 and 60 °C. The activated carbon obtained from sugarcane bagasse (CAs/BAz) exhibited the highest $CH_4$ adsorption, reaching 60.31 % at 60 °C.*

***Keywords:*** *Activated carbons, greenhouse gases, methane, adsorbent.*

**Resumen**

*Se sintetizaron materiales carbonáceos a partir de bagazo de caña de azúcar (BAz), cáscaras de coco (CC) y semillas de durazno (SD) mediante carbonización y activación con ácido nítrico. Los materiales fueron caracterizados por FTIR, DRX y MEB. Los resultados FTIR mostraron grupos funcionales típicos de carbones activados, mientras que los patrones DRX evidenciaron estructuras grafíticas parcialmente amorfas con dominios nanométricos (<100 nm). Las micrografías MEB revelaron superficies heterogéneas con grietas y aperturas, principalmente en los carbones derivados de BAz y SD. Finalmente, se evaluó la adsorción de metano ($CH_4$), observándose un mayor desempeño para los carbones activados respecto a los no activados a 40 y 60 °C. El carbón activado obtenido a partir de bagazo de caña de azúcar (CAs/BAz) presentó la mayor adsorción de $CH_4$, alcanzando 60,31 % a 60 °C.*

***Palabras clave****: Carbones activados, gases de invernadero, metano, adsorbente.*

## 1 Introduction

Livestock production and agricultural activities have contributed significantly to the increase in anthropogenic greenhouse gas emissions, such as methane, carbon dioxide, and nitrous oxide, into the atmosphere. The increase in the concentration of these gases has contributed to global surface warming and to the deterioration of the ozone layer in the stratosphere. Among these gases, $CO_2$ is considered the most abundant and the main contributor to global warming.

Although the major natural and anthropogenic sources of methane worldwide (millions of tons/year) remain lower than those of $CO_2$, methane emissions have been increasing at a considerable rate. Furthermore, methane exhibits an environmental impact approximately 21 to 30 times greater than that of $CO_2$, suggesting that, over time, methane could become the predominant greenhouse gas (Carmona et al., 2005).

In this context, transportation systems operating through incomplete fuel combustion (automobiles, trucks, and motorcycles) generate waste products that are released into the environment, not only in large quantities but also with pollutants that increase the emission of gases and solid particles with severe environmental impact. Activated carbons (ACs) possess high chemical affinity, elevated porosity and surface area, and exceptional adsorption capacity. In addition, they allow adsorbate recovery and regeneration of the activated carbon used as an adsorbent material for different types of gases, thereby contributing to the reduction of environmental pollutants (Johnson et al.,

1995). Interest in these carbonaceous materials is associated with several important properties, including: (1) thermal stability, (2) resistance to acid attack, (3) predominantly hydrophobic character, (4) relatively low cost, and (5) porous structure. Consequently, in recent years, there has been a substantial increase in studies related to their synthesis and potential applications in gas adsorption and separation, as well as in industrial processes in general (Lozano, 2001).

Considering the above, the aim of this research is to synthesize activated carbons from abundant biomass sources such as sugarcane bagasse, peach kernels, and coconut shells, and to characterize them by Fourier Transform Infrared Spectroscopy (FTIR), X-ray Diffraction (XRD), and Scanning Electron Microscopy (SEM). Subsequently, their gas adsorption capacity, particularly for methane ($CH_4$), will be evaluated using gas chromatography, contributing to studies focused on reducing greenhouse gas emissions and, consequently, improving current climate conditions.

## 2 Experimental Procedure

### 2.1 Synthesis of Activated Carbons

Activated carbons (ACs) were synthesized from: (1) sugarcane bagasse, (2) peach kernels, and (3) coconut shells, using the modified impregnation method described by Kim and Ahn (2010) and later investigated at the Kinetics and Catalysis Laboratory of the Universidad de Los Andes by Marín† (Marín, 2015) and Prado (Prado, 2018). The synthesis procedure consisted of two main stages: the preparation of carbonaceous materials and the subsequent activation of the carbons.

#### *2.1.1 Preparation of Carbonaceous Materials*

The raw materials were treated through a carbonization process, including sugarcane bagasse (Blanco et al., 1999), peach kernels, and coconut shells (Kim and Ahn, 2010).

##### *2.1.1.1 Carbons Derived from Sugarcane Bagasse*

Sugarcane bagasse samples were washed with distilled water to remove impurities. The samples were air-dried and subsequently placed in a muffle furnace at 600 °C using a heating rate of 5 °C $min^{-1}$ for 1 hour. The resulting solid material was sieved until a particle size less than or equal to 80 mesh (250 µm) was obtained.

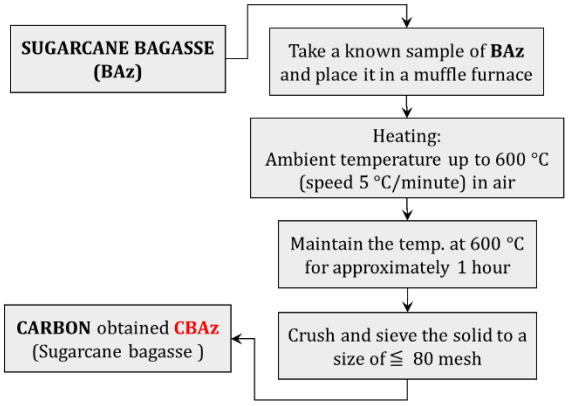


**Fig. 1.** Schematic representation of the preparation of carbon (CBAz) derived from sugarcane bagasse.

The carbonization process was carried out in a muffle furnace, which allowed strict control of the temperature ramp and residence time. The dried samples were heated from room temperature to 700 °C at a heating rate of 5 °C $min^{-1}$ under an air atmosphere and maintained at this temperature for approximately 1 hour. The resulting solid was crushed, ground, and sieved until a particle size less than or equal to 80 mesh (250 µm) was obtained (Blanco et al., 1999). The schematic procedure for obtaining carbon from sugarcane bagasse is shown in Figure 1.

##### *2.1.1.2 Carbons Derived from Peach Kernels*

The collected peach kernel samples were washed with distilled water to remove residual pulp. Subsequently, the samples were placed in a drying oven at 100 °C for 5 hours. The peach kernels were then dried at 200 °C for 12 hours prior to the subsequent thermal treatment.

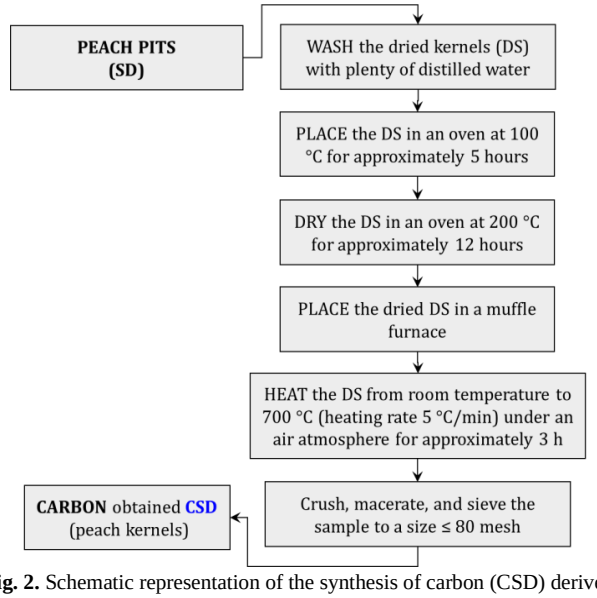


**Fig. 2.** Schematic representation of the synthesis of carbon (CSD) derived from peach kernels.

The carbonization process was carried out in a muffle furnace. The dried samples (~6.0 ± 0.1 kg) were heated from room temperature to 700 °C at a heating rate of 5 °C $min^{-1}$ under an air atmosphere and maintained at 700 °C for approximately 3 hours. The resulting solid was crushed, ground, and sieved until a particle size less than or equal to 80 mesh (250 µm) was obtained (Kim and Ahn, 2010). The schematic procedure for obtaining carbon from peach kernels is shown in Figure 2.

*2.1.1.3 Carbons Derived from Coconut Shells*

The coconut shell samples were sanded, washed, and boiled in distilled water at approximately 100 °C for 5 hours to remove residual organic matter. Subsequently, the cleaned shells were dried in an oven at 200 °C for 12 hours prior to thermal treatment.

The carbonization process of the cleaned and dried coconut shells was carried out in a muffle furnace. The samples were heated from room temperature to 700 °C at a heating rate of 5 °C $min^{-1}$ under an air atmosphere and maintained at 700 °C for approximately 3 hours. The resulting material was crushed, ground, and sieved to obtain a particle size close to 80 mesh (Kim and Ahn, 2010). The schematic procedure for obtaining carbon from coconut shells is shown in Figure 3.

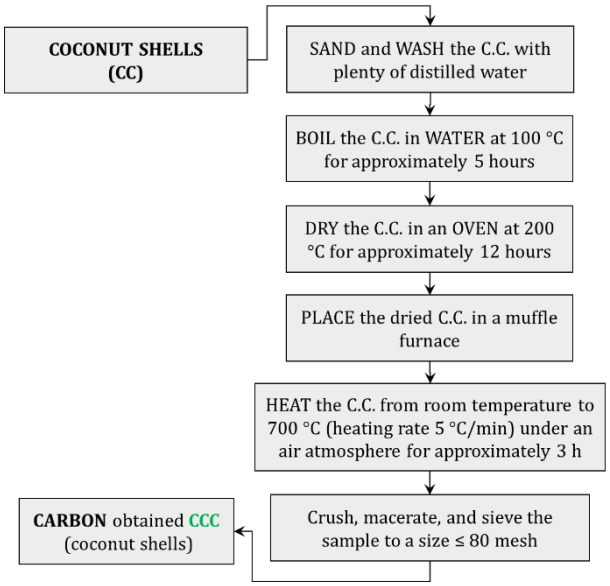


**Fig. 3.** Schematic representation of the synthesis of carbon (CCC) derived from coconut shells.

*2.1.2 Carbon Activation*

The chemical activation of the prepared carbons, obtained from sugarcane bagasse (CBAz), peach kernels (CSD), and coconut shells (CCC), was carried out in a reflux system using concentrated nitric acid ($HNO_3$, Merck). The first step of the activation process consisted of adding approximately 400 mL of nitric acid into a three-neck glass flask, followed by the slow addition of four (4.0) g of carbon material.

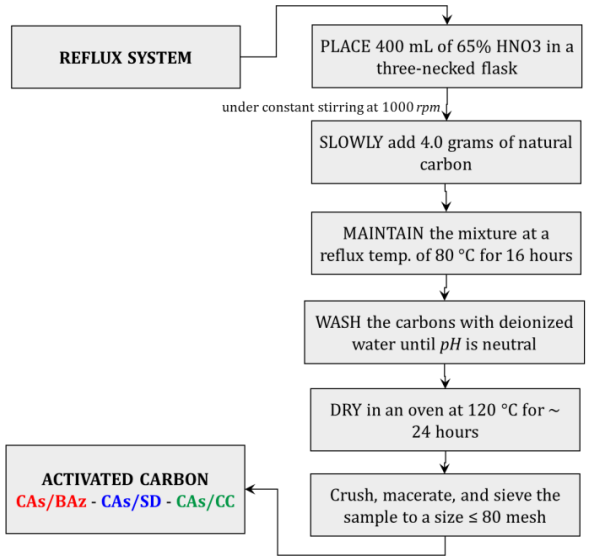


**Fig. 4.** Schematic representation of the activation process of the synthesized carbons (Cas/Baz, Cas/SD, and Cas/CC).

The entire process was carried out under constant stirring (~1000 rpm). Subsequently, the mixture was maintained under reflux conditions at a constant temperature of approximately 75 °C for 16 hours. After chemical activation, the resulting activated carbons were washed with abundant deionized water until neutral *pH* was reached. Finally, the activated carbons (Cas/Baz, Cas/SD, and Cas/CC) were dried in an oven at 120 °C for 24 hours (Kim and Ahn, 2010). The schematic representation of this procedure is shown in Figure 4.

## 2.2 Synthesized Materials

The activated carbons (Acs) obtained from different natural sources (Cas/Baz, Cas/SD, and Cas/CC) through carbonization followed by acid impregnation are presented in Table 1.

**Table 1.** Activated carbons obtained by carbonization/acid impregnation from different raw materials (Baz, SD, and CC).

| Material | Method | Code |
|---|---|---|
| Carbon (Baz) | C/Ac. Imp. | CBAz |
| Carbon (SD) | C/Ac. Imp. | CSD |
| Carbon (CC) | C/Ac. Imp. | CCC |
| Activated carbon (Baz) | C/Ac. Imp. | Cas/Baz |
| Activated carbon (SD) | C/Ac. Imp. | Cas/SD |
| Activated carbon (CC) | C/Ac. Imp. | Cas/CC |

*Baz = Sugarcane bagasse; CC = Coconut shells*
*SD = Peach kernels; C/Ac. Imp. = Carbonization / acid impregnation*

### 2.3 Characterization

The prepared carbonaceous materials were characterized by Fourier Transform Infrared Spectroscopy (FTIR) using a PerkinElmer Frontier infrared spectrophotometer located at the Kinetics and Catalysis Laboratory, Faculty of Sciences, Universidad de Los Andes (ULA). Powder X-ray Diffraction (XRD) analyses were performed using an automated Phillips PW 1050/25 diffractometer with Cu Kα radiation (λ = 1.5416 Å) at the Crystallography Laboratory, Faculty of Sciences, ULA. Scanning Electron Microscopy (SEM) analyses were carried out using a HITACHI S-2500 scanning electron microscope (1992 model) at the Electron Microscopy Center of the Universidad de Los Andes. All analyses were performed on both activated and non-activated samples.

## 3. Results and Discussion

### 3.1 Fourier Transform Infrared Spectroscopy (FTIR)

The infrared spectra of the synthesized carbons are shown in Figure 5. The FTIR band assignments for the non-activated carbons (CBAz, CSD, and CCC) are presented in Table 2.

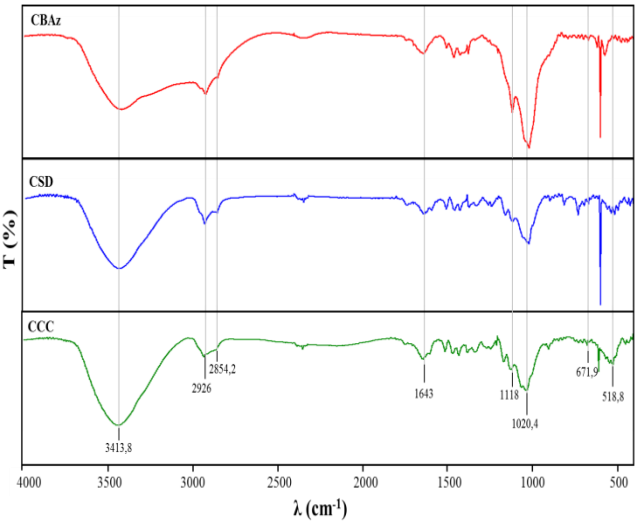


**Fig. 5.** FTIR spectra of non-activated carbons (CBAz, CSD, and CCC) obtained from Baz, SD, and CC.

**Table 2.** FTIR bands of non-activated carbons (CBAz, CSD, and CCC) obtained from Baz, SD, and CC.

| ν (ref.) $cm^{-1}$ | ν ($cm^{-1}$) | Bond | Assignment |
|---|---|---|---|
| 3400 | 3413.8 | O–H | Symmetric and asymmetric stretching vibrations of the O–H group |
| 2950–2845 | 2926–2854.2 | C–H | Symmetric and asymmetric vibrations of aliphatic C–H bonds (-$CH_2$ -$CH_3$) |
| 1650–1600 | 1643 | C=C | Stretching vibrations of the C=C bond (aromatic compounds) |
| 1440–880 | 1118–1020.4 | C–H | In-plane bending vibrations of the C–H bond |
| 650 | ~671.9 | H–C=C | Out-of-plane bending vibrations of aromatic compounds |
| 455 | ~518.8 | H–C=C | Out-of-plane bending vibrations of aromatic compounds |

**Table 3.** FTIR bands of activated carbons (Cas/Baz, Cas/SD, and Cas/CC) obtained from CBAz, CSD, and CCC.

| N (ref.) $cm^{-1}$ | ν ($cm^{-1}$) | Bond | Assignment |
|---|---|---|---|
| 3400 | 3403.6 | O–H | Symmetric and asymmetric stretching vibrations of the O–H group |
| 2950–2845 | 2928–2854.9 | C–H | Symmetric and asymmetric vibrations of aliphatic C–H bonds (-$CH_2$ -$CH_3$) |
| 1765–1645 | ~1720 | C=O | Stretching vibrations of the C=O bond (ketones, aldehydes, lactones, or carboxylic groups) |
| 1650–1600 | 1603 | C=C | Stretching vibrations of the C=C bond (aromatic compounds) |
| 1260 | 1202.9 | C–O | Stretching vibrations of the C–O bond (esters and/or phenols) |
| 1180 | 1191.8 | C–O | Stretching vibrations of the C–O bond (carboxylic acids) |
| 790 | 791.5 | C–H | Out-of-plane bending vibrations of the C–H bond |
| 650 | 726.7 | C–H | In-plane bending vibrations of the carbon–hydrogen (C–H) bond |
| 455 | 518.8–466 | H–C=C | Out-of-plane bending vibrations of aromatic compounds |

The broad band observed near 3400 $cm^{-1}$ is attributed to stretching vibrations associated with hydroxyl groups ($OH^-$), indicating the presence of moisture in the synthesized samples (non-activated carbons) (Primera et al., 2011). The peaks between 2926 and 2854.2 $cm^{-1}$ correspond to the symmetric and asymmetric vibrations of aliphatic C–H bonds (–$CH_2$ and –$CH_3$) (Rosquete, n.d.). The band at 1643 $cm^{-1}$ is associated with stretching vibrations of the C=C bond,

characteristic of aromatic compounds (Primera et al., 2011). The absorption peaks between 1118 and 1020.4 $cm^{-1}$ are attributed to in-plane bending vibrations of the carbon–hydrogen (C–H) bond (Primera et al., 2011). Around 671.9 $cm^{-1}$ and 518.8 $cm^{-1}$ (slightly shifted), characteristic signals corresponding to out-of-plane bending vibrations of aromatic compounds are observed (Yin et al., 2009).

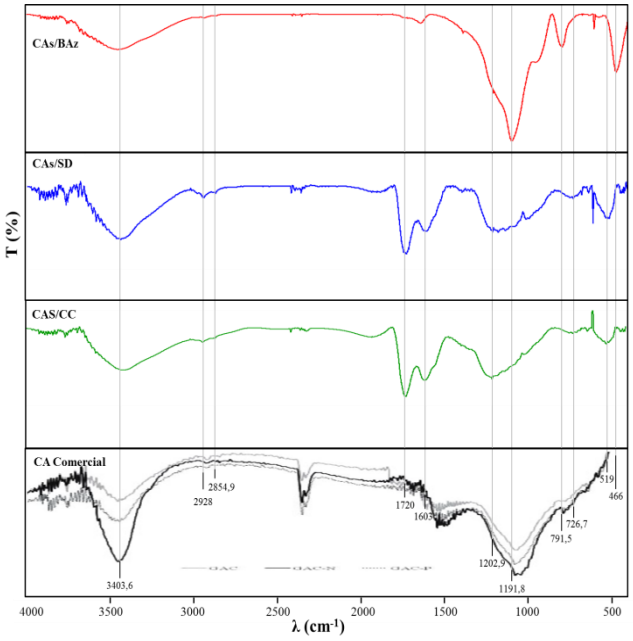


**Fig. 6.** FTIR spectra of activated carbons (Cas/Baz, Cas/SD, and Cas/CC) obtained from CBAz, CSD, and CCC.

The FTIR spectra of the activated carbons (Cas/Baz, Cas/SD, and Cas/CC) are presented in Figure 6 and Table 3. The broad band at approximately 3403.6 $cm^{-1}$ corresponds to stretching vibrations of hydroxyl groups ($OH^-$), indicating the presence of moisture in the samples (Primera et al., 2011). The small bands between 2928 and 2854.9$cm^{-1}$ are attributed to the symmetric and asymmetric vibrations of aliphatic C–H bonds (–$CH_2$ and –$CH_3$) (Rosquete, n.d.). The signal observed near 1720 $cm^{-1}$ is associated with stretching vibrations of the C=O bond originating from ketones, aldehydes, lactones, or carboxylic groups (Rosquete, n.d.). The band located at 1603 $cm^{-1}$ corresponds to stretching vibrations of the C=C bond, characteristic of aromatic compounds (Primera et al., 2011). The medium-intensity peak at 1202.9 $cm^{-1}$ and the high-intensity peak at 1191.8 $cm^{-1}$ correspond to stretching vibrations of the C–O bond in esters and/or phenols and carboxylic acids, respectively (Primera et al., 2011).

The bands observed near 791.5 $cm^{-1}$ and 726.7 $cm^{-1}$ correspond to in-plane bending vibrations of carbon–hydrogen bonds (Rosquete, n.d.). The signals at lower wavelengths, below 550 $cm^{-1}$, are attributed to out-of-plane bending vibrations of aromatic compounds (Yin et al., 2009).

### 3.2 X-ray Diffraction (XRD)

Figure 7 shows the diffraction patterns of the non-activated carbons (CBAz, CSD, and CCC) and activated carbons (Cas/Baz, Cas/SD, and Cas/CC). The identification of the phase(s) present in the synthesized carbons was performed using: (1) the X'Pert HighScore Plus 2.1 software with the PDF2-2004 database from the ICDD, which identified the presence of a hexagonal graphitic carbon-type phase (space group: P63mc), corresponding to card 00-002-0456 (Harcourt et al., 1942); and (2) comparison with articles published in recognized scientific journals (Yin et al., 2009).

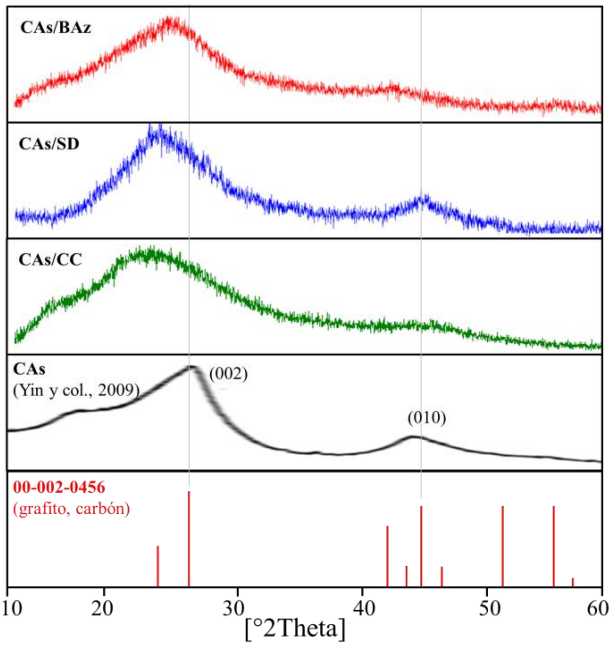


**Fig. 7.** XRD patterns of non-activated carbons (CBAz, CSD, and CCC) and activated carbons (Cas/Baz, Cas/SD, and Cas/CC). Activated carbon at 800 °C (Yin et al., 2009). Reference card: 00-002-0456 (Graphite).

These results indicate that the diffraction peaks obtained correspond to the (002), (010), and (111) planes, respectively. The peak associated with the (002) plane can be related to stacked-layer structures with aromatic characteristics, whereas the peaks corresponding to the (010) and (111) planes are associated with non-planar aromatic structures present in lower proportions (Yin et al., 2009).

The most intense peak observed near 25° is attributed to the formation of graphitic plates, generating a carbon–pore structure that provides experimental evidence for the presence of carbon–pore surfaces. This behavior was also reported by Rampe et al. (2011), who concluded that increasing the calcination temperature leads to a reduction in the interlayer spacing and an increase in both the crystalline diameter and the average height between the aromatic layers of the synthesized carbons. As a result, the amorphous carbon structure progressively transforms into a semicrystalline

structure with improved layer arrangement and a more stable equilibrium in the position of carbon atoms.

3.4 Scanning Electron Microscopy (SEM)

The SEM micrographs of the nitric acid-activated carbons obtained from sugarcane bagasse, peach kernels, and coconut shells are shown in Figure 8.

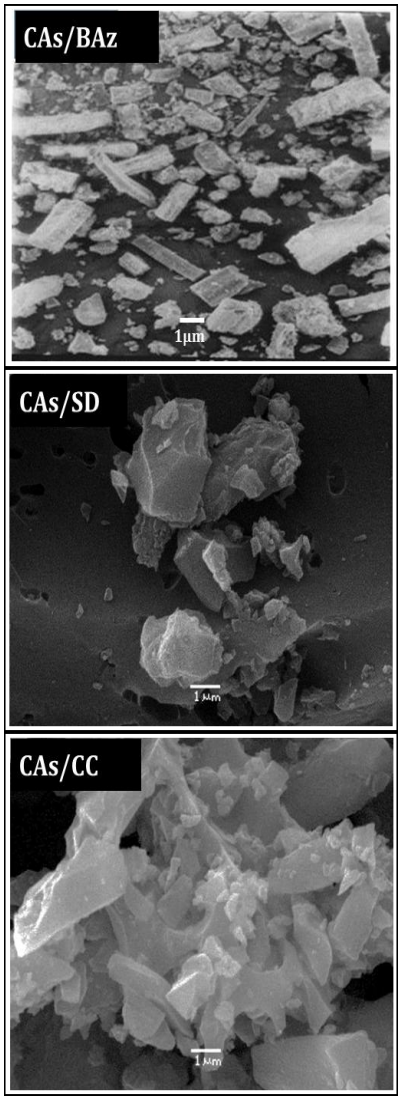


**Fig. 8.** Scanning Electron Microscopy (SEM) micrographs of the synthesized activated carbons: CAs/CC (coconut), CAs/SD (peach kernel), and CAs/BAz (sugarcane bagasse).

The carbons exhibited particles with sizes ranging from 1 to 10 µm, presenting highly heterogeneous morphologies. In some cases, sharp edges and generally smooth surfaces were observed, together with the presence of significant cracks and openings that influence the total surface area of the material.

CAs/CC (coconut-derived carbon) showed irregular particles with sharp edges and a highly irregular surface. However, a considerable number of dispersed particles were observed on its surface, suggesting a high specific surface area. In the case of the activated carbon CAs/SD (peach kernel-derived carbon), sharp edges and an amorphous surface were also observed, together with a significant number of cracks and openings in its morphology. The SEM micrographs of the activated carbon CAs/BAz (sugarcane bagasse-derived carbon) revealed particles of variable size with porous structure and amorphous morphology, exhibiting sharp edges and generally smooth surfaces.

Overall, the carbons obtained from coconut shells presented fewer surface irregularities compared to those derived from peach kernels and sugarcane bagasse. Nevertheless, it can be concluded that the carbonaceous adsorbents were synthesized under optimal conditions (Primera et al., 2011).

### 3.5 Methane ($CH_4$) Adsorption Test

#### *3.5.1 Instrumental Response (Gas Chromatography)*

A Hewlett-Packard gas chromatograph (HP 6890 Plus, GC System series) equipped with a thermal conductivity detector (TCD) was used for the adsorption tests. The response factor of the thermal conductivity detector was calculated using nitrogen as the carrier gas at a flow rate of 30 mL $min^{-1}$.

#### *3.5.2 Pretreatment*

Approximately 200 mg of non-activated carbons (CBAz, CSD, and CCC) and activated carbons (CAs/BAz, CAs/SD, and CAs/CC) were placed inside a U-shaped stainless-steel reactor. The solid pretreatment was carried out by flowing approximately 30 mL $min^{-1}$ of nitrogen gas through the reactor while heating from room temperature to 120 °C, where the samples were maintained for 90 minutes.

#### *3.5.3 Calibration (Gas Chromatography)*

The optimization of the adsorption test conditions was achieved by calibrating parameters such as adsorbent mass, hydrocarbon flow rate, temperature range, and space velocity. The optimal conditions for studying methane adsorption on activated carbons are presented in Table 4.

**Table 4.** Experimental conditions for CG analyses.

| Parameter | Value |
|---|---|
| Total flow rate (mL $min^{-1}$) | ~30 |
| Temperature range (°C) | 40–60 |
| Activated carbon mass (mg) | ≥ 30 |
| Space velocity range $\times 10^{-3}$ (mL $g^{-1}$ $h^{-1}$) | 120–240 |

### *3.5.4 System Conditions for Adsorption*

After completion of the pretreatment of the carbonaceous materials, approximately 103 mL $min^{-1}$ of a $CH_4/N_2$ gas mixture (3/100) was passed through the reactor according to the gas under study. The adsorbent (ACs) was subjected to a temperature ramp from room temperature to the adsorption temperatures of 40 and 60 °C, where it remained for approximately 100 minutes. The adsorption scheme is shown in Figure 9.

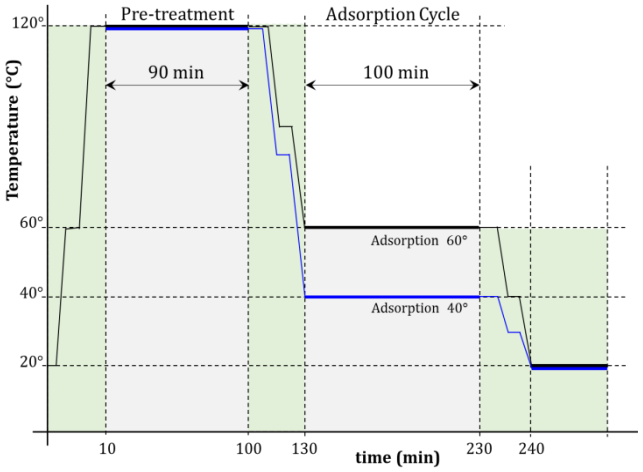


**Fig. 9.** Schematic representation of methane ($CH_4$) adsorption on non-activated carbons (CBAz, CSD, and CCC) and activated carbons (CAs/BAz, CAs/SD, and CAs/CC).

### *3.5.5 Adsorption Test Results*

Figure 10 shows the methane ($CH_4$) adsorption cycle for the prepared solids, including non-activated carbons (CBAz, CSD, and CCC) and nitric acid-activated carbons (CAs/BAz, CAs/SD, and CAs/CC), within a temperature range between 40 and 60 °C. A linear methane behavior (conductimetric response measured by gas chromatography) was observed before passing through the reactor, particularly at times below 25 minutes.

Once the hydrocarbon entered the reactor containing the carbonaceous adsorbent sample, it was observed that the amount of methane adsorbed on the activated carbons increased compared to the non-activated carbons at both adsorption temperatures, 40 and 60 °C. After saturation of the adsorbent (the carbons), the initial methane concentration conditions were recovered. This increase in the adsorption capacity of the activated carbons (CAs/BAz, CAs/SD, and CAs/CC) compared to the non-activated carbons (CBAz, CSD, and CCC) may be attributed to the smaller mesopore size and lower crosslinking height of the polyaromatic molecules that constitute the carbon structure. These characteristics favor the activation process with the mineral acid, producing activated carbons with high porosity (intermediate pores) and elevated micropore volume.

These novel and interesting properties provide the activated carbons with a high adsorption capacity (Martínez et al., 2013). Furthermore, the adsorption capacity of the activated carbons increases due to surface modification, which introduces chemical species that alter the surface acidity, making it more reactive toward hydrocarbon molecules such as methane.

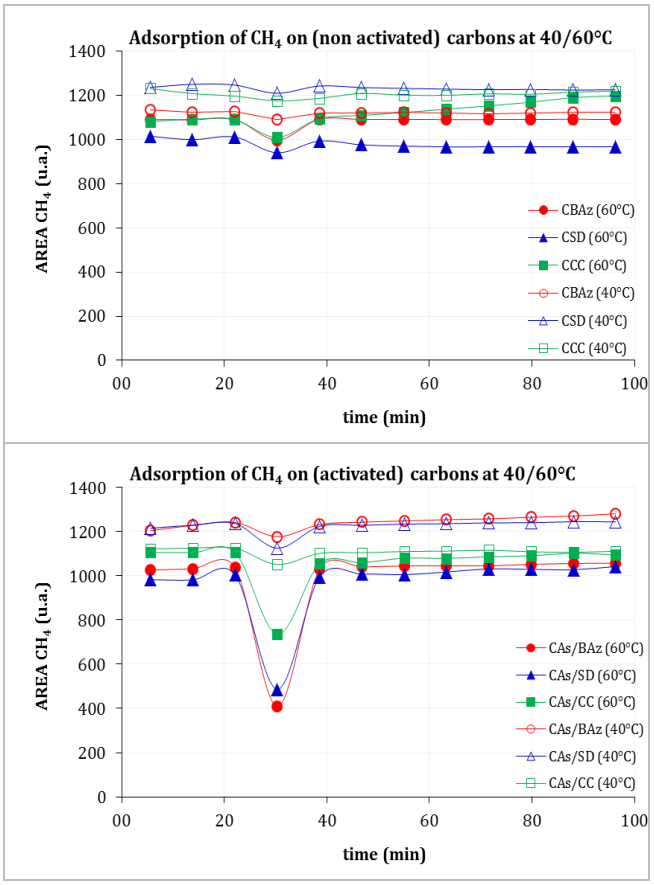


**Fig. 10.** Methane adsorption on non-activated carbons (CBAz, CSD, and CCC) and activated carbons (CAs/BAz, CAs/SD, and CAs/CC) at 40 and 60 °C.

The nonpolar nature of most carbon materials and the forces involved in the different adsorption processes preferentially promote the retention of nonpolar high-molecular-weight molecules (long-chain hydrocarbons, phenols, dyes, among others). In contrast, substances such as $CH_4$, $CO_2$, $H_2$, $N_2$, $O_2$, and even water are not readily adsorbed by carbon at room temperature. This behavior explains the experimental results obtained, where the highest methane adsorption values were observed at 60 °C, ranging from 33.5 to 60.3 % for the activated carbons (ACs), compared to the same solids tested at 40 °C, whose adsorption percentages ranged from 6.42 to 12.06 %, generally below 10.0 % (see Figure 11 and Table 5).

**Table 5**. Percentage methane adsorption data for non-activated carbons (CBAz, CSD, and CCC) and activated carbons (CAs/BAz, CAs/SD, and CAs/CC) at 40 and 60 °C.

| Adsorbent | Time (min) | Methane Area (a.u.) | Adsorption (%) |
|---|---|---|---|
| **60 °C** | | | |
| CAs/BAz | 30.3 | 409 | 60.32 |
| CAs/SD | 30.4 | 487 | 50.79 |
| CAs/CC | 30.4 | 735 | 33.47 |
| CBAz | 30.4 | 998 | 8.50 |
| CSD | 30.2 | 940 | 6.81 |
| CCC | 30.3 | 1010 | 7.16 |
| **40 °C** | | | |
| CAs/BAz | 30.4 | 1177 | 12.06 |
| CAs/SD | 30.4 | 1126 | 8.27 |
| CAs/CC | 30.4 | 1052 | 6.42 |
| CBAz | 30.4 | 1090 | 3.41 |
| CSD | 30.4 | 1210 | 2.78 |
| CCC | 30.3 | 1175 | 3.04 |

Figure 12 presents the methane ($CH_4$) adsorption capacities of the different activated carbons (CAs/BAz, CAs/SD, and CAs/CC) and non-activated carbons (CBAz, CSD, and CCC) at 40 and 60 °C. In all cases, the interaction or adsorption force between methane (adsorbate) and the carbon surface (adsorbent) is weak and mainly governed by Van der Waals interactions, favoring physisorption. Therefore, high energies are not required for hydrocarbon adsorption onto the adsorbent surface (Droguett, 1983).

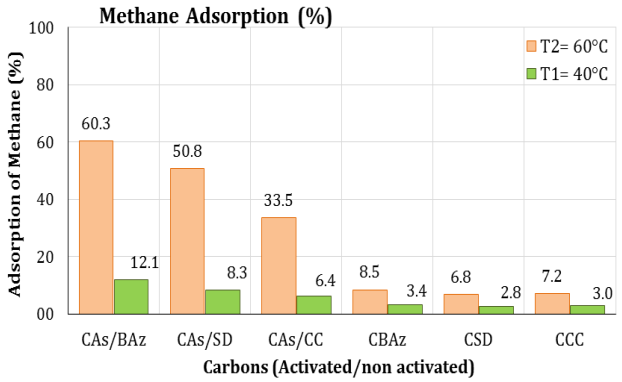


**Fig. 11.** Percentage methane adsorption on non-activated carbons (CBAz, CSD, and CCC) and activated carbons (CAs/BAz, CAs/SD, and CAs/CC) at 40 and 60 °C.

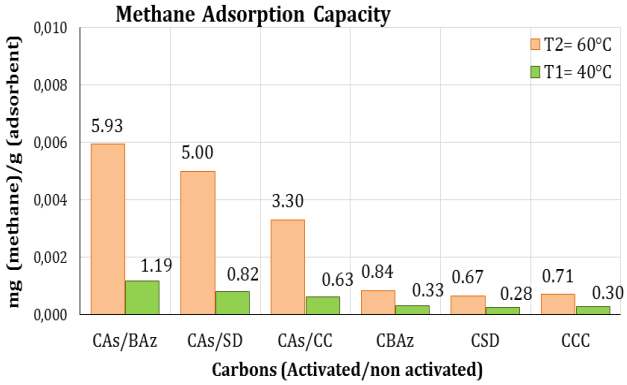


**Fig. 12.** Methane adsorption capacity of non-activated carbons (CBAz, CSD, and CCC) and activated carbons (CAs/BAz, CAs/SD, and CAs/CC) at 40 and 60 °C.

**Table 6.** Methane adsorption capacity data for non-activated carbons (CBAz, CSD, and CCC) and activated carbons (CAs/BAz, CAs/SD, and CAs/CC) at 40 and 60 °C.

| Adsorbent | ppm ($CH_4$) adsorbed | mg ($CH_4$) adsorbed | Adsorption Capacity (mg $g^{-1}$ adsorbent) | Adsorption Capacity (mg $g^{-1}$ adsorbent) |
|---|---|---|---|---|
| **60 °C** | | | | |
| CAs/BAz | 9339.13 | 1.187 | 5.934 | 29.668 |
| CAs/SD | 7867.79 | 1.001 | 4.999 | 24.994 |
| CAs/CC | 5188.40 | 0.659 | 3.296 | 16.482 |
| CBAz | 1316.46 | 0.167 | 0.836 | 4.182 |
| CSD | 1053.13 | 0.134 | 0.669 | 3.346 |
| CCC | 1115.12 | 0.142 | 0.708 | 3.542 |
| **40 °C** | | | | |
| CAs/BAz | 1874.02 | 0.238 | 1.191 | 5.953 |
| CAs/SD | 1285.48 | 0.163 | 0.817 | 4.084 |
| CAs/CC | 991.22 | 0.126 | 0.630 | 3.149 |
| CBAz | 526.58 | 0.067 | 0.335 | 1.673 |
| CSD | 433.66 | 0.055 | 0.276 | 1.378 |
| CCC | 464.63 | 0.059 | 0.295 | 1.476 |

*g (adsorbent) = 200 mg / 1000 mg; initial $CH_4$ mass = 1.968 mg*

The activated carbon obtained from sugarcane bagasse, CAs/BAz, tested at 60 °C (which exhibited the highest percentage adsorption among all synthesized carbons, 60.32 %), showed an adsorption capacity of approximately 1.187 mg of $CH_4$ per 1.968 mg of methane injected into the total 103 mL gas flow circulating through the system (Table 6).

This result indicates that the adsorption capacity of the activated carbon CAs/BAz was 5.934 mg of methane per 200 mg of initial adsorbent, corresponding to approximately 29.67 mg of methane per gram of activated carbon. A good adsorbent should exhibit an adsorption capacity between 1.5 and 20 % of its own mass, which corresponds to approximately 15-200 mg of methane adsorbed per gram of activated carbon (Hanzawa et al., 2002). The adsorption capacities of the remaining adsorbents are presented in Table 6.

## 4 Conclusions

The infrared spectroscopy analyses performed on the carbons before and after activation with $HNO_3$ revealed the presence of functional groups characteristic of carbonaceous materials, as well as nitrate groups that remained in the samples even after washing the carbonized products with deionized water.

The X-ray diffraction analyses exhibited broad diffraction peaks, indicating that the synthesized carbons possess an amorphous structure with nanometric crystalline domains (≦ 100 nm). In addition, a predominant hexagonal graphitic carbon-type phase (space group: P63mc) was identified using the PDF2-2004 ICDD database (card 00-002-0456) and through comparison with previously published scientific studies.

The SEM micrographs provided evidence of the morphology of the synthesized carbons. The particles obtained from coconut shells exhibited smaller particle sizes compared to those derived from sugarcane bagasse and peach kernels. The presence of cracks and openings in the carbon structures facilitates the penetration of gaseous molecules into the adsorbent interior, which may play a fundamental role in methane adsorption processes.

Methane adsorption tests, evaluated by gas chromatography, demonstrated that the $HNO_3$–activated carbons exhibited significantly higher methane adsorption capacities compared to the non-activated carbons, particularly at higher temperatures between 40 and 60 °C. After saturation of the carbon adsorbents, the initial adsorbate concentration was recovered.

Temperature had a significant influence on the adsorption process. At 60 °C, the activated carbons exhibited the highest methane adsorption capacities, with adsorption percentages ranging from 6.8 % to 60.32 %, compared to the same activated carbons tested at 40 °C, where adsorption values ranged from 2.8 % to 12.06 %.

The activated carbon obtained from sugarcane bagasse (CAs/BAz), evaluated at 60 °C, exhibited the highest methane adsorption percentage among all synthesized carbons, with approximately 1.187 mg of $CH_4$ adsorbed per 1.968 mg of methane injected into the 103 mL total gas flow circulating through the system.

The adsorption capacity of the activated carbon CAs/BAz was determined to be 5.934 mg of methane per 200 mg of initial adsorbent, corresponding to approximately 29.67 mg of methane per gram of activated carbon. A suitable adsorbent should exhibit an adsorption capacity between 1.5 and 20 % of its own mass, corresponding to approximately 15–200 mg of methane adsorbed per gram of activated carbon.

## References

Blanco J., Bonelli P., Cerrella E., Cukierman A., (**1999**), *Activación química de bagazo de caña de azúcar para la obtención de carbones activados*. Avances en Energías Renovables y Medio Ambiente (AMERVA), Vol. 3, 1-9.

Carmona J., Bolívar D., Giraldo L., (**1989**), *El gas metano en la producción ganadera y alternativas para medir sus emisiones y aminorar su impacto a nivel ambiental y productivo*. Revista Colombiana de Ciencias Pecuarias, Vol. 18(1), 49-63.

Droguett S.E., (**1983**), *Elementos de Catálisis Heterogénea*, Serie de Química: Monografía, OEA. Programa Regional de Desarrollo Científico y Tecnológico, Número 26 de Serie de química, Universidad de Texas, USA, 43-46.

Hanzawa Y., Miyajima N., Hatori H., Yamada Y., (2002), Pore Structure and Methane Adsorption Properties of Surface Modified Activated Carbon, TANSO, Vol. 203, 123-126.

Harcourt G.A., (**1942**), Tables for the identification of ore minerals by X-ray powder patterns, *The American Mineralogist*, Vol. 27, 63-113.

Johnson K., Johnson D., (**1995**), *Methane emissions from cattle*, Department of Animal Science, Vol. 73(8), 2483-2492.

Kim K-J., Ahn H-G., (**2010**), The adsorption and desorption characteristics of a binary component system of toluene and methylethylketone on activated carbon modified with phosphoric acid, *Carbon*, Vol. 48(8), pp. 2198-2202.

Lozano D., (**2001**), Preparación y caracterización de materiales carbonosos avanzados para la separación de gases y el almacenamiento de gases y energía. [Tesis Doctoral], Departamento de Química Inorgánica, Universidad de Alicante, Alicante-España, 1-460.

Marín-Astorga† K., (**2015**), *Síntesis y caracterización de adsorbentes del tipo carbonáceos para trazas de metano*, [Trabajo Especial de Grado], Laboratorio de Cinética y Catálisis, Departamento de Química, Facultad de Ciencias, Universidad de Los Andes, Mérida-Venezuela, pp. 1-84.

Martínez M., Molina M., Rodríguez F., (**2013**), *Preparación de carbones activados con KOH a partir de residuos de petróleo*. Adsorción de hidrógeno, Departamento de química inorgánica, Universidad de Alicante, España.

Prado J., (**2018**), *Síntesis y caracterización de carbón activado obtenido a partir de residuos lignocelulósicos de la caña de azúcar, cáscara de coco y semillas de durazno y su empleo como adsorbente de $CO_2$, $H_2$ y $CH_4$*, [Trabajo Especial de Grado], Laboratorio de Cinética y Catálisis, Departamento de Química, Facultad de Ciencias, Universidad de Los Andes, Mérida-Venezuela, pp. 1-122.

Primera O., Colpas F., Meza E., Fernández R., (**2011**), Carbones activados a partir de bagazo de caña de azúcar y zuro de maíz para la adsorción de cadmio y plomo. *Revista de la Academia colombiana de ciencias exactas físicas y naturales*, Vol. 35(136), 387-396.

Rampe J., Setiaji B., Trisunaryanti W., Triyono I., (**2011**), Fabrication and Characterization of carbon composite from coconut shell carbon, *Indian Journal Chemistry*, Vol. 11 (2), pp.124-130.

Rosquete C., S/A. Análisis orgánico (tablas). Laboratorio de Productos Naturales, Facultad de Ciencias, Departamento de química, Universidad de los Andes.

Yin Y., Zhang J., Sheng C., (**2009**), Effect of pyrolysis temperature on the char micro-structure and reactivity of NO reduction, *Korean Journal Chemistry Engineering*, Vol. 26(3), pp. 895-901.

***Received:*** *April 22, 2026*

***Accepted:*** *July 7, 2026*

***Pérez Dávila, Patricia:*** *Ph.D. in Drug Chemistry, 2017, Scientific Research Institute, Faculty of Pharmacy and Bioanalysis, Universidad de Los Andes; Professor of Polymer Laboratory at the Faculty of Sciences, ULA. Mérida, Venezuela.*

***https://orcid.org/0000-0003-0591-2351***

***Prado Alvarado, Jonas:*** *Bachelor's Degree in Chemistry, 2018, Chemistry Department (Kinetics and Catalysis Laboratory) at the Faculty of Sciences, Universidad de Los Andes, Mérida. pradojonas991@gmail.com*

***https://orcid.org/0009-0005-5520-2990***

***Vizcaya, Marietta:*** *Ph.D. in Drug Chemistry, 2014, Scientific Research Institute, Faculty of Pharmacy and Bioanalysis, Universidad de Los Andes; Professor of Polymer Laboratory at the Faculty of Sciences, ULA. Mérida, Venezuela. Email: marietta@ula.ve*

***https://orcid.org/ 0000-0002-2064-4175***

***Rondón Contreras, Jairo:*** *Ph.D. in Applied Chemistry, mention Materials Study, 2015, Universidad de Los Andes; Professor of Biomedical & Chemical Engineering Departments, at the Polytechnic University of Puerto Rico, San Juan, PR-USA. Email: jrondon@pupr.edu*

***https://orcid.org/0000-0002-9738-966X***

***Rodríguez Sulbarán, Pedro:*** *Doctor of Science in Chemistry, 2025, Universidad de Concepción, Chile; Ph.D. in Applied Chemistry, mention Materials Studies, 2015, Universidad de Los Andes; Professor of Chemistry Department (Kinetics and Catalysis Laboratory), at the Faculty of Sciences, ULA. Mérida, Venezuela. Correo electrónico: pedrojrs@gmail.com*

***https://orcid.org/0000-0002-1309-8532***

***Lugo González, Claudio Antonio:*** *Ph.D. in Applied Chemistry, mention Materials Studies, 2017, Universidad de Los Andes; MSc. in Applied Chemistry, mention Materials Studies, 2009, Universidad de Los Andes; Professor of Chemistry Department (Kinetics and Catalysis Laboratory), at the Faculty of Sciences, ULA. Mérida, Venezuela. Email: claudiolugo@ula.ve*

***https://orcid.org/0000-0001-8003-0354***

*Artículo de Investigación. Revista Ciencia e Ingeniería. Vol.47, No.3 pp. 293−306, agosto-noviembre, 2026.*
*ISSN 1316-7081. ISSN Elect. 2244-8780 Universidad de los Andes (ULA)*

# Multivariate analysis of köppen-geiger climate similarity and discriminant factors across 70 major cities in Latin America and the Caribbean

# Análisis Multivariante de la similitud climática köppen-geiger y factores discriminantes en 70 metrópolis de Latinoamérica y el Caribe

**González-Calderón, Álvaro[1]*; Pacheco-Angulo, Carlos[1]; Peña-Guillen, Jesús[2]; Bianchi, Guillermo[3]; Yarbuh, Ismael[4]; González, Héctor[5]**

[1] Faculty of Forestry and Environmental Sciences, University of The Andes, Venezuela.
[2] Faculty of Pharmacy and Bioanalysis. Chair of biostatistics, University of The Andes, Venezuela.
[3] Faculty of Science, Chair of biostatistics, University of The Andes, Venezuela.
[4] Faculty of Marine Sciences, Autonomous University of Baja California, Ensenada, Baja California, Mexico.
[5]Faculty of Engineer, University of The Andes, Venezuela.
***alvarof1971@gmail.com**

**Abstract**

The study assesses climatic similarity according to the Köppen-Geiger classification in 70 metropolitan areas in Latin America and the Caribbean (2014–2018), based on the integration of 25 urban, bioclimatic, geographic, socioeconomic, and sociopolitical indicators. Two datasets were constructed: one incorporating average elevation (metropolis) and another classifying elevation (low (1), intermediate (3), and high (3)). Multivariate statistical methods were employed, including cluster analysis (MC) and discriminant analysis (MD) based on the dependent variables (VDsc): Climate Zone, Population Stratification, and Geographic Location. Data validation was performed using Student's t-test, analysis of variance (ANOVA) for independent samples, and Tukey's post hoc test. Cluster structures were defined using the silhouette method, and Euclidean distance metrics were employed to assess similarity patterns.The results indicate that VDsc Climate Zone shows the highest similarity among urban groups (61%), suggesting relatively strong Köppen-Geiger climate consistency in the region. In turn, the MD (VDsc Climate Zone) yielded a low classification error (5.6%), highlighting the robustness of the clustering approach. Among the discriminating indicators that differentiate clusters are the Human Development Index and the Rule of Law Index. These results suggest that regional urban climate similarity does not depend solely on bioclimatic factors, but also on existing socioeconomic and governance interrelationships, allowing for a broader interpretation of climate patterns in complex metropolitan systems.

**Keywords:** Köppen-Geiger climate similarity, dependent variables, multivariate models, discriminant indicators.

**Resumen**

*El estudio evalúa la similitud climática según la clasificación Köppen-Geiger en 70 áreas metropolitanas de América Latina y el Caribe (período 2014-2018), a partir de la integración de 25 indicadores urbanos, bioclimáticos, geográficos, socioeconómicos y sociopolíticos. Se construyeron dos conjuntos de datos: uno que incorpora la elevación media (metrópolis) y otro que discrimina la elevación baja (1), intermedia (3) y alta (3). Se emplearon métodos estadísticos multivariados, incluidos los análisis de conglomerados (MC) y discriminante (MD) a partir de las variables dependientes (VDsc): Zona Climática, Estratificación de la Población y Localización Geográfica. La validación de los datos se realizó con la prueba t de Student, análisis de varianza (ANOVA) para muestras independientes y prueba post hoc de Tukey. Las estructuras de los clústeres se definieron con el método de silhouette, y se emplearon métricas de distancia euclidiana para evaluar los patrones de similitud. Los resultados indican que VDsc Zona Climática presenta la mayor similitud entre los*

*grupos urbanos (61 %), lo que sugiere una coherencia climática Köppen-Geiger relativamente fuerte en la región. A su vez el MD (VDsc Zona climática) arrojó un bajo error de clasificación (5.6 %), lo que destaca la solidez del enfoque de agrupamiento. Entre los indicadores discriminantes que diferencian clústeres, tenemos los Índices de Desarrollo Humano y Estado de Derecho. Estos resultados sugieren que la similitud climática urbana regional no depende únicamente a factores bioclimáticos, sino a las interrelaciones socioeconómicas y de gobernanza existentes, lo que permite interpretar con mayor amplitud los patrones climáticos en sistemas metropolitanos complejos.*

***Palabras clave*****:** *Similitud climática Köppen Geiger, variables dependientes, modelos multivariantes, indicadores discriminantes.*

## 1. Introduction

The global population reached 8 billion people in 2022, of whom approximately 55% live in urban areas (United Nations Sustainable Development Goals, UN, 2023). In Latin America and the Caribbean (LAC), the urban areas of its metropolises are quite heterogeneous in terms of population strata, accounting for 80% of the regional population and 13% of the global population (UN-HABITAT, 2016). This population impact directly affects the regional metropolitan climate, according to scientific evidence (Hiroito et al., 2026; Wu et al., 2019). However, climate studies in metropolitan areas can be approached from different perspectives, depending on the urban, economic, political, and geographic realities of each specific region. Furthermore, these studies may have limitations in terms of the scales of analysis, which increases uncertainty and information gaps in climate projections (Lauwaet et al., 2015).

In studies on climate and socio-environmental dynamics in urban areas across Latin America and the Caribbean (LAC) over the past decade, regional and international experts have focused their efforts on geospatial analyses at the local metropolitan scale (Boccolini, 2025; Pacifici et al., 2019), the national scale (Casadei et al., 2021; Baumgartner, 2025; Henríquez et al., 2017), and regional (Wu et al., 2019; Dobbs et al., 2014) scales. In climate and cartographic analysis at various scales, the Köppen-Geiger climate classification has been used as a methodological framework due to its regular updates (Beck et al., 2018). However, various authors over the past 30 years (Grimmond and Souch, 1994) have recommended developing new cartographies based on Köppen-Geiger but better adapted to urban conditions in LAC, as seen in regional studies over the past decade (González-Calderón et al., 2025a; González-Calderón et al., 2025b).

However, to contribute new climate-related findings in metropolitan areas, it is necessary to include approaches that examine the relationships between Köppen-Geiger climate similarity and socioeconomic indicators (carbon, energy, population, income, pollution), urban indicators (heat islands, urban sprawl, population density), and sociopolitical indicators (climate risks, global risks, governance, rule of law)to name the most critical ones as well as new analytical frameworks that allow for the observation urban and climatic complexities in the region.

With regard to the analysis and assessment of Köppen-Geiger climate similarity in metropolitan areas, such analyses can be conducted at the regional metropolitan scale using multivariate models; these analyses offer several advantages: 1) it constitutes a non-parametric method that does not require specific probability distributions nor depend on strict statistical assumptions, such as linearity or symmetry, and allows for the inclusion of categorical indicators, such as climate codes; 2) it allows Köppen-Geiger subclassifications to be grouped into clusters that are internally homogeneous and distinct from one another; and 3) it facilitates the graphical visualization of the shortest distance between Köppen-Geiger subclassifications through probabilities of belonging to the same cluster, using estimation methods such as Euclidean distance matrices, specifically as a metric to evaluate similarity patterns among Köppen-Geiger metropolitan groups.

To conduct these analyses, the study was structured around two main criteria. The first criterion involved the selection of dependent variables based on: a) the Köppen-Geiger climate zone of the analyzed metropolitan areas, b) the population stratification of the metropolitan areas, and c) their geographic location. The second criterion was the application of multivariate cluster models (MC) to organize metropolitan groups based on climatic similarity, and the application of discriminant analysis (DA) for the analysis and validation of the cluster data generated by the MC. In accordance with these criteria, the main objectives of the study are: 1) To organize metropolitan areas according to low1, medium3, and high5 elevations. 2) To organize Köppen-Geiger clusters using MC based on climatic similarity and employing dependent variables (Climate Zone, Population Stratification, and Geographic Location). 3) Validate misclassification errors in the data using MD and identify the most discriminating indicators (D) in Köppen-Geiger clusters, which will allow for differentiation between these clusters and the climate clusters.

## 2 Methodology

### *2.1 Description of the study area*

The Latin America and Caribbean (LAC) region comprises 33 countries, located in three subregions: South America, Mesoamerica, and the Caribbean. This region is also characterized by significant climatic and geographic variability according to the recent Köppen-Geiger climate

classification (Beck et al., 2018).

In particular cities in Latin America and the Caribbean (LAC) exhibit significant population stratification (UN-Habitat, 2016) and a wide variety of urban landscapes depending on their Köppen-Geiger classification (see Figure. 1). Therefore, the study proposed including seventy major metropolises (Table 1) based on the high diversity of climates and the population significance of these metropolises (Economic Commission for Latin America, ECLAC 2017. As an example, Figure. 1 shows a random selection of 16 types of LAC metropolises based on their different Köppen-Geiger climates; furthermore, Figure. 1 illustrates a sample of the great diversity of urban landscapes existing in the region, indicating the high level of urban-climatic heterogeneity in LAC. These examples of metropolises and their respective climates are: 1) arid-desert (Maracaibo (Bsh); Tijuana (Bsk); Lima (Bwh); Arequipa (Bwk); 2) temperate (Buenos Aires (Cfb); k) Quito (Cfb); l) Greater Valparaíso (Csb); Santiago, Chile (Csc); Guatemala City (Cwb); La Paz (Cwc); 3) tropical (Rio de Janeiro (Af); b) Santo Domingo (Am); c) Cali (As); d) Panama City (Aw); 4) subtropical (Guadalajara (Cwa). Furthermore, Table 1 details each of the 70 metropolitan areas included in this study and organizes them in to the Köppen-Geiger climate groups to which they belong according to the updated regional classification (Beck et al., 2018).


**Figure.1.** Location of metropolises Köppen–Geiger climate **a**) Rio de Janeiro (Af); b) Santo Domingo (Am), c) Cali (As); d) Ciudad de Panamá (Aw); e) Maracaibo (Bsh); f) Tijuana (Bsk); g) Lima (Bwh); h) Arequipa (Bwk); i) Rosario (Cfa); j) Buenos Aires (Cfb); k) Quito (Cfb); l) Gran Valparaíso (Csb); m) Santiago de Chile (Csc), n) Guadalajara (Cwa); o) Ciudad de Guatemala (Cwb); p) La Paz (Cwc).

**Table 1.** Metrópolis according to their location Köppen-Geiger [(a)]

| CLIMATE | KÖPPEN-GEIGER | SUB-GROUP METROPOLISES | |
|---|---|---|---|
| Tropical | Af | Ecuatorial | Salvador, Manaos, Belem, Rio de janeiro, Santos |
| | Am | Monsoon | Joao Pessoa, Managua, Santo Domingo, San Juan, Sao Luis, Recife, San Pedro Sula, Bucaramanga, Cali, Medellin |
| | As (Aw) | Tropical savanah | Caracas, Ciudad de Panamá, Fortaleza, La Habana, Natal, Brasilia, Santa-Cruz, Barranquilla, Guayaquil, Mérida, Goiania, Maracay, San Salvador, Tegucigalpa, Valencia, Vitoria. |
| Sub tropical | Cwa | Subtropical with dry winters | Belo horizonte, Campinas, Córdoba, Guadalajara, San Miguel de Tucumán, Cuernavaca, San José. |
| | Cfa | Humid subtropical | Asunción, Puerto Alegre, Rosario, Sao Paulo. |
| Arid | Bsh | Steppes (hot) | Maracaibo, Monterrey, León, Querétaro, Cartagena, |
| | Bsk | Steppes (cold) | Cochabamba, Tijuana, San Luis Potosí. |
| Desert | Bwh | Desertic (hot) | Lima, Torreon, Mexicali |
| | Bwk | Desertic (cold) | Ciudad Juarez, Mendoza, Arequipa |
| Temperate | Csb | Mediterranean with fresh summers | Concepción, Valparaíso |
| | Csc | Cold-summer Mediterranean | Santiago de Chile. |
| | Cwc | Cold subtropical | La Paz |
| | Cfb | West coast maritime (oceanic) | Buenos Aires, Curitiba, Montevideo, Bogotá, Quito, |
| | Cwb | Temperate with dry winters | Toluca, C.D México, Morelia, Puebla, C.D Guatemala |

(a) 70 cities included in this study; the climate code colors correspond to the latest classification (Beck et al., 2018).

### *2.2 Data on selected indicators*

A five-year period (2014–2018) was selected, using robust data on meteorological, bioclimatic, geographic, urban, socioeconomic, and sociopolitical indicators for LAC metropolises. This time frame was chosen because an updated Köppen-Geiger classification map was reported for the 2014–2018 period (Beck et al., 2018) and periodic data were reported for new sociopolitical indices (democracy, rule of law, global risks, climate risks, and social gaps) and socioeconomic indices (carbon emissions, particulate matter, human development, social inequality, and population). The indicator data were extracted from reports by nongovernmental organizations, scientific articles, and global platforms. In the first case, the indicators and abbreviations for bioclimatic variables (temperature (T), precipitation (P), humidity (H), and aridity (Ia)) were taken from the World Meteorological Organization (WMO, 2021), geographic–urban indicators (altitude (alt), urban area (UA), urban heat islands (UHI)) from Wu et al. (2019), and population (P), population density (Pd), and urban expansion (UG) (Cox, 2025).

Socioeconomic data including population (Pop), social inequality (GINI), income (GDP), and human development (HDI)—were drawn from data provided by the World Bank (2021) and the United Nations Development Programme (UNDP, 2018); pollution (PM2.5-PM10) from reports by the World Health Organization (WHO, 2018), and carbon emissions (Cf-CO2U) from Morán et al. (2018). Specifically, the energy data for the 70 metropolitan areas were recalculated for this study in accordance with the IPCC Guidelines (2006) and the protocol for national greenhouse gas inventories; the calculation focuses on quantifying fuel combustion and electricity consumption by sector. For this energy calculation in kilowatt-hours (kWh), data on carbon emissions in metropolitan areas (Moran et al., 2018) were used, and emissions were broken down by sector (residential, commercial, industrial, transportation) according to sector-specific emission factors for the local electricity grid, using Equation 1 (IPCC Guidelines, 2006).

$$KWh = Em\ (KG\ CO2\ e) / FE\ (Kg\ CO2e/Kwh). \quad (1)$$

Where KWh is the kilowatt-hour of electricity consumption, Em is the carbon dioxide equivalent emissions per sector, and FE is the carbon dioxide equivalent emission factor per sector, expressed in kilowatt-hours per year.

Finally, the selected sociopolitical indicators were: the Democracy Index (DI) (Economic Intelligence Unit, EIU, 2015, 2019), the rule of law as measured by the World Justice Project (WJP, 2021), the Global Climate Risk Index (CRI) (Germanwatch, 2021), the Multidimensional Poverty Index (MPI) from the United Nations Development Programme (UNDP, 2023, 2024), and the Global Risks Index (WR) (World Economic Forum, 2024).

### *2.3 Statistical Tests and Multivariate Methods*

To organize the data for the 70 metropolitan areas, a recoding scheme was applied in the database (APPENDIX 1) based on the following dependent variables: 1) Köppen-Geiger climate classification (Beck et al., 2018), population stratum (United Nations Habitat Organization (UN-Habitat), 2020) and Geographic Coordinates (Geographic Coordinate System (GCS)). Subsequently, two databases were organized for each dependent variable (DVcs), including or excluding the altitude (P) of the metropolises, based on: a) Köppen-Geiger Climate Zone (DVcs-Climate Zone, DVcs-Climate ZoneP); b) Population Stratification (DVscPopulationStratification,DVcsPopulationStratificatio nP); c) Geographic Location (DVcs-Geographic Location, DVcs-Geographic LocationP), resulting in a total of six analyses.

Using the recoded data, a Köppen-Geiger cluster analysis was performed using a conglomerate model (CM) with the statistical software R versión 4.0.2 **(**R Development Core Team, 2023) where the silhouette method was applied to measure the quality and appropriate number of clusters, and to indicate how well each observation unit fits within its own cluster; therefore, a Euclidean distance matrix was established for each case, which allowed for the initial definition of some climate groups. The maximum value of the silhouette curve will indicate the appropriate number of clusters, based on the coefficient that estimates the average distance between clusters. Subsequently, for the analysis and validation of the data, the following methods and procedures were employed:

1**. Application of the Student's t-test for the difference in means between independent samples.** This test was used to compare the means of two groups using 95% confidence intervals, which estimate the difference between population means. Confidence intervals consist of a lower limit (Li) and an upper limit (Ls), from which it can be seen that both limits may have positive or negative signs, or the lower limit may have a negative sign and the upper limit a positive sign; that is, the value zero is included between the two confidence limits as a possible value for estimating the difference in population means. If the 95% confidence interval does not contain the value zero, this implies that there are statistically significant differences between the means of the indicator being compared for both groups; consequently, this particular indicator has the ability to discriminate between the groups because it estimates that their means are different (one mean being greater or less than the other). Otherwise, it is concluded that the indicator does not discriminate between the groups, because their means are equal. For the comparison of means of three or more groups, one-way analysis of variance (ANOVA) for independent samples was applied, after verifying compliance with statistical assumptions, based on the following statistical hypotheses:

***Null hypothesis (H0)****:* the means of the three or more groups are equal.

***Alternative hypothesis (H1):*** the means of at least two of the groups are different.

2. The decision criterion is as follows: if the p-value of the F-test statistic is less than or equal to 0.05, H0 is rejected; otherwise, it is not. In this way, the indicators that showed statistically significant differences were identified. If H0 is not rejected for a particular indicator, that indicator will not be included in the discriminant function because it lacks the ability to distinguish between groups. Conversely, if H0 is rejected for a particular indicator, it will be included in the discriminant function because it has the ability to distinguish between groups; however, the rejection of H0 does not imply that all the means of each group differ from one another.

3. After rejecting H0 and accepting H1, Tukey's test was applied to identify groups with differing means; however, for the purpose of constructing the discriminant function, the ultimate goal is to determine whether there are statistically significant differences between the group means, regardless of whether there are differences between pairs of means when making a comparison (means of three or more groups).

4. To validate the data and test the null hypothesis, a discriminant model (DM) was applied to assess statistically significant differences in the MC clusters, and one-way ANOVA was calculated to validate the discriminant indicators (D) within the dataset ($p < 0.0001$). Next, the data membership was evaluated using a random partition of the information, with 70% selected as the training set and the remaining 30% used to validate each group model. Finally, the selection of the D (clusters) was based on the highest mean values in the clusters (group means) according to the results of the linear discriminant equations (LD).

## 3. Results and Discussion

### *3.1 Cluster organization*

The Euclidean distance matrix (see Figure. 2) allowed us to define climate groups based on the principal diagonal; the squares (bright red) represent a distance of zero, corresponding to the same statistical unit. As the color shifts from red to blue, the distance between climates increases, and consequently, they belong to different clusters. In this case, pure red represents dist (climate.i, climate.j) = 0 and pure blue represents dist (climate.i, climate.j) = 1. Furthermore, climates belonging to the same cluster are displayed in consecutive order.

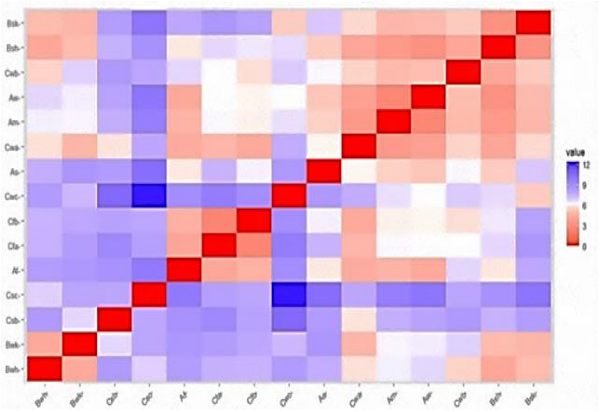

**Figure. 2**. Matrix of Euclidean distances (Köppen-Geiger climates).

Using R software version 4.0.2 (R Development), the percentage of climatic similarity within each cluster was evaluated based on the VDsc, with and without P. The silhouette method suggested a general configuration of between 2 and 8 clusters, as indicated by the peak of the silhouette curve (see Figure. 3): VDsc-Climate Zone (2), VDsc-Climate Zone P (3), VDsc-Population Stratification (5), VDsc-Population stratification P (5), VDsc-Geographic location (8), VDsc-Geographic Location P (6). However, for VDsc-Climate Zone and VDsc-Climate ZoneP, the silhouette curve recommends a smaller number of clusters (2 and 3, respectively). This implies greater climatic homogeneity in these VDsc categories.

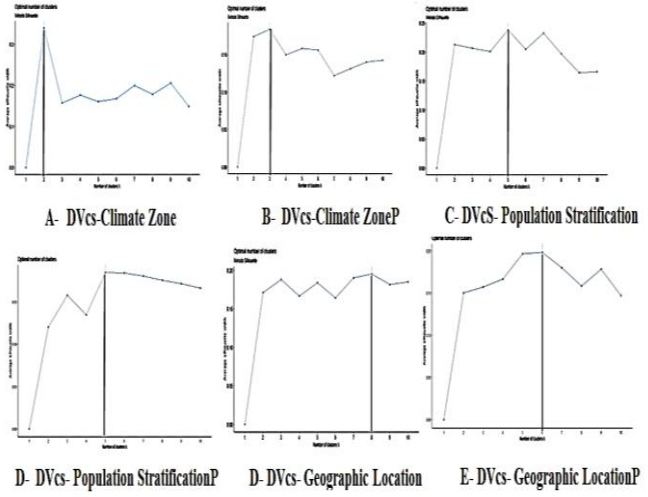


**Figure. 3.** Number of clusters recommended by the silhouette method

### *3.2 Köppen-Geiger similarity and number of clusters*

The DVcs-Climate Zone yielded the highest similarity percentage (61%), followed by the DVcs -Climate Zone P (51.5%). In the other cases, lower percentages were

obtained, such as DVcs -Population stratification (50.1%), DVcs-Population stratificationP (46.7%), DVcs-Geographic location (47.8%), and DVcs-Geographic locationP (50.1%).

The inclusion or exclusion of P resulted in differences in similarity, mainly in the climate zone, suggesting that P may influence the dispersion of cluster data. On the other hand, the clusters and dendrograms (detailed in Fig. 4) indicate that as similarity increases, the silhouette method suggests a smaller number of clusters, reflecting greater climatic homogeneity. In contrast, when similarity decreases, the silhouette method suggests a larger number of clusters (6–8), indicating more heterogeneous and diverse climates. The results of the decision-making process regarding the number of Köppen-Geiger clusters for each DVcs are described below.

DVcs-Climate Zone

The DVcs climate zone yielded two main clusters (Figure. 4a). Cluster 1 included desert, hot, cold, and temperate climates according to Bwh, Bwk, Csb, and Csc. Cluster 2 grouped tropical and subtropical climates (Af, Cfa, As, Am, Aw, and Cwa), as well as two subgroups: one temperate (Cfb, Cwc, and Cwb) and one semi-arid (Bsh, Bsk).

DVcs-Climate Zone P

The DVcs-climate zone P comprises three clusters (Figure. 4b). Cluster 1 grouped altitudinal zones 1, 3, and 5 of the tropical-subtropical type (1Af, 1Am, 1Aw, 1Cfa, 3Af, and 3Cwa), as well as tropical, subtropical, and temperate climates of altitudinal zone 5 (5As, 5CWa, and 5Cfb). Cluster 2 grouped temperate climates at elevation 5 (5Cwc and 5Cwb), arid-desert climates (5Bsk, 5Bwh, and 5Bsh), tropical high-altitude climates (5Aw), tropical low-altitude climates (3Am, 3Aw), and a warm arid low-altitude climate (1Bsh). Finally, cluster 3 grouped subtropical, temperate, and arid-desert climates of elevation 3 (3Cfa, 3Csc, 3Bwk, 3Bsh, and 3Bwh), as well as a temperate-arid subgroup of zone 1 (1Bsk, 1Cfb, and 1Bwh) and a single desert climate of zone 5 (5Bwk).

DVcs- Population Stratification

The DVcs-Population Stratification analysis identified five clusters (Figure. 4c). Cluster 1 grouped megacities with tropical, subtropical, and temperate climates (AfMC, CfaMC, CfbMC, and CwbMC). Cluster 2 grouped temperate climates with medium-to-large population strata (CsbMI and CscMG). Cluster 3 grouped an arid-semi-arid subgroup that includes a desert megacity (Bwh) and climates with medium-to-intermediate population strata (BskMM, BshMM, BwhMM, BwkMI, BwhMI, and BwkMM), as well as a temperate climate with a medium population stratum (CwbMM). Cluster 4 grouped intermediate-to-medium-stratum tropical and temperate climates (AmMI and CwcMM). Finally, Cluster 5 corresponded to a major subgroup of medium-intermediate population strata with tropical, subtropical, temperate, and arid climates (AfMM, AwMM, AmMM, AsMM, CwaMI, CwaMM, CfaMM, CfbMM, and CfbMG BshMI).

DVcs- Population Stratification

The DVcs -population stratification P analysis reveals five clusters (Figure. 4d). Cluster 1 comprises tropical, subtropical, and temperate megacities in altitudinal zones 1, 3, and 5 (1AfMC, 1CfbMC, 3CfaMC, 5CwbMC). Cluster 2 grouped temperate, subtropical, and desert climates with intermediate, medium, and large population strata at elevations 1, 3, and 5 (1CfbMM, 3BwkMM, 3CwaMI, 3CscMG, 1CsbMI, and 5CwaMM). Cluster 3 grouped arid and semi-arid climates at levels 1, 3, and 5 associated with medium-intermediate population strata (1BskMM, 5BwkMM, 5BwkMI, 5BskMM, 5BshMM, 5BwhMM, 3BshM, and 3BwhMI), as well as a desert megacity (1BwkMC). Cluster 4 grouped tropical climates at elevations 1 and 3 with medium-to-intermediate population strata (1AmMI, 3AmMM). Finally, cluster 5 grouped a main subgroup of arid, temperate, and tropical climates at elevations 1, 3, and 5 corresponding to medium, large, and intermediate population strata (3AfMM, 5CwaMI, 1AfMM, 1AmMM,1AwMM,5CfbMM,1CfaMM,3CwaMM,5AsMM, 5CfbMG,5CwcMM,1BshMM,1BshMI,5CwbMM,3AwMM and 5AwMM).

DVcs- Geographic Location

DVcs Geographic Location initially grouped eight clusters into dendrograms; however, based on homogeneity criteria, three main clusters were selected from within the dendrograms (Figure. 4e). Cluster 1 grouped arid, temperate, and subtropical climates located in ZI, ZTS, and ZTN (BskGCS-ZI, CwcGCS-ZI, CsbGCS-ZTS, BwkGCS-ZTS, CwaGCS-ZTS, BwkGCS-ZI, BskGCS-ZTN, BwhGCS-ZTN, and BwkGCS-ZTN. Cluster 2 grouped dry temperate, arid, and semi-arid climates in ZI, ZTS, and ZTN (CscGCS-ZTS, BwhGCS-ZI, BshGCS-ZTN, and CwbGCS-ZI). Cluster 3 mainly grouped tropical and subtropical climates ranging from ZI to ZTS (CfaGCS-ZTS, AsGCS-ZI, AfGCS-ZI, AfGCS-ZTS, AwGCS-ZI, AmGCS-ZI, and CwaGCS-ZI), as well as temperate and semi-arid climates ranging from ZTS to ZI (CfbGCS-ZTS, CfbGCS-ZI, and BshGCS-ZI).

DVcs- Geographic LocationP

Based on homogeneity criteria, three clusters were selected (Figure. 4f). Cluster 1 grouped arid, semi-arid, dry temperate, and subtropical climates at elevations 1, 3, and 5, distributed from the ZTS to the ZTN (3BwkGCS-ZTS,

1BshGCS-ZI,1BSkGCS-ZTN,5BwkGCS-ZTN,5BwkGCS-ZI,3BshGCS-ZI,3BwhGCS-ZTN,1CsbGCSZTS,3CscGCS-ZTS,1CfbGCS-ZTS and 3CwaGCS-ZTS). Cluster2 grouped tropical, subtropical, temperate, arid, and semi-arid climates at elevations 1,3and 5, mainly in the ZI (3AmGCS-ZI,5CwcGCS-ZI,5CwbGCS-ZI,5BskGCS-ZI,5BshGCS-ZI, 5AsGCSZI,5CfbGCSZI,5AwGCSZI,1BshGCSZI,3AwGCS-ZI, 5CwaGCS-ZI), 1AmGCS-ZI, 1AwGCS-ZI), as well as a warm desert subgroup at elevation 5 in the ZTN (5BwhGCS-ZTN). Finally cluster 3 grouped tropical, subtropical and temperate Mediterranean climates at elevations 1,3, and 5 from ZTS to ZI (3CfaGCS-ZTS, 3AfGCSZI,1AfGCSZI,1AfGCSZTS,3CwaGCSZI,1CfaGCS-ZTS,and5CfbGCS-ZTS).

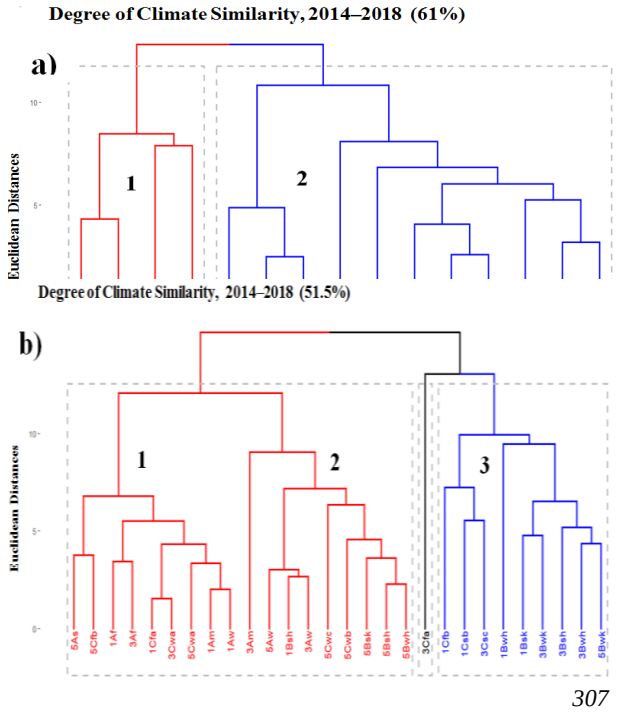




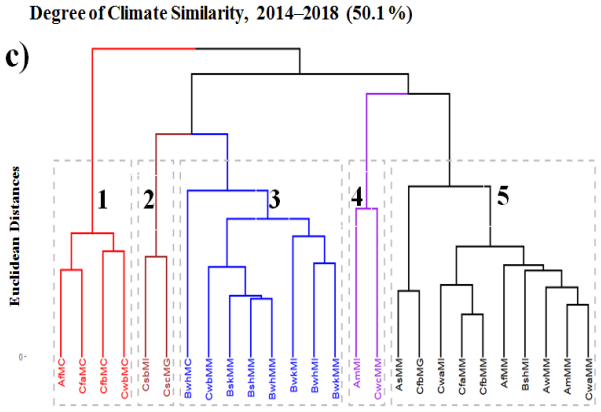


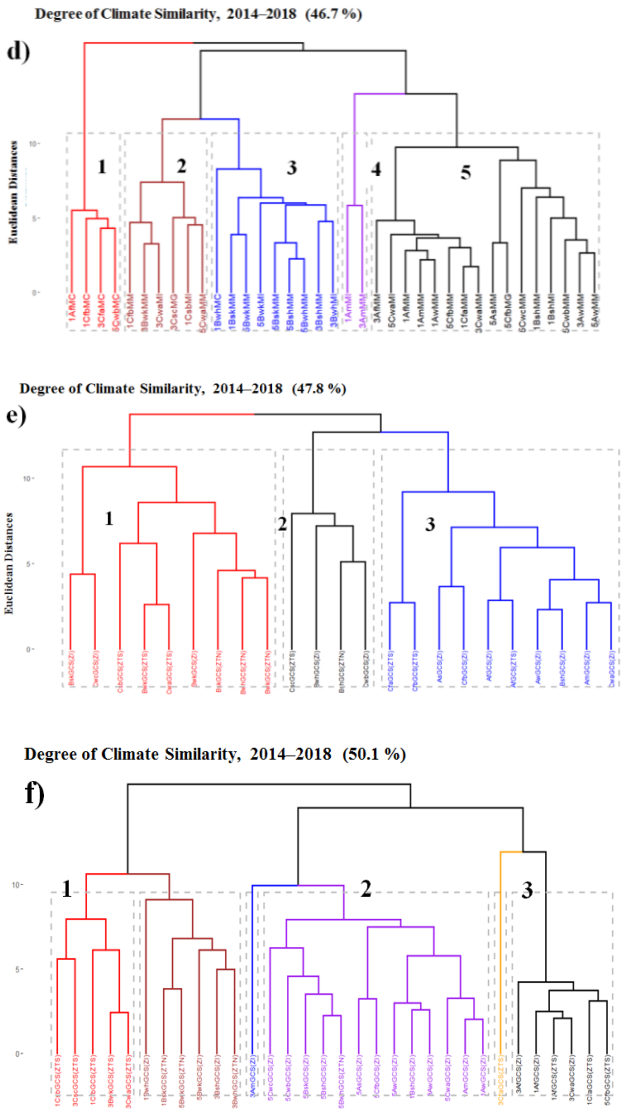


**Figure. 4.** Köppen-Geiger clusters based on climatic similarity: a) DVcs-Climate Zone; b) DVcs-Climate Zone P; c) DVcs-Population Stratification; d) DVcs-Population Stratification P; e) DVcs-Geographic Location; f) DVcs-Geographic Location P.

### *3.3 Cluster Validation with MD*

Significant indicators were evaluated using the Student's t-test to assess the difference in means between indicators. In general, all indicators were statistically significant for the difference in means, with the exception of energy intensity (EI). The data for Fisher's Linear Functions (LD) and the discriminant indicators (D) for each VDcs are detailed in Figures. 5a, b, c, d, e, f.

DVcs- Climate Zone: In LD1, the values accounted for 87.4% of the total variability associated with the first eigen value. In the predicted data, 300 observations (98.3%) were

correctly classified into the first cluster, and 37 observations (82.4%) into the second cluster. The model had a hit probability of 96.58% (overall error of 3.42%). With 70% of the test data, the model yielded a hit probability of 96.32% (overall error of 3.68%). The main discriminants (D), according to Fischer's Linear Functions (LD) shown in Fig. 5a, corresponded in LD1 to socioeconomic and sociopolitical indicators, such as the Human Development Index (HDI) and the Rule of Law Index (WJP), which explain 87% of the data in cluster 2, characterized by tropical and subtropical climates (Af, Cfa, As, Am, Aw, Cwa), as well as two subgroups: one temperate (Cfb, Cwc, Cwb) and another semi-arid (Bsh, Bsk). In the data validation (30%), eighty-nine observations (96.7%) were correctly classified in the first cluster, and eleven observations (78.5%) in the second, yielding a probability of correct classification of 94.34% (overall error of 5.66%). The analyzed group and the D data were as follows:

*(Group 1: T + UHI + P + H + Ai + UA + Pd + UG + Cf + PM25 + PM10 + E + GDP + **HDI** + GINI + DI + WR + **WJP,** data = todos).*

| **a)** | |
|---|---|
| ## Coefficients of linear discriminants: | |
| ## **LD1** | |
| ## Tm -2.556964e-01 | ## E 4.841893e-06 |
| ## UHI -5.589141e-01 | ## GDP -3.784208e-05 |
| ## Pp 5.534892e-03 | ## **HDI 3.513901e+00** |
| ## H -3.594557e-02 | ## GINI -1.337285e-02 |
| ## AI -2.112587e-01 | ## DI -5.803131e-01 |
| ##UA -3.225837e-04 | ## WR 1.156023e-02 |
| ## Dp 8.216582e-05 | ## **WJP 9.420736e+00** |
| ## UG -1.133921e-01 | |
| ## Cf 4.464681e-01 | |
| ## PM25 -6.593838e-03 | ## **LD1** |
| ## PM10 2.330291e-02 | **0.874** |

**Figure. 5a**. Coefficients of Linear discriminants DVcs-Zona Climática

DVcs-Zona ClimáticaP: LD1 explained 68.82% and LD2 explained 31.11% of the total variability (100%) associated with the first eigenvalue. In the predicted data, fifty-nine observations (62.1%) were correctly classified in the first cluster, one hundred sixty observations (92%) in the second cluster, and sixty-seven observations (85%) in cluster 3. The model had a hit probability of 82.29% (overall error of 17.71%). At the 70% threshold, a hit probability of 81.68% was obtained (overall error of 18.03%). The main Ds (Fig. 5b) identified were: LD1, socioeconomic indicators, such as the Human Development Index (HDI), which explains 64% of the data in cluster 3, characterized by arid–desert climates of elevations 1, 3, and 5 (1Bsk, 1Bwh, 3Bwk, 3Bsh, 3Bwh, and 5Bwk), temperate climates at elevations 1 and 3 (1Cfb, 1Csb, and 3Csc), and subtropical climates (3Cfa). LD2 corresponded to multidimensional poverty (MPI), with a 36% contribution in cluster 1, characterized by tropical-subtropical climates at elevation 1 (1Af, 1Am, 1Aw, 1Cfa), elevations 3 (3Af, 3Cwa), tropical-subtropical climates at elevation 5 (5As, 5CWa), and temperate climates (5Cfb). In the validation set (30%), nineteen observations (65.5%) were correctly classified in the first cluster, forty-five (84.9%) in the second, and twenty-one (87.5%) in the third. The model yielded a probability of correct classification of 80.19% (overall error of 19.81%). The analyzed group and the D values were as follows:

*(Group 2: T + UHI + P + H + AI + UA + Pd + UG + Cf + PM25 + PM10 + E + GDP + **HDI** + GINI + DI + **MPI** + CRI + WR + WJP, data = todos).*

| **b)** | |
|---|---|
| ## Coefficients of linear discriminants: | |
| ## **LD1** **LD2** | ## **LD1** **LD2** |
| ## Tm -1.963735e-01 1.266355e-01 | ## E 2.524385e-04 -2.494369e-04 |
| ## UHI -3.352328e-01 7.038552e-02 | ## GDP 1.272773e-05 1.852154e-05 |
| ## Pp 2.746760e-03 -5.962579e-03 | ## **HDI 3.735223e+**00 -3.817467e-01 |
| ## H -1.132694e-02 1.782206e-02 | ## GINI 2.189446e-02 -1.376801e-02 |
| ## AI -1.378548e-01 2.119149e-01 | ## DI -5.474027e-02 4.148062e-01 |
| ## UA -3.887148e-04 -6.873801e-05 | ## **MPI -1.827996e+01** 2.774986e+01 |
| ## Dp -7.301534e-05 -2.415177e-05 | ## IRC -1.305665e-04 2.303140e-03 |
| ## UG 4.104605e-01 3.650446e-01 | ## WR 2.096249e-01 2.393951e-02 |
| ## Cf -6.322513e-01 8.746610e-01 | ## WJP -3.195253e+00 -1.221432e+01 |
| ## PM25 -1.556801e-02 3.075582e-02 | ## **LD1** **LD2** |
| ## PM10 2.968480e-02 1.761032e-05 | **0.6441** **0.3559** |

**Figure. 5b**. Coefficients of Linear discriminants DVcs-Climate Zone P

DVcs- Population Stratification: LD1 explained 64.6%, LD2 19.4%, LD3 11%, and LD4 4% of the total variability (100%). In the first cluster, twenty observations (100%) were correctly classified; in the second, two hundred six (92%); in the third, sixty-seven (78.8%); in the fourth, nine (90%); and in the fifth, twenty observations (100%). The model had a hit probability of 92.0% (overall error of 8.0%). At a 70% test set, a hit probability of 93.45% was obtained (overall error of 6.55%). The main Ds were (Fig. 5c): LD1, the socioeconomic indicator Cf, which explains 65% of the data in cluster 5, characterized by tropical, subtropical, and temperate climates (AfMM, AwMM, AmMM, AsMM, CwaMI, CwaMM, CfaMM, CfbMM, CfbMG BshMI). LD2 explained 19% of the data using socio-political discriminants associated with the MPI in cluster 4, characterized by tropical and temperate climates in the middle-to-upper strata (AmMI, CwcMM), as well as HDI-WJP socioeconomic-sociopolitical discriminants in cluster 5 with tropical, subtropical, and temperate climates (AfMM, AwMM, AmMM, AsMM, CwaMI, CwaMM, CfaMM, CfbMM, CfbMG, BshMI). LD3 explained 11% of the data using the socio-political discriminant (DI) in cluster 5, associated with tropical, subtropical, and temperate climates of the middle-intermediate stratum (AfMM, AwMM, AmMM, AsMM, CwaMI, Cwa, CfaMM, CfbMM, CfbMG, BshMI). LD4 explained 5% of the data

using the MPI sociopolitical discriminant in cluster 4, characterized by intermediate-mid-stratum tropical and temperate climates (AmMI, CwcMM), and the discriminant D in cluster 5, associated with mid-stratum tropical-subtropical climates (AfMM, AwMM, AmMM, AsMM, CwaMI, CwaMM, CfaMM, CfbMM, CfbMG, BshMI). At the 30% level, six observations were correctly classified in cluster 1 (100%), fifty-nine in the second, twenty-three in the third (88.46%), three in the fourth (100%), and six in the fifth (100%). The model had a probability of correct classification of 91.5% (overall error of 8.49%). The analyzed group and the Ds were as follows:

*(Group 3: T + UHI + P + H + Ai + UA + Pd + UG + Pob + **Cf** + CO2U + PM25 + PM10 + E + GDP + Ec + **HDI** + GINI + **DI** + **MPI** + CRI + WR + **WJP**, data = EDT).*

**c)**

## Coefficients of linear discriminants:

| | LD1 | LD2 | LD3 | LD4 |
|---|---|---|---|---|
| ## Tm | -1.031481e-01 | -2.511564e-01 | 1.893354e-01 | -3.025492e-02 |
| ## UHI | -1.094328e-01 | -5.312495e-02 | -5.726338e-01 | 2.820398e-01 |
| ## Pp | 9.379955e-04 | 2.420910e-03 | -3.010313e-03 | 4.466051e-03 |
| ## H | -1.314303e-02 | -2.213944e-02 | -2.821690e-02 | 2.185923e-02 |
| ## AI | -3.493348e-02 | -1.103735e-01 | 9.312495e-02 | -1.631734e-01 |
| ## AU | -6.476825e-04 | -4.736709e-05 | 2.835232e-04 | 5.229903e-04 |
| ## Pd | 2.341185e-05 | -8.455955e-06 | -3.279583e-05 | 3.133422e-05 |
| ## UG | 6.725911e-02 | 4.074391e-01 | 1.358000e-01 | 2.970179e-01 |
| ## Pob | -1.153870e-07 | 1.691227e-07 | -9.353967e-08 | 2.799051e-07 |
| ## Cf | **4.826588e-01** | -9.929316e-02 | -2.124822e+00 | -7.007743e-01 |
| ## CO2U | 1.964870e-09 | -5.272576e-08 | 3.069093e-09 | -2.090217e-08 |
| ## PM25 | 6.060888e-02 | -1.589199e-02 | 1.716485e-02 | -2.030105e-02 |
| ## PM10 | -1.100215e-02 | 5.410402e-02 | -8.088687e-03 | 1.904079e-02 |
| ## E | -1.718553e-04 | 1.312024e-04 | 5.083545e-04 | 2.984005e-04 |
| ## GDP | 9.684098e-05 | -4.696003e-05 | 5.930511e-05 | 1.084296e-04 |
| ## PIBU | -3.209622e-11 | 5.946692e-12 | 7.267208e-12 | -1.756860e-11 |
| ## DHI | 1.911195e-01 | **5.664848e+00** | -6.601283e+00 | -1.891247e-01 |
| ## GINI | 1.912382e-02 | 3.210715e-02 | 1.116507e-02 | 2.888097e-02 |
| ## DI | -9.818861e-02 | -2.370415e-01 | **1.039366e+00** | **1.139351e+00** |
| ## MPI | -2.330643e+01 | **9.001050e+00** | 1.075668e+01 | **1.890509e+01** |
| ## CRI | -1.742389e-03 | -5.339699e-03 | -6.420046e-03 | 1.958136e-02 |
| ## WR | 5.995910e-02 | 6.367696e-02 | -1.233945e-01 | -1.316368e-01 |
| ## WJP | -4.754784e+00 | **3.854008e+00** | -1.565761e+01 | -4.375040e+00 |

##Proportion of trace:

| ## LD1 | LD2 | LD3 | LD4 |
|---|---|---|---|
| 0.6546 | 0.1903 | 0.1096 | 0.0456 |

**Figure.5c.**Coefficients of Linear Discrimination (DVcs) – Population Stratification.

DVcs-Population StratificationP: LD1 explained 60.1%, LD2 23.1%, LD3 12%, and LD4 0.4% of the total variability (100%) associated with the first eigenvalue. In the predicted data, thirty-five observations (89.7%) were correctly classified in the first cluster, twenty (100%) in the second, fifty-five observations (83.2%) in the third, thirty observations (75%) in the fourth, and one hundred fifty-nine (91.3%) in the fifth. The model had a prediction accuracy of 85.43% (overall error of 14.57%). At 70%, the prediction accuracy was 88.12% (overall error of 11.88%). The main Ds identified (Fig. 5d) were: LD1, the sociopolitical WJP, which explains 53.95% of the data in cluster 4, characterized by tropical climates at elevations 1 and 3 with medium-intermediate population sizes (1AmMI, 3AmMM), and the MPI in cluster 3, arid and desert climates at elevations 1, 3, and 5 with intermediate, medium, and megacity population strata (1BskMM, 5BwkMM, 5BwkMI, 5BskMM, 5BshMM, 5BwhMM, 3BshMM, 3BwhMI, 1BwkMC). LD2 explained 25% of the data through the socioeconomic variable HDI in cluster 4, characterized by tropical climates at elevations 1 and 3 with an intermediate-to-medium population stratum (1AmMI, 3AmMM). LD3 explained 14% of the data using the socioeconomic-sociopolitical HDI-WJP in cluster 4, associated with tropical climates at elevations 1.3 and an intermediate-middle socioeconomic stratum (1AmMI, 3AmMM). LD4 explained 7% of the data using the HDI in cluster 4, characterized by tropical climates at elevations 1.3 with an intermediate-to-medium population stratum (1AmMI, 3AmMM). At 30%, eleven observations (91.6%) were correctly classified in the first cluster, six (100%) in the second, nineteen (90.47%) in the third, eight observations (66.6%) in the fourth, and fifty-two observations (94.54%) in the fifth. The model had a probability of correct classification of 90.57% (overall error of 9.43%). The analyzed group and the D values were:

*(Group 4: T + UHI + P + H + Ai + UA + Pd + UG + Pob + Cf + CO2U + PM25 + PM10 + E + GDP + Ec + **HDI** + GINI + Di + **MPI** + CRI + WR + **WJP**, data = EDT).*

**d)**

## Coefficients of linear discriminants:

| | LD1 | LD2 | LD3 | LD4 |
|---|---|---|---|---|
| ## T | 9.825061e-02 | -5.980919e-02 | 6.065041e-02 | -5.561179e-02 |
| ## UHI | 2.552795e-01 | 1.567675e-01 | -3.198137e-01 | -1.192029e-01 |
| ## P | -5.944077e-04 | -1.155341e-04 | -1.003070e-03 | 2.487387e-03 |
| ## H | 9.861419e-04 | 3.760102e-02 | -5.139314e-02 | -5.404051e-03 |
| ## Ai | 1.630903e-02 | 2.997191e-03 | 1.876556e-03 | -8.736291e-02 |
| ## UA | 1.277564e-03 | -7.113342e-04 | -5.686717e-04 | 4.902985e-04 |
| ## Pd | -6.764504e-05 | -4.432701e-05 | -5.193006e-05 | 6.818490e-05 |
| ## UG | -2.869688e-01 | -1.984622e-01 | 2.853995e-01 | -8.599047e-02 |
| ## Pob | 1.497875e-07 | 3.092173e-08 | 2.517365e-07 | 3.971040e-07 |
| ## Cf | -1.938650e+00 | -1.939484e+00 | -5.535766e-03 | -1.419028e+00 |
| ## CO2U | -5.502999e-08 | 2.744848e-08 | -2.671824e-08 | 1.204599e-08 |
| ## PM25 | -2.239285e-02 | -2.640296e-02 | -3.888357e-02 | 1.712715e-02 |
| ## PM10 | 4.899685e-03 | 4.951951e-03 | 4.277051e-02 | -1.337017e-02 |
| ## E | 5.498675e-04 | 5.262279e-04 | 1.844643e-04 | 3.852822e-04 |
| ## GDP | -6.567096e-05 | -6.408081e-06 | -1.038503e-06 | 7.349103e-05 |
| ## PIB | 3.206638e-11 | -7.403884e-12 | -3.609347e-12 | -3.239431e-11 |
| ## HDI | -2.391473e+00 | **7.272044e+00** | **2.668520e+00** | **1.702363e+00** |
| ## GINI | -3.327577e-03 | -1.182164e-02 | -1.637774e-02 | 8.766614e-02 |
| ## DI | 4.015723e-01 | -7.359410e-01 | -1.092568e-01 | 1.999380e-01 |
| ## MPI | **3.216869e+01** | 1.567768e+01 | -3.494943e+00 | -6.700180e+01 |
| ## CRI | -7.492727e-04 | 3.937064e-03 | -4.204126e-03 | -9.618873e-03 |
| ## WR | -1.141543e-01 | -1.512331e-02 | 7.670284e-02 | -7.048551e-02 |
| ## WJP | **4.171974e+00** | 2.517836e+01 | **1.911230e+00** | -7.331396e+00 |

**## Proportion of trace:**

| ## LD1 | LD2 | LD3 | LD4 |
|---|---|---|---|
| ## 0.5395 | 0.2462 | 0.1424 | 0.0719 |

**Figure.5d.**.Coefficients of Linear discriminants DVcs-estratificación poblacionalP.

DVcs-Geographic Location: The results were: LD1 accounted for 68.34% and LD2 for 31.66% of the total variability (100%). In the predicted data, forty-three observations (46%) were correctly classified in the first cluster, forty-three observations (86%) in the second, and two hundred forty observations (96%) in the third. The model had a hit probability of 87.43% (overall error of 12.57%). At 70%, a hit probability of 86.94% was obtained (overall error of 13.06%). The main Ds in LD (Fig. 5e) were as follows: LD1 corresponded to the socio-political DI, which explains 66% of the data in cluster 1, characterized by arid, desert, and subtropical climates from ZI to ZTN (BskGCS-ZI, CwcGCS-ZI, CsbGCS-ZTS,

BwkGCS-ZTS, CwaGCS-ZTS, BwkGCS-ZI, BskGCS-ZTN,BwhGCS-ZTN,BwkGCS-ZTN). LD2 corresponded to MPI (33% of the data in cluster 3), in tropical, subtropical, temperate, and arid climates from ZI to ZTS (CfaGCS-ZTS, CfbGCS-ZTS, AsGCS-ZI, CfbGCS-ZI, AfGCS-ZI, AfGCS-ZTS, AwGCS-ZI, BshGCS-ZI, AmGCS-ZI and Cwa GCS-ZI). The WJP model explained 33% of the data (cluster 2) in temperate Mediterranean and arid-desert climates from ZTN to ZTS (CscGCS-ZTS, BwhGCS-ZI, BshGCS-ZTN, CwbGCS-ZI). In the first cluster, 30% of the data were correctly classified (33.3% of observations); in the second, 12% (80%); and in the third, 69% (92%). The model had a probability of correct classification of 81.91% (overall error of 18.09%). The analyzed group and the D values were as follows:

*(Group 5: T + UHI + P + H + Ai + UA + Pd + UG + Pob + CO2U + E + GDP + Ec + HDI + GINI + **DI** + **MPI** + WR + **WJP**, data = EDT).*

**e)**

## Coefficients of linear discriminants:

| | LD1 | LD2 |
|---|---|---|
| ## T | 3.249188e-02 | 1.440877e-0 |
| ## UHI | 1.651492e-01 | -5.818917e- |
| ## P | -3.115379e-04 | -5.254654e-0 |
| ## H | 5.670070e-02 | 2.110833e-0 |
| ## Ai | 2.185356e-02 | 1.926973e-0 |
| ## UA | 6.587021e-04 | 4.414466e- |
| ## Pd | -2.104734e-06 | 5.662389e- |
| ## UG | 6.896203e-02 | 7.492398e- |
| ## Pob | -1.842953e-07 | -4.011257e-07 |
| ## Cf | -3.817282e-01 | -1.886603e-01 |
| ## CO2U | 3.278228e-08 | 1.618322e-07 |
| ## E | -8.053558e-05 | -1.329463e-04 |
| ## GDP | -2.187200e-05 | 7.592688e-05 |
| ## Ec | -6.702968e-13 | -3.789834e-12 |
| ## HDI | -3.210427e+00 | 9.113197e-02 |
| ## GINI | 9.155145e-02 | -2.267800e-02 |
| ## **DI** | **6.536410e-01** | -8.003617e-01 |
| ## **MPI** | -2.784947e+01 | **1.201859e+00** |
| ## WR | 1.357036e-01 | -5.686446e-02 |
| ## **WJP** | -1.398587e+01 | **1.005793e+01** |

## **Proportion of trace:**

| | LD1 | LD2 |
|---|---|---|
| ## | **0.66** | **0.33** |

**Figure 5e.** Coefficients of Linear discriminants DVcs- Geographic Location.

VDsc- Geographic LocationP: LD1 explained 65.14% of the total variability, and LD2 explained 34.86% (100%). In the predicted data, 176 observations (88%) were correctly classified in the first cluster, 59 observations (59.78%) in the second, and 60 observations (80%) in the third. The model has a probability of correct classification of 84.29% (overall error of 15.71%). At the 70% threshold, a hit probability of 86.94% was obtained (overall error of 15.57%). The Ds (Fig. 5f) were: LD1, based on urban-bioclimatic (UHI), socioeconomic (Cf), and sociopolitical (MPI and WJP) indicators, accounting for 66% of the data. In cluster 1, the Ds were UHI-MPI in arid, semi-arid, and temperate climates at elevations 1, 3, and 5 from ZTN-ZTS (3BwkGCSZTS, 1BshGCSZI, 1BSkGCSZTN, 5BwkGTN, 5BwkGZI, 3BshGCSZI, 3BwhGCSZTN, 1CsbGCSZTS, 3scGCSZTS, 1CfbGCSZTS, 3CwaGCS-ZTS). In cluster 2, Cf-WJP included tropical, subtropical, arid, and semi-arid climates at elevations 1, 3, 5, mainly in ZI (3AmGCSZI, 5CwcGCSZI,5CwbGCSZI,5BskGCSZI,5BsCSZI,5AsGCSZI,5CfbGCSZI,5AwGCSZI,1BshGCSZI,3AwGCSZI,5CwaGCS-ZI,1AmGCS-ZI,1AwGCSZI,and5BwhGCSZTN).LD2 corresponded the urban-bioclimatic UHI, which explained 33% of the data (cluster 1), associated with arid, semi-arid, dry temperate, and subtropical climates ranging from ZTN toZTS(3BwkGCSZTS,1BshGCSZI,1BSkGCSZTN,5BwkGCSZN,5BwkGCSZI,3BshGCSZI,3BwhGCSZTN,1CsbGCSZT, 3CscGCSZTS, 1CfbGCS-ZTS, and 3CwaGCS-ZTS). At 30%, fifty-three observations (83.3%) were correctly classified in the first cluster, sixteen (69.56%) in the second, and eighteen in the third. The model has a hit probability of 82.08% (overall error of 17.92%). The analyzed group and the Ds were as follows:

*(Group.6 ~ T + **UHI** + P + H + Ai + UA + Pd + UG + Pob + **Cf** + CO2U + PM25 + PM10 + E + GDP + Ec + HDI + GINI + DI + **MPI** + CRI + WR + **WJP**, data = EDT).*

**f)**

Coefficients of linear discriminants:

| | LD1 | LD2 |
|---|---|---|
| ## T | 2.458773e-01 | -1.575990e-02 |
| ## **UHI** | **2.944345e-01** | **2.42644** |
| ## P | -5.595659e-03 | -5.203170e-0 |
| ## H | 5.017177e-03 | 8.038625e-0 |
| ## AI | 2.350867e-01 | 6.602790e-0 |
| ## UA | 1.701694e-03 | -9.420953e- |
| ## Pd | 8.920549e-05 | 2.987594e- |
| ## UG | 1.088632e-01 | 1.711240e- |
| ## Pob | -2.609060e-07 | -1.604487e |
| ## **Cf** | **2.064441e+00** | -6.675510e- |
| ## CO2U | -2.134826e-08 | -4.56579 |
| ## PM25 | -4.208021e-02 | 2.513465e-02 |
| ## PM10 | 3.468920e-02 | -2.349374e-02 |
| ## E | -6.626427e-04 | 1.383731e-04 |
| ## GDP | -4.628690e-05 | -9.146982e-06 |
| ## Ec | 1.219103e-11 | 2.406801e-11 |
| ## HDI | -5.124125e+00 | -1.863713e+00 |
| ## GINI | -9.759080e-03 | 4.739755e-02 |
| ## DI | -4.968645e-02 | 5.773422e-01 |
| ## **MPI** | **1.552463e+01** | -2.866513e+01 |
| ## CRI | 4.389778e-03 | -1.441390e-03 |
| ## WR | -1.540690e-01 | 2.134234e-01 |
| ## **WJP** | **2.838096e+00** | -1.820523e+01 |

## **Proportion of trace:**

| | LD1 | LD2 |
|---|---|---|
| ## | 0.6702 | 0.3298 |

**Figure .5f.** Coefficients of Linear discriminants DVcs- Geographic LocationP

## *3.4. Classification errors and D in groups*

A key step was to verify compliance with the statistical assumptions of normality and equal variances. To this end, the Shapiro-Wilk test (normality) and Levene's test (equal variances) were applied. However, these statistical assumptions were not met, a situation that frequently occurs when there is no experimental control over the indicators being analyzed. To address this limitation, the Central Limit Theorem (CLT) was applied, which states that as the sample size increases (in this case, 350 observations), the probability distribution of the test statistic tends to approximate a normal distribution. This criterion allows for the approximation of multiple commonly used distributions, such as the binomial, Poisson, chi-square, Student's t, and gamma distributions, among others, when their parameters increase and the analytical calculation becomes more complex (Devore, 2001). Overall analyses revealed varying classification errors across the groups (Tables 2,3). The most reliable results are DVsc-Climate Zone (5.56%) and DVsc-Population Stratification

(8.49%), and the least reliable are DVsc-Geographic Location (18.9%), DVsc-Geographic LocationP (17.92%), and DVsc-Population StratificationP (9.4%).The generally recognized features were sociopolitical (MPI, WJP, DI) and socioeconomic (HDI,Cf). In other cases, the Köppen-Geiger bioclimatic patterns (T,H,P) did not constitute features within the clusters. In (DVsc-Climate Zone, lowest classification error), 87% of the data (cluster 2) corresponds to human development and the rule of law (HDI and WJP) in tropical, subtropical, temperate, and arid environments. In DVsc-Climate Zone, the Koppen-Geiger similarity percentage (61%) contributed to the lower classification error; however, this degree of similarity was not sufficient for the bioclimatic patterns to be classified as *D*, nor was the climate-related socio-political index (CRI). This finding regarding the CRI differs from studies, reports, and maps (United Nations, 2016; Germanwatch,2021) that link heterogeneity, population density, poverty, and inequality in metropolitan areas to climate change risks and to urban vulnerability in hotspots across the Caribbean and Central America. However, it is advisable to continue monitoring the CRI, given global changes in vulnerable geographies (Pugh et al., 2016) and the differential susceptibility of certain regions (world) to variations in precipitation (Giorgi, 2006).

In DVsc-Population Stratification, Cf, as a critical indicator (IPCC, 2021), explained a significant percentage of the data (65%) but was associated with cluster 5 (tropical and subtropical climates with medium-to-large population strata, temperate climates with medium-to-large strata, and hot arid climates with intermediate strata). Other socioeconomic and sociopolitical variables, such as human development, rule of law, and multidimensional poverty (HDI-MPI-WJP), contributed only 19% of the information in cluster 4, in tropical and temperate climates with medium-to-large populations (AmMI and CwcMM). In this regard, the influence of the MPI is unprecedented, as it not only affects the quality of life of the regional metropolitan population but also influences the climatic and socio-environmental dynamics of tropical monsoon metropolises (AmMI), such as Managua (high temperatures 27–28 °C), and cold subtropical metropolises at high altitudes (3,600 meters above sea level, such as La Paz (Cwc). In another case, DVsc-GeographicLocationP, 67% of the data (clusters 1 and 2) identified urban-bioclimatic, socioeconomic, and sociopolitical factors associated with UHI, Cf, MPI, and WJP. The results (Table 3) show that UHI is strongly related to WJP and MPI in arid, desert, subtropical, tropical, and temperate environments at elevations 1, 3, and 5, from ZTN to ZTS. This result is expected regarding the relationship between UHI and Cf; however, the influence of WJP on heat islands is unprecedented, as previous studies mainly associate UHI with social vulnerability (Klein-Rosenthal et al., 2014; Harlan et al., 2007). Nevertheless, this result should be interpreted as a relative approximation of reality, due to the high classification error (17.92%) of DVsc-GeographicLocationP.

.

**Table.2.** DVcs, LD, Classification error and climatic similarity.

| VDsc | LD *D* | E (%) | S (%) |
|---|---|---|---|
| VDcs Climate Zone | LD1 (87%) (IDH-WJP) | **5.66** | **61** |
| VDcs Climate Zone P | LD1 (64%) (HDI)<br>LD2 (36%) (IPM) | 19.81 | 51.5 |
| VDcs - Population stratification | LD1 (65%) (Cf)<br>LD2 (19%)(DIH,MPI,WJP)<br>LD3 (11%) (DI)<br>LD4 (5%) (DI-MPI) | **8.49** | **50.1** |
| VDcs - Population stratificationP | LD1 (54%) (MPI-WJP)<br>LD2 (25%) (HDI)<br>LD3 (14%) (HDI-WJP)<br>LD4 (7%) (HDI) | 9.43 | 46.7 |
| VDcs - Geographic Location | LD1 (67%) (DI)<br>LD2 (33%) (MPI-WJP) | 18.9 | 47.8 |
| VDcs - Geographic LocationP | LD1 (67%) (Cf-UHI-MPI-WJP) LD2 (33%) (UHI) | 17.92 | 50.1 |

(a) The VDcs with the lowest classification error are highlighted in gray**.** Where: ***D*.** discriminant **E**, Error, **S**: Similarity.

**Table 3.** Discriminants (D) in Koopen-Geiger clusters in the VDsc with the lowest classification error. (highlighted in gray).

| VDsc | FEATURES OF KOOPEN GEIGER GROUPS |
|---|---|
| VDcs Climate Zone (5.66%) LD1 (87%) (HDI-WJP) | **A 61% climate similarity** across temperate, arid, semi-arid, tropical, and subtropical climates. The D-scores for human development and the rule of law **characterize 87% of the metropolises.** |
| | Tropical and subtropical (Af, Cfa, As, Am, Aw, Cwa), temperate (Cfb, Cwc, Cwb), semi-arid (Bsh, Bsk). |
| VDcs - Population stratification (8.49%) LD1 (65%) (Cf) | **A 50.1% climate similarity** in tropical, subtropical, and arid climates across medium-to-intermediate population size and megacities. Socioeconomic indicators such as carbon (Hcpc) influence climate-socio-environmental dynamics **(62% of metropolises).** |
| | Tropical-subtropical(AfMM, AwMM, AmMM, AsMM, CwaMI,CwaMM,CfaMM)Temperate(CfbMM,CfbMG), Arid (BshMI). |
| LD2 (19/%) (MPI) | A small group comprising 3% of tropical and temperate regions, characterized by sociopolitical factors such as multidimensional poverty (MPI); however, this dimension accounts for only 19% of the data. |
| | Tropical (AmMI), Temperate (CwcMM). |
| LD2 (19/%) (HDI-WJP) | A diverse group (63%) tropical, subtropical, temperate, and semi-arid cities of medium, intermediate, and large size, characterized by D socioeconomic and sociopolitical (HDI,WJP). |
| | Tropical-subtropical (AfMM, AwMM, AmMM, AsMM, CwaMI, CwaMM, CfaMM), Temperate (CfbMM, CfbMG), Hot semi-arid (BshMI). |
| LD3 (11%) (DI) | A group comprising 63% of tropical, subtropical, temperate, and semi-arid metropolises characterized by the sociopolitical variable democracy (ID), which characterizes the same groups as LD2 (HDI-WJP), but with a share of only 11% of the data. |
| | Tropical-subtropical (AfMM, AwMM, AmMM, AsMM, CwaMI, CwaMM, CfaMM); Temperate (CfbMM, CfbMG); Hot semi-arid (BshMI). |

(a) The VDcs climate zone (5.66%) successfully groups climates with high similarity (61%) and thus allows for the formation of a more climatically homogeneous cluster (87% of metropolitan areas).

## 4. Conclusions

The Köppen-Geiger meteorological characteristics (T, P,H) did not constitute metropolitan districts in Latin America and the Caribbean (LAC) based on climatic similarity criteria. On the other hand, the carbon footprint indicator (Cf) was classified as D based on the population stratum and in linear combination with the ICU and the WJP. This result suggests that the carbon impact in metropolitan areas has a limited scope depending on the population's sociopolitical-climatic dynamics and due to hotspots affecting metropolitan environments with social segregation. In DVsc-PopulationStratification, it was verified that social gaps (MPI) are related to human development (HDI), democracy (DI), and the rule of law (WJP) in a small group (3%) of climates with extreme monsoon and cold subtropical temperatures or geographies (altitude).

The Köppen-Geiger similarity index (61%) in the DVsc Climate Zone, along with the lower classification error (5.66%), made it possible to reliably group 87% of regional metropolises based on socioeconomic and sociopolitical factors (HDI-WJP) into tropical, subtropical, and semi-arid climates. This finding implies that human development and the political rights of the population influence the climatic and socio-environmental morphology of regional metropolises (see Table 3). Furthermore, the Köppen-Geiger patterns present in this cluster (87%) do not alter the D status of the aforementioned urban socioeconomic and sociopolitical factors. In this regard, governance and socioeconomic conditions are better able to identify urban characteristics than meteorological indicators traditionally used in regional climate studies.

Finally, population density (Pd), metropolitan area size (UA), energy (E), and climate risk (CRI) did not emerge as significant factors in any of the multivariate analyses conducted. These results allow us to rule out these indicators, which are considered critical in the scientific literature (IPCC, 2021), but which do not provide sufficient evidence to characterize metropolitan groups under the methodological approach of climate similarity.

## References

Baumgartner, W. H. (2025). Gentrificación verde en América Latina. Universalidades, especificidades y particularidades en Brasil. Revista de Geografía Norte Grande, (93), 1-17. https://doi.org/10.4067/S0718-34022026000100110.

Beck, H., Zimmermann, N., McVicar, T.R., Vergopolan, N.,Berg,A., Wood,E.F.(2018). Present and future Köppen-Geiger climate classification maps at 1-km resolution. *Scientific Data*, (5), *180-214*. https://doi.org/10.1038/sdata2018.214.

Boccolini, S. M. (2025). Metrópolis más que urbanas: reconceptualizando los territorios de soporte de la vida urbana. Revista de Investigaciones Geográficas: una mirada desde el Sur, (69), 3-23. https://doi.org/10.5354/0719-5370.2025.76776.

Casadei, P., Semmartin, M. y Garbulsky, M.F. (2021). Análisis regional de las islas de calor urbano en la Argentina. *Ecología Austral*, *31*(1), 190–203. https://doi.org/10.25260/EA.21.31.1.0.970.

Comisión Económica Para La America Latina (CEPAL) (2017). Observatorio Demográfico de América Latina y el Caribe 2017: Tablas de mortalidad = Demographic Observatory of Latin America and the Caribbean 2017: Life tables. https://www.cepal.org/es/publicaciones/42361-observatorio-demografico-america-latina-caribe-2017-tablas-mortalidad.

Cox, W. (2025). *Demographia World Urban Areas: 2025 Edition*.Demographia/ChapmanUniversity.https://blogs.chapman.edu/wpcontent/uploads/sites/56/2025/06/Demographia-World-Urban-2025.pdf.

Devore, J. (2001). *Probabilidad y Estadística para Ingeniería y Ciencias.* Séptima edición. CengageLearning.https://intranetua.uantof.cl/facultades/csbasicas/matematicas/academicos/jreyes/DOCENCIA/APUNTES/APUNTES%20PDF/Probabilidad%20y%20Estadistica%20para%20Ingenieria%20y%20Ciencias%20%20Jay%20Devore%20%20Septima%20Edicion.pdf

Dobbs, C., Nitschke CR, y Kendal D. (2014). Global Drivers and Tradeoffs of Three Urban Vegetation Ecosystem Services. *PLoS ONE*, (9), 1-9. https://doi:10. 1371/journal.pone.0113000.

Economist Intelligence Unit (2019). *Democracy index 2019*: *A year of democratic setbacks and popular protest*.https://www.eiu.com/n/campaigns/democracy-index-2019/.

Economist Intelligence Unit. (2015). *Democracy index 2015: Democracy in an age of anxiety*.https://www.eiu.com/public/topical_report.aspx?campaignid=DemocracyIndex201

Germanwatch. (2021). *Global Climate Risk Index 2021: Who suffers most from extreme weather events? Climate-related loss events in 2019 and 2000 to 2019*.https://www.germanwatch.org/sites/default/files/Global%20Climate%20Risk%20Index%202021_2.pdf.

Giorgi F. 2006. Climate change hot-spots. Geophysical Research Letters, 33 (17), 1-4. https://doi.org/10.1029/2006GL025734.

González Á., Pacheco, C., Henao.,A., Monjardin, S.,, Plata, W., y Peña, J. (2025a). Identification of discriminating indicators and criteria for sustainability, resilience, and liveability in Latin American and. Revista Ciencia e Ingeniería. 46(1), 87102.https://www.researchgate.net/publication/391425684_Identification_of_discriminating_indicators_a

nd_criteria_forsustainability_resilience_and_liveability_in_Latin_American_and_Caribbean_metropolises.

González-Calderón, Á., Pacheco-Angulo, C., y Peña-Guillén, J. (2025b). Caracterización socio-ambiental y urbana de algunos emplazamientos metropolitanos de Latinoamérica y el Caribe mediante técnicas multivariantes, 2014-2018. *Revista Geográfica Venezolana*, 66(1), 106-131. https://doi.org/10.53766/RGV/2025.66.1.07.

Grimmond, C.S.B., Souch, C. (1994). Surface description for urban climate studies: A GIS based methodology. *Geocarto International* 1, (47), 59. https://doi.org/10.1080/10106049409354439

Harlan, S., Brazel, A.J.,Jenerette, G.D., Jones, N.S., Larsen, L, Prashad, L ., Stefanov, W.L. (2007). In the shade of affluence: the inequitable distribution of the urban heat island. *Equity and the Envir*onment, (15), 173–202. https://doi: 10.1016/S0196-1152(07)15005-5.

Henríquez, C., Mallea, C., Henríquez-Dole, L y Samaniego, H. (2017). Dispersión y Escalamiento Urbano en el Sistema de Ciudades Chileno Urban Sprawland Scaling in the Chilean Cities System. *Investig. Geogr*, (54),5-22.https://doi:10.5354/0719-5370.2017.48039.

Hiroito.,M., Rodrigues Pereira,M.M y Pereira de Freitas Neto, R. (2026). Machine Learning and Remote Sensing Applications in Urban Heat Island research: a bibliometric analysis. revista regeo, São José dos Pinhais,17,(2),124.https://doi.org/10.56238/revgeov17n2-098.

Intergovernmental Panel on Climate Change (IPCC) (2006). 2006 IPCC Guidelines for National Greenhouse Gas Inventories. Volume 2, Energy. https://www.ipccnggip.iges.or.jp/public/2006gl/pdf/2_Volume2/V2_1_Ch1_Introduction.pdf.

Intergovernmental Panel on Climate Change. (IPCC) (2021): Summary for PolicymakersTechnical Summary Frequently Asked Questions Glossary. Part of the Working Group I Contribution to the Sixth Assessment Report of the Intergovernmental Panel on ClimateChange.https://www.ipcc.ch/report/ar6/wg1/downloads/report/IPCC_AR6_WGI_SummaryVolume.pdf.

Klein-Rosenthal, J., Kinney, P. L., and Metzger, K. B. (2014). Intra-urban vulnerability to heat-related mortality in New York City, 1997-2006. *Health & Place*,(*30)*,4560.https://doi:10.1016/j.healthplace.2014.07.014.

Lauwaet, D., Hooyberghs, H., Maiheu, B., Lefebvre, W., Driesen, G., Van Looy, S., De Ridder, K., (2015). Detailed Urban Heat Island Projections for Cities Worldwide: Dynamical Downscaling CMIP5 Global Climate Models. Climate (3), 391–415. https://doi.org/doi: 10.3390/cli3020391.

Moran, D., Kanemoto, K., Jiborn, M., Wood, R., Tobben, J., & Seto, K. (2018). Carbon footprints of 13 000 cities. *Environ. Res. Lett*, (13), 06404, 1-10. https://doi.org/10.1088/1748-9326/aac72a.

Pacifici, M., Rama, F y de Castro Marins, K. (2019). Analysis of temperature variability within outdoor urban spaces at multiple scales. Urban Climate, (27), 90-104. https://doi.org/10.1016/j.uclim.2018.11.003.

Pugh, T., Muller C, Deryng, J.E.D., Folberth, C., Olin, S., Schmid, E., Arneth, A. (2016). Climate analogues suggest limited potential for intensification of production on current croplands under climate change. Nature Communications, (7), 1-8. https://doi.org/10.1038/ncomms12608.

R Core Team. (2023). *R: A language and environment for statistical computing* (Versión 4.3) [Software]. R Foundation for Statistical Computing. https://www.R-project.org/.

United Nations. 2016. Habitat iii regional report Latin America and the Caribbean.Sustainable Cities with Equality. Mexico. 978-92-1-133393-0, 978-92-1-1327595.https://unhabitat.org/sites/default/files/documents/2019-05/habitatiii-regional-report-lac.pdf.

United Nations (UN). (2023). Sustainable Development Goals Report. Special Edition. United Nations.https://unstats.un.org/sdgs/report/2023/TheSustainableDevelopmentGoalsReport2023_Spanish.pdf.

United Nations Development Programme (UNDP). (2018). Human Development Indicators and Indices: 2018StatisticalUpdateTeam.https://hdr.undp.org/system/files/documents/2018humandevelopmentstatisticalupdate.pdf.

United Nations Development Programme (UNDP). (2024). The 2023/2024 Human Development Report. Breaking the gridlock. Reimagining cooperation in a polarizedworld.https://hdr.undp.org/system/files/documents/global-reportdocument/hdr202324reporten.pdf.

United Nations Development Programme and Oxford Poverty and Human Development Initiative. (UNDP). (2023). Global multidimensional poverty index 2023. Unstacking global poverty: Data for high impactaction.https://hdr.undp.org/system/files/documents/hdp-document/2023mpireporten.pdf.

United Nations Habitat Organization (UN-Habitat).(2020). Global State of Metropolises. Population Data Booklet.https://unhabitat.org/globalstateofmetropolis2020%E2%80%93populationdatabooklet.

World Bank Group. (2021). Free and open access to global developmentdata.https://data.worldbank.org/country/latin-america-and-caribbean.

World Economic Forum (WEF) (2024). *The Global Risks Report2024*.19thEdition.https://www3.weforum.org/docs/WEF_The_Global_Risks_Report_2024.pdf.

World Health Organization (WHO) (2018). *Guías de calidad del aire relativas al material particulado*.: https://www3.paho.org/hq/index.php?option=com_to

pics&view=rdmore&cid=9833&Itemid=40799&lang=es.

World Justice Project. (WJP). (2021). Rule of Law Index. Current and Historical Data: https://worldjusticeproject.org/ourwork/research-and-data/wjp-rule-law-index2021/current-historical-data.

World Meteorological Organization (WMO) 2021. World Meteorological Information Service.https://worldweather.wmo.int/es/home.html.

Wu, X., Wang, G., Yao, R., Wang, L., Yu, D., Gui, X. (2019). Investigating Surface Urban Heat Islands in South America Based on MODIS Data from 2003–2016. *Remote Sens*, (11), 1212, 1-16. https://doi:10.3390/rs1110.

***Received:*** *april 30, 2026*

***Accepted:*** *july 10, 2026*

***González-Calderón, Álvaro***. *Architect. Master of Science in Renewable Natural Resource Management and Environment, CIDIAT-ULA. Dr. Candidate in Forestry and Environmental Sciences, University of The Andes.* ***https://orcid.org/0000-0002-1997-7351***

***Pacheco-Angulo, Carlos.*** *Forestry Engineer University of The Andes, Ph.D Geographic Information Technologies. Madrid,Spain.Email:pachecocar@gmail.com.* ***https://orcid.org/0000-0001-8724-9287***

***Peña-Guillen,Jesús.*** *Bachelor in Mathematics, PhD Statistics, Faculty of Economics and Administrative Sciences, University of The Andes.Venezuela.Email: penaguillenjesusalberto@gmail.com.* ***https://orcid.org/0000-0003-2942-7086***

***Bianchi, Guillermo.*** *Biologist, Master of Science in Applied Statistics, University of The Andes, Venezuela.Email: gbianchip@gmail.com.* ***https://orcid.org/0000-0002-8307-4472***

***Yarbuh, Ismael.*** *Master of Science in Renewable Natural Resource Management and Environment, CIDIAT-ULA. PhD in Earth Sciences (Geology), CICESE, Mexico. Postdoctoral Fellow, Mexican Center for Innovation in Geothermal Energy (CEMIEGEO-CICESE), Ensenada, Baja-California.E-mail:uyarbuh@uabc.edu.mx* ***https://orcid.org/0000-0002-7146-3841***

***González, Héctor.*** *Electrical Engineer, University of the Andes Venezuela Email:hectogonza@gmail.com* ***https://https://orcid.org/0009-0000-9098-6552***

***Apendix 1.*** Criteria for recoding Metropolis samples according to DVcs

| DVcs | CATEGORIZATION OF METROPOLIS | RECODING OF METROPOLIS |
|---|---|---|
| DVcs - Climate Zone | Köppen-Geiger regional climates<br>Af, Am, Aw, AsBsh, Bsk, Bwh, Bwk, Cfb, Cfa, Csc, Csb, Cwc, Cfa, Cwa: Cwb | Average elevation<br>(KGBsh, Bsk, Cwb), |
| DVcs - Population Stratification | Regional population ranges<br>500,000–999,000 (Intermediate Metropolises (MI))<br>>1 million–4,999,000 (medium-sized cities (MM))<br>>5,000 million–9,999,000 million (MG)<br>=>10 million inhabitants Megacities (MC) | Population segment<br>(BskMI, CscMM, BwkMG, AwMC) |
| DVcs Geographic Location | Regional geographical parallels<br>(ZTN) Arctic Circle (Latitude 66.33° N) – Tropic of Cancer (Latitude 23.5° N)<br>(ZI) Tropic of Cancer GCS (Latitude 23.5° N) – Tropic of Capricorn (Latitude -23.5°)<br>(ZTS) Capricorn-Capricorn Tropic GSC (Latitude -23.5) – Antarctic Circle (Latitude -66.33). | Geographic location<br>(CwaGCS (ZTN), AmGCS (ZI), BwhGCS (ZTS). |
| DVcs – Climate Zone P | Köppen-Geiger regional climates<br>Af, Am, Aw, AsBsh, Bsk, Bwh, Bwk, Cfb, Cfa, Csc, Csb, Cwc, Cfa, Cwa: Cwb | Climate - elevation discrimination (P)<br>Includes suffixes 1, 3, and 5 |
| DVcs - Population StratificationP | Regional population ranges<br>500,000–999,000 (Intermediate Metropolises (MI))<br>>1 million–4,999,000 (medium-sized cities (MM))<br>>5,000 million–9,999,000 million (MG)<br>=>10 million inhabitants Megacities (MC) | Population stratum—quota<br>Includes suffixes 1, 3, and 5 |
| DVcs - Geographic LocationP | Regional geographical parallels<br>(ZTN) Arctic Circle (Latitude 66.33° N) – Tropic of Cancer (Latitude 23.5° N)<br>(ZI) Tropic of Cancer GCS (Latitude 23.5° N)–Tropic of Capricorn (Latitude -23.5)<br>(ZTS) Capricorn-Capricorn Tropic GSC (Latitude -23.5) – Antarctic Circle (Latitude -66.33). | Geographic location, elevation (P)<br>Prefixes 1, 3, and 5 are included |

*Artículo de Investigación. Revista Ciencia e Ingeniería. Vol. 47, No. 3 pp. 307-316, agosto-noviembre, 2026.*
*ISSN 1316-7081. ISSN Elect. 2244-8780 Universidad de los Andes (ULA)*

# Hydrogeological simulation of the El Vigía aquifer for water supply purposes in the area between Brisas del Chama and Los Pozones. Mérida-Venezuela

# Simulación hidrogeológica del acuífero de El Vigía con fines de abastecimiento de agua en la zona comprendida entre Brisas del Chama y los Pozones. Mérida-Venezuela

**Bastidas, Naila[1]*; Matheus, María[1]; Mora, Luis[2]; Toro-Mora, Rosibeth [3,4]**
[1] Escuela de Ingeniería Geológica, Universidad de Los Andes, Mérida, Venezuela
[2] Centro Interamericano de Desarrollo e Investigación Ambiental y Territorial - Universidad de los Andes - Venezuela
[3] Grupo de Investigación TERRA. Universidad de Los Andes, Mérida, Venezuela
[4] Departamento de Geodinámica Interna, Universidad de Zaragoza, Zaragoza, España.
*alejaa.matheus23@gmail.com*

**Abstract**

*The semi-confined El Vigía aquifer, located in the Alberto Adriani municipality, Mérida state, has high potential and water quality to supply the city and nearby towns. However, the potable water supply is insufficient for the local population. This study conducted a hydrogeological simulation of the aquifer using the free Visual Bluebird software, based on an analytical elements model adapted to modern operating systems. A photogeological analysis and geological survey at a 1:50,000 scale identified Tertiary sedimentary formations, alluvium, and Quaternary terraces. A geological fault, assumed as a blind thrust, was detected, increasing hydraulic conductivity in its surroundings. Using the Thornthwaite water balance model, an annual recharge of 206.2 mm was estimated, equivalent to 11.26% of precipitation. The data obtained defined well protection perimeters and generated hydrogeological maps to propose exploiting a new well field northwest of the fault. Zones requiring special monitoring to prevent contamination were also identified to improve water resource management and preservation in the region.*

**Keywords:** semi-confined aquifer, analytical elements, hydrogeological simulation, water management, hydraulic conductivity.

**Resumen**

*El acuífero semiconfinado de El Vigía, ubicado en el municipio Alberto Adriani, estado Mérida, posee un alto potencial y calidad de agua para el abastecimiento de la ciudad y pueblos cercanos. Sin embargo, el suministro de agua potable es insuficiente para la población local. Este estudio realizó una simulación hidrogeológica del acuífero utilizando el software libre Visual Bluebird, basado en un modelo de elementos analíticos adaptados a sistemas operativos modernos. Se efectuó un análisis fotogeológico y un levantamiento geológico a escala 1:50.000, identificando formaciones sedimentarias Terciarias, Aluviones y Terrazas del Cuaternario. Se detectó una falla geológica, asumida como cabalgamiento ciego, que aumenta la conductividad hidráulica en su entorno. Mediante el modelo de balance hídrico Thornthwaite se estimó una recarga anual de 206,2 mm, equivalente al 11,26% de las precipitaciones. Con los datos obtenidos, se definieron perímetros de protección de pozos y se generaron mapas hidrogeológicos para proponer la explotación de un nuevo campo de pozos al noroeste de la falla. Asimismo, se identificaron zonas que requieren vigilancia especial para prevenir la contaminación, con el fin de mejorar la gestión y preservación del recurso hídrico en la región.*

**Palabras clave**: acuífero semiconfinado, elementos analíticos, simulación hidrogeológica, gestión del agua y conductividad hidráulica.

## 1 Introducción

In the city of El Vigía, located in the Alberto Adriani municipality of Mérida state (Figure 1), there are aquifer units that supply both the city and nearby towns. However, despite having this source, residents do not have an optimal drinking water service, as its extraction currently requires methods that involve high costs and make access to the resource difficult.

To address this issue and reinforce previous studies (Rivas, 2000; Terán, 2003; Contreras and Suárez, 2006; Jégat and Ramírez, 2008; Velázquez and Vivas, 2008; Briceño and Tovar, 2012; Peñaloza and Rojas, 2012; Pérez and Sánchez, 2014; Mora *et al*., 2018) that address this situation using various methodologies, we propose a hydrogeological simulation of the El Vigía aquifer between Brisas del Chama and Los Pozones using analytical element methods with Visual Bluebird 2.0 software, which seeks to generate models, maps, and well protection perimeters that allow for the identification of the most suitable areas for exploitation.

The specific proposal is to develop a new field of wells, with the aim of ensuring a more efficient supply and improving the quality of life of the community.

### *1.1 Regional geology*

The state of Mérida is crossed by a topographic-tectonic uplift known as the Cordillera de Mérida in a SW-NE direction, from the Táchira depression to the Barquisimeto depression, respectively. Within it lies the Sierra Nevada de Mérida, in the same direction, with a length of 320 km and an average width of 3 to 7 km. It is mainly formed by Upper Precambrian rocks (basement) belonging to the Sierra Nevada Association and, discordantly, Paleozoic to Mesozoic rocks (Tostós Association and formations such as Sabaneta and Palmarito) are found on top of them, with the presence of complex faults and folds (González *et al*., 1980).

The town of El Vigía is located in the Andean foothills; it sits on much younger sedimentary formations belonging to the Cenozoic era, mainly from the Miocene and Pliocene epochs, consisting of detrital material (clays, sandstones, and conglomerates) deposited in fluvial and alluvial environments (Figure 2A).

According to González *et al*., (1980), the study area is bounded to the north by the Maracaibo Lake depression and to the south by the Mérida Mountain Range, reflecting a geological evolution influenced by both tectonic provinces. Following the retreat of the Cretaceous seas and the emergence of a new continental shelf (Boesi *et al*., 1993), a compressive tectonic regime was established during the Palaeogene. This event, which predominated after the post-Palaeogene deformations, generated northward-trending thrusts and developed lateral ramp faults, shaping the current structural landscape of the Mérida mountain range. From the Neogene onwards, and particularly during the Miocene and Pliocene, successive Andean uplifts contributed to the emergence and maximum stacking of the Venezuelan Andes (Audemard and Audemard, 2002). Finally, in the Quaternary period, active and continuous tectonics favored the deposition of fluvial-alluvial sediments on the El Vigía plain, while episodes of compressional deformation continued to occur, which still influence the current dynamics of the relief and subsoil.

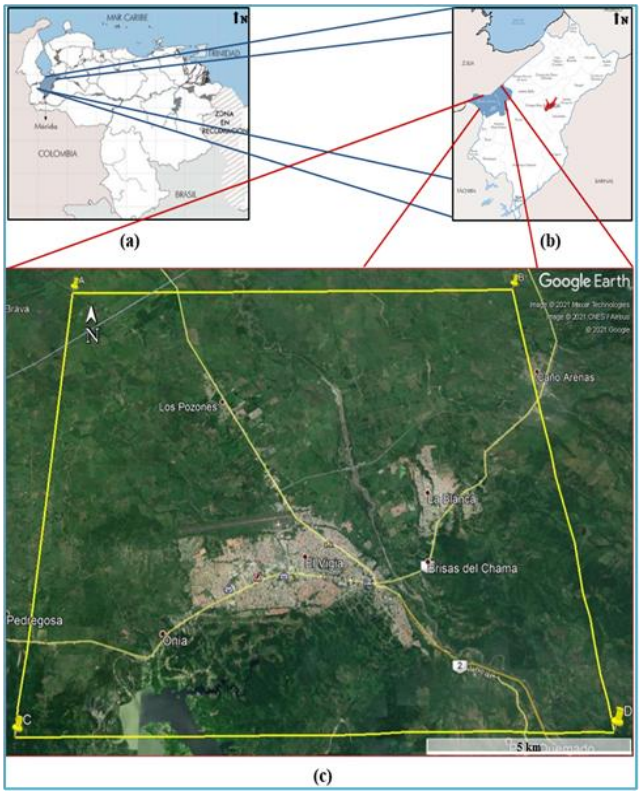


**Figure 1**. Relative location of the study area and, in the yellow box, its boundaries. The vertices that comprise it are defined below and expressed in UTM coordinates, DATUM WGS 84, zone 19N: A) 962100N, 200350E; B) 962100, 215120; C) 949050, 200350; and D) 949050, 200350.

### *1.2 Local geology*

From a lithostratigraphic and structural perspective, the El Vigía area is characterised by relatively simple geology, with approximately 75% of the surface covered by Quaternary deposits associated with alluvial plains and fluvial-alluvial terraces of the Chama and Onía rivers. The remaining 25% is made up of the Isnotú and Betijoque sedimentary formations (Figure 2A and 2B).

The Miocene Isnotú Formation is dominated by clays with intercalations of sandstones, coal and conglomerates,

while the Upper Miocene to Pliocene Betijoque Formation consists of massive conglomerates, siltstones, sandstones and clays. The Quaternary deposits, predominantly alluvial, are heterometric and poorly stratified, integrating rock fragments from the Precambrian to the Cretaceous, and are arranged in longitudinal and transverse systems, including terraces ranging in age from the Pleistocene to the Holocene, with thicknesses between 5 and 50 metres (Briceño and Tovar, 2012; Sutton, 1946, cited in LEV, 1997).


**A**

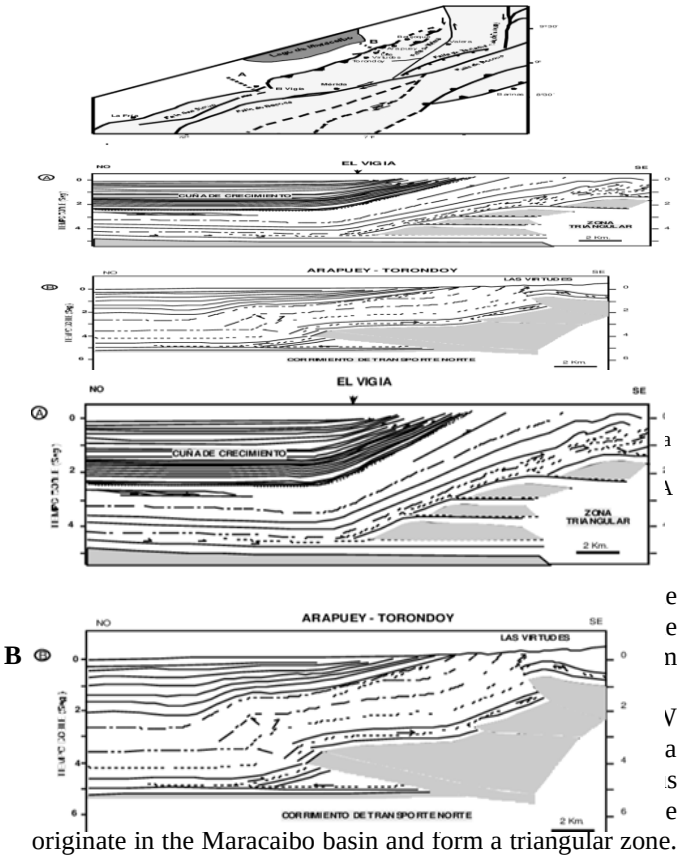


**B**

etijoque
ted along

global geodynamic perspective, north-western South America is a region of convergence and interaction between the South American, Caribbean, Nazca, Cocos and North America tectonic plates. Throughout geological time, the relative movements between these plates—including collisions, subduction, and lateral slippage—have shaped the evolution of the relief, the development of the Andes mountain range, and seismic activity in the region. In particular, the active subduction of the Nazca plate beneath the South American plate has produced episodes of orogenesis and mountain uplift from the Neogene to the present day, while interaction with the Caribbean plate introduces complex strike-slip movements and deformations in the Maracaibo Block. As a result, the area has been shaped by successive tectonic events that continue to generate deformation and seismicity processes, giving the region an active and multi-episodic structural dynamic.

The Norandino flank, according to its deformation characteristics, was divided by Audemard and Audemard (2002) into two sectors: the SW segment of El Vigía and the NE segment of Valera, as shown in Figure 3.

**B** **A**

originate in the Maracaibo basin and form a triangular zone. The Tertiary sedimentary sequence dips to the NW at high angles; the upper part of the sequence comprises the Upper Miocene and Pliocene-Pleistocene. The triangular zone is composed of four faults that have NW vergence (Figure 3A).

## 2 Methodology and results

The research adopted a systematic methodology divided into three main phases, beginning with i) information gathering (bibliographic, meteorological, hydrological, cartographic data and inventory of wells) and photogeological analysis, ii) collection of surface geological data, and finally, iii) processing of the data obtained in the previous stages, where aquifer recharge is estimated, Visual Bluebird 2.0 software is implemented, well protection perimeters are established, and 2D geological and hydrogeological models are generated.

### *2.1. Meteorological and hydrogeological inventory*

The meteorological information used in this study was obtained from the database of the former Ministry of Environment and Natural and Renewable Resources (MARNR), through the Directorate of Hydrology and Meteorology and the National Hydrological and Meteorological Information System (SINAIHME).

The data correspond to the El Vigía station (serial 3035), located at coordinates 08°36'27" N, 71°37'47" W and at an altitude of 130 m above sea level. Monthly averages of precipitation between 1945 and 2006, evaporation between 1955 and 1984, and average, maximum, and minimum temperatures between 1970 and 1984 were analyzed.

Analysis of the climate series revealed average precipitation of approximately 1830 mm/year (1945-2006) and average temperatures of 28°C (1970-1984), as well as reference evapotranspiration values of 1426 mm/year estimated using the FAO Penman-Monteith method and the evaporation tank.

For the well inventory, data from the field known as "Los Pozones" was used, originally compiled by INOS (1987) and subsequently referenced by Rivas (2019). This database includes detailed information on eight piezometers, including geographical coordinates, extraction flows, elevations, depths, diameters, and the static and dynamic levels of the wells. These data are essential for the proper hydraulic characterization of the aquifer and for the development of the analytical simulation model that allowed for the accurate assessment of the behavior and dynamics of the aquifer system.

Based on this data, it was determined that the effective porosity for this area is around 20%, while the hydraulic conductivity reaches values close to 10 m/day suggesting excellent conditions for groundwater flow and storage. The average thickness of the saturated zone of the aquifer is approximately 70 m, with a hydraulic gradient of 0.00448, an angle (θ) equal to 13° (Contreras and Suárez, 2006) and a base elevation of 7 m.

### *2.2. Photogeological analysis*

High-resolution satellite images obtained with SAS Planet software and Digital Elevation Models (DEM) from the ALOS satellite with PALSAR radar were used to detect topographic and geological changes using microwaves. The area was divided into two parts, taking the course of the Chama River as a reference line: i) the right slope (E) and ii) the left slope (W).

On the right slope (E), the geomorphology reveals a channel of the Mucujepe River with parallel drainage patterns that evolve from intertwined to meandering, supported by poorly consolidated sediments belonging to Cretaceous, Tertiary, and Quaternary deposits.

The active tectonic regime is evidenced by abrupt changes in the direction of drainage, consistent with the concave-convex topography of the area and possibly related to a blind reverse fault defined by Sieh *et al*. (1997).

On the left slope, the river network is dominated by the Onía River and its tributaries, which have dendritic and disordered patterns depending on the varied relief, with a significant presence of Quaternary sediments and sedimentary rocks.

The predominant vegetation is grassland and trees on both slopes, influenced by the characteristics of the sediments and topography (Figure 4).

Based on these images and Digital Elevation Models, a geological map of the study area was produced, using high resolution digital elevation models (DEM) from ALOSPALSAR as the topographic base and the Geological Map of the Azulita Region, Mérida State (Ministry of Mines and Hydrocarbons, 1975) and the F-3.C surface geology map (Creole Petroleum Corporation, 1956), both at a scale of 1:50,000. In addition to all the information obtained through photogeological analysis and in the field stage with the description of outcrops and observation of geomorphological and hydrogeological features (Figure 5).

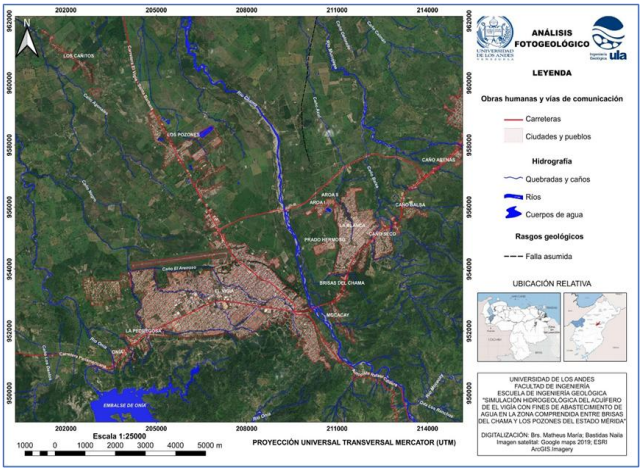


**Figure 4.** Photogeological analysis. Satellite image adapted from SAS Planet.

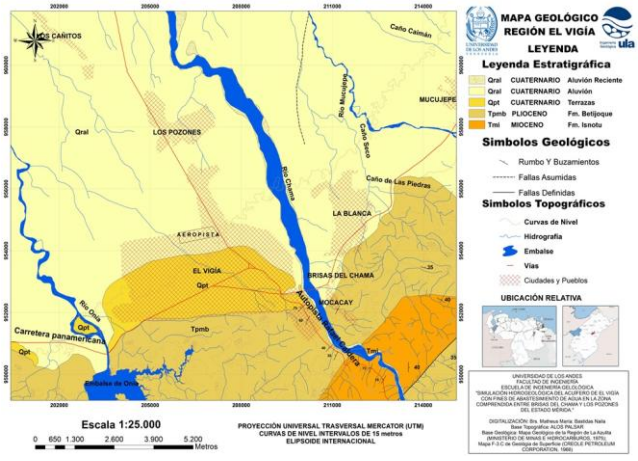


**Figure 5.** Geological map of the study area at 1:25000.

Geological section A-A' is located on the right bank of

the Chama River, oriented NW-SE (Figure 6). To the SE are the molassic formations of the Andean foothills or northern Andean front of the Andes mountain range (Isnotú and Betijoque formations) and to the NW is the Maracaibo basin plain, where the Betijoque Formation and unconsolidated Quaternary alluvial sediments outcrop. In this section, it can be seen that these molassic units (Isnotú and Betijoque) are deformed by previous orogenic episodes and by the current relative movements between the Caribbean and South American plates, generating structures with NW-SE vergence, such as the dextral Mocacay fault with a vertical component to the SE, where the Isnotú Formation rides over the Betijoque Formation, and to the NW, on the Maracaibo Lake plain, a prograding deformation that migrates towards the foreland basin, interpreted as a blind thrust or blind fault (Figura 6).

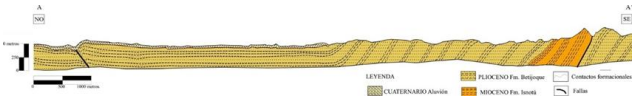


Considering the characteristics observed in the geological section with regard to the lithology and geological structures present, it can be highlighted, in terms of hydrogeological behavior, that most of the study area consists of unconsolidated sediments (gravel, sand, silt, and clay), which have high hydraulic conductivity and porosity, favoring the accumulation of large volumes of groundwater.

With regard to the geological fault located on the right bank of the Chama River, reference can be made to Távara and Sanz (2010), who state that a geological fault acts as an impermeable barrier on one side due to its movement and jump when encountering impermeable sediments, but, on the other hand, it constitutes an escape route for water, forcing the aquifer flow to ascend through it. With regard to the behavior of hydraulic conductivity in fault zones, Mook *et al*. (2001) indicate that in unconsolidated aquifers, hydraulic conductivity and porosity generally decrease with increasing depth. It has been statistically demonstrated that hydraulic conductivity in areas near or within faults also decreases with depth, remaining high up to 1000 m. This general and continuous decrease with depth is caused by mechanical factors related to the terrain and rock. Therefore, groundwater recharge is not distributed evenly throughout the aquifer but is concentrated in layers of high hydraulic conductivity near the surface.

*2.3.* Balance hídrico y recarga del acuífero

A monthly water balance model was implemented using the USGS graphical interface (2010), which facilitates parameter editing and estimates key hydrological components for specific sites, although it underestimates potential evapotranspiration (ETp) in arid areas and overestimates it in humid areas. Local parameters such as latitude (8° decimals from SINAIHME) and soil retention capacity (100 mm) were calibrated using historical precipitation (1945-2006) and average temperature (1970-1984) from the El Vigía station, generating outputs such as runoff (50% of the surplus) and infiltration (50%) as summarised in Table 1.

It should be noted that part of the water that infiltrates remains in the subsurface layers of the soil or is returned to the surface, so it is estimated that only half of the in-filtrated water (25% surplus) achieves deep percolation, thus recharging the aquifer.

Reference evapotranspiration (ETo) was calculated using the ETo Calculator (Penman-Monteith FAO equation) and compared with the Class A tank method (FAO-56); for the ETo Calculator, monthly data from SINAIHME (temperatures, moderate wind U2=2 m/s, Rs=0.16, subhumid psychrometric) were used to obtain values in mm/day, while the evaporimeter tank used data from 1955-1986 with Kp=0.85 (irrigated crops, RH=74.91%), but it overestimates ETo and lacks recent measurements in Venezuela, so ETo Calculator was prioritized due to its physical robustness. Finally, crop evapotranspiration (ETc) was estimated by Kc × ETo, with Kc-NDVI from Mutiibwa and Irmak (2013) and Cuesta *et al*. (2005) using LANDSAT-8 (30 m, 6 polygons ~3000 ha via Agro Dashboard); average NDVI showed perennial vegetation, resulting in ETc=1334.47 mm/year (average stage, perennial crops), validating the approach for agricultural monitoring and droughts.

**Table 1.** Average inflow and outflow values from the Thornthwaite monthly water balance model for the period 1945-2006

| | E | F | M | A | My | Jn | Jl | A | S | O | N | D | Anual |
|---|---|---|---|---|---|---|---|---|---|---|---|---|---|
| P prom (mm) | 129,1 | 123,1 | 138 | 233 | 168,2 | 104,3 | 93,9 | 100,4 | 111,8 | 199,5 | 235,9 | 193 | 1830,2 |
| T med prom (° C) | 26,6 | 27,1 | 27,8 | 27,8 | 28,5 | 28,9 | 28,1 | 28,8 | 28,5 | 27,9 | 27,6 | 26,9 | 27,875 |
| ETP | 104 | 99,6 | 119,3 | 119,8 | 133,3 | 134,2 | 131 | 133,3 | 122,1 | 117,2 | 107,8 | 105,1 | 1426,7 |
| Humedad del suelo | 100 | 100 | 100 | 100 | 100 | 64,9 | 37,8 | 23,4 | 19,7 | 92,1 | 100 | 100 | 937,9 |
| ETR | 104 | 99,6 | 119,3 | 119,8 | 133,3 | 134,2 | 116,3 | 109,7 | 109,9 | 117,2 | 107,8 | 105,1 | 1376,2 |
| Excedente | 68,6 | 17,3 | 11,8 | 101,5 | 26,5 | 0 | 0 | 0 | 0 | 0 | 108,4 | 78,3 | 412,4 |
| Escorrentía | 34,3 | 8,65 | 5,9 | 50,75 | 13,25 | 0 | 0 | 0 | 0 | 0 | 54,2 | 39,15 | 206,2 |
| Infiltración | 34,3 | 8,65 | 5,9 | 50,75 | 13,25 | 0 | 0 | 0 | 0 | 0 | 54,2 | 39,15 | 206,2 |
| Percolación | 17,15 | 4,325 | 2,95 | 25,375 | 6,625 | 0 | 0 | 0 | 0 | 0 | 27,1 | 19,575 | 103,1 |

*2.4. Hydrogeological modelling and 2D simulation*

The two-dimensional hydrogeological modelling of the El Vigía aquifer (Figure 7) was constructed in Visual Bluebird 2.0, integrating data on porosity, hydraulic conductivity (k=10 m/day), transmissivity, existing wells (5 and 9 in Los Pozones), geological-structural analysis and recharge, with overlapping elements such as the Onía, Mucujepe and Chama (main drainage), a large recharge area and heterogeneities.

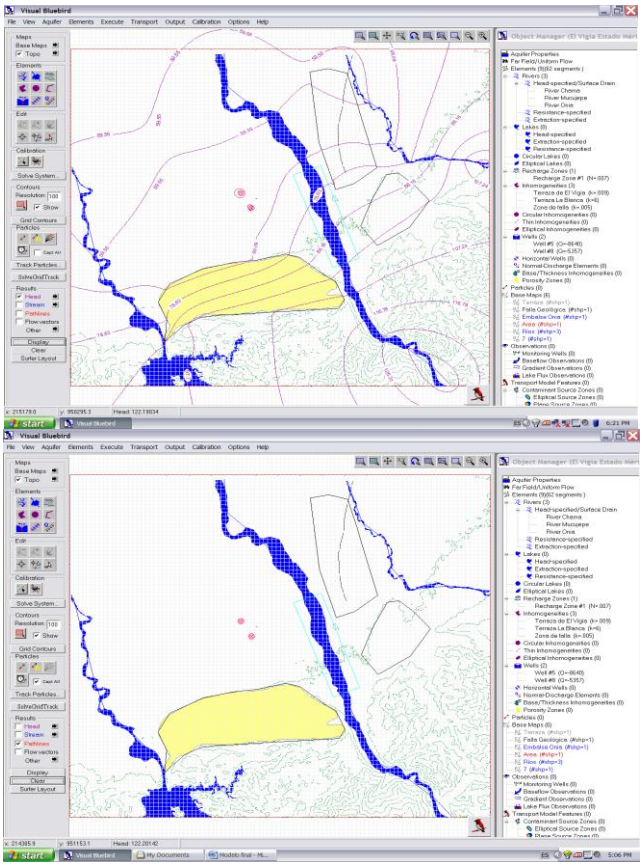

**Figure 7**. Two-dimensional hydrogeological model of the El Vigía aquifer. Image taken from the software.

The contour lines show low conductivities in urban terraces (El Vigía, La Blanca) and high conductivities towards the northeast due to a reverse fault (NE-SW blind thrust), which acts as an impermeable barrier and flow rise conduit (Figure 8), enhancing water tables suitable for artisanal exploitation but vulnerable to industrial depletion.

The semi-confined aquifer has a preferential SE-NW flow from the foothills (piezometric 150-300 m) towards the alluvial plain, with alluvial-fluvial fan lithology (Terán, 2003; Contreras and Suárez, 2006; Mora, 2018; Rivas, 2019) dominated by gravel, sand, silt, and heterometric clays; in fault zones, permeability decreases with depth due to mechanical compaction (Mook, 2001), concentrating surface recharge in permeable layers and delimiting zones of high/low conductivity influenced by the northwest fault.

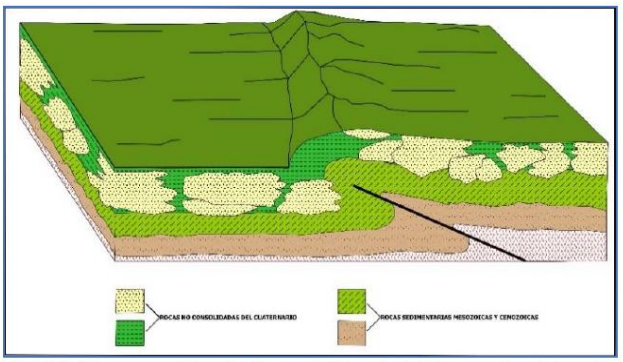


**Figure 8.** Idealized schematic model of the assumed fault area of the El Vigía aquifer.

## *2.5. Well-protected area and perimeters*

One of the methods used to protect the groundwater that makes up the El Vigía aquifer consists of establishing "well protection perimeters," which have been used in various countries through the development of programmes to protect groundwater from anthropogenic contamination, including countries in the European Economic Community, the United States, Eastern Europe, the former USSR, Spain, etc. a method that was proposed to address this problem several decades ago, according to Baró *et al*. (2008).

Considering that in our country there is no regulation for well protection perimeters, we made use of the legislation established in various countries such as Spain, with the development of analytical methods to delimit this zoning.

Mora (2018) states that the literature recommends setting immediate protection perimeters of 30 days to act in the event of a nearby contaminating event, 50 days to mitigate the effects of bacterial contamination, 1-year perimeters to regulate hazardous activities, and 5 to 10 years to regulate risky activities, which is common in most legislation worldwide.

The delimitation of protection perimeters was carried out with the help of Visual Bluebird 2.0 software using particles that can be tracked for a specific period of time to delineate capture zones and estimate important areas for aquifer protection.

In fact, a simulation of 20 particles was carried out at the different recommended time intervals: 30 days, 50 days, 1 year, 5 years, 10 years, and 20 years. Figure 9 shows the set of perimeters obtained based on the aforementioned travel time criteria.

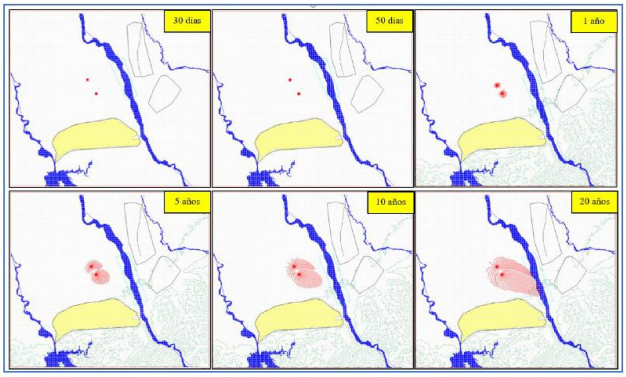


**Figure 9.** Simulation of 20 particles at different time intervals.

Figure 10 shows the delimitation of the protection perimeters of wells, where the Chama River recharges their catchment area, and indicates that this area should be defined to grant it special surveillance against aquifer contamination due to the presence of existing communication routes, which make this area highly vulnerable to the risk of contamination that could alter the quality of usable groundwater. Based on the above, it is necessary to implement surveillance of these sectors within the Local Urban Development Plan (PDUL) for land use planning and environmental protection.

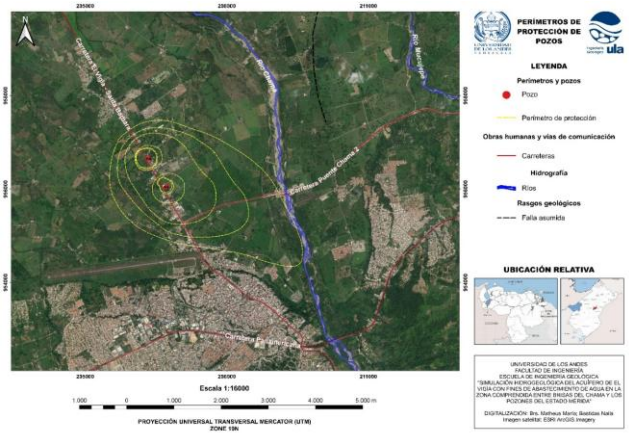


**Figure 10.** Delimitation of the area and protection perimeters of wells in the study area.

A new field of wells was proposed to supply water to areas far from urban settlements and main transport routes, minimising the risk of contamination from accidental spills from heavy vehicles. This area has excellent hydrogeological properties (high hydraulic conductivity, porosity, transmissivity and permeable thicknesses), according to Rivas (2000), favoring the use of the aquifer.

Surface runoff was estimated using the SCS method (number of curve), considering soil cover and antecedent moisture, where greater vegetation density improves infiltration and reduces runoff (Duque and Mora, 2020), although urbanized areas, roads and slopes limit it the selected site (Figure 11) integrates protection perimeters for 5-, 10- and 20-year horizons.

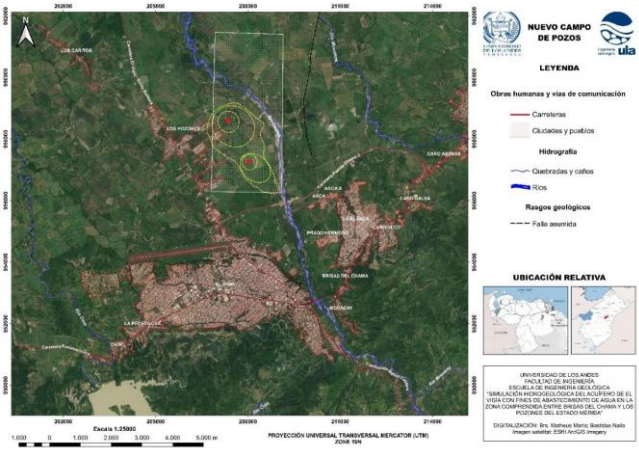


**Figure 11.** Delimitation of area and perimeters of protection of wells in study.

## 5 Conclusion

Using Visual Bluebird 2.0 software, a 2D model was created consisting of hydrogeological elements Bastidas *et al*. Science and Engineering Journal. Vol. 44, No. 1, December – March 2023 that condition the exploitation of groundwater present in the El Vigía aquifer and used them to interpret the values of the hydrogeological parameters associated with it, taking into account the calculated values of the water balance.

Likewise, this software was used to map the protection perimeters of wells, noting that the Chama River recharges the catchment area of the wells and that this area should be defined to provide special surveillance against contamination of the aquifer due to the presence of the El Vigía-Santa Bárbara del Zulia road and the new bridge over the Chama River that connects El Vigía with San Rafael de Mucujepe. Considering the threat posed by heavy goods vehicles that are accidentally exposed to spilling contaminants, this area is highly vulnerable to contamination risks that could alter the quality of the groundwater. All this is aimed at generating geological and hydrogeological models and maps as databases for the area that can be used to properly manage water resources, benefiting the population.

Based on the above data, the exploitation of a new field of wells to the northwest of the assumed geological fault is proposed, considering the conditions of the surface of the terrain and the infiltration capacity, which increases when the vegetation cover is dense. In addition to this, previous studies demonstrate the existence of very favourable values in terms

of the hydrogeological properties of the soil (hydraulic conductivity, porosity, transmissivity) and excellent thicknesses of permeable rock for exploiting the potential of the aquifer in this region.

**Referencias**

Audemard, F. E., & Audemard, F. A. (2002). Structure of the Mérida Andes, Venezuela: Relations with the South America-Caribbean geodynamic interaction. *Tectonophysics, 345*, 299-327. https://doi.org/10.1016/S0040-1951(01)00218-9

Baró, J., Expósito, J., & Esteller, M. (2008). Payment for water environmental services for the implementation of protection perimeters for water sources intended for human consumption. *Ciencia Ergo Sum, 15*(3), 311-316.

Boesi, H., Lorente, M., Mompart, L., Murat, B., Testamarck, J., & Facon, R. (1993). Facies and sedimentary environments of the Cretaceous La Luna Formation in San Pedro del Río section, Venezuelan Andes: A multidisciplinary study. Proceedings of the *International Congress of the American Association of Petroleum Geologists (AAPG)*, Caracas. https://www.osti.gov/biblio/6064898

Briceño, V., & Tovar, Y. (2012). *Hydrogeophysical characterization of the eastern sector of the city of El Vigía, Alberto Adriani municipality, Mérida state* [Degree thesis, University of the Andes, Mérida]. https://doi.org/10.15304/rr.id8568

Contreras, J., & Suárez, B. (2006). *Estimation of the recharge of the aquifer of the Chama River floodplain located in the city of El Vigía, Alberto Adriani municipality of Mérida state* [Thesis, University of the Andes, "Rafael Rangel" University Centre, Trujillo].

Creole Petroleum Corporation. (1956). *F-3-C surface geology map* [Map, scale 1:50,000].

Cuesta, A., Montoro, A., Jochum, A., López, P., & Calera, A. (2005). Metodología operativa para la obtención del coeficiente de cultivo desde imágenes de satélite. *ITEA, 101*(3), 212-224. https://www.aida-itea.org/aida-itea/files/itea/revistas/2005/101-3/ITEA_101-3_212-224.pdf

Duque, R., & Mora, L. (2020). *Precipitation-runoff relationship class* [Teaching material, CIDIAT-ULA, Mérida, Venezuela]. https://doi.org/10.5772/2728

González, C., Iturralde, J., & Picard, X. (1980). *Geology of Venezuela and its oil basins* (Vols. I-II). Caracas: Ediciones FONINVES. https://cir.nii.ac.jp/crid/1570854174936078464

Guerrero, O. (2019). *Geology of the Venezuelan northern Andean flank: Geomorphological features* [University of the Andes, "TERRA" Research Group, Mérida]. https://www.researchgate.net/publication/331983619

Jégat, H., & Ramírez, G. (2008). *Assessment of groundwater availability between the El Vigía area (Mérida state) and the northern part of Táchira state* [Degree thesis, University of the Andes, Mérida]. https://www.researchgate.net/profile/Herve-Jegat

Ministry of Energy and Mines. (1997). *Stratigraphic lexicon of Venezuela* (3rd ed., Public. Esp. 12). *Geology Bulletin*.

Mook, W., Gat, J., Rozanski, K., Stichler, W., Geyh, M., Seiler, K., & Yurtsever, Y. (2001). *Environmental isotopes in the hydrological cycle: Principles and applications* [IHP-V Technical Documents in Hydrology]. UNESCO-IAEA, Paris. https://www.hydrology.nl/images/docs/ihp/Mook_I.pdf

Mora, L. (2018). *Contributions to the study of aquifer contamination by hydrocarbon derivatives* [Doctoral thesis, University of the Andes, Mérida].

Mora, L., Suárez, B., Contreras, J., Jégat, H., & Mejías, J. (2018). Estimation of recharge using a model based on analytical elements. El Vigía Aquifer, Venezuela. *Advances and challenges in science and engineering*, 677-684.

Mutiibwa, D., & Irmak, S. (2013). AVHRR-NDVI-based crop coefficients for analysing long-term trends in evapotranspiration in relation to changing climate in the U.S. High Plains. *Water Resources Research, 49*(1), 231-244. https://doi.org/10.1029/2012WR012591

Peñaloza, W., & Perdomo, M. (2005). *Morpho-structural evolution of the Mesa Bolívar landslide in the Chiguará area of Mérida State* [Degree thesis, University of the Andes, Mérida]. https://www.researchgate.net/publication/44717899

Pérez, N., & Sánchez, C. (2014). *Hydrogeological study for the establishment of a field of wells to be exploited by Aguas de Mérida C.A., in the area between the sectors of Aroa II Prado Hermoso de El Vigía, Alberto Adriani municipality, Mérida state* [Thesis, University of the Andes, Mérida].

Rivas, M. (2000). *Study of groundwater reserves in the El Vigía area, Mérida state* [Thesis, University of the Andes, Mérida]. http://bdigital.ula.ve/storage/pdftesis/pregrado/tde_arquivos/10/TDE-2013-03-14T11:35:11Z-1920/Publico/rivasmarisela_parte1.pdf

Rivas, W. (2019). *Planning strategies for the sustainable use of groundwater in the El Vigía aquifer. Case study: Aguas de Mérida C.A. well field* [Master's thesis, CIDIAT-ULA, Mérida].

Távara, L., & Sanz, E. (2010). Hydrogeology and hydrodynamics of the Gormaz springs aquifer and its importance in the base flow of the Duero River, Spain. *Water Technology and Sciences, 1*(3), 5-20. https://www.scielo.org.mx/scielo.php?pid=S2007-24222010000300001&script=sci_abstract&tlng=en

Terán, P. (2003). *Determination of well protection perimeters in some drinking water wells in the municipality of Alberto Adriani, Mérida state* [Degree thesis, University of the Andes, Mérida].

USGS. (2010). *Thornthwaite Monthly Water Balance Model* [Software, version 1.1.0]. https://www.usgs.gov/software/thornthwaite-monthly-water-balance-model

Velázquez, H., & Vivas, Y. (2008). *Evaluation of groundwater reserves in the southern part of Lake Maracaibo, between the Torondoy and Chama rivers, specifically between the Caja Seca and El Vigía sectors* [Thesis, University of the Andes, Mérida]. https://doi.org/10.1016/j.jconrel.2023.05.042

***Received:*** *December 13th, 2025*

***Accepted:*** *February 1st, 2026*

***Bastidas, Naila****: Geological Engineer from the Faculty of Engineering at the University of the Andes ULA-Mérida*
*https://orcid.org/0009-0005-0848-3814*

***Matheus, María Alejandra:*** *Geological Engineer, Faculty of Engineering, University of the Andes (ULA), Mérida. Email: alejaa.matheus23@gmail.com*
*https://orcid.org/0009-0002-2642-8833*

***Mora-Mora, Luis:*** *Civil Engineer, Lisandro Alvarado Central Western University Doctor of Applied Sciences (Faculty of Engineering), University of Los Andes, Facultad de Ingeniería. Profesor Titular (CIDIAT).*
*Email: luismora@ula.ve*
*https://orcid.org/0000-0002-3499-4520*

***Toro-Mora, Rosibeth:*** *Specialist in Water Supply, Collection and Treatment Management (CIDIAT-ULA) and PhD in Geological Sciences (Zaragoza, Spain). Professor in the field of field geology and collaborator in Hydrogeology and Geophysics at the School of Geological Engineering at ULA-Mérida.*
*Email:* rosibeth@ula.ve
https://orcid.org/ 000-0002-0000-0002-9428-8716

*Artículo de Investigación. Revista Ciencia e Ingeniería. Vol. 47, No. 3 pp. 317-326, agosto-noviembre, 2026.*
*ISSN 1316-7081. ISSN Civil. 2244-8780 Universidad de los Andes (ULA)*

# Similitudes y semejanzas para un modelo físico del rio Chama Mérida Venezuela

# Similarity and resemblance for a Chama River physical model at Merida, Venezuela

**Aldana[1] Villasmil, Gerardo José; González[2], Marzia; Medina[3], Jesús**
[1] La Universidad del Zulia Facultad de Ingeniería Centro de Investigaciones del Agua, Maracaibo, Zulia VE.
[2] La Universidad del Zulia Facultad de Humanidades y Educación Departamento de Química, Maracaibo VE
[3]Universidad Nacional Experimental Rafael María Baralt Programa Ingeniería y Tecnología, C. Ojeda, Zulia VE
**gerardoaldavilla7@gmail.com**

**Resumen**

*La tormenta Bret que afecto a los estados Zulia, Trujillo, Mérida (1988) y Táchira en 1985, vuelve hacer su impacto en junio 2025, pero esta vez débil en el estado Zulia. El estado Mérida fue impactado con un evento hidrológico de Avenida en el rio Chama en el páramo a 3600 msnm desbordando su cauce y cubriendo el área del lecho original en 7 puntos: Apartaderos, Cruz de Mucuruba, Escaguey, Tabay, El Arenal (Don Perucho), Cafetal y Las González. El caudal se incrementó desde 400 $m^3/s$ hasta 2700 $m^3/s$ (6 veces). Cada punto tiene sus propias características en relación con las dimensiones, rugosidad, geología, fricción en las paredes rectangulares y en el lecho. Se tomo un volumen de control coordenadas N 8° 38'39", O 70° 58'00" en la zona de Tabay que incluye 1700 m de longitud y 250m de ancho con 2 tramos rectos y 1 curvo para el prototipo. Se realizaron los cálculos de la similitud geométrica, cinemática y dinámica para un modelo físico propuesto Esc. 1:50 dimensiones: L =34 m, W = 5 m y H distorsionada = 15cm se utilizó el número de Reynolds y las fuerzas de presión, gravedad y Coriolis, para conseguir las semejanzas dinámicas con el prototipo. Las conclusiones indican que existe semejanza entre ambos y se recomienda su construcción para modelar, calibrar y extrapolar aplicaciones en construcción de puentes, construcción de objetos físicos para encontrar disminuir el esfuerzo cortante en los bordes y taludes del rio Chama.*

**Palabras clave:** modelo físico, numero de Reynolds, similitud, semejanzas.

**Abstract**

*The Bret storm, a main raining for 1985 in the states Zulia, Trujillo, Merida (1988) and Tachira, Venezuela has come back on June month of 2025, this time awake on Zulia area. Merida state was hit hardly with Avenue hydraulic phenomenon on Chama River at the moorland 3600 m over sea level overlanding up its flow water over the embankment until occupying original width cross section. Seven points were impacting along Trasandina current roadside like Apartaderos, Cruz de Mucuruba, Escaguey, Tabay, El Arenal, Cafetal and the Gonzalez. Flow rate increased 6 times from 400 $m^3/s$ to 2700 $m^3/s$. A volume control was taken as prototype located at coordinates N 8º38'39", W 70º 58'00", to study one of the affecting areas like Tabay, this is about 1700 m length and 250 m width and 5m water level that include 2 straight and one curve reach for the prototype. Math calculations were done to reach geometry, Kinematic and dynamic similarity and resemble to achieve statement of a physical model proposal scaled down 1:50, L = 34m, W = 5m and Hdistorted = 15cm dimension with. A dimensional number Reynolds and pression, gravity and Coriolis forces demonstrate good agreement for 2D channel between prototype and physical model. Conclusion following that exists resemble and similarity in both studies and then, its highly recommend for construction to analyzed and calibrate and extrapolate results for bridges construction and shear stress force control on Chama River embankment.*

**Keywords:** physical model, Reynolds number, similarity and resemble

## 1. Introducción

Hacia la cota 4000 msnm aparece la pequeña planicie aluvial de Llano Redondo. Luego la quebrada cambia su curso hacia el sur y en la cota 3600 msnm recibe la quebrada El Águila a partir de allí la quebrada Mifafi se denomina rio Chama (Silva, 1999). La longitud total del rio Chama es de 200 km hasta la desembocadura en el lago de Maracaibo, el primer tramo (alto) constituido desde la quebrada hasta el Arenal es de 100 Km y el segundo tramo (medio-bajo) desde el Arenal hasta el lago 100 km.

Las características morfológicas de cada tramo son diferentes; el primero con pendiente 8%, lecho conformado por roca de 1 m aproximado de diámetro, sección transversal rectangular, taludes recubiertos con arcilla, roca y vegetación (bambuco). El segundo tramo 1500 msnm con pendiente 3,6%, lecho conformado por grava y arena, sección plana y trapezoidal, taludes de roca maciza (geología tipo cañón) (Ferrer y Laffaille, 2005) y vegetación en el centro del lecho y márgenes.

El rio Chama en el primer tramo se puede considerar para caudales promedios de 400 m3/s (valor estimado en sitio) y ancho W=50 m (puente El Arenal) casi no variable equivalente a 1D, pero ante un evento tipo Avenida ocurrido en junio 2025, donde el caudal se incrementó 6 veces (Aldana, 2025) hasta 2700 m3/s y el W = 250m por definición es de 2D. Los modelos físicos de escala reducida del tamaño del prototipo es un método confiable (Aldana, 2004) para ajustar y predecir eventos producidos a escala real (prototipo) y por su tamaño es costoso simular su análisis y soluciones.

Se han utilizado en diseño de puentes (Jiang, 2021) para estudiar problemas de sedimentación y crecidas en ríos (Yu, Zhang y Col., 2025). Modelos físicos en escala reducida igual o menor de 1:50 han sido utilizados en lagunas de estabilización maduración y sedimentadores (Aldana y Pérez, 2010) reactores anaerobios (Pérez y Aldana, 2013), humedales (Ferrer y Col., 2013) utilizando números Adimensionales tales como: Reynolds, Froude, Peclect tienen suficiente significado y aproximación para la similitud Geométrica, Cinemática y Dinámica (Aldana y Col. 2005), existente entre la relación relativa del modelo y prototipo.

La construcción y calibración del modelo físico es una de las etapas más importante ya que requiere realizar curvas de calibración para la bomba de suministro de agua, correcciones por temperatura para la viscosidad cinemática y ajustes de la distorsión de escala para la dimensión de la altura H (más desfavorable) (Aldana y Col., 2005).

Existe limitada investigación sobre modelos físico 1D, 2D y en particular para el rio Chama. La trayectoria del rio lo hace en forma de meandros debido a la fuerza de Coriolis (Cañón y Espinoza, 2003)) lo que genera en la curva una fuerza transversal de mayor magnitud que la misma fuerza paralela al flujo en los tramos rectos. (Cheng, 2012) analizo el impacto sobre estructuras de puentes incluyendo la altura o tirante y la velocidad del agua. (Jieng, 2021) estudio el efecto hidrodinámico del flujo y su impacto en los puentes en tramos curvos del rio.

## 2. Metodología

Las ecuaciones utilizadas son las siguientes: la Ec. de Continuidad para modelos matemáticos de dos dimensiones:

$$E1=E2–hCF–hCA \quad (1)$$

Donde:

hCF = perdidas por coeficiente de fricción (m)
hCA = perdidas por coeficiente de arrastre (m)

$$dVol/dt+dVx/dx+dVy/dy+dVz/dz -hCF - hCA= Vxi +Vyj +Vzk \quad (2)$$

donde: Vzk = 0

La semejanza geométrica entre modelo y prototipo o las relaciones entre todas las dimensiones correspondientes y homólogas en modelo y propotipo son iguales.

$$Lmodelo/Lprototipo = Lrelativa \Rightarrow Lm/Lp = Lr \quad (3)$$

$$Amodelo/Aprototipo = L^2modelo/L^2prototipo =L^2r \quad (4)$$

Existe semejanza cinemática entre modelo y prototipo si:

a) Las trayectorias de las partículas móviles homólogas son geométricamente iguales.

b) Las relaciones entre las velocidades de las partículas homólogas son iguales.

$$Velocidad: Vm/Vp = Lm/Tm/Lp/Tp = Lm/Lp:Tm/Tp = Lr/Tr \quad (5)$$

$$Aceleración: Am/Ap = Lm/T^2m/Lp/T^2p =Lm/Lp : T^2m/T^2p = L^3r/T^2r \quad (6)$$

$$Caudal: Qm/Qp = L^3m/Tm/L^3p/Tp = L^3m/L^3p : Tm/Tp = L^3r/Tr \quad (7)$$

Esta semejanza para alcanzar su objetivo en el prototipo debe cumplir con un número adimensional tal como numero de

Reynolds, (Polprasert y Bhattarai, 1985) ajustado a canales en función de las fuerzas que apliquen.

$$\text{No Reynolds} = L*W*Z/[(W - 2Z)*\theta*\nu] \quad (8)$$

*donde: L, W,Z = longitud, ancho y profundidad del prototipo o modelo*

*θh = tiempo de retención hidráulico (s)*

*ν = viscosidad cinemática ($m^2/s$)*

Ecuación de Manning

$$V=1/n*Rh\text{^}3/2*S\text{^}1/2 \quad (9)$$

Perdidas por fricción hCF

$$Ff = Cd*0,5*Vagua*\rho lodo* \text{ Area Transv.} \quad (10)$$

Perdidas por arrastre hCD

$$Fa = Cd*0,5*Vagua*\rho lodo* \text{ Area Transv} \quad (11)$$

Entre dos sistemas semejantes geométrica y cinemáticamente existe semejanza dinámica si las relaciones entre las fuerzas homologas en modelo y prototipo son las mismas.

Fuerzas del Fluido producidas por el rio.

$F_p$: Fuerzas de Presión: $\boldsymbol{p * A = \rho L^2}$

$F_G$: Fuerzas de Gravedad: $\boldsymbol{M * g = \rho L^3 g}$

$F_E$: Fuerzas de Coriolis: f =-2 Ω seno φ M: ($s^{-1}$)

φ (latitud rio) = 8º 38’; Ω (velocidad angular de la tierra) = $0,73x10^{-4}$ $s^{-1}$

Volumen de Control

Se selecciono un volumen de control para el caso No 4 según Tabla 1, referente a Tabay en La Ceibita como prototipo, de dimensiones L= 1700m, W = 50 - 250m y H = 3- 5 m, constituido por dos tramos rectos de L = 500m c/u y uno curvo de L =700m en dos escenarios Qm y Qmax.. como se muestra en la Figura 1.

Para el modelo se seleccionó una escala reducida ajustada de 1:50 con dimensiones: L = 34m W = 1-5 m y H = 6 cm. Se tomo un modelo distorsionado en la altura de 15 cm (escala distorsionada 2,5%).

La temperatura promedio del rio Chama es de 13ºC (medida en Tabay) y la viscosidad cinemática del agua a 18ºC = $1,006x10^{-6}$ $m^2/s$, se realizó una corrección por temperatura usando la ec. de Aldana 2004:

$$\nu = \nu 18^oC * e^{-0,0803(T)} \quad (12)$$

$\nu corr\ 13^oC = 9,571x10^{-7}$ $m^2/s$

**Tabla 1**. Características geográficas de los puntos críticos de la creciente rio Chama. Evento 24-06-25.

| No | C. Norte | C. Oeste | Long km/nm | Sitio | Municipio |
|---|---|---|---|---|---|
| 1 | 8º47’47” | 70º51’22” | 30/3424 | ApartaderosCaminoReal | Rangel |
| 2 | 8º42’27” | 70º58’59” | 6/2418 | Cruz de Mucuruba | Card. Quintero |
| 3 | 8º41’15” | 70º56’38” | 12/2205 | Escaguey | Rangel |
| | | | | | |
| 4 | 8º38’39” | 70º58’00” | 1/1703 | Tabay La Ceibita | Santos Marquina |
| 5 | 8º37’25” | 71’03’20” | 7/1645 | El Arenal | Libertador |
| 6 | 8º35’47” | 71º07’19” | 5/1523 | Cafetal | Libertador |
| 7 | 8º29’50” | 71º19’41” | 20/955 | Las González | Campo Elías |

**Fig.1**. Prototipo se muestra el volumen de control para La Ceibita cerca de Tabay. Ref. Google Earth, 2022

## 3. Materiales

El modelo se recomienda ser construido con bloques de 15 cm de espesor (concreto) sobre una base piso vaciada en concreto y altura de pared perimetral de 25 cm, la pendiente del modelo 8% se le da elevando el lecho con material de relleno y alisando ver Figura 2.

La fricción en el lecho con grava y arena se genera con piedras corte angular de granulometría 2 cm. En los taludes

se siembra bambuco y se colocan objetos fijos que simulen viviendas a escala reducida 1:50.

n1 = 0,025 roca cortada; n2 = 0,050 vegetación alta

Se recomienda que el modelo sea construido en un terreno privado bajo área techada, con los servicios y cercado para seguridad. Área construcción = 250 m$^2$. Ver Figura 3.

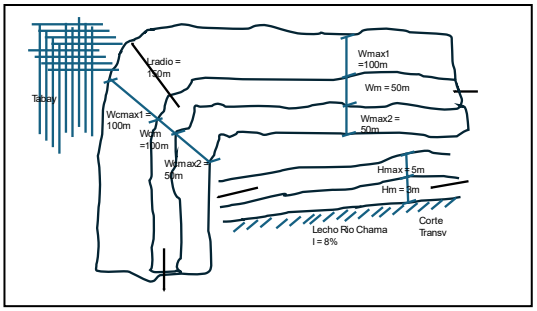


**Fig. 2**. Esquema del prototipo para construcción del modelo rio Chama.

En la Tabla 2 se presentan los cálculos para canal con el Qm, se refleja similitud geométrica entre el modelo y prototipo para el No de Reynolds y el área transversal con Ar = 0,0004. No se observó similitud para las dimensiones L, W y H en la relación relativa.

**Tabla 2**. Similitud geométrica para canal y Qm

| **Canal** | **L (m)** | **W (m)** | **H (m)** | **V (m^3)** | **A transv** | **Re canal** |
|---|---|---|---|---|---|---|
| **Para Qm** | | | | | | |
| Prototipo | 1700 | 50 | 3 | 255000 | 150 | 1682182,32 |
| Modelo | 34 | 1 | 0,06 | 2,04 | 0,06 | 672,87293 |
| Rcm/Rcp | 0,0004 | | | | | |
| Am/Ap | 0,0004 | | Hay similitud con el No Re y área Ar | | | |
| | | | Geometrica | | | |

## 4. Resultados y Discusión

Se realizaron los cálculos para cada tipo de similitud

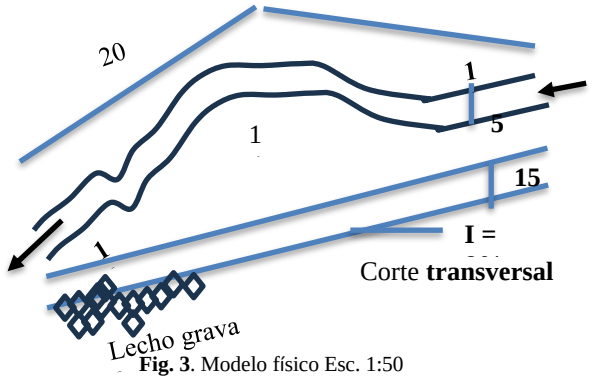


**Fig. 3**. Modelo físico Esc. 1:50
L= 34m, W = 5m, H = 15 cm

utilizando las ecs 3 hasta 9 para luego encontrar la semejanza entre prototipo y modelo. Se utilizaron varios casos: a) canal para los tramos rectos y b) curvo; en ambos se calcularon todas las similitudes y semejanzas para los escenarios: 1) Qmedio = 400 m$^3$/s y 2) Qmax = 2700 m$^3$/s.

Se elaboro un programa en una hoja de Excel y se analizaron 12 casos incluyendo: 2 caudales; para valores medios y máximos en el evento ocurrido el 24/06/25, 3 similitudes y 2 tramos: recto (canal) y curvo, se presentan para la discusión 7 casos.

En la Tabla 3 se presenta los cálculos para curva con el Qmax, se refleja similitud geométrica entre el modelo y prototipo para el No de Reynolds y área transversal relativa.

**Tabla 3.** Similitud geométrica para curva y Qmax

| | **L (m)** | **W (m)** | **H (m)** | **V (m^3)** | **A transv** | Re canal |
|---|---|---|---|---|---|---|
| **Para curva Qmax** | | | | | | |
| Prototipo | 700 | 250 | 5 | 875000 | 1250 | 1058235,61 |
| Modelo | 14 | 5 | 0,1 | 7 | 0,5 | 423,294245 |
| Rm/Rp | 0,0004 | | | | | |
| Am/Ap | 0,0004 | | | | | |
| Lm/Lp | 0,02 | | Hay similitud con No Re y Ar, no hay similitud con Lr | | | |
| | | | Geometrica | | | |

En la Tabla 4 se presenta los cálculos para canal con el Qm,

se refleja similitud cinemática entre el modelo y prototipo solo para el Q relativo. No hay para Tiempo, Velocidad ni Aceleración.

Existen dos tiempos:

a) θh = tiempo hidráulico = 3600 s (tiempo igual para el modelo y prototipo = 1h para flujo medio).

b) Tiempo teoricop = 900s (15min); tiempo teórico modelo = 900/50 = 18 s (tiempo que ocurre el evento o Avenida).

La velocidad y la aceleración se consideran iguales porque ocurre en una fracción de tiempo muy corto de 1 s.

La velocidad fue medida aguas arriba del puente El Arenal con objetos flotantes (naranjas) para Qm y vario en el rango de 2 a 8 m/s.

**Tabla 4**. Similitud Cinemática para canal y Qm

| **Canal** | **T (s)** | **V (m/s)** | **A (m/s^2)** | **Q (m^3/s)** |
|---|---|---|---|---|
| **Para Qm** | | | | |
| Prototipo | 900 | 2 | 2 | 116,666667 |
| Modelo | 18 | 0,04 | 0,00222222 | 0,0466667 |
| Tm/Tp | 0,02 | | | |
| Vm/Vp | 0,02 | | | |
| Am/Ap | 0,00111111 | | Hay similitud cinemática para Q. No hay para T, A | |
| Qm/Qp | 0,0004 | | | |

En la Tabla 5 se presenta los cálculos para la curva con el Qm, se refleja similitud cinemática entre el modelo y prototipo solo para la Velocidad relativa. No hay para Tiempo, Velocidad ni Aceleración ni Caudal.

Los vectores de velocidad y fuerza tienen dos componentes en la curva:

a) En la dirección x = Lradio prototipo = 150 m, el ángulo α =0,72 arctg (2,50/200).

Fx =150*sen(0,72) = 1,88 Nw,

b) En la dirección y, (Artículo de Investigación. Revista Ciencia e Ingeniería. Vol. 47, No. 3 agosto-noviembre, 2026).

Fy = 150*cos(0,72) = 150 Nw, se considera despreciable Fx.

La fuerza resultante viene dado $Fr = \sqrt{Fy^2+Fx^2}$. De la misma forma para el vector velocidad Vy = 42,20 m/s. La velocidad en la curva para el prototipo aumenta 20 veces con respecto a la velocidad en el canal desde 2 m/s hasta 42,20 m/s.

Al dividir la Vm entre la Vp el valor es 0,00094785, (exponencial es $10^{-4}$) existiendo similitud cinemática para la curva, lo cual no ocurre en el canal donde Vm/Vp = 0,02 (exponencial es $10^{-2}$).

Si comparamos los valores calculados en las Tablas 4 y 5, existe similitud cinemática para Qm/Qp = 0,0004 en el tramo, no ocurre así para la curva Qm/Qp = 0,00720002'

De la misma forma no ocurre similitud cinemática según se observa en las Tablas 4 y 5, para los tiempos Tm/Tp ni para las aceleraciones Am/Ap para los tramos en el canal ni para la curva.

En conclusión, la similitud cinemática para la velocidad y el caudal son las variables que dominan para el diseño del modelo demostrado tanto en el canal como en la curva.

**Tabla 5.** Similitud Cinemática para curva y Qm

| | **T (s)** | **V (m/s)** | **A (m/s^2)** | **Q (m^3/s)** |
|---|---|---|---|---|
| **Para curva Qm** | | | | |
| Prototipo | 900 | 42,200619 | 42,200619 | 972,22 |
| Modelo | 18 | 0,04 | 0,00222222 | 7 |
| Tm/Tp | 0,02 | | | |
| Vm/Vp | 0,00094785 | | | |
| Am/Ap | 5,2659E-05 | | Hay similitud cinemática para Velocidad no hay para T, A,Q | |
| Qm/Qp | 0,00720002 | | | |

En la Tabla 6 el tiempo para el evento de la Avenida en el modelo se distorsiono 10% F.S. = 0,1, para conseguir similitud Tr. La velocidad se incrementó en el evento de 8 m/s a 100 m/s (12,5 veces).

El caudal aumento a un Qmax = 1888,89 m^3/s casi 12,5 veces el Qm, lo que produce un gran impacto en la tangente de la curva.

La relación de tiempo distorsionado con un factor de 0,1 entre el Tm/Tp = 0,0002 (exponencial $10^{-4}$) y al relacionar con ese valor de Qmax existe similitud cinemática.

No hay similitud cinemática en la curva para Qmax en las variables de Velocidad Vm/Vp = 0,002426, Aceleración Am/Ap = 0,01348058 ni en el Caudal Qm/Qp = 0,02058824.

El factor de distorsión de 10% para el tiempo en la curva y simular el evento de la Avenida es muy sensible, lo que amerita realizar calibraciones una vez construido el modelo físico.

Estas curvas de calibración deben ser muy específicas entre el caudal y el área de la curva en el modelo a construir escala 1:50.

En la sección transversal de la curva el ancho se incrementa tanto en el prototipo y en el modelo, pero, la profundidad se distorsiona desde 6 cm a 15cm por la escala vertical, lo que hace muy sensible las variables de aceleración y velocidad.

Esto requiere ser estudiado con mucho detalle en el futuro modelo y construir curvas de calibración para la profundidad y el caudal. Determinar qué relación existe si es una variación lineal o curva y determinar los coeficientes de las ecuaciones.

**Tabla 6.** Similitud Cinemática para curva y Qmax.

| | **T (s)** | **V (m/s)** | **A (m/s^2)** | **Q (m^3/s)** |
|---|---|---|---|---|
| **Para curva Qmax** | | | | |
| Prototipo | 900 | 65,9384672 | 65,9384672 | 1888,88889 |
| Modelo | 0,18 | 0,16 | 0,88888889 | 38,8888889 |
| Tm/Tp | 0,0002 | F.D. = 0,1 | | |
| Am/Ap | 0,01348058 | | Hay similitud cinemática para el Tiempo distorsionado Tr | |
| Vm/Vp | 0,0024265 | | | |
| Qm/Qp | 0,02058824 | | | |

Dichas ecuaciones se determinarían controlando el caudal y midiendo que velocidades se obtendrían en el cauce del modelo. Para ello se pueden utilizar objetos flotantes, por ejemplo, uvas con ejes verticales (palitos de madera) que mantengan la flotación y la verticalidad del objeto. Es decir que no se hundan y determinen velocidad superficial.

Las ecuaciones, además, nos permitirían visualizar cual es el comportamiento independiente y el grado de complejidad o libertad de las curvas.

Otros factores que se tendrían que considerar es la rugosidad de las paredes (taludes) y del lecho. Varios tipos de materiales habría que utilizar y seleccionar el que aproxime mejor ajuste.

En conclusión, las variables más desfavorables que tendría un futuro modelo físico es simular el Qmax, en una curva a escala reducida a 1:50 y con profundidad distorsionada 2,5 veces es decir 15cm equivalente a lo que ocurrió el 24 de junio de 2025, en el punto crítico de Tabay.

En la Tabla 7 se muestran los valores en el canal con Qmax, los cuales varían para la fuerza de presión, ejercida por el fluido en el prototipo en términos de $1x10^{10}$ Nw, similar para la fuerza de gravedad, y (-) $1x10^{7}$ Nw para la fuerza de Coriolis, siendo valores negativos.

Los valores del modelo son $1x10^{7}$, $1x10^{5}$ y $-1x10^{2}$, respectivamente. La similitud dinámica en el canal con Qmax para un evento de Avenida, existe solo para las fuerzas de presión Fm/Fp = 0.0004 pero, no hay similitud dinámica en el canal con el modelo para las fuerzas de gravedad Fm/Fp = 0,000008 ni para las fuerzas de Coriolis Fm/Fg = 0,000008.

Tampoco existe similitud dinámica por supuesto para las masas, viscosidad cinemática del fluido y las longitudes entre el modelo y el prototipo.

Estas magnitudes de las tres fuerzas en conjunto demuestran la potencia natural del fluido, la cual arrastro, viviendas (2 pisos) de 300 Tn de peso, puentes de concreto y metálicos, camiones 350, animales vacunos, arboles de 30m de altura como una hoja de papel (en sentido figurado).

En conclusión, la similitud dinámica entre el modelo y el prototipo en el canal y para un Qmax o de Avenida solo se puede alcanzar para las fuerzas de presión. Esto es bastante representativo porque se puede iniciar la calibración del modelo en el canal y luego, extrapolar los coeficientes para la curva.

En el caso del futuro modelo a construir las fuerzas dinámicas para el evento crítico a simular en Tabay, la fuerza de presión presenta buena correlación en comparación a las de geometría y cinemáticas

Esto es significativo para el modelo futuro porque involucra las fuerzas de presión que son muy elevada.

**Tabla 7**. Similitud Dinámica en el canal para Qmax.

| CanalPara Qmax | Fpresion Nw | Fgravedad | Fcoriolis | Masa (kg) | T (oC) | ν (m^2/s) | L (m) |
|---|---|---|---|---|---|---|---|
| Prototipo | 3468000000 | 1,0301E+10 | -1325758,44 | 1050000000 | 18 | 1,006x10^-6 | 1700 |
| Modelo | 1387200 | 82404 | -10,6060675 | 8400 | 13 | 9,57x10^-7 | 34 |
| Fm/Fp | 0,0004 | 0,000008 | 0,000008 | | | | |
| Mm/Mp | 0,000008 | | | | | | |
| νm/νp | 0,956 | | Hay similitud dinámica para la Fuerza de Presión | | | | |
| Lm/Lp | | | | | | | 0,02 |

La similitud dinámica para la curva y Qm, se logra en las tres fuerzas de presión, gravedad, Coriolis y Masas, es el caso de semejanza con el prototipo más significante. En el caso de Qmax solo se logra similitud con la Fuerza de Presión.

En resumen, las tres similitudes se cumplen para el modelo y prototipo siendo la geométrica significativa en el tramo canal y curva para los dos escenarios. La Cinemática resulto ser significativa tanto en el tramo canal como en curva y con las relaciones relativa de Caudal, velocidad para el primer escenario y con Tiempo distorsionado 10 % en curva para el segundo.

La similitud dinámica es significativa tanto para el tramo de curva en el primer escenario siendo este el más significativo de todos, y en el segundo escenario para las fuerzas de presión en el tramo canal.

Las fuerzas de Coriolis actúan en los tramos rectos del rio (alto y bajo) después de 30 km de longitud en Apartaderos (ver Tabla 1) elevando la energía cinética en forma de olas de 1 m hasta 2 m y socavando en el lecho del rio (Cañón y Espinoza, 2003).

En la Tabla 7 la similitud dinámica en el canal para Qmax se encuentra con la fuerza de presión, Fpr ejercida por el fluido en el prototipo en términos de $1x10^{10}$ Nw, similar para la fuerza de gravedad, y $-1x10^{7}$ Nw para la fuerza de Coriolis, pero, para esas dos últimas no hay similitud dinámica en el canal con el modelo.

En la Tabla 7 la fuerza de Coriolis está en el orden de -10 E+06 en el prototipo y representada en el modelo por -10 E+02.

En la Tabla 7 la relación entre la viscosidad cinemática del modelo y del prototipo se logra alcanzar cerca de la unidad (0,956). Esta relación es significativa porque existe similitud dinámica.

En la Tabla 8 se muestra la similitud dinámica en la curva para caudales medios.

En el rio Chama (medio) las distancias de los meandros son más cortos entre sí, incrementado los tramos curvos con longitudes que varían de 1 a 12 Km (ver Tabla 1), las fuerzas internas y olas se incrementan produciendo erosión, socavación y esfuerzos cortantes tangenciales a la derecha de los taludes en los tramos curvos (Cañón y Espinoza, 2003), libro de Aldana Mecánica de los fluidos y modelos físicos, 2025.

Basado en estos conocimientos sobre el rio Chama se debe evitar las construcciones cerca del margen del rio y deben estar retirados al menos 500 m de cada lado y a 800m preferible en las progresivas del rio medio, vale decir: Escaguey, Cacute, Mucuruba, Tabay, El Arenal.

Los puntos más críticos están ubicados en el rio Chama medio; donde las longitudes de los meandros son muy cortas la fuerza de Coriolis afecto más, y el impacto de erosión en taludes de 30 m de altura. Por lo tanto, cada punto crítico (ver Tabla 1) requeriría del diseño, análisis, construcción y calibración de modelos físicos por separado.

La calibración de varios modelos físicos para el rio Chama significa gastos de inversión, en la ubicación del terreno cerca del rio, construcción, seguridad, protección, personal y mantenimiento de cada modelo físico. Esta infraestructura funcionaria como centros de investigación y formación de recursos humanos.

**Tabla 8**. Similitud Dinámica en la curva y Qm

| **Curva** | | | | | | | |
|---|---|---|---|---|---|---|---|
| **Para Qm** | **Fpresion Nw** | **Fgravedad** | **Fcoriolis** | **Masa (kg)** | **T (oC)** | **v (m^2/s)** | **L (m** |
| Prototipo | 490000000 | 1144500 | -147,306494 | 116666,667 | 18 | 1,006x10^-6 | 700 |
| Modelo | 196000 | 457,8 | -0,0589226 | 46,6666667 | 13 | 9,57x10^-7 | 14 |
| Fm/Fp | 0,0004 | 0, 0004 | 0,004 | | | | |
| Mm/Mp | 0,0004 | | | | | | |
| vm/vp | 0,95 | | | | | | |

Las estructuras de puentes, drenajes, pasos peatonales y otras, tipo envergaduras metálicas y concreto armado deben diseñarse para periodos de retornos de 50 a 100 años y Tr = 60 min, debido a que los datos pluviométricos se incrementan de 45 mm (< 20 años) a 65 mm (>75 años) (Delgadillo y Col., 2004).

## 5. Conclusiones

Este estudio demostró la factibilidad y alta recomendación para la construcción de un modelo físico calibrado de escala reducida 1:50 para la investigación y análisis del rio Chama que tiene elevado grado de complejidad.

El modelo físico es un modelo distorsionado tanto en el tirante de agua F.S.= 2,5% más en la variable tiempo 10% resultando un error del 12,5% de ajuste y extrapolación de resultados. La literatura recomienda 25% máximo de error para modelos físicos.

Los modelos físicos a escala reducida son muy significativos, porque permiten el ajuste geométrico, cinemático y dinámico entre el prototipo y el modelo. Estos modelos son de gran utilidad en la construcción de obras de envergaduras como puentes, muros y taludes en los ríos.

El rio Chama y el rio Motatan los cuales están ubicados al sur y al norte de la ciudad de Merida, respectivamente, son de caudales elevados ambos y superiores a los 1800m^3/s, lo que hace necesario el uso de modelos físicos para su estudio y reducción de inversión por la escala.

Para la construcción del modelo se recomienda realizar algunos convenios entre universidades tales como: ULA, LUZ, UNERB e instituciones públicas y privadas, de manera de formar recursos humanos en el área.

## Referencias


Aldana, G. y col. (2005). The development and calibration of a physical model to assist in optimising the hydraulic performance and design of maturation ponds. *Water Science and Technology* http://www.scopus.com/inward/record.url?eid=2-s2.0-23844539691&partnerID=MN8TOARS

Aldana V. G., (2004). Hydraulic behaviour and performance improvement of waste stabilizsation ponds using a computational fluid dynamic and physical model. *Ph.D. Thesis web University of Surrey Centre for Environmental Health and Engineering. http//www.unisurrey.ac.uk.*

Aldana, G.y col. (2010) Simulación del patrón de flujo y del tiempo de retención hidráulico en lagunas de estabilización y reactores anaerobios de flujo ascendente (RAFA) a través de un modelo físico. *Revista Técnica De La Facultad De Ingeniería Universidad Del Zulia.* http://www.scopus.com/inward/record.url?eid=2-s2.0-79551486535&partnerID=MN8TOARS

Aldana Villasmil Gerardo J. Libro: Mecánica de los Fluidos y Modelos Físicos. Teoría y Aplicaciones Cap. 10. *Amazon Editorial (2025) ISBN:* 978-980-18-6409-7 (Publicado julio 2025)

Aldana V. G. (2025) Notas de catedra: Simulación y Modelaje de la Hidrodinámica en cuerpos de agua. Maestría en Ingeniería Ambiental *División de Postgrado Fac. Ingeniería LUZ.*

Cañon J. y col. (2003) Modelaje del Efecto de Coriolis y su influencia en la erosión geológica. *Boletín de Ciencias de la Tierra – Num. 15, noviembre - Medellín - ISSN 0*

*1 2 0 - 3 6 3*

Chen J. y col. (2012) Influence of Bridge Construction on Water Flow Movement in Different Characteristic *Reaches* of the *Middle and Lower Yangtze River. Eng. J. Wuhan. Univ.,45,340–344+355.* https://kns.cnki.net/kcms2/article/abstract

Delgadillo A. y col. (2004). Caserío La González-urbanización Villa Libertad: un estudio de amenazas múltiples y vulnerabilidad en la cuenca media del río Chama (Andes Venezolanos). *Memorias del V Congreso Venezolano de Geografía. 1-14. Mérida Venezuela (29 noviembre-3 diciembre). (CD-ROM; Trabajo Nº 17: Tema III Geomorfología. Amenazas Naturales y Riesgos Ambientales).*

Ferrer C. y col. (2005) Un estudio de amenazas múltiples en la cuenca media del río Chama (Andes centrales venezolanos): caso zanjón El Paraíso *Revista Geográfica Venezolana, Número especial, 93-117.*

Ferrer G. y col. (2013) Determinación del tiempo retención hidráulico en humedales construidos de flujo horizontal usando un trazador químico. *Revista Técnica De La Facultad De Ingeniería Universidad Del Zulia.* http://www.scopus.com/inward/record.url?eid=2-s2.0-84894176093&partnerID=MN8TOARS

Jiang F. (2021) Impact of Pier Layout Forms on the Hydraulic Characteristics of Bend Flow. *Master's Thesis, Hebei University of Engineering, Handan, China.*https://doi.org/10.3390/app15126581

León Silva G. (1999) Análisis hidrográfico e hipsométrico de la cuenca alta y media del rio Chama, estado Mérida, Venezuela. *Revista Geográfica venezolano. Vol. 40, Num. 1.*

Pérez, J. y col. (2013) Modelación física de un reactor anaerobio de flujo ascendente (RAFA). R*evista Técnica De La Facultad De Ingeniería Universidad Del Zulia.* http://www.scopus.com/inward/record.url?eid=2-s2.0-84894175062&partnerID=MN8TOARS

Polprasert, Ch. y col. (1985). Dispersion model for stabilization ponds. *Journal of Environmental Engineering 111(1), 45-59.*

Yu Zhang y col. (2025) Physical Model Research on the Impact of Bridge Piers on River Flow in Parallel Bridge Construction *Projects. Appl. Sci. 15, 6581. https://doi.org/10.3390/app15126581*

***Recibido:*** *21 de enero de 2026*

***Aceptado:*** *21 de junio de 2026*

***Aldana Villasmil Gerardo:*** *Ph.D. in Enviromental Engineering, 2004, University of Surrey, Guilford, UK. Water Research Centre Engineering Faculty. University of Zulia LUZ.*
*https://orcid.org/0009-0001-3769-075X*

***González, Marzia:*** *M.Sc.. in Enviromental Science, 2012, Universidad del Zulia LUZ. Division de Postgrado de Ingenieria,Maracaibo,Zu,VE. Correo electrónico: marziag21@hotmail.com*
*https://orcid.org/0009-0008-2590-7166*

***Medina, Jesús:*** *Doctorate in Education, 2024, Universidad Experimental Rafael Maria Baralt UNERMB. M.Sc in Mathematical Universidad del Zulia LUZ (2011), Zu, VE.. Correo electrónico: jesusalbertomedinamarquez@gmail.com*
*https://orcid.org/0009-0007-0866-4118*

*Artículo de Investigación. Revista Ciencia e Ingeniería. Vol. 47, No. 3 pp. 327-336, agosto-noviembre, 2026.*
*ISSN 1316-7081. ISSN Elect. 2244-8780 Universidad de los Andes (ULA)*

# Characterization of limnoterrestrial Tardigrades (Tardigrada) in some locations in Caracas, Venezuela

# Caracterización de los Tardígrados (Tardigrada) limnoterrestres en algunas localidades de Caracas, Venezuela

**Tezara, Rodrigo[1]; Guerrero, Ricardo[2]; Torres, Rubén[2]; Morón, Julio[2]; Guerrero, Edmundo[2]; Ramos-Villarroel, Ana[1*]**
[1]Instituto Venezolano de Investigaciones Científicas (IVIC), Miranda, Venezuela.
[2]Universidad Central de Venezuela (UCV). Caracas, Venezuela
*ay2170@gmail.com

**Abstract**

The objective of this research was to characterize and identify the tardigrade genera present in limnoterrestrial communities in four locations in the Gran Caracas (Sebucán, San Bernardino, Facultad de Ciencias UCV, and Guatire) and to evaluate their distribution and diversity in urban environments. Samples of mosses and lichens were collected from different substrates, processed by controlled hydration, and filtered with graduated sieves to concentrate the specimens. Taxonomic identification was performed under an optical microscope (100–320x) using morphological criteria of claws, cuticle, and bucco-pharyngeal apparatus, following the systematic arrangement of (Pilato and Binda, 2010) and the updated species list (Degma et al., 2021). A total of 670 individuals were recorded, of which 240 were identified to genus level, grouped into the classes Eutardigrada and Heterotardigrada, with 15 genera belonging to seven families. Sebucán and the Faculty of Sciences had the highest richness (14 genera each), while San Bernardino had the lowest (7 genera), showing a pattern of diversity associated with local microclimatic conditions. The beta diversity index ($\beta = 1.2$) indicated low turnover between communities, and the Jaccard index reflected high similarity between Sebucán and the Faculty of Sciences (≈87%). Twelve new genera were recorded for Venezuela, doubling the known national diversity and consolidating the country as one of the most diverse in Tardigrades of the Neotropics. The results support the urban ecology hypothesis: urbanization reduces taxonomic richness and promotes communities dominated by resistant genera such as Minibiotus and Minilentus.

**Keywords:** Tardigrada; Eutardigrada; Heterotardigrada; cryptobiosis; limnoterrestrial organisms.

**Resumen**

*El objetivo de esta investigación fue caracterizar e identificar los géneros de tardígrados presentes en comunidades limnoterrestres de cuatro localidades (Sebucán, San Bernardino, Facultad de Ciencias UCV y Guatire) de la Gran Caracas, Venezuela, y evaluar su distribución y diversidad en ambientes urbanos. Las muestras de musgos y líquenes fueron recolectadas de distintos sustratos, procesadas mediante hidratación controlada y filtradas con tamices graduados para concentrar los ejemplares. La identificación taxonómica se realizó bajo microscopio óptico (100–320x) utilizando criterios morfológicos de garras, cutícula y aparato bucofaríngeo, siguiendo el arreglo sistemático (Pilato y Binda, 2010), así como la lista actualizada de especies (Degma et al., 2021). Se registraron 670 individuos, de los cuales 240 fueron identificados hasta el nivel de género, agrupados en las clases Eutardigrada y Heterotardigrada, con 15 géneros pertenecientes a siete familias. Los sitios de Sebucán y la Facultad de Ciencias presentaron la mayor riqueza (14 géneros cada una), mientras que San Bernardino mostró la menor (7 géneros), evidenciando un patrón de diversidad asociado a las condiciones microclimáticas locales. El índice de diversidad beta ($\beta = 1,2$) indicó bajo recambio entre comunidades, y el índice de Jaccard reflejó alta similitud entre Sebucán y la Facultad de Ciencias (≈87%). Se registraron 12 nuevos géneros para Venezuela, duplicando la riqueza nacional conocida y consolidando al país como uno de los más diversos en Tardígrados del Neotrópico. Los resultados apoyan la hipótesis de la ecología urbana: la urbanización reduce la riqueza taxonómica y promueve comunidades dominadas por géneros resistentes como Minibiotus y Minilentus.*

***Palabras clave:*** *Tardigrada; Eutardigradal; Heterotardigrada; criptobiosis; organismos limnoterrestres.*

## 1. Introduction

Tardigrades (from the Latin tardigradus, meaning "slow-moving"), a term coined by Spallanzani in 1776 (Harmunt., 2018) and commonly known as water bears, are microscopic (50–1,200 µm) bilaterally symmetrical, protostome, and schizocoelous animals. Despite their small size, they possess a highly complex morphology and anatomy (León-Espinosa., 2018). A unique characteristic of this group is their ability to enter cryptobiosis, a state of dormancy that allows them to colonize a wide variety of microhabitats through the passive dispersal of cryptobionts, eggs, and active adults, withstanding extreme conditions such as high or sub-zero temperatures, desiccation, hypoxia, osmotic stress, and even vacuum and space radiation. For this reason, tardigrades are considered extremophile organisms (Nelson., 2018; Muñoz and Capote., 2019).

The phylogenetic status of tardigrades has been the subject of extensive debate. They are currently placed within the superphylum Ecdysozoa, which groups organisms that shed their cuticle in a process called ecdysis (Aguinaldo et al., 1997). It is believed that tardigrades may have originated in a marine environment before colonizing limnic and terrestrial habitats (Edgecombe., 2010). Historically, they were linked to arthropods or nematodes due to morphological similarities such as the trirradial pharynx or anhydrobiosis (Kinchin., 1994). However, modern molecular analyses confirm their inclusion in Ecdysozoa alongside nematodes (Borner et al., 2014).

Within this context, various phylogenetic hypotheses have been proposed. The Tactopoda hypothesis (Budd., 2001) posits Arthropoda and Tardigrada as sister groups, based on structural similarities such as the cuticle, the ganglionated ventral nerve cord, and the presence of a trilobate brain (Telford et al., 2008; Persson et al., 2014). In contrast, the Lobopodia hypothesis (Nielsen., 2012) places them as a sister group to a clade comprising Arthropoda and Onychophora, supported by recent molecular analyses (Campbell et al., 2011). Although there is no definitive consensus, both hypotheses acknowledge the evolutionary affinity of tardigrades with panarthropods.

Various experiments have been conducted to assess the survival of tardigrades. Hypsibius exemplaris possesses genes capable of detecting ionizing radiation, maintaining DNA integrity, and constantly triggering the repair of genetic material (Allccahuaman-Huauya., 2024).

Currently, the phylum Tardigrada consists of the classes Heterotardigrada, Mesotardigrada, and Eutardigrada. The class Mesotardigrada is monotypic and is based on the species Thermozodium esakii, discovered in hot springs in Japan; this species is now considered doubtful due to the loss of specimens of that genus following a seismic event (León-Espinosa., 2018). The Heterotardigrada include marine, coastal, and semi-terrestrial species grouped into the orders Arthrotardigrada and Echiniscoidea. The former has been described as a paraphyletic group based on molecular data (Jørgensen et al., 2010; Guil and Giribet., 2012), while the latter is considered monophyletic (Nichols et al., 2006). For their part, the Eutardigrada, predominant in limnoterrestrial environments, comprise the orders Apochela and Parachela (Schuster et al., 1980), and their monophyly has been confirmed by genetic analyses. Recent molecular studies also suggest that Eutardigrada and Heterotardigrada are sister groups within the phylum (Nelson and Rebecchi., 2010).

Morphologically, tardigrades have elongated bodies and bilateral symmetry, with four pairs of lobopodial legs ending in claws (Figure 1). The body is divided into five "segments": one cephalic, three trunk segments, and one caudal segment, with sizes ranging from 50 to 1200 µm, exceptionally reaching 2 mm (Nelson and Adkins., 2001). The mouth may be frontal or subventral, and the legs are located in a lateroventral position. Heterotardigrada possess sensory appendages (cirri, papillae, and dorsal or lateral spines), whereas Eutardigrada lack them, except for some lateral papillae in the order Apochela (León-Espinosa., 2018).

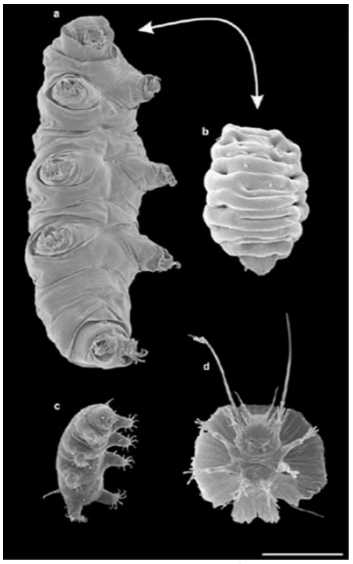


**Figure 1.** Morphological diversity of tardigrades (Møbjerg et al., 2018). a) Eutardigrade in active state. b) Eutardigrade in cryptobiosis. c) Heterotardigrade in active state. d) Heterotardigrade in cryptobiosis.

The taxonomy of the group is based on the morphology of sclerotized structures (Nelson and Rebecchi., 2010):

The claws (Figure 2) are of great diagnostic value. In Heterotardigrada, four symmetrical claws may be smooth or have a ventral spur (Møbjerg et al., 2018); in Eutardigrada, the claws form diplo claws joined in pairs (León-Espinosa., 2018).

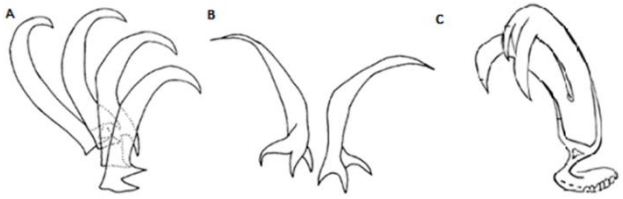


**Figure 2.** Typical morphology of claws in (a) a specimen of the Echiniscidae family. (b) a specimen of the Carphanidae family. (c) A typical eutardigrade claw. (Nelson y col., 2020).

The cuticle (Figure 3) is chitinous and permeable, consisting of an epicuticle, an intracuticle, and a procuticle. Heterotardigrada exhibit dorsal plates and ornamentation, whereas Eutardigrada have smooth or porous cuticles and are referred to as "naked tardigrades" (León-Espinosa., 2018).

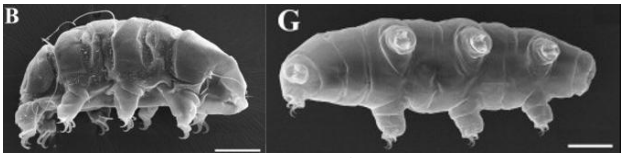


**Figure 3.** Electron micrographs of tardigrades: (B) Echiniscus sp. showing cuticular plates, spines, and filaments (Heterotardigrade); (G) Paramacrobiotus (Eutardigrade).

The buccopharyngeal apparatus (Figure 4) has a complex feeding system consisting of a buccal tube, stylet, and muscular pharynx, with morphological variations that reflect different feeding habits: carnivorous, herbivorous, or microbivorous (Pilato and Binda, 2010; León-Espinosa., 2018).

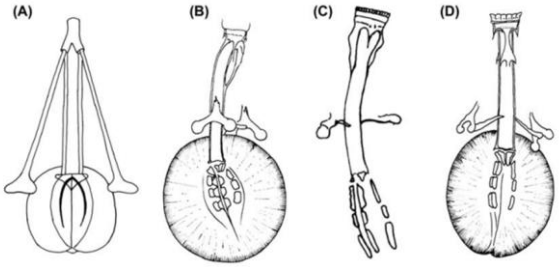


**Figure 4**. Diagram of the buccopharyngeal apparatus. (León-Espinosa, 2018).

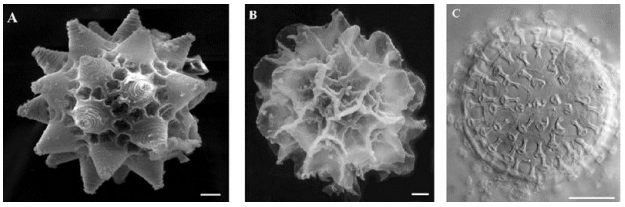


**Figure 5.** Electron micrographs of tardigrades: (B) Echiniscus sp. showing cuticular plates, spines, and filaments (Heterotardigrade); (G) Paramacrobiotus (Eutardigrade).

Eggs (Figure 5) are structures used for taxonomic identification, particularly in Eutardigrada, featuring specific ornamentations (pores, reticulations, processes) and ranging in size from 50 to 235 μm (Bertolani and Rebecchi., 1993).

In terms of their internal anatomy, tardigrades lack circulatory and respiratory systems; their body cavity is filled with fluid and bounded by the integument (Møbjerg., 2018). The digestive system is divided into anterior, middle, and posterior intestines, with a cloaca in Eutardigrada and a preanal gonopore in Heterotardigrada. The nervous system is of the "ladder" type, with four pairs of ventral ganglia connected longitudinally (Schultze et al., 2014). They possess a single dorsal gonad suspended by ligaments (Bertolani., 2001) and exhibit both gonochoristic and hermaphroditic reproduction. Fertilization can be external, within the exuvia, or internal via copulation (Jørgensen et al., 1999). In the face of extreme environmental conditions, tardigrades exhibit adaptive mechanisms that include cryptobiosis, osmoregulation, diapause, and encystment (Guidetti and Møbjerg., 2018). Cryptobiosis is a reversible ametabolic state induced by environmental stress and comprises several types:

Anhydrobiosis, characterized by the almost complete loss of water and the formation of a "barrel-shaped" structure with suspended metabolism, from which the organism can recover upon rehydration (Guidetti and Møbjerg., 2018). Cryobiosis, which allows organisms to survive at temperatures below −196 °C thanks to proteins that inhibit the formation of ice crystals (Nelson and Rebecchi., 2010). Osmobiosis, a response to high osmotic pressures in marine and limnoterrestrial euryhaline species (Nelson et al., 2010). Anoxibiosis, induced by the absence of oxygen; the organism becomes immobile and rigid, able to survive from hours to several days (Nelson and Rebecchi., 2010). Encystment, the formation of oval cysts with a thickened cuticle and reduced metabolism, capable of surviving for months without food (Nelson and Rebecchi., 2010).

These mechanisms, together with the ancestral cryptobiosis present in all lineages (Hygum et al., 2016), explain the extraordinary resistance of tardigrades to desiccation, extreme temperatures, hypoxia, and radiation, establishing the phylum as one of the most resilient animal groups on the planet.

The overall objective of this study is to characterize and identify, down to the lowest possible taxonomic level, the tardigrades present in limnoterrestrial samples collected at various locations in the Capital Region and the state of Miranda. To this end, the previously described taxonomic, morphological, and ecological aspects will be integrated, applying a detailed analysis of sclerotized structures such as claws, cuticle, buccopharyngeal apparatus, and eggs, which are diagnostic characteristics of the species. The research will not only seek to characterize local diversity but will also provide valuable data on the distribution of these microorganisms in specific

habitats in Venezuela, laying the groundwork for the characterization and understanding of the biogeographic and ecological patterns of this phylum in certain locations within the Gran Caracas.

## 2 Materials and Methods

The study area was the Capital Region of Venezuela, which consists of the Capital District and the states of Miranda and La Guaira. The Capital District, in turn, comprises the Libertador municipality and four municipalities in the state of Miranda: Baruta, Chacao, El Hatillo, and Sucre. The terrain is mountainous, with the Caracas Valley (the largest) bounded to the north by the Cordillera de la Costa (Waraira Repano National Park or El Ávila) and to the south by the Cordillera del Interior, the former being the higher of the two (maximum elevation: Pico Naiguatá at 2,765 m above sea level). The climate is highland tropical, with an average annual temperature of 21.6 °C and annual precipitation ranging from 900 to 1,300 mm in the Caracas Valley. In higher areas, above 1,500 m a.s.l., rainfall may be higher (>2,000 mm) due to orographic rainfall that concentrates clouds at these altitudes (INAMEH, 2013). Cloud forests form on the high peaks; at lower thermal levels, between 800 and 1,500 m a.s.l., the predominant natural vegetation is semideciduous forest and xerophytic forest on the northern slope facing the coast (Steyermark and Huber, 1978).

The locations where the sampling was conducted were the San Bernardino neighborhood in the Libertador Municipality at 10°30’49’’N -66°53’55’’W, the Sebucán neighborhood in the Municipality of Sucre 10°30’05’’ -66°50’11’’W, and the UCV Faculty of Sciences in Las Tres Gracias 10°29’13’’N -66°53’41’’W, and the Villa Hermosa Residential Complex located in the city of Guatire (10°28’48’’N -66°33’19’’W).

Sampling sites in terrestrial habitats were selected based on the visual presence of conspicuous moss and lichen communities. At these sites, all substrates were sampled (sampling units: living and dead trees, rocks, and man-made structures). Samples of moss and/or lichen mats were collected by scraping the substrate surface with a spatula. In other locations where the substrate was continuous (such as a wall), samples were collected systematically across the surface.

The collected samples were immediately placed in prelabeled paper bags, allowing the plant material to dry slowly and naturally. In this way, the tardigrades had sufficient time to enter an anhydrobiotic state.

The collection and processing of the tardigrades were carried out in several stages.

The Degma (2010) method was used to concentrate the sample:

A small fragment of the sample (approximately 5 x 5 cm) was taken and submerged in filtered water to prevent any possible contamination. The sample was then refrigerated for 24 hours to allow the tardigrades sufficient time to emerge from their anhydrobiotic state. The hydrated sample was then placed in a Petri dish, where entomological forceps were used to mechanically break up the plant material, with the aim of hydrating all specimens, eggs, and exuviae. The broken-up sample was transferred to a beaker, where more water was added, and each fragment was vigorously stirred with glass rods to dislodge as many organisms as possible from the plant material.

Subsequently, each sample was placed on top of a series of sieves graded from largest to smallest mesh size (0.6 to 0.3 mm). After shaking the set of sieves, the wash water was collected in another beaker. The container was then rinsed again with more distilled water. Next, the material remaining in the sieves was rinsed with plenty of distilled water, concentrating the tardigrades in the finest sieve.

Tardigrades, their eggs, and exuviae were collected from the concentrate as described below:

The contents of the finest sieve were placed in a Petri dish using a pipette filled with distilled water, leaving only a thin film of sediment. Subsequently, using a dropper, the specimens were transferred to a Boerner-style perforated plate with 10 wells or compartments (each 1.5 cm in diameter), to which a small amount of distilled water was added. The area surrounding the specimens was cleared using entomological pins. In this way, the tardigrades could be observed under a Wild-Heerbrugg M5A stereoscopic microscope (20-40x). The tardigrades found in each well were extracted using a pair of entomological needles and placed in Eppendorf tubes, to which a few drops of glacial acetic acid had previously been added. This was done to organize, straighten, and fix the organisms within a few minutes.

The specimens were processed using the systematic arrangement (Pilato and Binda, 2010) cross-referenced with the “Current Checklist of Tardigrada Species” (Degma et al., 2021). Individuals were identified to the taxonomic rank of the genus using a Leica DMIL inverted optical microscope (100–320x). The diagrams and descriptions available in the most recently published literature (Degma et al., 2021) were used.

With regard to community parameters, the genera present at the different sites were first recorded in a presence/absence table. The total number of genera (richness) per site was also determined.

Alpha (average local richness), beta (replacement), and

gamma (total or global richness) diversities were calculated (Ricklefs and Miller., 2000). Beta diversity (β) was obtained from the ratio of gamma diversity (Ɣ) to alpha diversity (***α***):

$$\gamma = \alpha \times \beta \Rightarrow \beta = \frac{\gamma}{\alpha}$$

The Jaccard index (Ij) was used to measure the similarity between the communities at two sampling sites, regardless of the taxonomic composition of both sites (Real and Vargas., 1996). The equation is expressed as follows:

$$I_j = \frac{c}{a + b - c}$$

Where:

a: the number of species present at site A.
b: the number of species present at site B.
c: the number of species present at both sites, A and B.

This index ranges from 0 to 1, representing environments that are completely dissimilar and completely similar to one another, respectively. The organisms were counted and reported in absolute and relative frequencies (pi). The latter were expressed as percentages obtained using the following equation:

$$\%p_i = \frac{n_i}{N} \times 100$$

Where $n_i$ is the total number of individuals in a genus and N is the total number of individuals across all genera. Relative abundances were plotted as stacked bar charts. These data were plotted as bar charts.

## 3 Results and Discussion

The study of tardigrades at four locations (the Sebucán residence, the San Bernardino residence, the UCV Faculty of Sciences, and the Villa Hermosa residential complex in Guatire) resulted in the collection of 670 individuals in total, constituting a significant quantitative database for a study of mesofauna in urban environments. The distribution of specimens was notably uneven across the areas, suggesting the existence of contrasting microenvironmental conditions. Sebucán stood out with the highest concentration, contributing 270 individuals (40.3% of the total sample), followed by the Faculty of Sciences, which contributed 170 individuals (25.4%). In contrast, Guatire and San Bernardino showed lower counts, with 100 (14.9%) and 130 (19.4%) individuals, respectively.

This uneven distribution of specimens suggests the existence of contrasting microenvironmental conditions among the studied areas. The high abundance recorded in Sebucán and the Faculty of Sciences reflects environments with more stable and favorable microclimates, while the lower counts in San Bernardino and Guatire could be associated with conditions that are more restrictive for the development of these communities.

Of the total sample, 240 individuals (35.8% of the total) could be identified to the genus level. Taxonomic identification allowed the specimens to be classified into the Classes Eutardigrada and Heterotardigrada.

The Class Eutardigrada was represented by the Orders Apochela (Family Milniisidae) and Parachela (Families Calohypsibidae, Eohypsibidae, Doryphoribiidae, Macrobiotidae, and Murrayidae), while the Class Heterotardigrada was represented solely by the Order Echiniscoidea (Family Echiniscidae).

A total of 15 genera were recorded, distributed across seven families (Figure 6 and Table 1), demonstrating the community's heterogeneity. The order Apochela was represented by the family Milniisidae (the only family in this order); Parachela included five families (Calohypsibidae, Eohypsibidae, Doryphoribiidae, Macrobiotidae, and Murrayidae), grouping the majority of freshwater tardigrades; while Echiniscoidea was represented exclusively by the family Echiniscidae. These results reflect a taxonomically diverse community, with a predominance of lineages typical of limnoterrestrial environments.

In terms of genus richness by site, it was notably higher at the Faculty of Sciences and Sebucán, with 14 genera each, indicating high taxonomic diversity in environments with more stable microclimates. In contrast, San Bernardino had the lowest richness, with only 7 genera approximately half that of the richest sites suggesting that a few genera account for a very high proportion of the community.

Six genera were found to be ubiquitous (present at all four sites): *Calcarobiotus*, *Minibiotus*, *Minilentus, and Xerobiotus* (all from the family Macrobiotidae), as well as *Macroversum* and *Murrayon* (both from the family Murrayidae). The ubiquity of these genera suggests a high degree of ecological plasticity and resistance to the environmental variations typical of urban ecosystems. Likewise, the predominance of the family Macrobiotidae underscores its importance in the colonization of habitats dominated by urban mosses and lichens.

The pattern of relative abundance by location revealed clear differences in community structure. At the Faculty of Sciences, *Minilentus* (31%) predominated, followed by *Minibiotus* (22%), indicating a relatively balanced

community but with marked dominance. In San Bernardino, *Minibiotus* (28%), *Murrayon* (22%), and *Xerobiotus* (22%) accounted for a large portion of the abundance, reflecting a less diverse and more dominated community. In Sebucán, *Minibiotus* (25%) was the most abundant genus, followed by *Calcarobiotus* and *Xerobiotus* (13% each), while in Guatire, Minibiotus (17%) was also dominant, followed by *Minilentus* and *Murrayon* (both at 11%). These patterns demonstrate how community structure responds to specific local conditions.

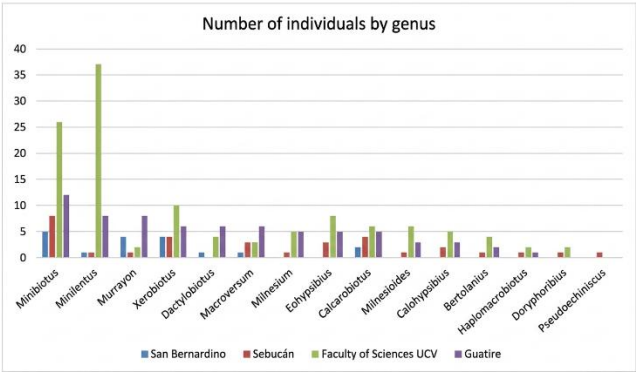


**Figure 6**. Graphical comparison of the number of individuals by gender found in the four locations sampled.

**Table 1**. Characterization of collected individuals. Taxa identified at sampling points. (X = presence).

| Class | Order | Family | Genus | San Bernardino | Sebucán | UCV Faculty of Science | Guatire |
|---|---|---|---|---|---|---|---|
| Eutardigrada | Apochela | Milnesiidae | *Milnesioides* | | X | X | X |
| | | | *Milnesium* | | X | X | X |
| | Parachela | Calohypsibiidae | *Calohypsibius* | | X | X | X |
| | | Eohypsibiidae | *Bertolanius* | | X | X | X |
| | | | *Eohypsibius* | | X | X | X |
| | | Doryphoribiidae | *Doryphoribius* | | X | X | |
| | | Macrobiotidae | *Calcarobiotus* | X | X | X | X |
| | | | *Minibiotus* | X | X | X | X |
| | | | *Minilentus* | X | X | X | X |
| | | | *Xerobiotus* | X | X | X | X |
| | | Murrayidae | *Dactylobiotus* | X | | X | X |
| | | | *Macroversum* | X | X | X | X |
| | | | *Murrayon* | X | X | X | X |
| Heterotardigrada | Echiniscoidea | Echiniscidae | *Pseudechiniscus* | | X | | |

The diversity analysis indicated an average alpha diversity (α) of 12 genera per site and a gamma diversity (γ) of 15 genera in total (see Table 2). The beta (β) index, calculated as the ratio γ/α, was 1.2. According to Whittaker's (1960) conceptualization, species diversity in a series of community samples across a given range of environments results from the combination of alpha and beta diversities, where the latter represents the magnitude of change in community composition along an environmental gradient.

**Table 2**. Comparative Beta Diversity Index between Localities

| Location | San Bernardino | Sebucán | Faculty of Science | Guatire |
|---|---|---|---|---|
| San Bernardino | 1 | - | - | - |
| Sebucán | 1.43 | 1 | - | - |
| Faculty of Science | 1.33 | 1.07 | 1 | - |
| Guatire | 1.3 | 1.11 | 1.04 | 1 |

**Table 3**. Jaccard Similarity Index (JS)

| Comparison | Similarity percentage (IJ) |
|---|---|
| Faculty of Science and Sebucán | ≈ 87% |
| Guatire and Sebucán | ≈69% |
| San Bernardino and other localities | ≈47-54% |

Guatire and Sebucán showed intermediate similarity (≈69%), while San Bernardino exhibited the lowest values (47%–54%) compared to the other sites.

The high turnover observed in San Bernardino is due to its low species richness and the presence of unique genera or the absence of common genera, establishing it as an ecological outlier within the study. This pattern is relevant, as beta diversity is of great importance in ecology, biogeography, and conservation biology, serving as a key concept for understanding ecosystem dynamics, functioning, and management (Legendre et al., 2005).

The variations observed are consistent with the Urban Ecology Hypothesis. Authors such as Shochat et al. (2006) and Peluffo and Rocha (2007) argue that urbanization imposes pressures that lead to a decline in taxonomic richness due to vegetation fragmentation, alterations in the hydrological cycle, and the heat island effect. These factors tend to homogenize microhabitats, favoring resistant and generalist species, such as Minibiotus and Minilentus.

This hypothesis is supported by the microclimatic differences recorded among the study sites, which directly influence moisture availability and the environmental stability necessary for the development of limnoterrestrial communities. Sites with greater generic richness, such as Sebucán and the Faculty of Sciences, exhibited more favorable conditions due to moisture retention associated with vegetation cover. In Sebucán, the vegetation on the walls helped maintain adequate moisture levels, while at the Faculty of Sciences, the presence of gardens and evergreen trees contributed to a humid and relatively stable microclimate an essential condition for poikilohydric organisms such as mosses and the tardigrades that inhabit them.

In contrast, San Bernardino showed lower species richness, attributed to the presence of more restricted areas directly exposed to solar radiation, which increases dryness and water stress, creating a less favorable environment for the establishment and maintenance of moss communities and, consequently, their associated tardigrades.

Finally, this study documented 12 genera of tardigrades that had not previously been recorded in Venezuela. Adding these to the 6 previously reported genera (Macrobiotus, Echiniscoides, Echiniscus, and Mopsechiniscus), the country's total taxonomic record now stands at 18 genera. This finding ranks Venezuela as the fifth country

with the highest tardigrade biodiversity in the Neotropics, ahead of Argentina (15 genera), though still behind Mexico (30 genera) and Brazil (25 genera), highlighting the importance of urban studies in expanding biogeographic knowledge of the group.

## 4 Conclusions

The study revealed a diversity of limnoterrestrial tardigrades comprising 15 genera, mostly belonging to the class Eutardigrada, with a single representative of Heterotardigrada, and highlighted the addition of 12 new records for Venezuela. The analyzed communities showed an uneven distribution in terms of abundance, with Sebucán being the site with the highest number of individuals, followed by the UCV Faculty of Sciences, both at intermediate elevations, while San Bernardino and Guatire Sebucán had comparatively lower abundances.

Regarding community structure, the genera Minibiotus, Minilentus, and Xerobiotus dominated the limnoterrestrial tardigrade communities. San Bernardino stood out for having the greatest genus turnover and the highest dissimilarity compared to the other sites, suggesting a unique faunal composition. At the regional level, the results indicate that Venezuela has a lower tardigrade richness compared to other countries in the Neotropical region, highlighting the need to expand sampling and research efforts to better understand the actual diversity of the group in the country.

The expansion of the national record doubles the known diversity for Venezuela and demonstrates great potential for faunal discovery, especially in non-urban areas. At the continental level, the presence of *Milnesium* sp. in all countries confirms its status as a successful cosmopolitan genus

## References


Aguinaldo, A. A., Turbeville, J. M., Linford, L. S., Rivera, S. T., Garey, J. R., Raff, R. A., & Lake, J. A. (1997). Evidence for a clade of nematodes, arthropods and other moulting animals. Nature, 387(6632), 489–493. https://doi.org/10.1038/387489a

Allccahuaman-Huauya, L., Macedo-Bedoya, J., Calderón Ayala, L., & Vicente Ruiz, H. L. (2024). Astrobiología de Tardígrados: Evaluación de su potencial para la vida en condiciones extremas Revista Científica de Astrobiología, 2 (1), 32–39. https://doi.org/ 10.69976/aspast.v2n1.3

Bertolani, R., & Rebecchi, L. (1993). A revision of the Macrobiotus hufelandi group (Tardigrada, Macrobiotidae), with some observations on the taxonomic characters of eutardigrades. Zoologica Scripta, 22(2), 127–152. https://doi.org/10.1111/j.1463-6409.1993.tb00347.x

Bertolani, R. (2001). Evolution of the reproductive mechanisms in tardigrades. A review. Zoologischer Anzeiger, 240(3-4), 247–252. https://doi.org/10.1078/0044-5231-00032

Borner, J., Rehm, P., Schill, R. O., Krogh, N. M., Hamilton, A., & Burmester, T. (2014). A transcription approach to ecdysozoan phylogeny. Molecular Phylogenetics and Evolution, 80, 79–87. https://doi.org/10.1016/j.ympev.2014.08.001

Budd, G. E. (2001). Tardigrades as 'stem-group arthropods': the evidence from the Cambrian fauna. Zoologischer Anzeiger, 240(3-4), 265–279. https://doi.org/10.1078/0044-5231-00034

Campbell, L. I., Rota-Stabelli, O., Edgecombe, G. D., Marchioro, T., Longhorn, S. J., Telford, M. J., Blaxter, M. L. (2011). MicroRNAs and phylogenomics resolve the relationships of Tardigrada and suggest that velvet worms are the sister group of Arthropoda. Proceedings of the National Academy of Sciences, 108(38), 15920–15924. https://doi.org/10.1073/pnas.1105499108

Degma, P., Bertolani, R., & Guidetti, R. (2021). Actual checklist of Tardigrada species (2009–2021, 34th Edition: 19-07-2021). University of Modena and Reggio Emilia, Módena, Italia. Extracted from https://iris.unimore.it/handle/11380/1178608

Edgecombe, G. D. (2010). Arthropod phylogeny: an overview from the perspectives of morphology, molecular data and the fossil record. Arthropod Structure & Development, 39(2-3), 74–87. https://doi.org/10.1016/j.asd.2009.10.002

Guidetti, R., & Møbjerg, N. (2018). Waters Bears: The Biology of Tardigrades / Chapter 9. Environmental Adaptations: Encystment and Cyclomorphosis. Págs 249 - 241. Editor Ralph O. Schill Institute of Biological Materials and Biomolecular Systems University of Stuttgart Stuttgart, Germany. https://link.springer.com/article/10.1007/s10750-005-1414-8

Guil, N., & Giribet, G. (2012). A comprehensive molecular phylogeny of tardigrades – adding genes and taxa to a poorly resolved Phylum-level phylogeny. Cladistics, 28(1), 21–49. https://doi.org/10.1111/j.1096-0031.2011.00364.x

Harmunt, G. (2018). Waters Bears: The Biology of Tardigrades / Chapter 1. From Johann August Ephraim Goeze to Ernst Marcus: A Ramble through the history of early research (1773 until 1929). Págs 1 - 56. Editor Ralph O. Schill Institute of Biological Materials and Biomolecular Systems University of Stuttgart Stuttgart, Germany.

Hygum, T. L., Clausen, L. K. B., Halberg, K. A., Jørgensen, A., & Møbjerg, N. (2016). Tun formation is not a prerequisite for desiccation tolerance in the marine tidal tardigrade Echiniscoides sigismundi. Zoological Journal of the Linnean Society, 178(4), 907–911. https://doi.org/10.1111/zoj.12444

Jorgensen, A., Mobjerg, N., & Kristensen, R. M. (1999). Ultrastructural studies on spermiogenesis and postcopulatory modifications of spermatozoa of Actinarctus doryphorus Schulz, 1935 (Arthrotardigrada: Halechiniscidae). Zoologischer Anzeiger, 238(3-4), 235-257

Jørgensen, A., Faurby, S., & Hansen, J. G. (2010). Molecular phylogeny of Arthrotardigrada (Tardigrada). Molecular Phylogenetics and Evolution, 54(3), 1006–1015. https://doi.org/10.1016/j.ympev.2009.10.006

Kinchin, I. M. (1994). The Biology of Tardigrades. Portland Press, Londres, Reino Unido. https://www.researchgate.net/publication/232625279_The_Biology_of_Tardigrades

Legendre, P., Borcard, D., & Peres-Neto, P. R. (2005). Analyzing beta diversity: partitioning the spatial variation of community composition data. Ecological Monographs, 75(4), 435–450. https://doi.org/10.1890/05-0549

León-Espinosa, G. (2018). Taxonomía de tardígrados (Tardigrada: Eutardigrada, Heterotardigrada) de musgo en localidades selectas del noreste de México. Universidad Autónoma de Nuevo León, San Nicolás de los Garza, México. Exported from https://www.researchgate.net/profile/Gisela-Aramiriam-Leon/publication/324897157_Taxonomia_de_tardigrados_TARDIGRADA_HETEROTARDIGRADA_EUTARDIGRADA_de_musgo_en_localidades_selectas_del_Noreste_de_Mexico/links/5ae9de02a6fdcc03cd90a478/Taxonomia-de-tardigrados-TARDIGRADA-HETEROTARDIGRADA-EUTARDIGRADA-de-musgo-en-localidades-selectas-del-Noreste-de-Mexico.pdf

Møbjerg, N. (2018). Waters Bears: The Biology of Tardigrades / Chapter 2. Morphology and Functional Anatomy. Págs 57 - 93. Editor Ralph O. Schill Institute of Biological Materials and Biomolecular Systems University of Stuttgart Stuttgart, Germany. https://doi.org/10.1007/978-3-319-95702-9_7

Muñoz, R., & Capote, A. (2019). Estado actual del conocimiento y métodos de estudio de tardígrados (Tardigrada: Heterotardigrada, Eutardigrada), con notas sobre tardígrados muscícolas de Cuba. Poeyana Revista Cubana de Zoología, 508, 18–27. Extracted from http://www.revistasgeotech.com/index.php/poey/article/view/276

Nelson, D. R., & Adkins, R. G. (2001). Distribution of tardigrades within a moss cushion: Do tardigrades migrate in response to changing moisture conditions? Zoologischer Anzeiger, 240(3-4), 493–500. https://doi.org/10.1078/0044-5231-00058

Nelson, D. R., Guidetti, R., & Rebecchi, L. (2010). Ecology and Classification of North American Freshwater Invertebrates / Chapter 14 Tardigrada. Págs 455 - 484. Editor(s) James H. Thorp, Kansas Biological Survey and Department of Ecology and Evolutionary Biology, University of Kansas, Lawrence, KS and Alan P. Covich, Institute of Ecology, Odum School of Ecology, University of Georgia, Athens, Elsevier. https://doi.org/10.1016/B978-0-12-374855-3.00014-5

Nelson, D. R., Guidetti, R., & Rebecchi, L (2020). Thorp and Covich's Freshwater Invertebrates (Fourth Edition). Chapter 15 - Phylum Tardigrada. Págs 505 - 522. Editor(s) D. Christopher Rogers, Kansas Biological Survey and, The Biodiversity Institute, University of Kansas, Lawrence, KS, USA. Cristina Damborenea, Consejo Nacional de Investigaciones Científicas y Técnicas, Museo de La Plata, Facultad Ciencias Naturales y Museo, Universidad Nacional de La Plata, Argentina and James Thorp, Kansas Biological Survey and Department of Ecology and Evolutionary Biology, University of Kansas, Lawrence, KS, USA https://dofi.org/10.1016/B978-0-12-804225-0.00015-0

Nelson, D.R. (2018). Waters Bears: The Biology of Tardigrades / Chapter 7 Tardigrade Ecology. Pags 163 - 210. Editor Ralph O. Schill Institute of Biological Materials and Biomolecular Systems University of Stuttgart Stuttgart, Germany. https://link.springer.com/chapter/10.1007/978-3-319-95702-9_7

Nichols, P., Nelson, D. R., & Garey, J. R. (2006). A family level analysis of tardigrade phylogeny. Hydrobiologia, 558(1), 53–60. Exported from https://link.springer.com/article/10.1007/s10750-005-1414-8

Nielsen, C. (2012). Animal Evolution: Interrelationships of the Living Phyla / Capitulo Phylum Tardigrada. 3rd Edition. Oxford University Press, Oxford, Reino Unido. Págs. 265–270. https://doi.org/10.1093/acprof:oso/9780199606023.001.0001

Persson, D. K., Halberg, K. A., Jørgensen, A., & Møbjerg, N. (2014). Brain anatomy of the marine tardigrade Actinarctus doryphorus (Arthrotardigrada). Journal of Morphology, 275(2), 173–190. https://doi.org/10.1002/jmor.20207

Pilato, G., & Binda, M. C. (2010). Definition of families, subfamilies, genera and subgenera of the Eutardigrada, and keys to their identification. Exported from https://www.mapress.com/zt/article/view/zootaxa.2404.1.1

Real, J. and Vargas, J.M. (1996). The Probabilistic Basis of Jaccard's Index of Similarity. Systematic Biology, 45(3), 380 - 385. https://doi.org/10.1093/sysbio/45.3.380

Ricklefs, R.E. and Miller, G.L. (2000). Ecology 4th Edition, W.H. Freeman, New York. Exported from https://www.scirp.org/reference/referencespapers?referenceid=1339118

Schultze, C., Nieves, R. C., & Schmidt-Rhaesa, A. (2014). Comparative immunohistochemical investigation on

the nervous system of two species of Arthrotardigrada (Heterotardigrada, Tardigrada). Zoologischer Anzeiger - A Journal of Comparative Zoology, 253(3), 225–235. https://doi.org/10.1016/j.jcz.2013.11.001

Schuster, R. O., Nelson, D. R., Grigarick, A. A., & Christenberry, D. (1980). Systematic criteria of the Eutardigrada. Transactions of the American Microscopical Society, 99(3), 284–303. https://doi.org/10.2307/3226004

Steyemark, J.A., and Huber, O. (1978). Flora of Avila. 971. Exported.from https://www.cabidigitallibrary.org/doi/full/10.5555/19800662119

Telford, M. J., Bourlat, S. J., Economou, A., Papillon, D., Glenner, H., Rota-Stabelli, O., ... Littlewood, D. T. J. (2008). The evolution of the Ecdysozoa. Philosophical Transactions of the Royal Society B: Biological Sciences, 363(1496), 1529–1537. https://doi.org/10.1098/rstb.2007.2243

Whittaker, R. H. (1960). Vegetation of the Siskiyou Mountains, Oregon and California. Ecological Monographs, 30(3), 279–338.

***Recibido:*** *15 de marzo de 2026*

***Aceptado:*** *16 de junio de 2026*

***Tezara Rodrigo,*** *Bachelor of Science in Biology, with a minor in Zoology, from the Faculty of Sciences at the Central University of Venezuela (UCV). Research Associate at the Center for Oceanology and Antarctic Studies. Venezuelan Institute for Scientific Research.*
***https://orcid.org/0009-0000-9259-8051***

***Guerrero Ricardo,*** *Doctor in Natural Science (Institute of Parasitology) Emeritus Professor (Instituto de Zoología y Ecología Tropical) Faculty of Science, Central University of Venezuela.*
***https://orcid.org/0000-0003-0925-9476***

***Torres Rubén,*** *Doctor in Science, with a mayor field in Ecology (Graduate Program in Ecology), Full-Time Assistant Professor and Researcher (Center for Ecology and Evolution, Laboratory of Aquatic Systems Ecology (Plankton)) (Instituto de Zoología y Ecología Tropical) Faculty of Science, Central University of Venezuela.*
***https://orcid.org/0000-0002-5251-333X***

***Morón Julio,*** *Assistant Curator (Collection-Laboratory) of the Phelps Ornithological Collection: Caracas, Venezuela. Visiting Researcher (Invertebrate Collection, Malacology Section) at the Biology Museum of the Central University of Venezuela*
***https://orcid.org/0009-0007-3213-9612***

***Guerrero Edmundo,*** *Instructor (Institute of Tropical Zoology and Ecology) at the Biology Museum of the Central University of Venezuela*
***https://orcid.org/0009-0006-1648-3301***

***Ana Ramos****, PhD in Agricultural and Food Sciences and Technology from the University of Lleida, Lleida, Spain. Researcher at the Center for Oceanology and Antarctic Studies. Venezuelan Institute of Scientific Research. Retired professor from the Universidad de Oriente, Monagas nucleus, Maturín, Venezuela.*
*https://orcid.org/0000-0003-4587-7327*

*Artículo de Investigación. Revista Ciencia e Ingeniería. Vol. 47, No. 3, pp. 337-346, agosto-noviembre, 2026.*
*ISSN 1316-7081. ISSN Elect. 2244-8780 Universidad de los Andes (ULA)*

# Quasi-LPV control of a magnetic levitation system using geometric interpolation

# Control quasi-LPV de un sistema de levitación magnética mediante interpolación geométrica

**Teppa-Garrán, Pedro[1*]; Zárraga, Diego[2]**
[1]Departamento de Gestión de Proyectos y Sistemas, Universidad Metropolitana, Caracas, Venezuela.
[2]Escuela de Ingeniería Eléctrica, Universidad Metropolitana, Caracas, Venezuela.
[*]pteppa@unimet.edu.ve

**Abstract**

*This article presents a gain-scheduling control strategy for constant reference tracking in a magnetic levitation system, utilizing a quasi-LPV model and a distance-based geometric interpolation mechanism. The system, involving the suspension of a metallic sphere, is characterized by highly nonlinear, inherently unstable open-loop dynamics where only position is measurable. These nonlinearities are embedded into an endogenous parameter vector that varies within a bounded domain defined by physical operating limits. Consequently, the plant is represented as a family of linear time-invariant models at the parametric vertices. At these vertices, local tracking controllers are designed via state feedback and pole placement, integrated with full-order observers to estimate unmeasurable states. The global controller and observer are synthesized through geometric interpolation, where weights are derived from the Euclidean distance between the estimated parameter vector and each vertex. This approach ensures convex combinations and positive weights across the operating range, simplifying implementation compared to traditional analytical methods. MATLAB/Simulink simulations on the full nonlinear model demonstrate satisfactory tracking performance, bounded control effort, and robustness against input disturbances and measurement noise, validating the efficacy of the proposed control architecture*.

**Keywords**: Magnetic levitation, quasi-LPV systems, gain-scheduling, geometric interpolation, nonlinear systems, state observers, United Nations SDG 9.

**Resumen**

*Este artículo presenta una estrategia de control por programación de ganancias para el seguimiento de referencias constantes en un sistema de levitación magnética, utilizando un modelo quasi-LPV y un mecanismo de interpolación geométrica. El sistema consiste en la suspensión de una esfera metálica caracterizada por una dinámica no lineal e inestabilidad a lazo abierto, donde solo la posición es medible. Las no linealidades se incorporan en un vector de parámetros endógenos que varía en un dominio acotado por los límites físicos, permitiendo representar la planta como una familia de modelos lineales invariantes en el tiempo en los vértices del dominio. En dichos vértices, se diseñan controladores locales mediante realimentación de estado y asignación de polos, integrados con observadores de orden completo para estimar los estados no medibles. El controlador y observador globales se sintetizan mediante interpolación geométrica, donde los pesos se derivan de la distancia euclidiana entre el parámetro estimado y cada vértice. Este enfoque garantiza combinaciones convexas y pesos positivos en todo el rango operativo, simplificando la implementación frente a métodos analíticos tradicionales. Simulaciones en MATLAB/Simulink sobre el modelo no lineal completo demuestran un seguimiento satisfactorio, esfuerzo de control acotado y robustez ante perturbaciones y ruido de medición, validando la eficacia de la arquitectura propuesta.*

**Palabras clave**: Levitación magnética, sistemas quasi-LPV, programación de ganancias, interpolación geométrica, sistemas no lineales, observadores de estado, ODS 9 de las Naciones Unidas.

## 1 Introduction

Magnetic levitation systems constitute a widely used benchmark plant in the field of automatic control due to the combination of pronounced nonlinearities, open-loop instability, and limitations in the measurement of state variables (Kuo, 1996; Khalil, 2002; Sira-Ramirez et al., 2005; Ogata, 2010). These characteristics make them a natural testbed for the evaluation of advanced control methodologies, particularly those aimed at nonlinear and inherently unstable systems, both in academic research and industrial-oriented applications (Bidikli, 2020; Wang et al., 2021; Teppa-Garran & Faggioni, 2023).

A common approach to the control of magnetic levitation systems consists of linearizing the plant around a fixed operating point and subsequently designing a linear controller (Lee et al., 2007; Hypiusova & Kozakova, 2017; Rusar et al., 2017). Although this approach yields satisfactory performance in small neighborhoods of the equilibrium point, its effectiveness degrades rapidly when the system operates over wider position ranges or is subjected to significant disturbances. This limitation has motivated the development of nonlinear, adaptive, sliding-mode, and predictive control strategies, which usually involve increased modeling effort and implementation complexity (Muthairi & Zribi, 2004; Shieh et al., 2010; Wang et al., 2021).

In this context, the theory of Linear Parameter-Varying (LPV) systems provides an attractive intermediate framework, as it allows nonlinear systems to be represented as families of linear models that depend on a bounded parameter vector (Rugh & Shamma, 2000; Rotondo, 2018; Bombois et al., 2021). In particular, quasi-LPV models, where the scheduling parameters are endogenous and depend on the system states, enable nonlinearities to be embedded directly into the parametric dependence of the model without relying on disconnected local linearizations (Robles et al., 2019).

Recent works have demonstrated the effectiveness of quasi-LPV formulations for modeling and control of nonlinear systems in a variety of applications, including aerospace systems, robotics, and industrial processes (Tan et al., 2000; Cisneros et al., 2018; Li et al., 2023). Moreover, the quasi-LPV paradigm has proven to be particularly suitable for gain-scheduling control designs based on state-space techniques, where classical linear tools such as pole placement, optimal control, or robust synthesis can be exploited (Teppa-Garrán & Andrade-Da Silva, 2009; Teppa-Garrán et al., 2025).

Within the LPV and quasi-LPV framework, gain-scheduling strategies require an interpolation mechanism to coherently combine the controllers designed at the vertices of the parametric domain. Analytical interpolation approaches, in which the interpolation weights are obtained by solving a system of linear equations enforcing the exact reconstruction of the parameter vector, have been proposed and successfully applied to inherently stable processes such as coupled tank systems (Teppa-Garrán & Andrade-Da Silva, 2009; Teppa-Garrán et al., 2025). However, when unstable systems with physical constraints on the control signal are considered, as is the case in magnetic levitation, analytical interpolation may present practical difficulties, particularly due to the possibility of negative interpolation weights or the need for additional conditioning.

In this scenario, distance-based geometric interpolation mechanisms offer a conceptually simpler alternative, as they naturally yield convex combinations of the local controllers and guarantee positive weights throughout the parametric domain (Leith & Leithead, 2000). These properties make geometric interpolation especially attractive for practical implementations, where actuator saturation and unidirectional control signals must be explicitly considered.

Motivated by these considerations, this work proposes the application of a quasi-LPV control scheme with Euclidean distance-based geometric interpolation to the magnetic levitation of a spherical object. Unlike previous quasi-LPV applications focused on stable or weakly nonlinear systems, this work explicitly addresses a nonlinear and open-loop unstable plant and consistently integrates the design of tracking controllers and full-order state observers using a single interpolation mechanism based on estimated parameters.

The main contribution of this article lies in demonstrating that geometric interpolation constitutes an effective and practical mechanism for the implementation of quasi-LPV controllers in magnetic levitation systems, offering a favorable trade-off between simplicity, robustness, and performance. Simulation results validate the proposed approach and highlight its potential as a practical alternative to more complex interpolation schemes or nonlinear control methodologies with higher computational cost.

Finally, this work is aligned with Sustainable Development Goal 9 (Industry, Innovation, and Infrastructure), as it contributes to the development of advanced modeling and control methodologies applicable to nonlinear systems of technological and industrial interest. In particular, the use of quasi-LPV control with geometric interpolation promotes more flexible and efficient automation solutions, supporting the strengthening of innovative industrial infrastructures.

## 2 Magnetic levitation system and quasi-LPV modeling

This section presents the mathematical modeling of the magnetic levitation system considered in this work and introduces its representation within the quasi-LPV framework. First, the nonlinear dynamic model of the plant is derived in state-space form, highlighting the main sources of nonlinearity and instability. Then, an equivalent quasi-LPV formulation is developed by embedding the nonlinear terms into an endogenous, bounded parameter vector. This representation provides the basis for the subsequent gain-

scheduling control design and the geometric interpolation scheme described in the following sections.

### 2.1 Nonlinear model of the magnetic levitation system

The magnetic levitation system considered in this work consists of a metallic sphere suspended vertically by the electromagnetic force generated by a single coil. This system is widely used as a benchmark in control engineering due to its strongly nonlinear dynamics and intrinsic open-loop instability, as well as the practical limitation that only the vertical position of the levitated object is directly measurable (Kuo, 1996; Khalil, 2002; Sira-Ramirez et al., 2005).

The dynamic behavior of the plant results from the coupling between the electrical dynamics of the electromagnet and the mechanical dynamics of the sphere (see Fig. 1). The electrical subsystem can be described by applying Kirchhoff's voltage law to the coil circuit, while the mechanical subsystem follows from Newton's second law applied to the vertical motion of the sphere. The electromagnetic force acting upon the sphere scales with the square of the coil current and is inversely proportional to the sphere's displacement, thereby exhibiting pronounced nonlinearity and inherent open-loop instability (Kuo, 1996; Bidikli, 2020).

By defining the state vector as

$$\boldsymbol{x}(t) = [x_1(t) \quad x_2(t) \quad x_3(t)]^T,$$

where $x_1(t)$ denotes the vertical position of the sphere, $x_2(t)$ its vertical velocity, and $x_3(t)$ the current flowing through the electromagnet, the nonlinear model of the magnetic levitation system can be expressed in state-space form as

$$\dot{x}_1(t) = x_2(t),$$

$$\dot{x}_2(t) = g - \frac{q{x_3}^2(t)}{mx_1(t)},$$

$$\dot{x}_3(t) = -\frac{Rx_3(t)}{L} + \frac{u(t)}{L},$$

where $u(t)$ represents the voltage applied to the electromagnet, $g$ is the gravitational acceleration, $m$ is the mass of the levitated sphere, $R$ and $L$ are the electrical resistance and inductance of the coil, respectively, and $q$ is a constant that characterizes the magnetic force generated by the actuator.

The strong nonlinear coupling between the electrical and mechanical subsystems, together with the rational dependence on the position state $x_1(t)$, makes the system unstable and highly sensitive to variations in operating conditions and disturbances. These characteristics motivate the adoption of modeling frameworks capable of capturing nonlinear behavior over a wide operating range without relying on linearization around a single equilibrium point.

The physical parameters of the magnetic levitation system used throughout this study, along with their numerical values, are summarized in Table 1. These parameters correspond to a standard laboratory-scale magnetic levitation setup and are employed consistently in the modeling and simulation results reported in this work.

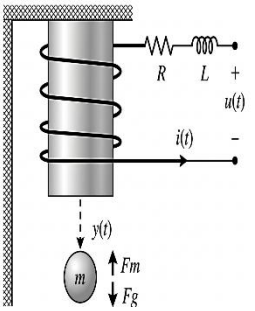


**Figure 1.** Magnetic levitation system.

**Table 1.** Physical parameters of the magnetic levitation system

| Parameter | Description | Value | Units |
|---|---|---|---|
| $g$ | Gravitational acceleration | 9.81 | $\mathrm{m/s^2}$ |
| $L$ | Coil inductance | 0.01 | H |
| $R$ | Coil resistance | 1.00 | Ω |
| $q$ | Electromagnetic force constant | 1.00 | $\mathrm{Nm/A^2}$ |
| $m$ | Mass of the levitated sphere | 1.00 | Kg |
| $x_{eq}$ | Desired equilibrium position of the ball | 0.50 | $m$ |
| $u_{eq}$ | Equilibrium input | 2.20 | V |

### 2.2 Quasi-LPV representation of the magnetic levitation system

To overcome the limitations associated with linearization around a single operating point, the nonlinear model of the magnetic levitation system described in Section 2.1 is reformulated within the quasi-LPV framework. In this approach, the nonlinear dynamics are embedded into a parameter-dependent linear structure, where the scheduling parameters are endogenous and depend explicitly on the system states.

Starting from the nonlinear model, the mechanical equation can be algebraically rearranged without altering the system dynamics as

$$\dot{x}_2(t) = g\frac{1}{x_1(t)}x_1(t) - \frac{q}{m}\frac{x_3(t)}{x_1(t)}x_3(t).$$

This manipulation allows the rational nonlinearities to be isolated in a vector of scheduling parameters, while preserving a linear dependence on the state variables. Accordingly, the endogenous parameter vector is defined as

$$\boldsymbol{\theta}(t) = [\theta_1(t) \quad \theta_2(t)]^T = \left[\frac{1}{x_1(t)} \quad \frac{x_3(t)}{x_1(t)}\right]^T.$$

With this definition, the nonlinear magnetic levitation system can be written in the quasi-LPV form

$$\dot{\boldsymbol{x}}(t) = \boldsymbol{A}(\boldsymbol{\theta}(t))\boldsymbol{x}(t) + \boldsymbol{B}\boldsymbol{u}(t), \qquad \boldsymbol{y}(t) = \boldsymbol{C}\boldsymbol{x}(t),$$

where the parameter-dependent state matrix is given by

$$\boldsymbol{A}(\boldsymbol{\theta}(t)) = \begin{bmatrix} 0 & 1 & 0 \\ g\theta_1(t) & 0 & -\frac{q}{m}\theta_2(t) \\ 0 & 0 & -\frac{R}{L} \end{bmatrix},$$

and the constant input and output matrices are

$$\boldsymbol{B} = \begin{bmatrix} 0 \\ 0 \\ \frac{1}{L} \end{bmatrix}, \qquad \boldsymbol{C} = [1 \quad 0 \quad 0].$$

In this representation, all nonlinear effects of the magnetic levitation system are fully captured by the dependence of the matrix $\boldsymbol{A}(\boldsymbol{\theta}(t))$ on the endogenous parameters $\theta_1(t)$ and $\theta_2(t)$ , while the model remains linear in the state and input variables. Notably, the gravitational term appears multiplied by the first scheduling parameter, which is consistent with the physical structure of the system and with the adopted quasi-LPV modeling strategy.

The scheduling parameters are naturally bounded due to physical constraints on the admissible position and current of the levitated sphere. These bounds define a compact parametric domain, whose vertices are used to generate the local linear models required for the gain-scheduling control and observer design presented in the following section.

### 2.3 Parametric domain and local linear models

The quasi-LPV representation derived in Section 2.2 depends on the endogenous scheduling parameter vector

$$\boldsymbol{\theta}(t) = \begin{bmatrix} \theta_1(t) \\ \theta_2(t) \end{bmatrix} = \begin{bmatrix} \frac{1}{x_1(t)} \\ \frac{x_3(t)}{x_1(t)} \end{bmatrix},$$

whose components are functions of the system states. Since the magnetic levitation system operates within physical constraints on position and current, the scheduling parameters are naturally bounded. These bounds define a compact parametric domain that contains all admissible trajectories of $\boldsymbol{\theta}(t)$ during operation.

Let the position and current of the levitated sphere be constrained to the intervals

$$x_1(t) \in [x_{1,min}, x_{1,max}], \quad x_3(t) \in [x_{3,min}, x_{3,max}],$$

where the limits are selected according to physical restrictions and the desired operating range around the nominal equilibrium point. From these bounds, the corresponding intervals for the scheduling parameters are obtained as

$$\theta_1(t) \in \left[\frac{1}{x_{1,max}}, \frac{1}{x_{1,min}}\right], \quad \theta_2(t) \in \left[\frac{x_{3,min}}{x_{1,max}}, \frac{x_{3,max}}{x_{1,min}}\right].$$

The Cartesian product of these intervals defines a compact rectangular region

$$\Omega = \{\theta \in \mathbb{R}^2 : \theta_1^- \le \theta_1 \le \theta_1^+, \theta_2^- \le \theta_2 \le \theta_2^+\},$$

which represents the admissible parametric domain of the quasi-LPV system.

The extreme combinations of the bounds of Ω define a finite set $\boldsymbol{\theta}^{(i)}, i = 1, \dots, N$, where $N = 4$ for the two-parameter case considered in this work. Evaluating the parameter-dependent matrix $A(\boldsymbol{\theta})$ at each vector yields a collection of linear time-invariant models of the form

$$\dot{\boldsymbol{x}}(t) = \boldsymbol{A}^{(i)}\boldsymbol{x}(t) + \boldsymbol{B}\boldsymbol{u}(t), \quad \boldsymbol{y}(t) = \boldsymbol{C}\boldsymbol{x}(t),$$

with

$$\boldsymbol{A}^{(i)} = A\left(\boldsymbol{\theta}^{(i)}\right), \quad i = 1, \dots, N.$$

These local linear models constitute the basis for the gain-scheduling control design. A local controller and a corresponding state observer are designed for each vertex, ensuring the desired tracking performance and stability properties at the extreme parameter combinations. The global controller and observer are subsequently obtained by interpolating the local designs as a function of the instantaneous value of the scheduling parameters, as detailed in the next section.

## 3 Control design

This section presents the design of the gain-scheduled control strategy for the magnetic levitation system based on the quasi-LPV model developed in Section 2. The objective is to achieve accurate tracking of constant reference positions while ensuring stability and bounded control effort over the entire admissible operating region. To this end, local tracking controllers and state observers are designed at the vertices of the parametric domain and subsequently combined through a geometric interpolation mechanism.

### 3.1 Tracking control problem formulation

The control objective considered in this work is the tracking of constant reference trajectories for the vertical position of the levitated sphere. Let the tracking error be defined as

$$e(t) = r(t) - y(t),$$

where $r(t)$ denotes the reference position and $y(t) = x_1(t)$ is the measured output. For constant reference inputs, zero steady-state error is achieved by incorporating integral action into the control law.

Following a state-space tracking control approach, an augmented system is constructed by including the error

dynamics. Taking the time derivative of the tracking error yields

$$\dot{e}(t) = -\dot{y}(t) = -\boldsymbol{C}\dot{\boldsymbol{x}}(t).$$

For each local linear model associated with a vertex of the quasi-LPV parametric domain, the augmented state vector is defined as

$$\boldsymbol{z}(t) = \begin{bmatrix} e(t) \\ \dot{\boldsymbol{x}}(t) \end{bmatrix}.$$

This formulation transforms the tracking problem into a regulation problem for an augmented linear system, enabling the systematic application of linear state-feedback design techniques.

### 3.2 Local tracking controller design

For each vertex of the parametric domain, a local tracking controller is designed using state feedback on the augmented system. The auxiliary control input is defined as

$$u_0(t) = -\boldsymbol{K}^{(i)}\boldsymbol{z}(t) = -\begin{bmatrix} k_e^{(i)} & \boldsymbol{K}_x^{(i)} \end{bmatrix}\boldsymbol{z}(t),$$

where $k_e^{(i)}$ is the gain associated with the integral of the tracking error, and $\boldsymbol{K}_x^{(i)}$ is the state-feedback gain vector. Integrating the auxiliary input yields the actual control signal applied to the plant,

$$u(t) = -k_e^{(i)} \int_0^t e(\tau)\, d\tau - \boldsymbol{K}_x^{(i)}\boldsymbol{x}(t)$$

The controller gains are computed independently at each vertex using pole placement techniques, selecting the closed-loop poles to satisfy predefined transient performance requirements while ensuring robustness across the operating region.

At each vertex, the resulting local tracking control structure consists of the plant model, the augmented state-feedback controller, and the reference input, as conceptually illustrated in Figure 2.

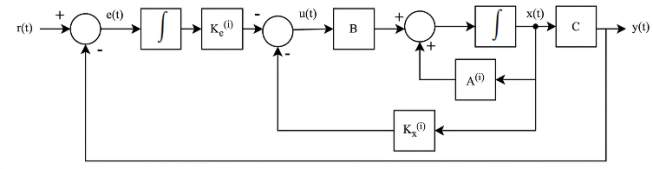


**Figure 2**. Local tracking control structure associated with a vertex of the quasi-LPV parametric domain.

### 3.3 Local state observer design

Since only the position of the levitated sphere is directly measurable, full state information must be reconstructed through state estimation. For this purpose, a full-order state observer is designed for each local linear model.

For the $i$-th vertex, the observer dynamics are given by

$$\dot{\hat{\boldsymbol{x}}}(t) = \boldsymbol{A}^{(i)}\hat{\boldsymbol{x}}(t) + \boldsymbol{B}u(t) + \boldsymbol{L}^{(i)}(y(t) - \boldsymbol{C}\hat{\boldsymbol{x}}(t)),$$

where $\hat{\boldsymbol{x}}(t)$ is the estimated state vector and $\boldsymbol{L}^{(i)}$ is the observer gain matrix. The observer gains are selected such that the estimation error dynamics are significantly faster than the closed-loop system dynamics, ensuring rapid convergence of the estimated states.

The estimated state vector is used both for state-feedback control and for the computation of the scheduling parameters required by the interpolation mechanism

### 3.4 Geometric interpolation of controllers and observers

The global control and observer gains are obtained by interpolating the local designs as functions of the instantaneous value of the scheduling parameter vector. The scheduling parameters are computed from the estimated state variables in order to ensure consistency between control and estimation.

For each vertex $\boldsymbol{\theta}^{(i)}$, the Euclidean distance to the current scheduling estimated parameter vector $\hat{\boldsymbol{\theta}}(t)$ is computed as

$$d_i(t) = \left\|\hat{\boldsymbol{\theta}}(t) - \boldsymbol{\theta}^{(i)}\right\|_2.$$

The Euclidean distance was selected due to its simplicity and its ability to provide smooth and intuitive weighting of the local designs within the parametric domain. The interpolation weights are then defined using a normalized complementary distance measure,

$$\alpha_i(t) = \frac{1 - d_i(t)/\sum_{j=1}^{N} d_j(t)}{\sum_{k=1}^{N}\left(1 - d_k(t)/\sum_{j=1}^{N} d_j(t)\right)}, \quad i = 1, \ldots, N,$$

which satisfies the convexity conditions

$$\alpha_i(t) \geq 0, \quad \sum_{j=1}^{N} \alpha_i(t) = 1.$$

Using these weights, the global controller and observer gains are obtained as

$$\boldsymbol{K}(t) = \sum_{i=1}^{N} \alpha_i(t)\boldsymbol{K}^{(i)}, \quad \boldsymbol{L}(t) = \sum_{i=1}^{N} \alpha_i(t)\boldsymbol{L}^{(i)}.$$

This interpolation scheme ensures continuous gain variations as the operating point evolves, a behavior that is illustrated in the simulation results presented in Section 4. The overall quasi-LPV control architecture, illustrating the interaction between the nonlinear plant, the local controllers and observers, and the geometric interpolation mechanism, is depicted in Figure 3.

## 4 Results

This section presents numerical simulation results obtained using the full nonlinear model of the magnetic levitation system. The objective of these simulations is to evaluate the tracking performance, control effort, state estimation accuracy, and robustness of the proposed quasi-LPV control strategy with geometric interpolation.

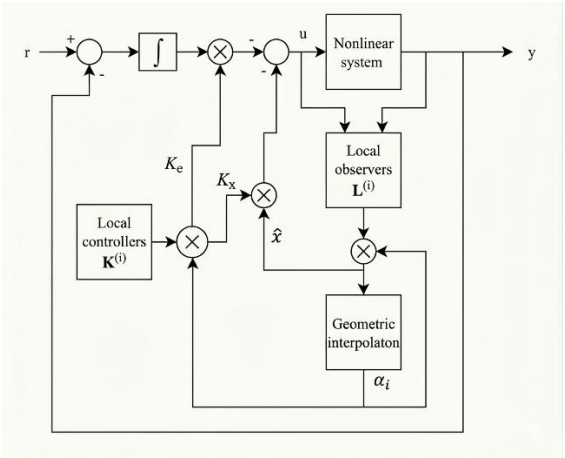


**Figure 3**. Overall quasi-LPV control architecture with geometric interpolation of local controllers and observers.

### 4.1 Simulation setup and test scenarios

All simulations were carried out in MATLAB/Simulink using the full nonlinear state-space model of the magnetic levitation system described in Section 2, with the physical parameters listed in Table 1. The control law and the computation of the scheduling parameters were executed using the estimated states derived from the local observers. To ensure consistency within the admissible operating range of the parametric domain, all initial conditions were set identically to zero.

The local tracking controllers were designed to satisfy time-domain performance specifications defined during the control synthesis stage. In particular, the desired closed-loop behavior was characterized by a limited overshoot and a specified settling time, which guided the selection of the closed-loop poles at each vertex of the quasi-LPV polytope. These specifications were chosen to ensure a fast and well-damped transient response while avoiding excessive control effort. The performance specifications were consistently met in all test scenarios.

The reference signal applied to the system consisted of constant position commands with successive step changes around the nominal equilibrium point. This test scenario was selected to evaluate the ability of the proposed control strategy to achieve accurate reference tracking and smooth transitions between operating points.

In addition to nominal tracking conditions, robustness-oriented simulations were conducted. These included external disturbances applied to the control input and additive noise in the position measurement, allowing assessment of the closed-loop behavior under non-ideal operating conditions.

### 4.2 Reference tracking performance

The tracking performance of the proposed control strategy is illustrated in Figure 4. This figure shows the time evolution of the sphere position $x_1(t)$ compared with the reference signal for a sequence of step changes.

As observed in the figure, the closed-loop system achieves accurate tracking of the reference position with zero steady-state error. The transient response remains well behaved, with no excessive overshoot or oscillatory behavior, despite the intrinsic open-loop instability and strong nonlinearities of the plant. These results confirm the effectiveness of the local tracking controllers and the geometric interpolation mechanism in achieving consistent performance across the operating range.

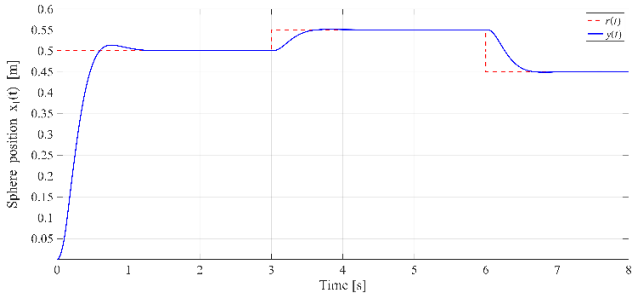


**Figure 4**. Reference tracking performance of the magnetic levitation system under the proposed quasi-LPV control scheme.

### 4.3 Control effort and actuation behavior

The corresponding control input $u(t)$ generated during the tracking experiment is shown in Figure 5. The control signal remains bounded throughout the simulation and exhibits smooth variations as the reference changes.

The absence of high-frequency oscillations or large control peaks indicates that the interpolated controller does not introduce aggressive or impractical actuation demands. This behavior is particularly relevant for magnetic levitation systems, where actuator saturation and unidirectional input constraints must be considered. The results demonstrate that the proposed control strategy achieves the desired tracking performance while maintaining a reasonable control effort.

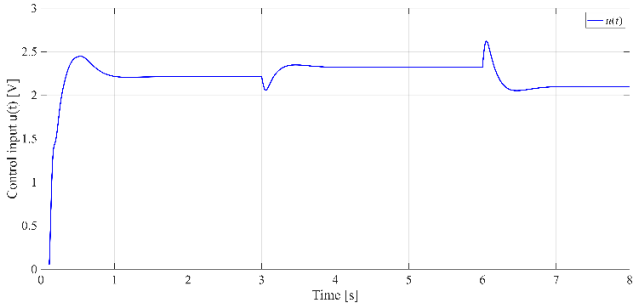


**Figure 5**. Control input corresponding to the reference tracking experiment.

### 4.4 Scheduling parameters and interpolation weights

The evolution of the scheduling parameters and the corresponding interpolation weights is shown in Figures 6 and 7, respectively. The parameters vary continuously within

their prescribed bounds as the operating point of the system changes.

The interpolation weights remain positive and sum to unity at all times, confirming that the geometric interpolation mechanism produces convex combinations of the local controllers and observers. The smooth variation of the weights ensures gradual transitions between local designs and prevents abrupt changes in the control law, contributing to the overall robustness and numerical stability of the closed-loop system.

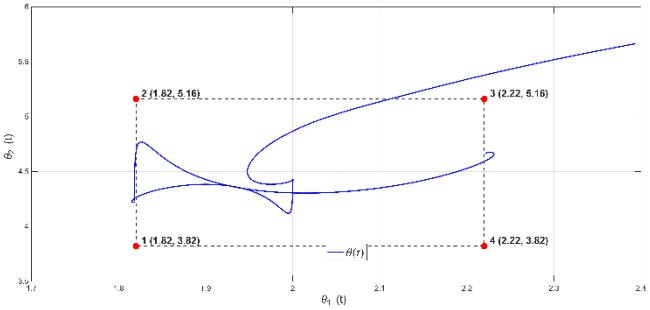


**Figure 6**. Time evolution of the scheduling parameter vector $\boldsymbol{\theta}(t)$ during the reference tracking experiment.

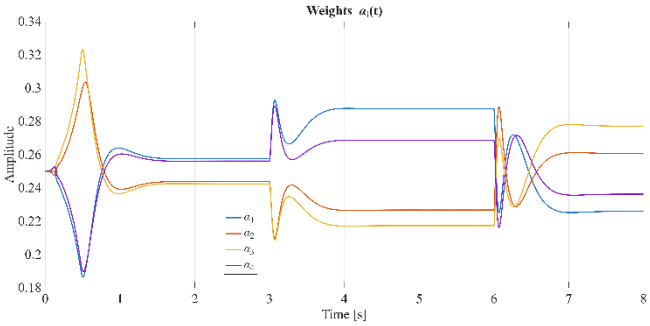


**Figure 7**. Time evolution of the geometric interpolation weights $\alpha_i(t)$ associated with the quasi-LPV controller.

### 4.5 Robustness assessment

The robustness of the proposed quasi-LPV control strategy was evaluated through simulation experiments addressing two representative non-ideal operating conditions: external disturbances applied to the control input and measurement noise affecting the system output. These scenarios are particularly relevant in magnetic levitation applications, where actuator imperfections and noisy sensing are commonly encountered.

The closed-loop response of the system under an external disturbance acting on the control input is shown in Figure 8. In this experiment, a constant additive disturbance of 0.21 V was applied to the control input starting at $t = 4.5$ s while the system was tracking a constant reference position. The disturbance produces a transient deviation in the output; however, the controller rapidly compensates for its effect and restores accurate reference tracking. No sustained oscillations or instability are observed after the disturbance is applied, indicating effective disturbance rejection capability.

The robustness of the proposed scheme with respect to measurement noise is analyzed next. In this case, additive noise was introduced in the measurement of the sphere position, which is the only directly measured output of the system. The noise signal corresponds to band-limited white noise with zero mean and finite variance, representing sensor noise and electronic measurement imperfections commonly encountered in practical implementations. The resulting closed-loop response of the system in the presence of measurement noise is shown in Figure 9. Despite the noisy measurement, the system remains stable and preserves satisfactory reference tracking. Small fluctuations in the output are observed as a consequence of the measurement noise; however, these oscillations remain bounded and do not compromise the overall tracking performance. The corresponding control signal generated under noisy measurement conditions is depicted in Figure 10. As expected, the control input exhibits oscillatory behavior associated with the observer-based compensation of the noisy output signal. Nevertheless, the control effort remains bounded and does not exhibit drift or instability, confirming that the observer and the geometric interpolation mechanism operate coherently in the presence of measurement noise.

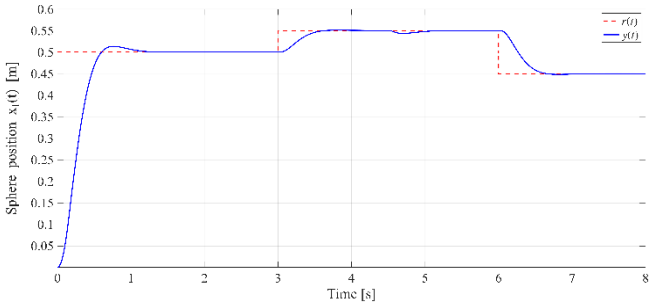


**Figure 8**. Closed-loop response under an input disturbance during reference tracking.

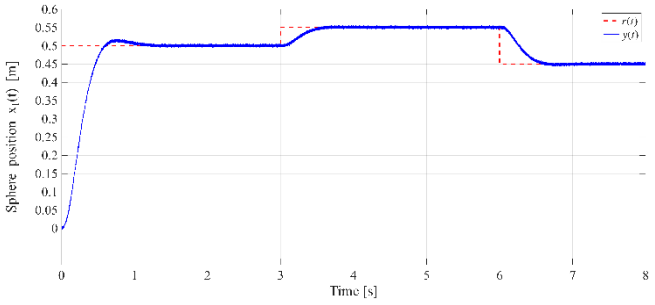


**Figure 9**. Closed-loop response under output measurement noise during reference tracking.

Overall, the robustness results indicate that the proposed quasi-LPV control strategy with geometric interpolation maintains stability and acceptable performance under both

input disturbances and output measurement noise. The separation between control and estimation dynamics, together with the smooth interpolation of local controllers and observers, contributes to the reliable behavior of the closed-loop system under non-ideal operating conditions.

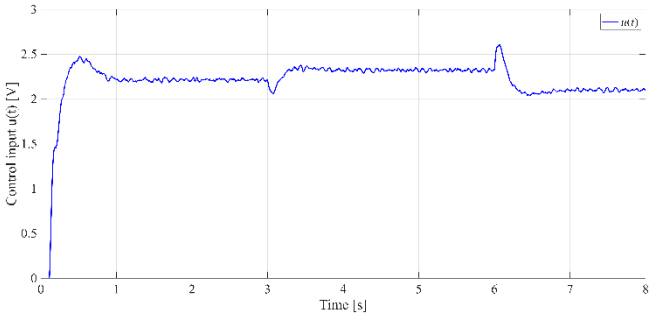


**Figure 10**. Control input under output measurement noise

## 5 Conclusions

This article has presented a gain-scheduling control strategy for a magnetic levitation system based on a quasi-LPV modeling framework and a geometric interpolation mechanism. By incorporating the nonlinear dynamics of the plant into an endogenous and bounded parameter vector, the original nonlinear system was represented as a family of linear time-invariant models evaluated over a compact parametric domain. This formulation enabled the systematic design of local tracking controllers and state observers using linear state-space techniques.

A central contribution of this work is the adoption of a distance-based geometric interpolation scheme to combine the local designs into a global controller and observer. Unlike analytical interpolation approaches, the proposed mechanism guarantees convex combinations and strictly positive interpolation weights throughout the operating region, which is particularly advantageous for magnetic levitation systems subject to physical constraints on the control input. This feature simplifies the implementation while preserving smooth gain variations and consistent closed-loop behavior.

Simulation results obtained using the full nonlinear model confirmed that the proposed control strategy achieves accurate tracking of constant reference positions with bounded control effort, despite the intrinsic open-loop instability of the plant and the presence of disturbances and measurement noise. The use of full-order state observers provided reliable estimation of the non-measurable states and ensured coherent scheduling parameter computation for the interpolation process.

Overall, the results demonstrate that geometric interpolation constitutes an effective and practically attractive alternative to analytical interpolation methods within quasi-LPV control schemes, particularly for nonlinear and open-loop unstable systems such as magnetic levitation plants. The proposed approach achieves a favorable balance between modeling fidelity, implementation simplicity, and control performance.

Future work will focus on experimental validation using a laboratory-scale magnetic levitation setup, the extension of the methodology to discrete-time implementations, and the incorporation of actuator and state constraints within the quasi-LPV framework.

## Acknowledgments

The authors are grateful for the support provided by the Research Program of the Metropolitan University in Caracas, Venezuela, through project number PI-B-02-24-25.

## References

Bidikli, B. (2020). An observer-based adaptive control design for the maglev system. Transactions of the Institute of Measurement and Control, 42(14), 2771–2786. https://doi.org/10.1177/0142331220932396

Bombois, X., Ghosh, D., Scorletti, G., & Huillery, J. (2021). LPV system identification for control using the local approach. International Journal of Control, 94(7), 390-410.

Cisneros, P. S., Sridharan, A., & Werner, H. (2018). Constrained predictive control of a robotic manipulator using quasi-LPV representations. IFAC-PapersOnLine, 51(26), 118–123. https://doi.org/10.1016/j.ifacol.2018.11.158

Hypiusova, M. & Kozakova, A. (2017). Robust PID controller design for the magnetic levitation system: Frequency domain approach. Proc. of 21st International Conference on Process Control, Slovakia, 274-279.

Khalil, H. K. (2002). Nonlinear systems (3rd ed.). Prentice Hall.

Kuo, B. C. (1996). Automatic control systems (7th ed.). Prentice Hall.

Lee, T., Su, J. & Yu, K. (2007) Implementation of the state-space feedback control scheme for a mag-netic levitation system. Proc 2nd IEEE Conference on Industrial Electronics and Applications, China, 548-553.

Leith, D. J., & Leithead, W. E. (2000). Survey of gain-scheduling analysis and design. International Journal of Control, 73(11), 1001–1025. https://doi.org/10.1080/002071700411311

Li, S., Nguyen, A.-T., Guerra, T.-M., & Kruszewski, A. (2023). Reduced-order model-based dynamic tracking for soft manipulators: Data-driven LPV modeling, control design and experimental results. Control Engineering Practice, 138, 105618. https://doi.org/10.1016/j.conengprac.2023.105618

Muthairi, N., & Zribi, M. (2004). Sliding-mode control of a magnetic levitation system. Mathematical Problems in Engineering, 2004, 93–107. https://doi.org/10.1155/S1024123X04309024

Ogata, K. (2010). Modern control engineering (5th ed.). Prentice Hall.

Robles, R., Sala, A., & Bernal, M. (2019). Performance-oriented quasi-LPV modeling of nonlinear systems. International Journal of Robust and Nonlinear Control, 29(5), 1230–1248. https://doi.org/10.1002/rnc.4444

Rotondo, D. (2018). Advances in gain-scheduling and fault tolerant control techniques. Springer. https://doi.org/10.1007/978-3-319-62902-5

Rugh, W. J., & Shamma, J. S. (2000). Research on gain-scheduling. Automatica, 36(10), 1401–1425. https://doi.org/10.1016/S0005-1098(00)00058-3

Rusar, L., Krhovjak, A. and Bobal, V. (2017). Predictive control of the magnetic levitation model. Proc. of 21st International Conference on Process Control, Slovakia, 345-350.

Shieh, H., Siao, J., & Liu, Y. (2010). A robust optimal sliding-mode control approach for magnetic levitation systems. Asian Journal of Control, 12(4), 480–487. https://doi.org/10.1002/asjc.210

Sira-Ramírez, H., Márquez, R., Rivas-Echeverria, F., & Llanes-Santiago, O. (2005). Control de sistemas no lineales: Linealización aproximada, extendida, exacta. Madrid: Pearson Prentice Hall.

Tan, W., Packard, A., & Balas, G. (2000). Quasi-LPV modeling and LPV control of a generic missile. In Proceedings of the American Control Conference (pp. 3692–3696). IEEE. https://doi.org/10.1109/ACC.2000.879259

Teppa-Garran, P., & Andrade-Da Silva, J. M. (2009). Control of linear parameter-varying systems using analytical interpolation. Ciencia e Ingeniería, 30(1), 93–101.

Teppa-Garran, P., & Faggioni, M. (2023). Robust tracking in two-degree-of-freedom control systems: magnetic levitation system. Latin American Applied Research, 53(4), 303-308.

Teppa-Garran, P., Muñoz-de Escalona, D., & Zambrano, J. (2025). Liquid level tracking for a coupled tank system using quasi-LPV control. Ingenius, (33), 15–26. https://doi.org/10.17163/ings.n33.2025.02

Wang, J., Chen, L., & Xu, Q. (2021). Disturbance estimation-based robust model predictive position tracking control for magnetic levitation systems. IEEE/ASME Transactions on Mechatronics, 27(1), 81–92. https://doi.org/10.1109/TMECH.2021.3092715

***Received:*** *april 20, 2026*

***Accepted:*** *june 20, 2026*

***Pedro Teppa-Garrán*** *received the B.S. degree in Electrical Engineering in 1990 at the Universidad Metropolitana (UNIMET) in Caracas, Venezuela, the Master degree in Electronic Engineering in 1994 and the Master degree in Mathematics in 1998; both of them, from the Universidad Simón Bolívar (USB), Caracas, Venezuela. He also received the Ph.D. in Control Systems in 2003 at Université Paul Sabatier in Toulouse, France and completed a Postdoctoral Research in LAAS-CNRS during 2012-2013 in Toulouse, France. He is currently a full professor of UNIMET*
*https://orcid.org/ 0000-0001-6384-3185*

***Diego Zárraga****: Electrical Engineer from UNIMET.*
*Email:diego.zarraga@correo.unimet.edu.ve*
*https://orcid.org/0009-0009-8920-6163*

*Artículo de Investigación. Revista Ciencia e Ingeniería. Vol. 47, No. 3 pp. 347-356, agosto-noviembre, 2026.*
*ISSN 1316-7081. ISSN Elect. 2244-8780 Universidad de los Andes (ULA)*

# Tamaño de cristalito, microdeformación de la red e identificación de segregado mediante ImageJ en el sistema semiconductor $Cd_{0,67-y}Mn_{0,33}Cr_yTe$ $(0,05 \leq y \leq 0,15)$

# Crystallite size, lattice microstrain, and segregate identification using ImageJ in the $Cd_{0,67-y}Mn_{0,33}Cr_yTe$ $(0,05 \leq y \leq 0,15)$ semiconductor system

**Villarreal, Manuel[1]*; Pimentel, Jorge[1]; Turatti, Agueda[1]; Sherdien, Richard[1]; Terán, Juan[1]; Silva, Pedro[2]**
[1]Instituto de Matemática, Estatística e Física, Universidade Federal do Rio Grande, Rio Grande/RS, Brasil.
[2]Laboratorio de Física de la Materia Condensada, Centro de Física, Instituto Venezolano de Investigaciones Científicas, Caracas, Venezuela.
*mavu8473@gmail.com

**Resumen**

*Se sintetizaron tres muestras del sistema semiconductor cuaternario $Cd_{0,67-y}Mn_{0,33}Cr_yTe$ (y = 0,05; 0,10; 0,15) mediante la técnica de fusión directa de sus elementos constituyentes. El tamaño medio de cristalito y la microdeformación de la red se determinaron a partir de análisis de difracción de rayos X, empleando el método de Williamson–Hall. Los resultados evidencian un adecuado crecimiento cristalino y una buena calidad estructural, observándose una disminución del tamaño medio de cristalito con el incremento de la concentración de Cr. Las micrografías fueron obtenidas mediante microscopía electrónica de barrido en modo de electrones retrodispersados. La eficiencia de la segmentación automática se evaluó utilizando el plugin Trainable WEKA Segmentation (TWS) integrado en ImageJ, mediante la métrica de exactitud, compa-rando los resultados con las zonas de segregación identificadas en mapas elementales obtenidos por espectroscopía de dispersión de energía. Los resultados muestran que el desempeño del método depende fuertemente de la topografía de la muestra, siendo más confiable en regiones planas y con buen contraste. Además, se presentan las proporciones segmentadas para cada muestra, lo que permite discutir las limitaciones y el potencial de la técnica en el análisis de materiales semicondutores complejos.*

**Palabras claves**: difracción de rayos X, método de Williamson-Hall, tamaño de cristalito, microdeformación de la red, segmentación automática, ImageJ, análisis de micrográfias.

**Abstract**

*Three samples of the quaternary semiconductor system $Cd_{0.67-y}Mn_{0.33}Cr_yTe$ (y = 0.05, 0.10, 0.15) were synthesized using the direct melting technique of their constituent elements. The average crystallite size and lattice microstrain were determined from X-ray diffraction analysis using the Williamson–Hall method. The results reveal adequate crystalline growth and good structural quality, showing a decrease in the average crystallite size with increasing Cr concentration. Micrographs were obtained by scanning electron microscopy in backscattered electron mode. The efficiency of the automatic segmentation was evaluated using the Trainable WEKA Segmentation (TWS) plugin integrated in ImageJ through the accuracy metric, comparing the results with segregation zones identified in elemental maps obtained by energy-dispersive spectroscopy. The results indicate that the performance of the method strongly depends on the sample topography, being more reliable in flat regions with good contrast. Additionally, the segmented proportions for each sample are presented, allowing the limitations and potential of the technique in the analysis of complex semiconductor materials to be discussed.*

**Keywords:** X-ray diffraction, Williamson-Hall method, crystallite size, lattice microstrain, automatic segmentation, ImageJ, micrograph analysis.

## 1 Introducción

Los materiales semiconductores magnéticos (MSM) se obtienen a partir de semiconductores convencionales mediante la sustitución parcial de átomos no magnéticos en la subred catiónica por iones magnéticos, tales como cromo, hierro, manganeso y cobalto. Esta modificación estructural permite el control simultáneo de las propiedades electrónicas y magnéticas del material, lo que abre nuevas perspectivas para el desarrollo de dispositivos avanzados, incluyendo memorias no volátiles, circuitos lógicos basados en espín y dispositivos de estado sólido reconfigurables. En este contexto, el creciente interés científico y tecnológico en estos sistemas radica en la posibilidad de integrar funcionalidades electrónicas y magnéticas en un único material, ampliando su potencial en aplicaciones espintrónicas (Dietl, 2010; Villarreal et al., 2012, 2013; Wolf et al., 2001; Yoon et al., 2006).

En los últimos años, la investigación se ha orientado hacia sistemas cuaternarios codopados con metales de transición, donde combinaciones como Mn-Fe o Mn-Cr permiten un ajuste fino de las propiedades estructurales y magnéticas. Entre estos sistemas, el $Cd_{1-x-y}Mn_xCr_yTe$ ha mostrado particular relevancia, reportándose temperaturas de Curie (Tc) de hasta 362 K para x = 0,37 e y = 0,10 (Hwang et al., 2013). En estos materiales, el comportamiento ferromagnético se atribuye a las interacciones de intercambio entre los iones magnéticos, siendo la concentración relativa de cada elemento un factor determinante en la temperatura de Curie y la magnetización (Hwang et al., 2013; Irie et al., 1995; Shen et al., 2009; Verma et al., 2022).

Desde el punto de vista estructural, estudios de difracción de rayos X han demostrado que el sistema $Cd_{1-x-y}Mn_xCr_yTe$ cristaliza en estructura cúbica tipo blenda de zinc, con una disminución lineal del parámetro de red al incrementar la concentración de Cr, en concordancia con la ley de Vegard. Este comportamiento sugiere la incorporación sustitucional de Cr en la red huésped de CdTe (Hwang et al., 2013). Sin embargo, en muestras policristalinas se ha evidenciado la formación de fases secundarias, particularmente $Cr_2Te_3$, cuya fracción aumenta con el contenido de Cr (Villarreal et al., 2026). Asimismo, el análisis microestructural mediante microscopía electrónica de barrido (MEB) revela que el incremento de Cr induce variaciones significativas en la microestructura y en la composición local, favoreciendo procesos de segregación más pronunciados a mayores concentraciones.

No obstante, la interpretación visual de las micrografías MEB puede verse limitada por factores como la topografía de la muestra, efectos de sombreado, grietas, fracturas y superposición de fases, lo que dificulta la identificación precisa de heterogeneidades. En este sentido, las técnicas de segmentación de imágenes basadas en aprendizaje automático han emergido como herramientas robustas para la clasificación de regiones en función de patrones de textura, contraste y morfología, mejorando la reproducibilidad y sensibilidad del análisis (Lormand et al., 2018; Mallick et al., 2016; Salum et al., 2022). Entre estas herramientas, el software ImageJ destaca por su amplia validación en la literatura y su versatilidad, gracias a la integración de múltiples *plugins*. En particular, el módulo Trainable WEKA Segmentation (TWS) constituye una técnica de aprendizaje supervisado para la clasificación de píxeles, basada en algoritmos como *Random Forest*. Aunque originalmente fue desarrollado para aplicaciones en bioimagen, su flexibilidad permite su adaptación a problemas de caracterización de materiales (Arganda-Carreras et al., 2017).

Sin embargo, el carácter semiautomático del TWS implica la intervención del usuario en etapas como la selección de regiones de interés y la definición de clases, lo que puede introducir variabilidad en los resultados, especialmente en imágenes con morfologías complejas o bajo contraste. Por ello, resulta fundamental evaluar cuantitativamente su desempeño y establecer las condiciones en las que proporciona resultados confiables (Fan et al., 2012; Fan & Lee, 2015; Iglesias, 2017; Kim et al., 2016).

Por otra parte, es importante distinguir entre el tamaño de cristalito y el tamaño de grano. Mientras que el tamaño de grano observado por MEB puede incluir múltiples dominios cristalinos, el tamaño de cristalito corresponde a regiones coherentes de difracción y se determina a partir de técnicas como la difracción de rayos X. Métodos como Scherrer, Williamson–Hall y el refinamiento de Rietveld son ampliamente utilizados para este propósito.

En este contexto, el presente trabajo tiene como objetivo determinar el tamaño promedio de cristalito y la microdeformación de la red cristalina mediante el análisis de difracción de rayos X utilizando el método de Williamson–Hall, así como evaluar la eficacia del módulo Trainable WEKA Segmentation en la identificación de zonas segregadas en micrografías del sistema $Cd_{0,67-y}Mn_{0,33}Cr_yTe$ ($0,05 \leq y \leq 0,15$). Asimismo, se analiza el desempeño del método frente a distintas morfologías y la influencia de factores como la topografía y la homogeneidad de las muestras sobre la confiabilidad de la segmentación, con el fin de delimitar los contextos más adecuados para su aplicación en el análisis microestructural.

## 2 Procedimiento Experimental

### 2.1 Sintesis de las muestras del sistema

Las muestras policristalinas de $Cd_{0,67-y}Mn_{0,33}Cr_yTe$ fueron sintetizadas mediante la fusión directa de los elementos constituyentes en ampollas de cuarzo evacuadas y previamente sometidas a pirólisis, con el fin de evitar reacciones indeseadas entre el material y el recipiente de cuarzo. Estas ampollas fueron dispuestas verticalmente en un horno

resistivo y calentadas hasta alcanzar la completa liquefacción. Durante la fase líquida, las ampollas se agitaron periódicamente para favorecer la homogeneización del material, tal como se reporta en la referencia (Villarreal et al., 2026).

### 2.2 Determinación estructural. Difracción de rayos X

Para la caracterización estructural mediante difracción de rayos X (DRX), se pulverizaron mecánicamente en un mortero aproximadamente 100 mg de cada muestra hasta obtener un polvo fino y homogéneo. El material se depositó sobre un portamuestras de fondo cero, utilizando una fina capa de vaselina como agente fijador. Los patrones de DRX en polvo se registraron a temperatura ambiente, en modo de reflexión θ/θ, empleando un difractómetro EMPYREAN equipado con un tubo de cobre (radiación CuKα y CuKβ: $\lambda_1$ = 1,5406 Å y $\lambda_2$ = 1,5444 Å), operando a 40 kV y 40 mA. Las mediciones se realizaron en el rango de 10° a 90° en 2θ, con un paso de 0,02° y un tiempo de conteo de 1 s por paso. El silicio se utilizó como patrón externo para la corrección instrumental. El análisis cuantitativo de los patrones de difracción se llevó a cabo mediante el método de Rietveld, lo que permitió obtener los parámetros estructurales y evaluar la calidad del ajuste.

Durante el análisis de los patrones de DRX, se observó un ensanchamiento de los picos de difracción. Este fenómeno puede originarse no solo por la contribución instrumental, sino también por efectos microestructurales intrínsecos al material, como el tamaño medio de cristalito y las deformaciones de la red cristalina. Para separar y cuantificar estas contribuciones, se aplicó el método de Williamson–Hall en su forma simplificada, asumiendo un ensanchamiento isotrópico, descrito por la ecuación:

$$\beta \cos(\theta) = (k\lambda/D) + 4\varepsilon \operatorname{sen}(\theta) \qquad (1)$$

donde β corresponde al ancho a media altura (FWHM) del pico de difracción, en radianes y corregido por el ensanchamiento instrumental; θ es el ángulo de Bragg (en radianes); k es el factor de forma (≈ 0,9); λ (= 0,15406 nm) es la longitud de onda de la radiación incidente; D representa el tamaño medio de cristalito; y ε corresponde a la microdeformación (*strain*) de la red cristalina.

### 2.3 Análisis microestructural. Identificación de segregado usando ImageJ

La microestructura de las muestras fue investigada mediante un microscopio electrónico de barrido (MEB), modelo JEOL JSM-6610LV, operando con una tensión de aceleración de 15 kV. Asimismo, se realizaron análisis por espectroscopía de energía dispersiva de rayos X (EDS, por sus siglas en inglés: *Energy Dispersive Spectroscopy*). Dado que las muestras presentan carácter metálico, no fue necesario someterlas a un proceso de metalización. El preparado consistió en la fijación de las muestras sobre *stubs* utilizados como soporte dentro de la cámara del microscopio.

En cada una de las tres muestras se obtuvieron micrografías con un aumento de 600 veces, empleando el modo de electrones retrodispersados (BEC, por sus siglas en inglés: *Backscattered Electron Composition*). El contraste observado en las micrografías resalta las variaciones en el número atómico de los elementos presentes. En este contexto, regiones con distinta apariencia, tales como granos dispersos a lo largo de la superficie, fueron seleccionadas para su análisis mediante EDS, junto con regiones homogéneas de la matriz cristalina. Este análisis permitió además la obtención de mapas elementales correspondientes a cada uno de los elementos químicos en las micrografías.

Las micrografías obtenidas presentan una resolución de 2560×1920 píxeles y fueron procesadas sin la aplicación de correcciones previas. El análisis de imágenes se realizó íntegramente en el software ImageJ, empleando el plugin TWS, accesible a través de la ruta Plugins → Segmentation → Trainable WEKA Segmentation. En cada micrografía, las regiones de interés fueron seleccionadas manualmente y clasificadas en dos clases: Clase 1, correspondiente a las zonas de segregación (regiones granuladas), y Clase 2, correspondiente a la matriz cristalina continua. Una vez completado el entrenamiento, el clasificador se aplicó a las tres micrografías, generando las respectivas máscaras de segmentación. Estas máscaras fueron convertidas a 8 bits (Image → Type → 8-bit) y posteriormente binarizadas (Process → Binary → Make Binary). En las imágenes resultantes, los píxeles blancos representan las zonas clasificadas como segregación de cromo, mientras que los píxeles negros corresponden a la matriz cristalina del material. Finalmente, las regiones segmentadas fueron cuantificadas mediante el comando Analyze → Analyze Particles, lo que permitió extraer parámetros como área total, área media, número de partículas y fracción superficial.

La validación de las segmentaciones se llevó a cabo mediante la comparación directa con los mapas elementales de cromo obtenidos por EDS, los cuales se utilizaron como referencia para evaluar la fidelidad del proceso de segmentación. Tanto las micrografías segmentadas como los mapas elementales fueron ajustados a la misma resolución mediante ImageJ y convertidos a formato binario. El desempeño de la segmentación realizada con TWS se evaluó utilizando la exactitud como métrica cuantitativa. A partir de la superposición de las imágenes binarizadas, se realizó el conteo de píxeles correcta e incorrectamente clasificados mediante el comando Image Calculator (Process → Image Calculator), empleando operaciones lógicas entre la imagen de referencia (mapa EDS) y la segmentación generada por TWS. Las operaciones utilizadas fueron AND, OR y Subtract, permitiendo identificar las

categorías de verdaderos positivos (VP), falsos positivos (FP), verdaderos negativos (VN) y falsos negativos (FN).

La operación AND se utilizó para determinar los verdaderos positivos (VP), es decir, los píxeles clasificados como presencia de Cr en ambas imágenes. Los falsos positivos (FP) se obtuvieron a partir de la intersección entre la imagen segmentada y la inversión del mapa elemental, representando regiones identificadas por TWS como ricas en Cr, pero no confirmadas por EDS. Los falsos negativos (FN) se determinaron mediante la intersección entre la inversión de la imagen segmentada y el mapa elemental, correspondiendo a regiones no identificadas por TWS, pero detectadas por EDS. Por último, los verdaderos negativos (VN) corresponden a las zonas donde ambas imágenes indican ausencia de Cr, pudiendo obtenerse directamente o como la diferencia entre el total de píxeles y la suma de VP, FP y FN.

El conteo de píxeles en cada categoría se realizó mediante el comando Measure (Analyze → Measure), configurado para cuantificar únicamente las áreas correspondientes a los píxeles blancos. Para garantizar la validez de la comparación, las imágenes fueron previamente alineadas y redimensionadas cuando fue necesario. El conteo de los píxeles resultantes de cada operación lógica se realizó mediante la herramienta *Measure* (Analyze → Measure), tras la generación de las imágenes intermedias. A partir de estos valores, fue posible calcular la exactitud (o precisión) según la ecuación:

$$\text{Exactitud} = (VP + VN) / (VP + VN + FP + FN) \qquad (2)$$

que expresa la proporción de píxeles correctamente clasificados (VP y VN) con respecto al total de píxeles.

## 3 Discusión y Resultados

### 3.1 Tamaño de cristalito y microdeformación de la red

La Fig. 1 presenta el refinamiento Rietveld final para el sistema $Cd_{0,67-y}Mn_{0,33}Cr_yTe$. Parte del análisis estructural de estos materiales ya ha sido reportado previamente (Villarreal et al., 2026), y se retoma aquí con fines de comparación y discusión de los resultados. Los refinamientos estructurales se realizaron utilizando 4000 puntos de intensidad y 15 reflexiones independientes, considerando un total de 26 parámetros instrumentales y cristalográficos, lo que condujo a índices de confiabilidad considerados excelentes. El análisis estructural reveló la presencia de dos fases cristalinas en los compuestos estudiados: una fase principal correspondiente a la estructura tipo blenda de zinc (grupo espacial F-43m, No. 216) y una fase secundaria asociada al compuesto binario $Cr_2Te_3$.

De acuerdo con los resultados del refinamiento Rietveld, la fracción en peso de la fase secundaria aumenta con el incremento de la concentración de Cr. Asimismo, se observa que la constante de red del sistema disminuye linealmente con el aumento de la concentración de Cr, en concordancia con la ley de Vegard, descrita por la relación $a = (6{,}432 - 0{,}219\ y)$ Å. Este comportamiento sugiere que los iones de Cr sustituyen parcialmente los sitios de Cd en la red huésped de CdTe, al menos hasta una concentración del 15%.

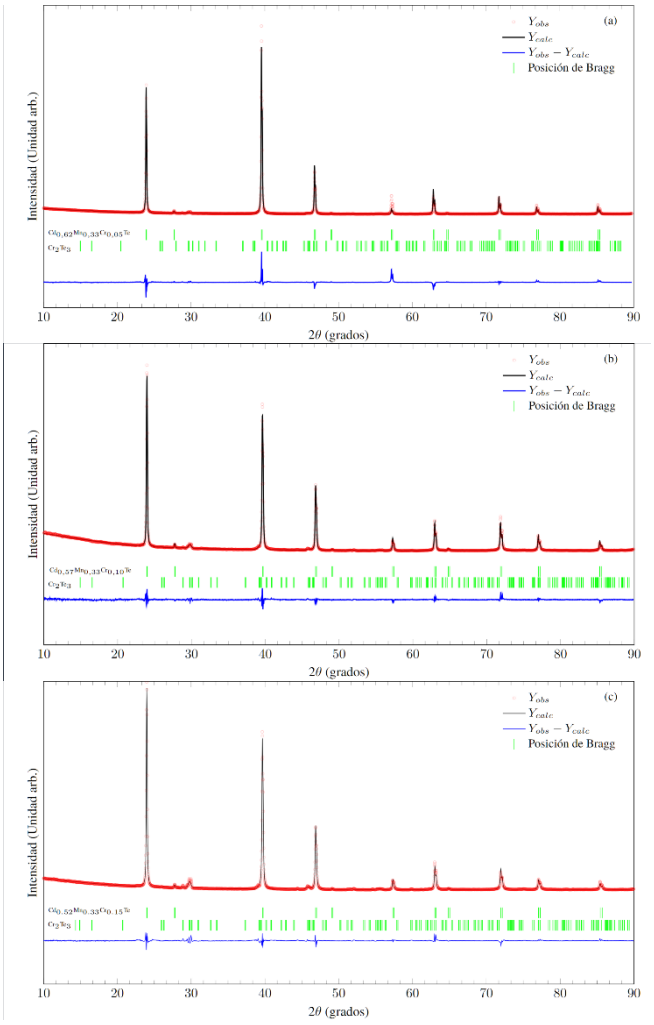


**Fig. 1**. Refinamiento Rietveld para el sistema $Cd_{0,67-y}Mn_{0,33}Cr_yTe$: (a) y = 0,05; (b) 0,10; (c) 0,15.

Las Tablas 1 y 2 presentan los parámetros obtenidos a partir del análisis de los difractogramas para las muestras con y = 0,05; y = 0,15, respectivamente. En el caso de la composición con y = 0,10, el ajuste mediante el método de Williamson–Hall resultó estadísticamente no significativo, evidenciado por un valor reducido del $\chi^2$ y una deficiente correlación lineal, lo que compromete la validez de los parámetros microestructurales estimados (tamaño de cristalito y microdeformación). En consecuencia, dichos resultados fueron descartados del análisis cuantitativo y no se incluyen. La muestra patrón (instrumental) empleada en las mediciones de

DRX fue el silicio. En la Tabla 3 se reportan los parámetros obtenidos del Silicio.

Tabla 1. Datos obtenidos para el compuesto $Cd_{0,62}Mn_{0,33}Cr_{0,05}Te$.

| hkl | θ (rad) | FWMH (rad) | $\beta_{cor}$ (rad) | βcos(θ) | 4sen(θ) |
|---|---|---|---|---|---|
| 200 | 0,24154 | 0,00164 | 0,00084 | 0,00081 | 0,95680 |
| 311 | 0,40789 | 0,00174 | 0,00105 | 0,00097 | 1,58668 |
| 400 | 0,49857 | 0,00182 | 0,00117 | 0,00103 | 1,91269 |
| 422 | 0,62602 | 0,00200 | 0,00135 | 0,00109 | 2,34368 |
| 333 | 0,67061 | 0,00209 | 0,00137 | 0,00108 | 2,48585 |

$\beta_{cor} = (\beta_{obs}^2 - \beta_{inst}^2)^{1/2}$; $\beta_{obs}$ = FWMH de la muestra;
$\beta_{inst}$ = FWMH de la muestra patrón.

Tabla 2. Datos obtenidos para el compuesto $Cd_{0,52}Mn_{0,33}Cr_{0,15}Te$.

| hkl | θ (rad) | FWMH (rad) | $\beta_{cor}$ (rad) | βcos(θ) | 4sen(θ) |
|---|---|---|---|---|---|
| 200 | 0,24231 | 0,00209 | 0,00154 | 0,00150 | 0,95978 |
| 311 | 0,40923 | 0,00232 | 0,00186 | 0,00171 | 1,59161 |
| 400 | 0,50053 | 0,00544 | 0,00526 | 0,00462 | 1,91956 |
| 422 | 0,62827 | 0,00666 | 0,00649 | 0,00525 | 2,35098 |
| 333 | 0,67308 | 0,00706 | 0,00688 | 0,00538 | 2,49359 |

Tabla 3. Datos obtenidos para la muestra patrón (Si).

| hkl | θ (rad) | FWMH (rad) |
|---|---|---|
| 111 | 0,24819 | 0,00141 |
| 220 | 0,41277 | 0,00138 |
| 311 | 0,48974 | 0,00140 |
| 400 | 0,60327 | 0,00148 |
| 331 | 0,66593 | 0,00157 |

En la Fig. 2 se presentan los diagramas de Williamson–Hall para los compuestos analizados. A partir de la ecuación (1), se estimaron el tamaño medio de cristalito (D) y la microdeformación de red (ε) considerando el modelo de deformación uniforme. Para el compuesto $Cd_{0,62}Mn_{0,33}Cr_{0,05}Te$ se obtuvieron: D = 210 nm y $\varepsilon = 1{,}8 \times 10^{-4}$, mientras que para $Cd_{0,52}Mn_{0,33}Cr_{0,15}Te$ se determinaron: D = 83 nm y $\varepsilon = 2{,}9 \times 10^{-3}$. La reducción de D con el incremento del contenido de Cr sugiere un aumento en los mecanismos de ensanchamiento asociados a tamaño finito, así como una mayor contribución de tensiones internas, lo que limita la coherencia cristalina. Este comportamiento puede atribuirse a la incorporación sustitucional de Cr en la red tipo blenda de zinc del CdTe, generando campos de deformación locales debido a la diferencia de radios iónicos y a la consecuente distorsión de la celda unitaria. Asimismo, la presencia creciente de la fase secundaria $Cr_2Te_3$ (cuya fracción en peso aumenta de 0,15% a 2,78%) puede actuar como centros de nucleación heterogénea o como barreras al crecimiento, favoreciendo la reducción del tamaño de los dominios coherentes de difracción.

En cuanto a la microdeformación, el incremento de ε con la concentración de Cr indica una mayor distribución de tensiones de red, asociada tanto a defectos puntuales (sustitucionales y vacancias) como a la interacción entre fases. No obstante, los valores obtenidos se mantienen dentro de un régimen bajo ($10^{-4}$ – $10^{-3}$), lo que sugiere que el sistema conserva un nivel moderado de desorden cristalino. En conjunto, el análisis W–H evidencia un compromiso entre tamaño de cristalito y microdeformación, coherente con los resultados de refinamiento estructural por DRX y consistente con un material policristalino de buena calidad estructural, aunque progresivamente afectado por la incorporación de Cr.

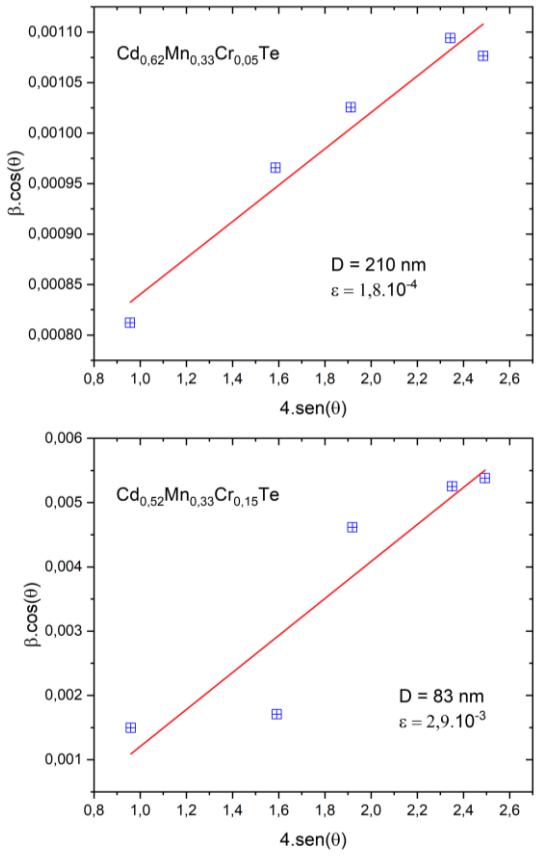


**Fig. 2.** Gráficos de Williamson-Hall para los compuestos $Cd_{0,62}Mn_{0,33}Cr_{0,05}Te$ y $Cd_{0,52}Mn_{0,33}Cr_{0,15}Te$.

### 3.2 Identificación de segregado mediante ImageJ

En las micrografías obtenidas por MEB en modo BSE, el contraste composicional está determinado por el coeficiente de retrodispersión electrónica (η), el cual depende aproximadamente del número atómico promedio ($\bar{Z}$) de las fases presentes. Así, regiones con mayor $\bar{Z}$ presentan mayor

rendimiento de electrones retrodispersados y se manifiestan con mayor intensidad (contraste brillante), mientras que regiones con menor $\bar{Z}$ aparecen más oscuras. Las imágenes, adquiridas a 600 veces en áreas seleccionadas aleatoriamente, permiten una evaluación representativa de la morfología y heterogeneidad composicional superficial. Las zonas de bajo contraste, excluyendo aquellas asociadas a contribuciones topográficas (efecto de inclinación local, bordes, microfracturas y escalonamientos), se asignan a segregaciones enriquecidas en Cr, en concordancia con la menor $\bar{Z}$ efectiva de dichas regiones en comparación con la matriz. Esta interpretación fue validada mediante análisis EDS puntual y mapeo elemental, evidenciando una mayor concentración de Cr en estas áreas, lo que sugiere la formación de fases secundarias tipo $Cr_xTe_y$ (Villarreal et al., 2026).

En la Fig. 3a (y = 0,05), la microestructura presenta una topografía relativamente uniforme, con baja densidad de dominios de contraste oscuro, lo que indica una limitada segregación composicional. Sin embargo, la presencia de variaciones topográficas locales introduce contribuciones al contraste que pueden degradar la relación señal/ruido en procedimientos de segmentación automatizada. En la Fig. 3b (y = 0,10), se observa un incremento en la fracción areal de regiones oscuras, acompañado de una mayor complejidad topográfica, lo que genera una superposición entre contraste composicional y topográfico; este efecto es particularmente relevante en zonas próximas a defectos superficiales, dificultando la clasificación basada únicamente en intensidad. Finalmente, en la Fig. 3c (y = 0,15), se evidencia una elevada densidad de precipitados oscuros, distribuidos de manera más homogénea en la matriz, lo que es consistente con un aumento en la fracción volumétrica de fases secundarias ricas en Cr. A pesar de la mayor rugosidad superficial, el contraste Z es suficientemente pronunciado, permitiendo una discriminación más robusta entre fases. En este contexto, la segmentación mediante TWS se ve favorecida por la mayor separabilidad estadística de las clases en el espacio de características, mejorando la precisión en la cuantificación de las segregaciones.

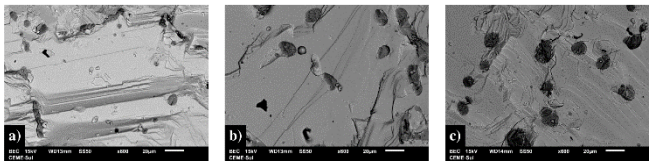


**Fig. 3.** Micrografias x600 obtenidas en modo BEC correspondientes a las tres muestras: (a) y = 0,05 (b) 0,10 (c) 0,15.

El análisis de las imágenes obtenidas en modo BEC evidencia una correlación directa entre el incremento de la concentración de cromo en la composición y el aumento tanto en la cantidad como en el tamaño de los segregados. Las regiones oscuras se vuelven progresivamente más numerosas y definidas a medida que aumenta el contenido de cromo. Mientras que la muestra con y = 0,05 presenta escasas zonas de segregación, las muestras con y = 0,10 e y = 0,15 muestran una presencia significativamente mayor de estos segregados. Estos resultados cualitativos son coherentes con los datos obtenidos mediante EDS y serán analizados con mayor detalle a través de la segmentación por TWS y el estudio de los mapas elementales de cromo.

La Fig. 4a presenta la segmentación realizada en la muestra con y = 0,05, evidenciando una buena correspondencia visual con las zonas de segregación ricas en Cr, en concordancia con el mapa elemental (Fig. 4d). No obstante, se observan algunas limitaciones del algoritmo, particularmente en las regiones central e inferior de la imagen, donde marcas lineales (posiblemente originadas por microarañazos o estrías) fueron clasificadas erróneamente como zonas segregadas. Estos accidentes topográficos, que no presentan un incremento en la concentración de Cr, generan errores en la clasificación por TWS debido a su similitud textural con los segregados. En la muestra con y = 0,10 (Fig. 4b), además de la persistencia de pequeñas estructuras topográficas mal clasificadas, se observa una región oscura en el cuadrante inferior que fue segmentada como segregación, pero que no se corresponde con el mapa elemental de cromo (Fig. 4e). Esta área podría estar asociada a una sombra producida por una topografía más pronunciada o a la presencia de contaminantes residuales en la superficie. Dado que el TWS se basa en patrones de textura y contraste para realizar la segmentación, regiones oscuras con una distribución de píxeles similar a la de las verdaderas zonas de segregación pueden ser confundidas con estas.

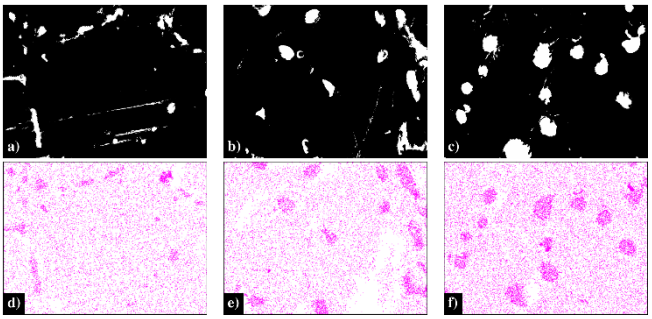


**Fig. 4.** Comparación entre las imágenes segmentadas por TWS (a, b, c) y los respectivos mapas elementales de Cr obtenidos por EDS (d, e, f) de las muestras analizadas.

Finalmente, la segmentación de la muestra con y = 0,15 (Fig. 4c) presenta una mayor concordancia con el mapa elemental (Fig. 4f). Aunque la superficie de la muestra contiene diversos accidentes topográficos, estos no generaron artefactos de contraste significativos, lo que favoreció el desempeño del algoritmo. La distribución de los precipitados segmentados coincide en su mayoría con las regiones de alta concentración de cromo, lo que indica un mejor rendimiento del TWS bajo estas condiciones.

Los valores de exactitud obtenidos para las tres muestras

analizadas fueron similares, situándose entre aproximadamente el 65% y el 70%, como se muestra en la Tabla 4. Esta proximidad indica que no existe una relación directa entre la exactitud y la concentración de cromo en las muestras, lo que sugiere que el desempeño del algoritmo TWS no depende de manera significativa de la variación composicional dentro del intervalo estudiado. En las muestras y = 0,05 e 0,10, se observó que regiones asociadas a accidentes topográficos fueron clasificadas erróneamente como zonas de segregación, tal como se ilustra en las Fig. 4a y 4b. Este tipo de error probablemente contribuyó a la reducción de la exactitud, evidenciando que el método requiere superficies con una topografía más homogénea para lograr un mejor desempeño.

A pesar de que la exactitud no es elevada, el nivel alcanzado resulta suficiente para identificar tendencias generales, como la observación de que el incremento del coeficiente estequiométrico de cromo conduce a una mayor proporción de la superficie cubierta por zonas de segregación. En este sentido, el método se muestra adecuado para análisis comparativos y cualitativos del comportamiento morfológico. Sin embargo, esta precisión no es suficiente para la cuantificación exacta del área ocupada por las zonas segregadas ni para el cálculo individual del área de dichas regiones.

Tabla 4. Valores de exactitud obtenidos para cada muestra segmentada por TWS.

| Muestra (y) | Exactitud (%) |
|---|---|
| 0,05 | 64,6 |
| 0,10 | 64,9 |
| 0,15 | 69,5 |

Además, se observa que el aumento del coeficiente estequiométrico de cromo está asociado a un incremento progresivo de la fracción superficial ocupada por zonas de segregación. Esta tendencia confirma que el aumento en la concentración de Cr favorece la formación de regiones ricas en este elemento, evidenciando una característica inherente al proceso de síntesis de las muestras. La Tabla 5 presenta los valores porcentuales obtenidos mediante el análisis de imágenes en ImageJ, mostrando claramente la relación directa entre el incremento de la concentración de cromo y la expansión del área superficial ocupada por los precipitados.

Tabla 5. Porcentaje de la superficie ocupada por zonas de segregación para cada muestra.

| Muestra (y) | Área ocupada por segregaciones (%) |
|---|---|
| 0,05 | 4,2 |
| 0,10 | 6,4 |
| 0,15 | 8,7 |

## Conclusiones

Se determinó el tamaño medio de cristalito y la deformación de la red para los compuestos cuaternarios $Cd_{0,62}Mn_{0,33}Cr_{0,05}Te$ y $Cd_{0,52}Mn_{0,33}Cr_{0,15}Te$. Los resultados obtenidos mediante el método de Williamson–Hall indican un buen crecimiento cristalino y una adecuada calidad estructural de los materiales. Se observó que el incremento en la concentración de Cr promovió una disminución del tamaño medio de cristalito, efecto que puede estar asociado tanto a una mayor homogeneidad estructural como al aumento en la cantidad de fase secundaria ($Cr_2Te_3$) presente en los compuestos.

El método de segmentación supervisada basado en aprendizaje automático, implementado mediante el plugin Trainable WEKA Segmentation, demostró un notable potencial para el análisis de micrografías en modo BEC, permitiendo identificar y comparar tendencias relacionadas con la formación de zonas segregadas. Los resultados evidenciaron que el desempeño del algoritmo está fuertemente condicionado por la topografía de la muestra: en las dos primeras muestras, regiones asociadas a accidentes topográficos fueron clasificadas incorrectamente como segregaciones, lo que redujo la exactitud de las segmentaciones. En contraste, la tercera muestra, que presentaba un relieve más homogéneo y un buen contraste químico, mostró resultados más consistentes y una mayor correspondencia con los mapas elementales de cromo obtenidos por EDS. Los análisis cuantitativos indicaron una exactitud entre el 65 % y el 70 %, valor suficiente para identificar tendencias generales de variación morfológica, aunque insuficiente para mediciones métricas precisas de las áreas segregadas. Asimismo, se observó que el aumento de la concentración de Cr favorece la expansión de la fracción superficial ocupada por zonas de segregación.

## Referencias

Arganda-Carreras, I., Kaynig, V., Rueden, C., Eliceiri, K. W., Schindelin, J., Cardona, A., & Sebastian Seung, H. (2017). Trainable Weka Segmentation: A machine learning tool for microscopy pixel classification. *Bioinformatics*, *33*(15), 2424–2426. https://doi.org/10.1093/bioinformatics/btx180

Dietl, T. (2010). A ten-year perspective on dilute magnetic semiconductors and oxides. *Nature Materials*, *9*(12), 965–974. https://doi.org/10.1038/nmat2898

Fan, J., Wang, R., Li, S., & Zhang, C. (2012). Automated cervical cell image segmentation using level set based active contour model. *2012 12th International Conference on Control Automation Robotics & Vision (ICARCV)*, 877–882. https://doi.org/10.1109/ICARCV.2012.6485273

Fan, M., & Lee, T. C. (2015). Variants of seeded region growing. *IET Image Processing*, *9*(6), 478–485. https://doi.org/10.1049/iet-ipr.2014.0490

Hwang, Y. H., Shen, S., Liu, X., Furdyna, J. K., Dobrowolska, M., & Um, Y. H. (2013). Room-temperature ferromagnetism in highly Cr-doped II-Mn-VI magnetic semiconductor $Cd_{1-x-y}Mn_xCr_yTe$. *Physical Review B*, *88*(7), 075205. https://doi.org/10.1103/PhysRevB.88.075205

Iglesias, J. E. (2017). Globally Optimal Coupled Surfaces for Semi-automatic Segmentation of Medical Images. En M. Niethammer, M. Styner, S. Aylward, H. Zhu, I. Oguz, P.-T. Yap, & D. Shen (Eds.), *Information Processing in Medical Imaging* (pp. 610–621). Springer International Publishing. https://doi.org/10.1007/978-3-319-59050-9_48

Irie, Y., Sato, T., & Ohta, E. (1995). Observation of high-temperature spin-freezing behavior in $Cd_{1-x-y}Mn_xFe_yTe$. *Physical Review B*, *51*(19), 13084–13090. https://doi.org/10.1103/PhysRevB.51.13084

Kim, Y. J., Lee, S. H., Park, C. M., & Kim, K. G. (2016). Evaluation of Semi-automatic Segmentation Methods for Persistent Ground Glass Nodules on Thin-Section CT Scans. *Healthcare Informatics Research*, *22*(4), 305–315. https://doi.org/10.4258/hir.2016.22.4.305

Lormand, C., Zellmer, G. F., Németh, K., Kilgour, G., Mead, S., Palmer, A. S., Sakamoto, N., Yurimoto, H., & Moebis, A. (2018). Weka Trainable Segmentation Plugin in ImageJ: A Semi-Automatic Tool Applied to Crystal Size Distributions of Microlites in Volcanic Rocks. *Microscopy and Microanalysis*, *24*(6), 667–675. https://doi.org/10.1017/S1431927618015428

Mallick, S., Kabir, M. S., & Sharif, A. (2016). Study on the properties of $Zn_{1-x}Ni_x$ high temperature solder alloys. *Journal of Materials Science: Materials in Electronics*, *27*(4), 3608–3618. https://doi.org/10.1007/s10854-015-4198-2

Salum, P., Güven, O., Aydemir, L. Y., & Erbay, Z. (2022). Microscopy-Assisted Digital Image Analysis with Trainable Weka Segmentation (TWS) for Emulsion Droplet Size Determination. *Coatings*, *12*(3). https://doi.org/10.3390/coatings12030364

Shen, S., Liu, X., Cho, Y. J., Furdyna, J. K., Dobrowolska, M., Hwang, Y. H., & Um, Y. H. (2009). Ferromagnetic behavior of CdMnCrTe quaternary system. *Applied Physics Letters*, *94*(14), 142507. https://doi.org/10.1063/1.3114423

Verma, V. K., Sakamoto, S., Ishikawa, K., Singh, V. R., Ishigami, K., Shibata, G., Kadono, T., Koide, T., Kuroda, S., & Fujimori, A. (2022). Cr doping-induced ferromagnetism in the spin-glass $Cd_{1-x}Mn_xTe$ studied by x-ray magnetic circular dichroism. *Physica B: Condensed Matter*, *642*, 414129. https://doi.org/10.1016/j.physb.2022.414129

Villarreal, M. A., Grima, P. J., Briceño, J. R., Lobo, H. E., Rosario, J. R., Díaz, J. C. & Gutiérrez, G. M. (2012). Una introducción a la Espintrónica. *Academia*, *11*(21), 43–58. http://erevistas.saber.ula.ve/index.php/academia/article/view/6110

Villarreal, M. A., Grima, P., Quintero, M., Moreno, E., Fernández, J., Silva, P., & Villegas, J. (2013). Propiedades magnéticas del sistema de aleaciones $CuAl_{1-x}Cr_xS_2$ (x = 0.50, 0.75). *Revista mexicana de física*, *59*(6), 521–526. http://www.scielo.org.mx/scielo.php?script=sci_abstract&pid=S0035-001X2013000600004&lng=es&nrm=iso&tlng=es

Villarreal, M. A., Turatti, A. M., Pimentel, J. L., Scherdien, R. N., Terán, J. C., Silva, P., Martinez, M. A. R., & Mantilla, J. C. (2026). Crystalline and Microstructural Properties of $Cd_{1-x-y}Mn_xCr_yTe$ Semiconductor System (x = 0.33 and $0.05 \leq y \leq 0.15$). *physica status solidi (a)*, *223*(3), e202500574. https://doi.org/10.1002/pssa.202500574

Wolf, S. A., Awschalom, D. D., Buhrman, R. A., Daughton, J. M., Von Molnár, S., Roukes, M. L., Chtchelkanova, A. Y., & Treger, D. M. (2001). Spintronics: A Spin-Based Electronics Vision for the Future. *Science*, *294*(5546), 1488–1495. https://doi.org/10.1126/science.1065389

Yoon, I. T., Kang, T. W., & Kim, D. J. (2006). Analysis of magnetic field dependent mobility in ferromagnetic $Ga_{1-x}Mn_xAs$ layers. *Solid State Communications*, *137*(3), 171–176. https://doi.org/10.1016/j.ssc.2005.10.004

***Recibido:*** *22 de abril de 2026*

***Aceptado:*** *30 de junio de 2026*

***Villarreal, Manuel:*** *Doctor en Química Aplicada. Profesor Titular de la Universidad de Los Andes (ULA), Venezuela. Su investigación se centra en el estudio de nuevos materiales semiconductores, abarcando su síntesis y caracterización mediante técnicas como difracción de rayos X y microscopía electrónica de barrido. Asimismo, investiga las propiedades magnéticas, eléctricas, térmicas y ópticas de sistemas semiconductores.*
***https://orcid.org/ 0000-0002-3863-4856***

***Pimentel, Jorge:*** *Doctor en Física. Profesor Asociado de la Universidade Federal do Rio Grande, Instituto de Matemática, Estadística y Física (FURG-IMEF), Brasil. Cuenta con experiencia en el área de la física de la materia condensada, con énfasis en superconductividad y magnetismo.*
*Correo electrónico: jlpimenteljr@gmail.com*
***https://orcid.org/ 0000-0003-0968-0834***

***Turatti, Agueda:*** *Doctora en Ciencia de Materiales. Profesora Asociada de la Universidade Federal do Rio Grande, Instituto de Matemática, Estadística y Física (FURG-IMEF),*

*Brasil. Cuenta con experiencia en el área de la física de la materia condensada, con énfasis en cerámicos y metales, así como en diversas técnicas de análisis y caracterización de materiales: difracción de rayos X, microscopía electrónica de barrido y de transmisión, ensayos de dureza Vickers y pruebas de desgaste abrasivo.*
*Correo electrónico: aguedaturatti@gmail.com*
***https://orcid.org/ 0000-0002-4732-8244***

***Scherdien, Richard:*** *Magister en Física. Técnico del Laboratorio de Física del Instituto de Matemática, Estadística y Física, Univerisdade Federal do Rio Grande (FURG-IMEF), Brasil. Su trabajo se centra en el estudio de nuevos materiales semiconductores, con énfasis en microscopía electrónica de barrido.*
*Correo electrónico: richardscherdien@furg.br*
***https://orcid.org/ 0009-0008-9889-1900***

***Terán, Juan:*** *Doctor en Ciencias de la Educación. Profesor Visitante de la Universidade Federal do Rio Grande (FURG-IMEF), Brasil. Cuenta con experiencia docente en el área de la física moderna, con énfasis en métodos y técnicas de enseñanza. Sus principales líneas de trabajo incluyen el pensamiento complejo, la bibliometría, la teoría de la relatividad, el espacio-tiempo, los semiconductores, la física computacional y la interdisciplinariedad.*
*Correo electrónico: juanfisico23@gmail.com*
***https://orcid.org/ 0000-0001-9384-2247***

***Silva, Pedro:*** *Doctor en Física. Es investigador en el Laboratorio de Física de la Materia Condensada del Instituto Venezolano de Investigaciones Científicas (IVIC), Venezuela. Su área de investigación se centra en las propiedades eléctricas y magnéticas de la materia, con énfasis en la resonancia de espín electrónico.*
*Correo electrónico: pejosi@gmail.com*
***https://orcid.org/ 0000-0002-6409-8735***

*Artículo de Investigación. Revista Ciencia e Ingeniería. Vol. 47, No.3 pp. 357-368, agosto-noviembre, 2026.*
*ISSN 1316-7081. ISSN Elect. 2244-8780 Universidad de los Andes (ULA)*

# Blue biorefinery: obtaining advanced lignocellulosic materials using marine biotechnology as a tool.

# Biorrefinería azul: obtención de materiales lignocelulósicos avanzados mediante la biotecnología marina como herramienta.

**Henríquez Koch, Ramón [1,2], Centeno Bordones, Guillermo [1,3*]**
[1]Center for Oceanology and Antarctic Studies, Venezuelan Institute for Scientific Research, Miranda, Venezuela
[2]Department of Thermodynamics and Transport Phenomena, School of Chemical Engineering, Faculty of Engineering, Central University of Venezuela, Caracas, Venezuela.
[3]University of Carabobo, Valencia, Venezuela.
* *gcenteno1@uc.edu.ve*

**Abstract**

*Marine biomass from macroalgae, microalgae, and seagrasses is emerging as a fundamental pillar for next-generation biorefineries. This review focuses on the structural fundamentals, experimental methods, and emerging applications of these biomaterials, highlighting the sustainable use of marine resources. The first section of the state of the art covers marine cellulose, or "blue cellulose," as a precursor to advanced materials such as microcellulose and marine nanocellulose. These nanomaterials, characterized by their high crystallinity, mechanical strength, and large surface area, are essential in high value-added biomaterial applications. The second section considers marine lignin as a valuable source of sustainable aromatic compounds. Lignin nanoparticles are crucial as natural antioxidants, UV filters, emulsion stabilizers, and precursors for advanced biocomposites. The exploitation of these marine biopolymers accelerates the transition to a circular and sustainable economy.*

***Keywords:*** *Blue cellulose, marine cellulose, marine nanocellulose, marine lignin, marine biotechnology, biomaterials*

**Resumen**

*La biomasa marina procedente de macroalgas, microalgas y praderas marinas se está consolidando como un pilar fundamental para las biorrefinerías de nueva generación. Esta revisión se centra en los fundamentos estructurales, los métodos experimentales y las aplicaciones emergentes de estos biomateriales, haciendo hincapié en el uso sostenible de los recursos marinos. La primera sección, que presenta el estado del arte, abarca la celulosa marina, o "celulosa azul", como precursora de materiales avanzados como la microcelulosa y la nanocelulosa marina. Estos nanomateriales, caracterizados por su alta cristalinidad, resistencia mecánica y gran superficie, son esenciales en aplicaciones de biomateriales de alto valor añadido. La segunda sección considera la lignina marina como una valiosa fuente de compuestos aromáticos sostenibles. Las nanopartículas de lignina son cruciales como antioxidantes naturales, filtros UV, estabilizadores de emulsiones y precursores de biocompuestos avanzados. La explotación de estos biopolímeros marinos acelera la transición hacia una economía circular y sostenible.*

***Palabras clave****: Celulosa azul, celulosa marina, nanocelulosa marina, lignina marina, biotecnología marina, biomateriales.*

## 1 Introducción

Cellulose and lignin are the most abundant structural biopolymers on the planet. They are the essential pillars of biomass, the bioeconomy, and the materials industry, as well as sustainable and sustainable energy. Cellulose is a linear polysaccharide, formed by β-D-glucose units linked by β (1→4) bonds, and is the main component of plant cell walls. Lignin, on the other hand, is a three-dimensional aromatic polymer that surrounds cellulose to provide rigidity, structural support, and impermeability. Both materials have gained relevance in the market for their applications as bioplastics, fibers, biosurfactants, bioadhesives, and biofuels (Habibi et al., 2010; Eichhorn et al., 2010).

The extraction of cellulose is an important process due to the diversity of sources from which this biomaterial can be extracted, notably agroforestry species, terrestrial and marine angiosperms, and phycophora. The traditional uses of this material can range from paper and packaging manufacturing to textiles and applications in the cellulose derivatives industry. In contrast, lignin is seen as a by-product in the processing of paper pulp and bioethanol, with only 2% of lignin estimated to be used in the production of high value-added materials (Habibi et al., 2010).

These lignocellulosic materials are being promoted in the polymer industry due to their natural aromatic origin (Habibi et al., 2010; Eichhorn et al., 2010), in response to the need to reduce dependence on petrochemical polymers and their carbon footprint. Biomaterials from marine sources have notable advantages over synthetic ones (Trivedi et al., 2016; Omran et al., 2021; Jose et al., 2025), because they are biodegradable, biocompatible, renewable, environmentally friendly, and also offer attractive production yields. Marine biotechnology has emerged as a strategic field that promotes the valorization of macroalgae, microalgae, cyanobacteria, and marine phanerogams for the use of functional lignocellulosic biopolymers.

Rapid algal growth, high productivity per surface area, and low freshwater use for the production of macroalgae and microalgae make them an attractive raw material compared to agricultural and forestry products (Geng et al., 2025; Iqbel et al., 2025). However, the limitations associated with taxonomic variability, the presence of salts, and effluent treatment act as an economic counterweight, hindering scaling up (Zaimes and Khanna, 2013).

Technological advances have made it possible to combine green processes (enzymatic hydrolysis, organosolv extraction, ultrasound, among others) to obtain lignocellulosic materials. These biomaterials generate industrial-scale production routes that favour their profitability and promote the circular economy (Geng et al., 2025).

There is growing interest in materials engineering in relation to cellulose and lignin, mainly in the pharmaceutical, medical, food, and cosmetics industries, as well as in interfacial phenomena, among others. Algal cellulose, for example, is used for its high crystallinity, which is inversely proportional to particle size (French et al., 2017; Mihranyan, 2011), improving this property as its dimensional scale decreases (Ioelovich, 2022). In the case of algal lignin, it is a reserve of versatile aromatic compounds (Karlsson et al., 2023; Melikoglu, 2025), used in the synthesis of resins and advanced carbonaceous materials (nanolignin, graphenes, and graphene oxides).

However, the engineering challenges involved in exploiting these resources remain to be solved (Sadaan et el., 2024). The presence of salts, biological variability, changing environmental conditions, and waste treatment affect the economic viability of industrial scaling (Klap et al., 2007). Nevertheless, advances in separation, purification, and molecular characterization processes have provided an important basis for the exploitation of these biomaterials, positioning them as high value-added products derived from clean technologies that contribute to the circular economy (Mateo et al., 2025; Zanchetta et al., 2025).

This work aims to provide a state-of-the-art review of marine lignocellulosic biomaterials from the perspective of their attractive properties for industry, the production process, and emerging applications for the development of sustainable biomaterials with high added value.

## 2. Results and Discussion

### 2.1 Marine cellulose

Cellulose is the most industrially produced polysaccharide in the world, with an estimated annual production of 7.5E10 tons. It has a linear structure composed of β-D-glucose monomers linked by β (1→4) bonds.

An alternative source of cellulose extraction is macroalgae and marine phanerogams, which have the particularity of forming cellulose with a highly crystalline system that is insoluble in water and has significant mechanical and thermal resistance (Habibi et al., 2010). The formula associated with this macromolecule $(C_6H_{10}O_5)_n$ is organized into microfibrils with larger alternating crystalline regions and smaller disordered or amorphous regions (French et al., 2017).

Green algae of the genus Ulva sp and Cladophora sp are the species most commonly used for the production of marine cellulose. Algae cellulose is characterized by its high degree of polymerization and crystallinity greater than 90% (Mihranyan, 2011).

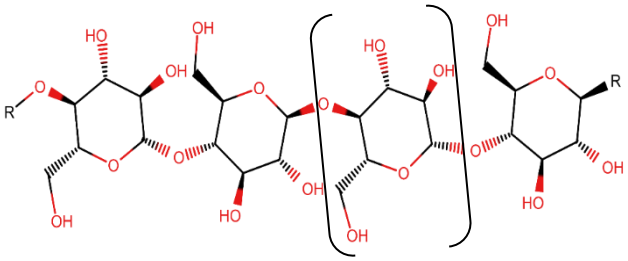


**Fig 1.** Polymeric configuration (Fisher projection) of cellulose, formed by D-glucose units linked by β-(1→4) bonds, unlike starch, which is α-(1→4). O: oxygen, H: hydrogen. FTIR spectra of non-activated carbons obtained from coconut shells (CC2) and peach pits (CD1).

The most common protocols for algal cellulose production begin with washing and drying the macroalgae, followed by an alkaline treatment stage with sodium hydroxide between 2 and 5% w/v at 80-90 °C for 2 to 4 hours to remove proteins, lipids, and other soluble polysaccharides, lignin, and pigments (Gomaa et al., 2021). This is followed by oxidative bleaching using 2% w/v sodium hypochlorite or 3% hydrogen peroxide at room temperature for 1 to 2 hours (Moral et al., 2019).

Other authors recommend using acetic or hydrochloric acid (1M) for demineralization if calcareous or siliceous remains are known to be present (Díaz-Vásquez et al., 2015). Continue with centrifugation (5000 rpm for 10-15 min) and separate the effluents. Finally, wash with distilled water until

a neutral pH is reached and dry by heat or freeze-drying (Svagan et al., 2023).

From the same cellulose, it is possible to obtain marine nanocellulose (nanofibrillar or nanocrystalline) by mechanical processes such as homogenization, ultrasound, or by chemical techniques of acid hydrolysis that generate fiber breaks in diameters of different scales (Wahlstrom et al., 2020). This biomaterial is used in tissue engineering, drug encapsulation, biosensors, cosmetics, biodegradable films, and food, taking advantage of its ability to form hydrogels (Patrichi et al., 2023).

### 2.2 Marine microcellulose

Also known as marine microcrystalline cellulose, it consists of D-glucose molecules linked together by β (1→4) glycosidic bonds (Tarchoun et al., 2019), rearranging themselves into a crystalline, three-dimensional system. This system is stabilized by intramolecular hydrogen bonds, which generate high rigidity, insolubility in water, and resistance to organic solvents (Poudel et al. 2025).

The most common sources of microcellulose are red macroalgae (Gracilaria, Gelidium), green algae (Ulva sp.), and especially marine microorganisms such as cellulolytic bacteria (Vibrio sp, Pseudoalteromonas sp) and microalgae of the genera Chlorella sp, Cladophora sp, Valonia sp, and Boergesenia sp (Madadi et al., 2021). Other references point to the extraction of microcellulose from crustacean and marine sponge waste rich in cellulosic and chitinous matrices (Pamungkas and Budhiyandi, 2021).

For the production of microcellulose, it is necessary to remove any lipid and mineral impurities from the source. This can be achieved by washing with 80% ethanol and 1% hydrochloric acid at room temperature for 2 hours, followed by a final wash with distilled water (Trivedi et al., 2016). The material is then subjected to basic hydrolysis (liquid:solid ratio 1:10 with 2-4% m/v sodium hydroxide) at a maximum temperature of 90°C for 2 to 4 hours, removing proteins, lignin, and hemicellulose from the effluent. The resulting solid is subjected to a bleaching stage with 2.5% sodium hypochlorite at 70°C for one hour to remove lignin and pigment residues (He et al., 2018).

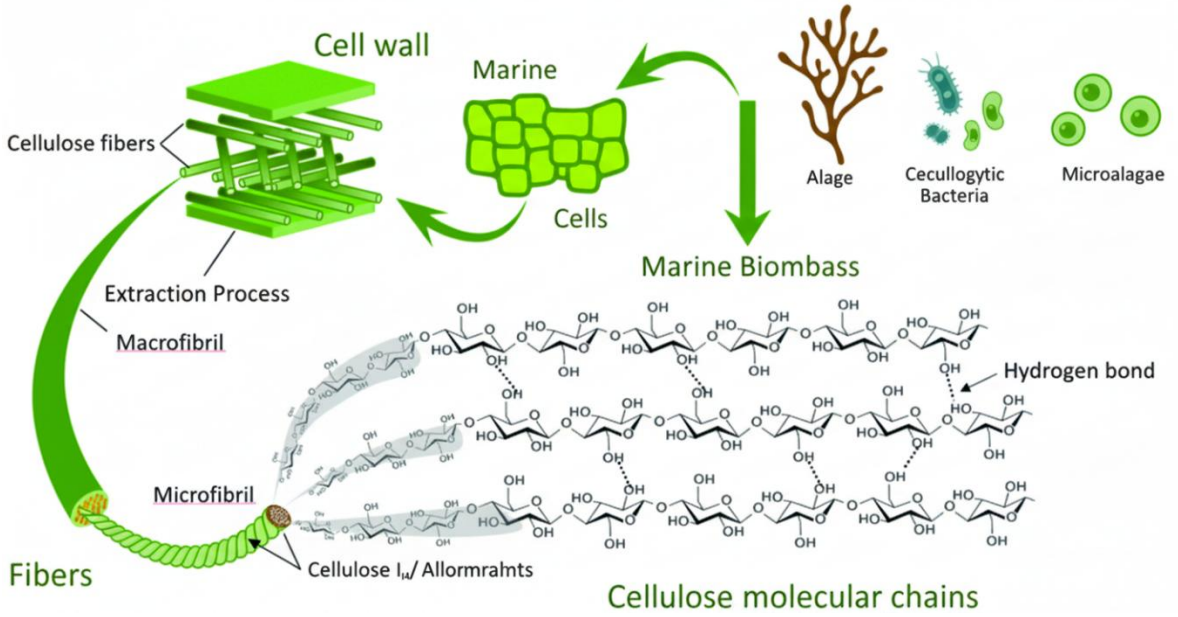


**Fig 2.** Composition of microcellulose as microfibrils; when hydrolysis is applied, they are released from the structure and generate microcrystalline regions. Inspired by Han. 29.

In order to increase the crystallinity of marine microcellulose, hydrochloric acid is used at a concentration between 2.5 and 3 N at 45°C for 1 hour (Revol et al., 1992), breaking down the non-crystalline areas. It is then washed with distilled water to remove excess acid until a neutral pH is reached, and then centrifuged (10,000 rpm for 10 min) until the phases are completely separated. Finally, sonication (20 kHz, 750 W, 15 min) is applied to disperse the cellulose microfibers (Dong et al., 1998).

Similar to other materials, microcellulose has applications in the field of biomedicine for tissue regeneration, controlled drug release, and scaffolds for tissue engineering, due to its biocompatibility and porosity (Trache et al., 2016). In cosmetics, it is used as a natural thickener, in

foods as stabilizers, surfactants, and biodegradable packaging (Kowalka et al., 2025). Its application is expanding due to the boom in the sugar chemical industry.

### 2.3 Marine nanocellulose

In recent years, marine nanocellulose has become popular as a biomaterial of interest in research and development. This is due to its high-performance physicochemical properties, such as its crystallinity, specific surface area, high mechanical strength, and ability to form stable three-dimensional networks (Yuan et al., 2021). This type of cellulose mainly occurs in three forms: cellulose nanofibers (CNF), cellulose nanocrystals (CNC), and bacterial cellulose (BC). Its structure is composed of linear chains of β-(1→4)-D-glucopyranose, with alternating crystalline and amorphous regions (Eichhorm et al., 2010, Ren et al. 2014).

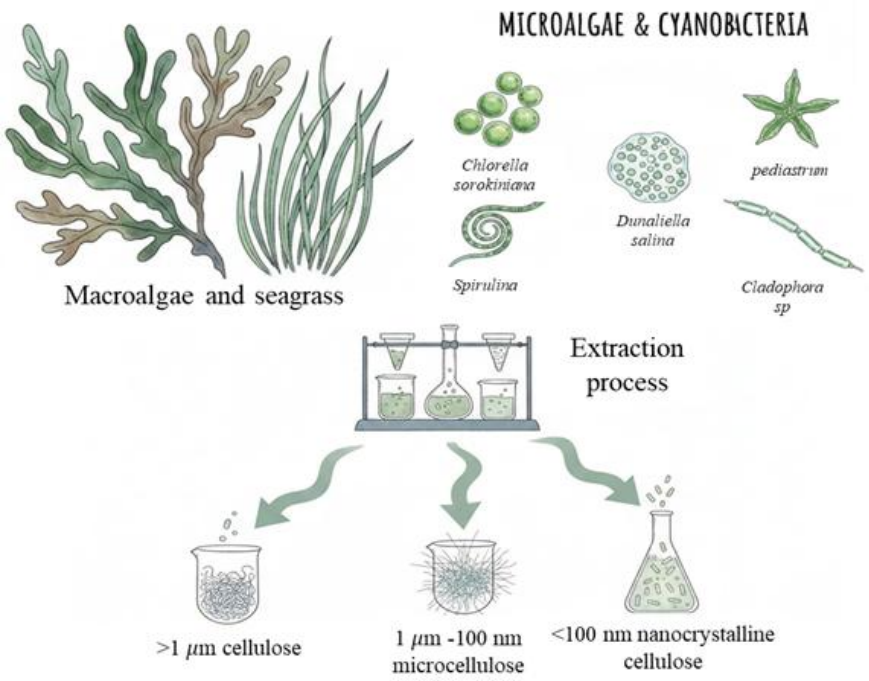


**Fig 3.** Types of marine cellulose from macroalgae, seagrasses, microalgae, and cyanobacteria.

Among marine sources of nanocellulose, macroalgae, microalgae, and cyanobacteria such as Chlorella sorokiniana, Spirulina, Dunaliella salina, and Cladophora sp. stand out (Plianwong and Sirirak, 2024). The structures of their cellulose have a higher crystallinity than terrestrial sources due to their denser organization in nanofibrils (Stromme et al., 2002).

The methods for extracting marine nanocellulose consist of a series of separation and purification processes. In the case of Cladophora glomerata, it is recommended to start with dry material and subject it to an alkaline treatment with 2% (m/v) caustic soda at 80°C for 4 hours to remove proteins and hemicelluloses. The bleaching process is carried out with 1.5% hydrogen peroxide at 60°C for 2 hours to remove pigments and other residual compounds (Mihhels et al., 2023).

The cellulose nanocrystals are then isolated by hydrolysis with 64% sulfuric acid (v/v) at 45°C for 45 min with constant stirring. This process breaks down amorphous regions, releasing crystals with lengths of 100 to 300 nm and diameters of 5 to 10 nm (Xu et al.,2022). The crystals are then washed with distilled water and dialysis is applied to remove excess acid. Finally, molecular centrifugation is applied at 10,000 rpm for 15 minutes to obtain the CNC (Ren et al., 2014).

When using green macroalgae, high-pressure homogenization (1500 bar) should be used for 10 cycles to release CNF, as an alternative technique to acid hydrolysis (Berglund et al., 2020). Finally, the material obtained is freeze-dried for proper storage.

The food industry uses nanocellulose as a biodegradable film for food due to its antimicrobial properties. It has also been used for the production of packaging, taking advantage of its transparency and mechanical strength (Casalini and

Giacinti, 2022). In the field of medicine, it is used in wound dressings, controlled drug delivery systems, and tissue regeneration support due to its porous structure (Machado et al., 2024). Nanocellulose has had an impact on colloidal chemistry due to the replacement of industrial surfactants with nanocellulose surfactants.

Marine-derived cellulose, microcellulose, and nanocellulose are compared in Table 1 below:

**Table 1.** Comparison of the characteristics of marine-derived celluloses.

| Property | Cellulose | Microcellulose | Nanocellulose (CNC/NFC) | References |
|---|---|---|---|---|
| Scale | Micrometric scale | 1–10 µm | 3–100 nm (CNC) | (Habibi et al., 2010; Eichhorm et al., 2010; Mihranyan, 2011; Tarchoun et al., 2019; Madadi et al., 2021; Zanchetta et al., 2025; Berglund et al.,2020; Moon et al., 2011). |
| Morphology | Thick fibers | Short, amorphous fibers | Rods or fibrils | (Habibi et al., 2010; Eichhorm et al., 2010; Pamunkas and Budhiyandi, 2021; He et al., 2018; Plianwong and Sirirak, 2024; Stromme et al., 2002; Mihhels et al., 2023). |
| Percentage of crystallinity | 40-80% (estimated) | 60-80% | 70-95% | (Eichhorm et al., 2010; French et al., 2017; Ioelovich, 2022; Revol et al., 1992; Dong et al.,1998; Stromme et al., 2002; Xu et al., 2022; Ren et al., 2014; Moon et al., 2011). |
| Applications | Support, paper, cardboard | Pharmaceutical excipients, additives | Biomedicine, packaging, etc. | (Zanchetta et al., 2025; Moral et al., 2019; Patrichi et al., 2023; Trache et al., 2016; Kowalka et al., 2025; Yuan et al., 2021; Casalini and Giacinti, 2022; Machado et al., 2024; Moon et al., 2011). |

### 2.4 Marine lignin

Lignin is a complex, amorphous aromatic polymer that provides rigidity, with high thermal stability and relative resistance to biological degradation. It is located in the cell walls of vascular plants and forms three-dimensional structures of phenylpropane units (p-hydroxyphenyl, coniferyl, and sinapyl) that interact through ether bonds (β-O-4, α-O-4, 4-O-5) and carbon-carbon (β–1, β–β, β–5, 5–5) bonds (Karlsson et al., 2023). These characteristics determine its reactivity and value as a raw material for aromatic compounds.

Broadly speaking, marine lignin sources can be classified into two categories: phanerogams and marine macroalgae. The former are vascular sources such as angiosperms that contain lignin in their structure in a similar way to terrestrial sources. Seagrass beds of Zostera sp, Posidonia sp, and Thalassea sp are exploitable sources of cellulose and lignin. On the other hand, macroalgae biosynthesize lignin in smaller proportions than marine phanerogams. There is scientific evidence identifying

complex aromatic groups of the macrophyte-assembly type or functional groups of macroalgae (Sargassum sp) that suggest taxonomic and environmental variations with the presence of high levels of lignin-type aromatic compounds (Li et al., 2012; Alzate-Gaviria et al., 2021).

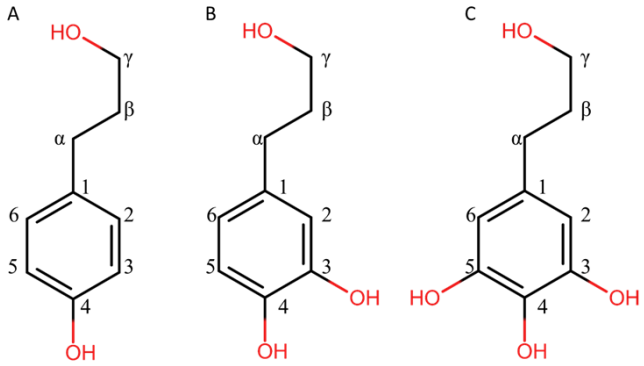


**Fig 4.** Lignin monomers in Fisher projection, (A) p-hydroxyphenyl, (B) coniferyl, (C) sinapyl. O: oxygen, H: hydrogen.

Marine lignin is extracted in a similar way to terrestrial lignin, but with the application of additional methods for salt treatment. First, it is dried and desalinated with fresh water, and then the material is crushed. The biomass is hydrolyzed in an alkaline medium of NaOH or KOH at a ratio of 1:10 to 1:20 of dry material to alkali solution with a concentration of 1 M. The process takes 1 to 4 hours at a temperature of 80 °C. Dissolved lignin and part of the hemicellulose and cellulose are obtained and removed by centrifugation. The resulting liquid phase is acidified to a pH of 2 with 1 M hydrochloric acid to precipitate the lignin, which is separated by filtration, and the material is then washed and dried (Ley et al., 2023; Li et al., 2012).

Another method used is organosolv, which guarantees the absence of sulfur (in the paper industry), a lower degree of condensation, and a higher content of β-O-4 bonds. The material is pretreated in the same way as in the previous method. Ethanol and water are used in a 60:40 ratio, for a solid:liquid ratio of 1:5-1:10. Hydrochloric acid at 0.1-0.5 M is added at a ratio of 1.5:50 acid:dry solid at a working temperature of 140-200 °C for 20-120 min and a pressure of 10-20 bar. It is then centrifuged to obtain the cellulose and water is added to the liquid phase to precipitate the lignin. It is centrifuged again to obtain the wet lignin ready for the drying process (Melikoglu, 2025; Saadan et al., 2024).

Lignin has many applications, including as a binding agent and a component of resins and panels when mixed with other polymers. It has also been used in chemical routes to obtain monomers such as phenols used in polymer synthesis. Activated carbon has been manufactured from lignin for use in water treatment and electrodes. Due to its high bioactivity, this biomaterial exhibits antioxidant and UV-screening properties and has pharmacological benefits (Yu and Kim, 2020; Liu et al., 2024; Centeno-Bordones, 2022). On the other hand, Gómez et al (Gómez et al., 2025). have studied oxidative processes of lignin to use it in the formulation of animal feed in order to take advantage of its metabolic energy in ruminants.

The marine lignin production industry faces challenges due to the variability of the raw material. Different taxonomies and climatic effects restrict yield and the efficiency of production processes. Brine management often involves treatment processes that affect economic profitability. In this regard, industrial scaling using the organosolv method requires the management of solvents that need to be reused to reduce costs (Saadan et al., 2024; Alam et al., 2024).

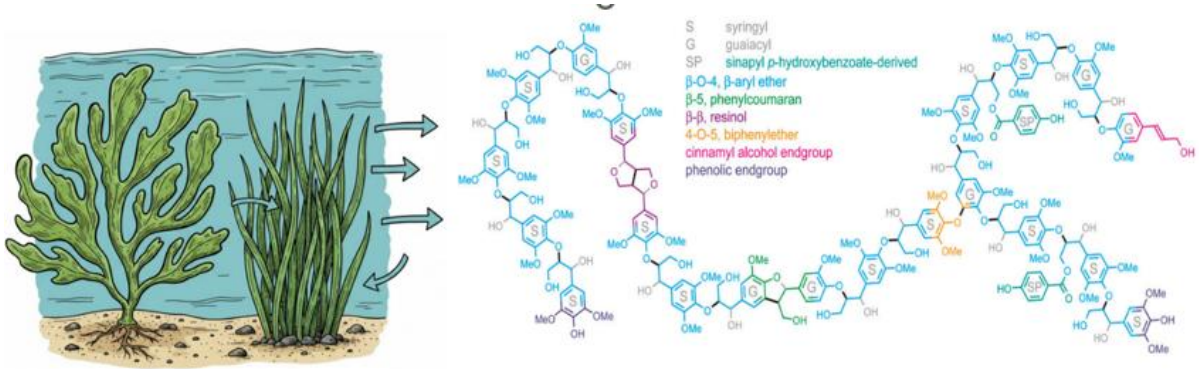


**Fig 5.** Reference molecule of marine lignin from macroalgae and seagrasses (Vanholme et al., 2010; Stewart et al., 2009).

## 2.5 Marine lignin

The reduction in particle size in lignin results in an increase in specific surface area, meaning that the reactivity and availability of functional groups (hydroxyls) are more reactive for their applications. This allows interactions through hydrogen bonds, Π-Π stacking, ionic chelation, and coupling reactions, facilitating integration with

biodegradable polymers (such as cellulose, chitosan, or algae polysaccharides). In addition to being an intrinsic antioxidant, it has thermal stability and the ability to absorb UV A, B, and C radiation (Camargos et al., 2025; Centeno-Bordones, 2022).

The traditional sources of extraction are the same as those outlined in the previous section. However, the key to obtaining this nanoproduct lies in its chemical processing methods. Nanolignin is obtained through top-down or bottom-up routes. The top-down route is based on size reduction through mechanical grinding, ultrasound, high-pressure homogenization, and steam explosion (Grappa et al., 2024). The literature has shown the effectiveness of obtaining spherical nanolignin with diameters between 50-300 nm through the top-down route. While the bottom-up route induces controlled precipitation, lignin dissolved in an organic solvent (acetone, ethanol, methanol, tetrahydrofuran) precipitates on contact with water, losing solvation and self-assembling to form nanoparticles. This process allows for easy scaling, but results in purification processes for solvent recovery. However, there are other methods such as: application of templating agents/assisted polymerization, hydrothermal processes, emulsification, and pH-directed self-assembly (Grappa et al., 2024).

A top-down method for obtaining lignin nanoparticles is the solvent exchange and ultrasound method applied by Centeno-Bordones, using black liquor effluent from cellulose extraction. Once the lignin has been precipitated in an acidic medium and dried, it is placed in contact with a water:alcohol (methanol or ethanol) mixture (6:4), keeping it under agitation for 30 minutes. This mixture is then subjected to continuous pulse sonication at 42,000 Hz and 135 W for 30 to 45 minutes. After this time, the solution is vacuum filtered through a 0.45 μm filter. Next, 200 mL of distilled water is added drop by drop and stirred at 400 rpm for 20 minutes. Finally, it is centrifuged for 30 minutes at 3,000 rpm. This methodology yields lignin nanoparticles between 15 and 65 nanometers in size (Centeno-Bordones, 2022).

Cellulose, nanocellulose, or chitosan composites increase their mechanical strength, thermal stability, and UV blocking capacity by incorporating nanolignin into their system. On the other hand, biomedicine is investigating nanolignin as an antioxidant agent, hydrophobic drug carrier, and component of bioactive hydrogels. Nanolignin's ability to interact with metals makes it useful in adsorption processes for water treatment and soil remediation. Positive effects have been demonstrated as a coating for antimicrobial agents, sustainable cosmetic formulations, and emulsion stabilizers (Bueno-Suescun et al., 2025).

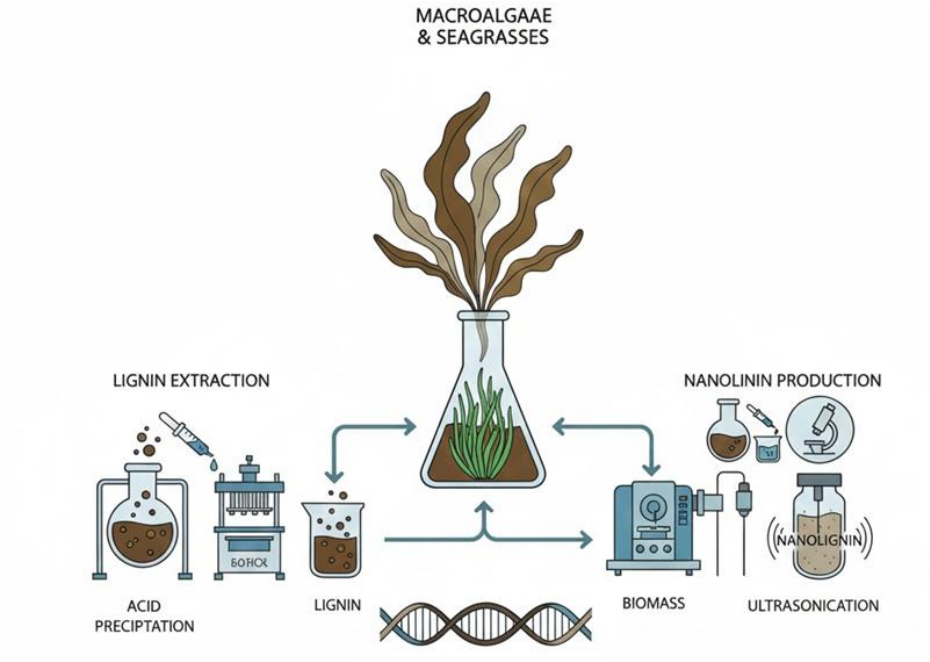


**Fig. 6.** Processes for obtaining lignin and marine nanolignin from macroalgae and seagrass.

## Conclusions

Blue cellulose, obtained from marine biomass, represents a paradigm shift in the bioeconomy. This unconventional marine source competes with terrestrial crops, offering a sustainable and abundant way to obtain biomaterials. Its importance lies in the fact that it allows the

production of microcellulose and nanocellulose, materials with superior properties of high strength and surface area. Thus, blue cellulose and its nanostructured derivatives are key to decarbonizing industry and moving towards a circular economy based on renewable ocean resources.

Blue cellulose and its different scales stand out for their physicochemical properties, derived from the structural adaptability of marine organisms. Marine cellulose has a high degree of crystallinity, enabling the development of biodegradable and biocompatible materials, while micro- and nanocellulose (extractable from microalgae and cyanobacteria) expand the capabilities for contributions to tissue engineering, controlled drug delivery, sustainable packaging, and the development of the advanced materials industry.

Marine lignin is an emerging frontier in blue biotechnology. Complex aromatic structures offer opportunities in the development of biopolymers, natural antioxidants, and advanced functional materials. However, it should be noted that its use faces technical challenges due to biological variability, brine treatments, and industrial scaling costs.

Marine biomaterials are renewable resources with high added value, favoring the transition to a circular economy and enhancing the value of marine resources. Optimizing their extraction, purification, and modification processes will expand their impact on the development of green technologies, turning marine ecosystems into strategic pillars of technological innovation and sustainable development.

## 3 References


Alam, M. M., Greco, A., Rajabimashhadi, Z., Corcione, C. E., (2024), Efficient and environmentally friendly techniques for extracting lignin from lignocellulose biomass and subsequent uses: A review, Cleaner Materials, vol. 13, pp.100253.

Alzate-Gaviria, L., Domínguez-Maldonado, J., Chablé-Villacís, R., Olguin-Maciel, E., Leal-Bautista, R. M., Canché-Escamilla, G., Caballero-Vázquez, A., Hernández-Zepada, C., Barredo-Pool, F.A, Tapia-Tussell, R., (2021), Alzate-Gaviria, L., Domínguez-Maldonado, J., Chablé-Villacís, R., Olguin-Maciel, E., Leal-Bautista, R. M., Canché-Escamilla, G., Caballero-Vázquez, A., Hernández-Zepada, C., Barredo-Pool, F.A and Tapia-Tussell, R. (2021). Presence of polyphenols complex aromatic "Lignin" in Sargassum spp. from Mexican Caribbean. Journal of Marine Science and Engineering, 9(1), 6. https://doi.org/10.3390/jmse9010006,

Berglund, L., Rakar, J., Junker, J. P., Forsberg, F., Oksman, K., (2020), Utilizing the natural composition of brown seaweed for the preparation of hybrid ink for 3D printing of hydrogels, ACS Applied Bio Materials, vol. 3(9), pp.6510-6520.

Bueno Suescun, E., Labrador Sánchez, H, Centeno Bordones, G., (2025), Bueno Suescun, E., Labrador Sánchez, H and Centeno Bordones, G. (2025). Síntesis de carboximetil lignina a partir de Megathyrsus maximus y su evaluación en propiedades interfaciales Rev. Colomb. Quim., 54, 1 (2025). https://doi.org/10.15446/rev.colomb.quim.v54n1.1183,

Camargos, C. H., Yang, L., Jackson, J. C., Tanganini, I. C., Francisco, K. R., Ceccato-Antonini, S. R., Faria, A. F., (2025), Lignin and nanolignin: next-generation sustainable materials for water treatment, ACS Applied Bio Materials, vol. 8(4), pp.2632-2673.

Casalini, S., Giacinti Baschetti, M., (2023), The use of essential oils in chitosan or cellulose-based materials for the production of active food packaging solutions: a review, Journal of the Science of Food and Agriculture, vol. 103(3), pp.1021-1041.

Centeno-Bordones, G., (2022), Centeno-Bordones, G. (2022). Obtención de nanopartículas de lignina a partir de Megathyrsus maximus para aplicaciones con potencial anti-UV Ciencia en Revolución, 8(24), 339. https://doi.org/10.5281/zenodo.8355980,

Dong, X. M., Revol, J. F., Gray, D. G., (1998), Effect of microcrystallite preparation conditions on the formation of colloid crystals of cellulose, Cellulose, vol. 5(1), pp.19-32.

Díaz-Vázquez, L. M., Rojas-Pérez, A., Fuentes-Caraballo, M., Robles, I. V., Jena, U., Das, K. C., (2015), Díaz-Vázquez, L. M., Rojas-Pérez, A., Fuentes-Caraballo, M., Robles, I. V., Jena, U., and Das, K. C. (2015). Demineralization of Sargassum spp. macroalgae biomass: selective hydrothermal liquefaction process for bio-oil production. Frontiers in Energy Research, 3, 6. https://doi.org/10.3389/fenrg.2015.00006,

Eichhorn, S. J., Dufresne, A., Aranguren, M., Marcovich, N. E., Capadona, J. R., Rowan, S. J., Weder, W., Thielemans, M. Roman, S. Renneckar, W. Gindl, S. Veigel, J. Keckes, H. Yano, K. Abe, M. Nogi, A. N. Nakagaito, A. Mangalam, J. Simonsen, T. Peijs., (2010), Current international research into cellulose nanofibres and nanocomposites, Journal of Materials Science, vol. 45(1), pp.1-33.

French, A. D., (2017), Glucose, not cellobiose, is the repeating unit of cellulose and why that is important, Cellulose, vol. 24(11), pp.4605-4609.

Geng, Y., Shaukat, A., Azhar, W., Raza, Q. U. A., Tahir, A., Abideen, M.A.B. Zia, M.A. Bashir, A. Rehim, (2025), Microalgal biorefineries: A systematic review of technological trade-offs and innovation pathways, Biotechnology for Biofuels and Bioproducts, vol. 18(1), pp.93.

Gomaa, M., Al-Badaani, A. A., Hifney, A. F., Adam, M. S., (2021), Industrial optimization of alkaline and bleaching conditions for cellulose extraction from the marine seaweed Ulva lactuca, Journal of Applied Phycology, vol. 33(6), pp.4093-4103.

Grappa, R., Venezia, V., Silvestri, B., Costantini, A., Luciani, G., (2024), Grappa, R., Venezia, V., Silvestri, B., Costantini, A., and Luciani, G. (2024). Synthesis of lignin nanoparticles: Top-down and bottom-up approaches. In Medical Sciences Forum, 1 (25). MDPI. https://doi.org/10.3390/msf2024025003,

Gómez, Y., Centeno-Bordones, G., Labrador, H., (2025), Evaluation of the different oxidative processes of lignin from the Venezuelan grass Megathyrsus Maximus, to activate metabolic energy, Ciencia e ingeniería, vol. 46, pp.75-86.

Habibi, Y., Lucia, L. A., Rojas, O. J., (2010), Cellulose nanocrystals: chemistry, self-assembly, and applications, Chemical reviews, vol. 110(6), pp.3479-3500.

Han, S., (2019), Han, S. (2019). Thermoelectric polymer-cellulose composite aerogels (Vol. 2028). Linköping University Electronic Press. https://doi.org/10.3384/diss.diva-161350,

He, Q., Wang, Q., Zhou, H., Ren, D., He, Y., Cong, H., Wu, L., (2018), Highly crystalline cellulose from brown seaweed Saccharina japonica: isolation, characterization and microcrystallization, Cellulose, vol. 25(10), pp.5523-5533.

Ioelovich, M. J., (2022), Microcellulose vs nanocellulose–a review, World J. Adv. Eng. Technol. Sci, vol. 5(2), pp.1-15.

Iqbal, K., Mishra, A., Sreedharan, S. M., (2025), The quintessence of algal biomass in bioplastic production: insightful advancement and sustainable use, Bioresources and Bioprocessing, vol. 12(1), pp.91.

Jose, S., Cowan, N., Davidson, M., Godina, G., Smith, I., Xin, J., Menezes, P. L., (2025), A comprehensive review on cellulose nanofibers, nanomaterials, and composites: manufacturing, properties, and applications, Nanomaterials, vol. 15(5), pp.356.

Karlsson, M., Romson, J., Elder, T., Emmer, Å., Lawoko, M., (2023), Lignin structure and reactivity in the organosolv process studied by NMR spectroscopy, mass spectrometry, and density functional theory, Biomacromolecules, vol. 24(5), pp.2314-2326.

Klap, V. A., Hemminga, M. A., Boon, J. J., (2000), Retention of lignin in seagrasses: angiosperms that returned to the sea, Marine Ecology Progress Series, vol. 194, pp.1-11.

Kowalska, M., Wozniak, M., Zbikowska, A., Okolus, J., Molik, A., (2025), Xanthan gum and microcrystalline cellulose as stabilizers in emulsions containing catalytically modified animal and vegetable fat, Catalysts, vol. 15(1), pp.41.

Ley, Y., Cheng, X. Y., Ying, Z. Y., Zhou, N. Y., Xu, Y., (2023), Ley, Y., Cheng, X. Y., Ying, Z. Y., Zhou, N. Y., and Xu, Y. (2023). Characterization of two marine lignin-degrading consortia and the potential microbial lignin degradation network in nearshore regions. Microbiology Spectrum, 11(3), e04424-22. https://doi.org/10.1128/spectrum.04424-22,

Li, X., Zhang, T., Sun, S., Lan, H., Yu, T., (2012), Lignin in marine environment and its analysis—A review, Journal of Ocean University of China, vol. 11(4), pp.501-506.

Li, X., Zhang, T., Sun, S., Lan, H., Yu, T., (2012), Lignin in marine environment and its analysis—A review, Journal of Ocean University of China, vol. 11(4), pp.501-506.

Liu, W., Xu, L., Cheng, H., Chen, Z., Zhou, H., Wang, Y., (2025), Insights into lignin bioconversion: lignin-derived compounds treatment of a novel marine fungus K-2, Journal of the Science of Food and Agriculture, vol. 105(3), pp.1651-1662.

Machado, B., Costa, S. M., Costa, I., Fangueiro, R., Ferreira, D. P., (2024), The potential of algae as a source of cellulose and its derivatives for biomedical applications, Cellulose, vol. 31(6), pp.3353-3376.

Madadi, R., Maljaee, H., Serafim, L. S., Ventura, S. P., (2021), Microalgae as contributors to produce biopolymers, Marine Drugs, vol. 19(8), pp.466.

Mateo, S., Fabbrizi, G., Moya, A. J., (2025), Lignin from plant-based agro-industrial biowastes: From extraction to sustainable applications, Polymers, vol. 17(7), pp.952.

Melikoglu, M., (2025), Organosolv lignin: A comprehensive review of pretreatment advancements and biorefinery integration, Next Materials, vol. 9, pp.101136.

Mihhels, K., Yousefi, N., Blomster, J., Solala, I., Solhi, L., Kontturi, E., (2023), Assessment of the Alga Cladophora glomerata as a Source for Cellulose Nanocrystals, Biomacromolecules, vol. 24(11), pp.4672-4679.

Mihranyan, A., (2011), Cellulose from cladophorales green algae: From environmental problem to high-tech composite materials, Journal of Applied Polymer Science, vol. 119(4), pp.2449-2460.

Moon, R. J., Martini, A., Nairn, J., Simonsen, J., Youngblood, J., (2011), Cellulose nanomaterials review: structure, properties and nanocomposites, Chemical society reviews, vol. 40(7), pp.3941-3994.

Moral, A., Aguado, R., Castelló, R., Tijero, A., Ballesteros, M. D. L. M., (2019), Potential use of green alga Ulva sp, for papermaking. BioResources, vol. 14(3), pp.6851-6862.

Omran, A. A. B., Mohammed, A. A., Sapuan, S. M., Ilyas, R. A., Asyraf, M. R. M., Rahimian Koloor, S. S., Petrů, M., (2021), Micro-and nanocellulose in polymer composite materials: A review, Polymers, vol. 13(2), pp.231.

Pamungkas, I.W, Budhiyanti, S.A., (2021), Pamungkas, I.W and Budhiyanti, S.A. (2021). Isolation and Characterization of Microcrystalline Cellulose from Alginate Residue of Brown Seaweed Sargassum Polycystum. Journal of Hunan University (Natural Sciences), 48, https://jonuns.com/index.php/journal/article/view/843,

Patrichi, C. A. M., Cioroiu Tirpan, D. R., Aljanabi, A. A. A., Trica, B., Gifu, I. C., Dobre, T., (2023), Extraction of cellulose from Ulva lactuca algae and its use for membrane synthesis, Polymers, vol. 15(24), pp.4673.

Plianwong, S., Sirirak, T., (2024), Cellulose nanocrystals from marine algae Cladophora glomerata by using microwave-assisted extraction, International Journal of Biological Macromolecules, vol. 260, pp.129422.

Poudel, J., Bhattarai, S., Nath, N., Tanti, B., (2025), An exclusive review of microcrystalline cellulose: Structure and applications, and limitations, Materials Today Communications, vol. 45, pp.112247.

Ren, S., Sun, X., Lei, T., Wu, Q., (2014), The Effect of Chemical and High-Pressure Homogenization Treatment Conditions on the Morphology of Cellulose Nanoparticles, Journal of Nanomaterials, vol. 2014(1), pp.582913.

Revol, J. F., Bradford, H., Giasson, J., Marchessault, R. H., Gray, D. G., (1992), Helicoidal self-ordering of cellulose microfibrils in aqueous suspension, International journal of biological macromolecules, vol. 14(3), pp.170-172.

Saadan, R., Hachimi Alaoui, C., Ihammi, A., Chigr, M., Fatimi, A., (2024), Saadan, R., Hachimi Alaoui, C., Ihammi, A., Chigr, M., and Fatimi, A. (2024). A brief overview of lignin extraction and isolation processes: From lignocellulosic biomass to added-value biomaterials. Environmental and Earth Sciences Proceedings, 31(1), 3. https://doi.org/10.3390/eesp2024031003,

Stewart, J. J., Akiyama, T., Chapple, C., Ralph, J., Mansfield, S. D., (2009), Stewart, J. J., Akiyama, T., Chapple, C., Ralph, J., and Mansfield, S. D. (2009). The effects on lignin structure of overexpression of ferulate 5-hydroxylase in hybrid poplar1. Plant physiology, 150(2), 621-635. http://doi.org/ 10.1104/pp.109.137059,

Strømme, M., Mihranyan, A., Ek, R., (2002), What to do with all these algae?, Materials Letters, vol. 57(3), pp.569-572.

Svagan, A. J., Vilaplana, F., Pettersson, T., Anusuyadevi, P. R., Henriksson, G., Hedenqvist, M., (2024), Centrifuge fractionation during purification of cellulose nanocrystals after acid hydrolysis and consequences on their chiral self-assembly, Carbohydrate Polymers, vol. 328, pp.121723.

Tarchoun, A. F., Trache, D., Klapötke, T. M., (2019), Microcrystalline cellulose from Posidonia oceanica brown algae: Extraction and characterization, International journal of biological macromolecules, vol. 138, pp.837-845.

Trache, D., Hussin, M. H., Chuin, C. T. H., Sabar, S., Fazita, M. N., Taiwo, O. F., Hassan, T, Haafiz, M. M., (2016), Microcrystalline cellulose: Isolation, characterization and bio-composites application—A review, International journal of biological macromolecules, vol. 93, pp.789-804.

Trivedi, N., Baghel, R. S., Bothwell, J., Gupta, V., Reddy, C. R. K., Lali, A. M, Jha, B., (2016), An integrated process for the extraction of fuel and chemicals from marine macroalgal biomass, Scientific reports, vol. 6(1), pp.30728.

Vanholme, R., Demedts, B., Morreel, K., Ralph, J., Boerjan, W., (2010), Lignin biosynthesis and structure, Plant physiology, vol. 153(3), pp.895-905.

Wahlström, N., Edlund, U., Pavia, H., Toth, G., Jaworski, A., Pell, A. J., Choong, F.X., Shirani, H., Nilsson, K.P, Richter-Dahlfors, A., (2020), Cellulose from the green macroalgae Ulva lactuca: isolation, characterization, optotracing, and production of cellulose nanofibrils, Cellulose, vol. 27(7), pp.3707-3725.

Xu, K., Chen, Y., Du, G., Wang, S., (2022), Xu, K., Chen, Y., Du, G., and Wang, S. (2022). Preparation, properties, and advanced functional applications of nanocellulose. In Wood Industry-Past, Present and Future Outlook. IntechOpen. https://doi.org/10.5772/intechopen.105807,

Yu, O., Kim, K. H., (2020), Lignin to materials: A focused review on recent novel lignin applications, Applied Sciences, vol. 10(13), pp.4626.

Yuan, Q., Bian, J., Ma, M. G., (2021), Advances in biomedical application of nanocellulose-based materials: a review, Current Medicinal Chemistry, vol. 28(40), pp.8275-8295.

Zaimes, G. G., Khanna, V., (2013), Microalgal biomass production pathways: evaluation of life cycle environmental impacts, Biotechnology for biofuels, vol. 6(1), pp.88.

Zanchetta, E., Mercier, B., Frabboni, M. Damergi, E., Ludwig, C and Pick, H. (2025). Purification of Cellulose and Chitin Polymers and Other Value-Added Products from the Microalga Chlorella vulgaris Using a

Green Biorefinery Process. Fermentation, 11, 120 https://doi.org/10.3390/fermentation11030120,

***Received:*** *november 22, 2025*

***Accepted:*** *february 22,2026*

***Ramon Henríquez Koch:*** *Chemical engineer from the Central University of Venezuela, research assistant at the Center for Oceanology and Antarctic Studies. Venezuelan Institute of Scientific Research. Email: kochhram@gmail.com*

***https://orcid.org/0009-0007-7941-4255***

***Guillermo Centeno Bordones:*** *Doctor in Technological Chemistry from the University of Carabobo, Valencia, Venezuela. Researcher at the Center for Oceanology and Antarctic Studies. Venezuelan Institute of Scientific Research.*

***https://orcid.org/0000-0003-1436-4764***

*Artículo de Investigación. Revista Ciencia e Ingeniería. Vol. 47, No. 3 pp.369-378, agosto-noviembre, 2026.*
*ISSN 1316-7081. ISSN Elect. 2244-8780 Universidad de los Andes (ULA)*

# Phytochemical and antioxidant characterization of extracts of *Mangifera indica L.* and *Passiflora edulis*

# Caracterización fitoquímica y antioxidante de extractos de *Mangifera indica L.* y *Passiflora edulis*

**Jiménez-Ruiz, Rudy[1*], Velásquez, Ingrid[1,2]**

[1]Soil and Environmental Technology Research Laboratory, Department of Chemistry. [2]Research Center Chemistry, Faculty of Engineering, University of Carabobo, Valencia, Venezuela

*rjimenez6@uc.edu.ve

**Abstract**

Secondary metabolites are bioactive compounds synthesized by plants, fungi, and microorganisms; more than 25% of drugs are derived from plant sources. Currently, agro-industrial waste such as passion fruit seeds and mango leaves represent residues that can be used as multifaceted raw materials. The purpose of this research was to compare the physicochemical characteristics of two natural extracts used as antioxidants and anti-inflammatories in biomedical applications. Yield, solubility, refractive indices, and phytochemical profile were determined by qualitative screening and Fourier transform infrared spectroscopy (FTIR). The results revealed the superiority of the mango leaf extract over passion fruit seeds in both polyphenol content and antioxidant capacity. The phytochemical screening confirmed that Mangifera indica L. possesses a wide diversity of secondary metabolites, including tannins, anthocyanins, and phytosterols, while in the Passiflora edulis triterpenes, however, coincided with the phenolic compounds and alkaloids. Both extracts showed insolubility in water and high affinity for short-chain alcohols. It is concluded that, although Passiflora edulis it is industrially more viable due to its high performance, the Mangifera indica L. it presents a superior bioactive profile; however, both can be used in the development of pharmaceutical, cosmetic, and food formulations; confirming that waste can be transformed into high value-added raw materials, promoting alternatives that reduce environmental impact and offer therapeutic alternatives.

**Keywords:** Mangifera indica, Passiflora edulis, antioxidant capacity, total polyphenols, phytochemical profile.

**Resumen**

Los metabolitos secundarios son compuestos bioactivos sintetizados por plantas, hongos y microorganismos; más del 25 % de los fármacos derivan de fuentes vegetales. Actualmente, los desechos agroindustriales como las semillas de parchita y hojas de mango, representan residuos que pueden ser aprovechados como materia prima multifacética. La finalidad de esta investigación fue comparar las características fisicoquímicas de dos extractos naturales empleados como antioxidantes y antinflamatorios en aplicaciones biomédicas. Se determinó el rendimiento, solubilidad, índices de refracción y perfil fitoquímico mediante tamizaje cualitativo y espectrofotometría de infrarrojos con transformada de Fourrier (FTIR). Los resultados revelaron la superioridad del extracto de hojas de mango sobre las semillas de parchitas tanto en el contenido de polifenoles como en capacidad antioxidante. El tamizaje fitoquímico confirmó que Mangifera indica L. posee una amplia diversidad de metabolitos secundarios, que incluyen taninos, antocianinas y fitoesteroles, mientras en la Passiflora edulis Triterpenos, sin embargo, coincidiendo los compuestos fenólicos y alcaloides. Ambos extractos mostraron insolubilidad en agua y alta afinidad por alcoholes de cadena corta. Se concluye que, si bien Passiflora edulis es industrialmente más viable por su alto rendimiento, la Mangifera indica L. presenta un perfil bioactivo superior, no obstante, ambas puedes ser empleadas en el desarrollo de formulaciones farmacéuticas, cosméticas y alimentos; confirmando que los desechos pueden ser transformados en materias primas de alto valor agregado, promoviendo alternativas que reducen el impacto ambiental y ofrecen alternativas terapéuticas.

Keywords: Mangifera indica, Passiflora edulis, antioxidant capacity, total polyphenols, phytochemical profile.

## 1 Introduction

In a plant, carbohydrates, amino acids, and proteins are the main metabolites that are primarily active during the development and maturation phases of plant tissues. Secondary metabolites, on the other hand, form the biological system and are produced throughout the developmental cycle to help plants survive and overcome natural obstacles (Azmir *et al*., 2013).

In recent years, research on medicinal plants has increased worldwide due to their applications in phytopharmacology. Among these molecules are phenolic acids, tannins, and flavonoids, which possess important biological properties such as activities antimicrobials, anti-inflammatory, anticancer and antioxidant (Allaguiet al., 2023). Plants and their plant extracts are a relevant source of bioactive compounds widely used in functional foods, as well as for therapeutic purposes.

It is important to highlight the properties of plants used in traditional medicine worldwide, which leverages phytochemistry to determine their applicability. The efficacy of an extract is associated with the synergistic interactions of multiple bioactive compounds present in it; these interactions may not be detectable when the individual compounds are evaluated in isolation (Wink, 2015).

Mangifera indica L., commonly known as mango, belongs to the Anacardiaceae family, its leaves contain a variety of bioactive compounds, including polyphenols, flavonoids, tannins, alkaloids, glycosides, steroids, triterpenoids, saponins, mangiferin, and anthocyanins. These compounds exhibit antioxidant, anti-inflammatory, and antimicrobial properties (Kaur.et al., 2025). Mangiferin, extracted mainly from the leaves and bark, has been studied for its antioxidant and anti-inflammatory properties, showing potential in the treatment of chronic diseases such as diabetes and cardiovascular diseases, among others. (Minniti,et al., 2023; Kumar, et al., 2021).

Mango leaves are considered waste, mainly generated by pruning the plant, but in reality they are of great importance, as they contain a huge variety of phytoactives, including phenolic compounds, crude proteins, essential oils, dietary fiber, vitamins and minerals (Mehmood et al., 2024).

It is worth noting that the main secondary metabolite present in Mangifera indica L. is Mangiferin, whose chemical structure is $C_{19}H_{18}O_{11}$ (1,3,6,7 tetrahydroxyxanthone-C2-β-D-glucoside), a phenolic compound, specifically a xanthone, which is a carbonyl compound consisting of a xanthene heterocycle oxidized at position 9. Mangiferin can be found in the leaves, bark, seeds, flower, fruit, and pulp of the mango, and has high pharmaceutical and nutraceutical value. (Forero and Pulido, 2016).

On the other hand, Passiflora edulis, commonly known as passion fruit, belongs to the Passifloraceae family. It possesses bioactive compounds such as alkaloids, flavonoids like vitexin, isovitexin, orientin, and isoorientin, and also contains anthocyanins, with antioxidant properties that help protect cells from oxidative damage, phenolic acids such as chlorogenic acid and caffeic acid, carotenoids, saponins, and phytosterols such as β-sitosterol. (Villada, et al., 2023. Patel, et al., 2011). However, the main component is piceatannol, which is a stilbenoid and a phenolic compound with the chemical structure $((HO)_2C_6H_3)_2CH)_2$ (4-[(*E*)-2-(3,5-Dihydroxyphenyl)ethene-1-yl]benzene-1,2-diol).
Stilbenoids, which are hydroxylated derivatives of stilbene, belong to the phenylpropanoid family, which is why piceatannol is also considered a phenolic compound. This compound is found primarily in the fruit seeds (Zomer et al., 2022).

Increasing attention has been paid to bioactive food compounds that may provide additional health benefits beyond basic nutritional needs. Among these identified bioactive constituents, polyphenols are the most studied, with growing evidence of their potential role in the prevention of chronic human diseases. They possess numerous biological and pharmacological properties, including neuroprotection, anti-inflammatory, antioxidant, antimicrobial, antihyperglycemic, antiallergic, and chemopreventive activity against cancer. Among these functions, anti-inflammatory activity is the fundamental principle behind many of these activities, as common causal factors in these diseases include inflammation, which leads to increased levels of inflammatory mediators such as pro-inflammatory cytokines, chemokines, and oxidative enzymes in immune cells (Wang et al., 2021).

The purpose of this research was to compare the physicochemical, photochemical and antioxidant characteristics of two natural extracts obtained from mango leaves and passion fruit seeds.

## 2 Experimental Procedure

### *2.1 Extraction of bioactive compounds*

The leaves of Mangifera indica L. and the seeds of Passiflora edulis were dried in an oven (VWR Scientific, model 1305U) at (100 ± 5) °C for 3 hours, until a constant weight was achieved (AOAC 925.10, 2012). Once dry, they were ground to reduce the sample size.
The extraction of bioactive compounds from both the *Mangifera indica* L. leaves and the Passiflora edulis seeds was performed using the Soxhlet method according to the methodology proposed by Ahmad et al. (2020), with some modifications. The extraction was carried out at 78 °C for 6 hours, using 96% ethanol as the solvent. After the extraction process, the solvent was removed by distillation using a rotary evaporator.

### *2.2. Phytochemical screening*

Phytochemical screening was performed using colorimetric tests, following the methodologies and evaluation criteria proposed by Verde-Star et al. (2016),

Shaikh and Patil (2020), and García-Granados et al. (2019), with some modifications, in order to identify the presence of phytoconstituents in the extracts. The tests performed were Dragendroff (Alkaloids), Salkowski (Phenolic Compounds), Ferric Chloride (Phenolic Compounds - Tannins), Shinoda (Flavonoids, Flavones, and Flavonols), Shibata (Flavonols and Flavones), Liebermann-Burchard (Phytosterols - Triterpenes), and Hydrochloric Acid Test (Anthocyanins).

*2.3 Caracterización de los extractos de hoja de mango y semillas de parchitas*

The refractive index (Covenin 702:2001), total polyphenol content (Jeszka-Skowron et al., 2016), and antioxidant capacity (Pacheco-Coello et al., 2020) were determined for the extracts obtained. The solubility of the extract was also assessed using the methodology proposed by Scotti et al. (2020), based on linear alcohols of different polarities. Fourier transform infrared spectrophotometry was also performed.

## 3 Results and discussion

*3.1 Extraction of bioactive compounds*

The extraction yield obtained from mango leaves (Mangifera indica L.) was 8.49%, a value that falls within the range reported by Kassi et al. (2019), who indicate that it ranges from 7.04% to 10.61%. More recent research, such as that by Zahoor et al. (2023), indicates that the yield can range from 6.33% to 9.88% depending on the variety. The extract was a greenish-brown color, very viscous in appearance, and had a characteristic odor.

The processing yield of passion fruit seeds was 34.13%, although other studies, such as Pantoja-Chamorro et al. (2017), reported values between 16.7% and 33.5%, noting that it depends on the technique, solvent, and geographic origin. Scotti et al. (2020), on the other hand, obtained a yield of 19.65%. The extract was an ochre-yellow color, viscous in appearance, and had a characteristic passion fruit odor.

In general, the extraction conditions play a determining role in the performance of the process, since parameters such as the type of solvent, temperature and extraction time, directly influence the diffusion and solubilization of the bioactive compounds (Hernández-Carranza et al., 2015), as well as the variety of the plant.

3.2 *Phytochemical screening*

Table 1 shows the metabolites determined for each extract, where the phytochemical behavior differed in some tests. Both extracts contained alkaloids. In the case of mango leaf, Ali et al. (2020) reported their presence and quantified them, obtaining a value of (0.300±0.141)%, while for passion fruit seed, Chaichit et al. (2026) reported the presence of beta-carbonyl alkaloids such as harmaline, harmine, harman, and harmol, while Yuan et al. (2017) reported the presence of cis- and trans-ferulothyramine.

Alkaloids are notable for their therapeutic properties for humans, such as: antimicrobial, analgesic, antimalarial, antiparasitic (Delovino and Carlos, 2026; Alshammaa, 2016), and sedative, acting as anxiolytics and antidepressants because they play an important role as modulators of stress and anxiety (Campos-Rodríguez et al., 2023).

**Table 1. Phytochemical screening of the extracts**

| Metabolite | Tests | *Mangifera indica* L. | *Passiflora edulis* |
|---|---|---|---|
| Alkaloids | Dragendorff | +++ | +++ |
| Phenolic Compounds | Salkowski | +++ | +++ |
| | Ferric chloride | +++ | - |
| Flavonoids. Flavones, Isoflavones and Flavonols | Shinoda | +++ | ++ |
| Flavonols and Flavones | Shibata | +++ | - |
| Tannins | Ferric chloride | +++ | - |
| Phytosterols | Liebermann-Burchard | +++ | - |
| Triterpenes | Liebermann-Burchard | - | +++ |
| Anthocyanins | Hydrochloric acid | +++ | - |

*+ Positive - Negative*

Regarding phenolic compounds, the results indicate a notable difference between the species. In the mango leaf extract, the presence of phenolic compounds such as flavonoids was confirmed, specifically flavones, isoflavones, and anthocyanins, as well as tannins, terpenes, terpenoids, and phytosterols. In the passion fruit seed extract, phenolic compounds such as flavonoids and flavones were found. This variability in phenol synthesis can be explained by the findings of García-Granados et al. (2019), who state that the absence of certain phenols and tannins in passionflower seeds, in contrast to their abundance in mango leaves, could be linked to the differential biosynthesis, distribution, and mobilization of their metabolites among the plant's structures.

Phenolic compounds have been proposed in numerous studies to be used as: antioxidants, anti-inflammatories, antimicrobials (gram-positive bacteria, gram-negative bacteria and yeasts), immunomodulators, antiallergics, antifungals, antiparasitics, antipyretics, hepatoprotectants, antidiabetics, antidiarrheals, antiplatelet agents, antivirals and antitumor agents (Amrita et al., 2009; Morais et al., 2016; Kumar et al., 2021; Mirza et al., 2021).

Regarding phytosterols, despite the test being negative in passion fruit extract, research has reported that they are minor components, and compounds such as campesterol, stigmasterol, β-sitosterol and lanosterol have been identified by gas chromatography coupled to mass spectrometry (Pantojas-Chamorro et al., 2017).

On the other hand, the Libermann-Burchardt test was negative for terpenes in mango leaf, however, research such as Kumar et al., (2021) reported monoterpenes, sesquiterpenes, smaller amounts of their analogues and traces of non-terpenoid hydrocarbons and oxygenated hydrocarbons.

### *3.3. Characterization of the extracts*

#### *3.3.1 Total polyphenols and antioxidant capacity*

Table 2 shows the parameters measured for each extract. In the case of the refractive index, commonly used as a reference for impurities in oil extracts, it was found that for the *Mangifera indica* L. leaf extract, it falls within the range reported by Zahoor et al. (2023), whose results ranged from 1.443 to 1.457. On the other hand, Nadeem and Imran (2016) mentioned a refractive index value of 1.457. Similarly, Kassi et al. (2019) reported values between 1.458 ± 0.001 and 1.480 ± 0.002. Regarding the seed extract of *Passiflora edulis*, the value found is similar to that reported by Scotti et al., (2020). When compared with other investigations such as Guzman et al., (2021) reported an index of 1.465 ± 0.005, while Cuong et al., (2019) obtained a refractive index of 1.472, slightly lower; the difference may be due to the plant's growing conditions.

**Table 2. Características fisicoquímicas de los extractos**

| Parameter | *Mangifera indica* L. | *Passiflora edulis* |
|---|---|---|
| Refractive index | 1.442 | 1.467 |
| Total polyphenols (mg/L) | 6190.15 ± 0,92 | 64.45 ± 0,01 |
| Antioxidant capacity (%) | 77.43 ± 0.98 | 26.27 ± 0.01 |

The total polyphenol content, as well as the antioxidant capacity of the extracts, shows a behavior that differentiates them in terms of their phytochemical composition (Table 2). Mango leaf extract is rich in polyphenols. Carranza-Ortiz et al. (2025) reported polyphenols ranging from 1036.531 to 5028.293 mg GAE/100 g, results similar to those reported by Wu et al. (2020), who obtained phenolic compounds from mango leaves using 70% ethanol as a solvent and reported a range of 1602 to 3229 mg GAE/100 g. According to Medina-Saavedra et al. (2020), this quantitative variability is due to the fact that these leaves are a significant source of bioactive compounds such as phenols, flavonoids, triterpenes, phytosterols, and polyphenols, among which mangiferin stands out. Domínguez-Ruvalcaba et al. (2025) complements this characterization by identifying other metabolites such as chlorogenic, hydroxybenzoic, caffeic and coumaric acids using HPLC-UV/VIS.

Meanwhile, the seed extract of *Passiflora edulis* revealed a lower concentration of total polyphenols than mango leaf. Noguera-Machado et al. (2019) reported an average total phenol content of 68.72 ± 0.69 mg GAE/g of extract, a value similar to that found in this study. Santana et al. (2017) highlight that the main polyphenol in passion fruit seeds is piceatannol, a stilbenoid with important biological activities such as antioxidant, anti-inflammatory, analgesic, and anticarcinogenic properties..

While mango leaf extracts register exceptional concentrations, passion fruit seeds typically average values between 16 mg GAE/g and 65 mg GAE/g depending on the extraction method.

The phenolic compounds present in the extracts can influence their antioxidant capacity (Table 2). Kulkarni and Rathod (2018) indicate that the high activity in mango leaves is mainly due to mangiferin and other constituents in the crude extract, which possess numerous hydroxyl groups that facilitate electron donation and the termination of free radical chain reactions. Meanwhile, Medina-Saavedra et al. (2021) evaluated the antioxidant activity of aqueous mango leaf extracts using the ABTS assay, obtaining a value of 59.13 mg trolox eq/100 g.

In the case of passion fruit seed extract, Malacrida and Jorge (2012) reported a value of 25.61%, indicating a moderate antioxidant capacity, which is intrinsically linked to its tocopherol composition, especially δ and γ tocopherols, which have superior biological activity compared to the α and β forms. Furthermore, phenolic compounds act synergistically with tocopherols to scavenge free radicals (Silva et al., 2023), while lipid fractions such as squalene and sterols act as protective agents against oxidation (Pantoja-Chamorro et al., 2017; Silva et al., 2023). The polyphenols in P. edulis seeds contain a high amount of piceatannol, which has been reported to have antioxidant activity; therefore, it is considered responsible for the antioxidant activity of the seed extracts.

#### 3.3.2 *Solubility of the extracts*

The solubility of ethanolic extracts of *Mangifera indica* L. leaves and Passiflora *edulis* seeds reflects physicochemical differences based on the nature of their predominant metabolites (Table 3). In the case of mango leaves, solubility is governed by mangiferin, a xanthone that constitutes approximately 41% of the extract content, with an intermediate polarity (Acosta et al., 2016). In contrast, the passion fruit seed extract has a dominant lipid fraction of approximately 81.7%, composed of unsaturated fatty acids and stilbenes such as piceatannol, which gives it a markedly lipophilic character (Krambeck et al., 2020; Santos et al., 2020).

Diaz et al. (2023) indicate that the solvent's dielectric constant is adjusted for polyphenols, while Peron et al. (2025) mention the solubility of the plant material's flavonoids. Both extracts were soluble in intermediate-chain alcohols (propanol, butanol, and pentanol). This behavior is based on the fact that these solvents offer a balance between

the ability to form hydrogen bonds and dispersion interactions, a determining factor for dissolving complex molecules (Rajakumar et al., 2014). Following the principle that like dissolves like, the decrease in polarity of these alcohols compared to water allows for efficient intermolecular interaction with both the aromatic nuclei of mangiferin and the hydrocarbon chains of the fatty acids in passionflower (Chaves et al., 2020).

Finally, both extracts are insoluble in water, confirming a shared hydrophobic repulsion. For *Mangifera indica* L., this insolubility is reinforced by lignocellulosic components such as lignin and cellulose present in the leaf structure (Kaur et al., 2025; Kumar et al., 2023). In the case of *Passiflora edulis*, the insolubility derives from repulsive forces towards water molecules, which prefer to form hydrogen bonds with each other rather than interact with the lipid chains of the extract (Díaz et al. 2023).

**Tabla 3.** Solubility of the extracts

| Solvent | *Mangifera indica L.* | *Passiflora edulis* |
|---|---|---|
| Water | --- | --- |
| Ethanol | ++++ | ++ |
| Propanol | ++++ | ++++ |
| Butanol | ++++ | ++++ |
| Pentanol | ++++ | ++++ |
| Hexanol | ++ | ++++ |
| Heptanol | ++ | ++++ |

++++ *Soluble* --- *Insoluble* ++ *partially soluble*

### 3.3.3 *Fourier transform infrared spectrophotometry (FTIR).*

The spectrum of the mango leaf extract (Fig. 1) shows a band at 1380.34 $cm^{-1}$ associated with the symmetric bending of the methyl groups (−CH3), which is similar to that reported by Rajakumar et al. (2014) who obtained a band at 1383 $cm^{-1}$ in the dried mango leaf powder, as an indicator of the presence of foliar lipids and terpenes, similar to Barnabas et al. (2022), who showed these groups in the band 1368.71 $cm^{-1}$.

The band of greatest intensity was located at 1044.42 $cm^{-1}$, with a strong intensity (35.45% transmittance). This is characteristic of the C-O vibration associated with lignin, hemicellulose, and polyphenolic compounds such as mangiferin. Kaur et al. (2025) highlight the region between 1030 and 1050 $cm^{-1}$, where the greatest absorption is concentrated due to the carbohydrate nature of the leaf matrix. The spectral region between 1200 and 1300 $cm^{-1}$ represents the C-O stretching signal of aromatic esters.

The band at 879.20 $cm^{-1}$ is associated with the presence of aromatic hydrocarbons and the carbon skeleton structure of terpenoids. Peron et al. (2025) reported a similarity in their study, reporting a band at 880.11 $cm^{-1}$.

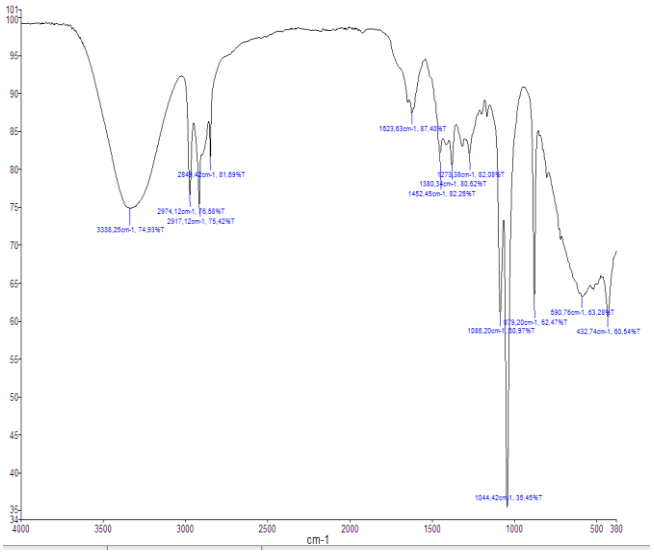


**Figure 1**. FTIR spectrum of crude extract of *Mangifera indica* L. leaves

On the other hand, the spectrum of the passion fruit seed extract (Fig. 2) showed a band at 3342.98 $cm^{-1}$, associated with the presence of hydroxyl groups (-OH). Rizwana et al. (2019) state that in the crude extract, a stretch appears at 3370.86 $cm^{-1}$, indicating the presence of an O–H bond, which could be an alcohol or phenol. At 2854.46 $cm^{-1}$, a –CH stretch shoulder is identified, confirming the unsaturation of the fatty acids, a region associated with the seed's lipid matrix (Santos et al., 2020). The bands located at 2924.01 and 2854.46 $cm^{-1}$ correspond to the asymmetric and symmetric methylene stretches, respectively.

The band at 1744.13 $cm^{-1}$ is associated with the carbonyl group (C=O), which has been reported in the literature at 1743.82 $cm^{-1}$ and is associated with esters linked to triglycerides (Rizwana et al., 2019). A prominent band was also identified at 1604 $cm^{-1}$, which is attributed to the C=C bond stretching vibrations characteristic of the aromatic rings present in the polyphenol structure. Rosário et al. (2022) observed a similar frequency at 1637 $cm^{-1}$, linked to carbonyl groups (C=O) and the elongation of amide groups (N-H). This shift suggests that the components of the extract are not in a free state but participate in specific molecular interactions.

Regarding the 1140 to 710 $cm^{-1}$ region, it shows significant structural complexity, formed by the 1160.19 - 1088.54 and 1046.54 $cm^{-1}$ bands; associated with C-O bond stretching in alcohols and phenolic compounds; and carbohydrate structures, specifically in D-glucose units and polysaccharides such as pectin, as reported by Rizwana et al. (2019). The 721.99 $cm^{-1}$ band is characteristic of long methylene chains in lipids.

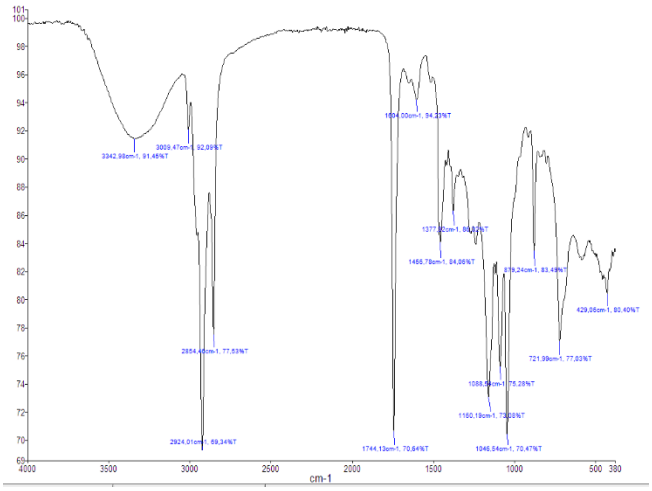


**Figure. 2.** FTIR spectrum of crude extract of *Passiflora edulis* seeds

## 4 Conclusion

The extracts possess distinct phytochemical characteristics, as well as different total phenol content and antioxidant capacity, giving each extract distinct antimicrobial and anti-inflammatory properties. The total polyphenol content in *Mangifera indica* L. significantly exceeds that of *Passiflora edulis*, which affects its antioxidant capacity, confirming the correlation between phenolic content and free radical scavenging ability. Phytochemical screening highlights the abundant bioactive components in both species, and FTIR analysis confirmed the diversity of their functional groups. It can be deduced that the nature of the compounds affects their solubility in solvents of different polarities, an important parameter for their inclusion in cosmetic and pharmaceutical formulations. It is concluded that, while *Passiflora edulis* is more industrially viable due to its high yield, *Mangifera indica* L. presents a superior bioactive profile; however, both can be used in the development of new products.

## Acknowledgements

To Fonacit for funding this research, project **Nº** 2025000029 CDCH-UC Call 2024.

## References

Acosta, J., Sevilla, I., Salomón, S., Nuevas, L., Romero, A., & Amaro, D. (2016). Determination of mangiferin solubility in solvents used in the biopharmaceutical industry. Journal of Pharmacy & Pharmacognosy Research, 4(2), 49-53. ISSN 0719-4250

Ahmad, A. (2020). Total Phenolic, Total Flavonoids Content and Antioxidant Activity of Mangifera sp. Leaf Extracts. Journal of agrobiotechnology, 11(1S), 69-78. https://doi.org /10.37231/jab.2020.11.1S.236

Ali B..Alfa A., Tijani K., Idris E., Unoyisa U., Junaidu Y. (2020). Nutritional Health Benefits and Bioactive Compounds of Mangifera indica L (Mango) Leaves Methanolic Extracts. Asian Plant Research Journal 6(2): 41-51. ISSN: 2581-9992.

Allagui, I.; Horchani, M.; Zammel, N.; Jalouli, M.; Elfeki, A.; Kallel, C.; Mansour, L.; Alwasel, S.; Harrath, A.; Jannet, H., Allagui, M. and Hcini, K (2023). Phytochemical Characterization, Antioxidant and Anti-Inflammatory Effects of Cleome arabica L. Fruits Extract against Formalin Induced Chronic Inflammation in Female Wistar Rat: Biochemical, Histological, and In Silico Studies. Molecules, 28(1), 2-18. https://doi.org /10.3390/molecules28010026

Alshammaa, D. (2016). Preliminary screening and phytochemical profile of Mangifera indica leave's extracts, cultivated in Iraq. International Journal of Current Microbiology and Applied Sciences, 5(9), 163-173. https://doi.org/10.20546/ijcmas.2016.509.01812

Amrita, B., Liakot, A., Masfida, A., y Begum, R. (2009). Studies on theantidiabe-tic effects of Mangifera indica stem-barks andleaves on nondiabetic, type 1 and type 2 diabetic modelrats. Bangladesh Journal of Pharmacology. 4(2), 110-114. https://doi.org /10.3329/bjp.v4i2.2488

Azmir, J.; Zaidul, I.S.M.; Rahman, M.M.; Sharif, K.M.; Mohamed, A.; Sahena, F.; Jahurul, M.H.A.; Ghafoor, K.; Norulaini, N.A.N.; Omar, A.K.M. . (2013). Techniques for extraction of bioactive compounds from plant materials: A review. Journal of Food Engineering, 117(4), 426-*436.* https://doi.org /10.1016/j.jfoodeng.2013.01.014

Barnabas, H. L., Aliyu, B. A., Gidigbi, J. A., Abubakar, A. B., & Markus, A. (2022). Comparative analysis of stable aqueous dispersion of silver nanoparticle synthesized from *Mangifera Indica* and Azadirachta Indica leaf extract. NanoNEXT, 3(4), 1-10. https://doi.org/10.54392/nnxt2241

Campos-Rodriguez, J., Acosta-Coral, K., Moreno-Rojo, C., & Paucar-Menacho, L. (2023). Maracuyá (Passiflora edulis): Composición nutricional, compuestos bioactivos, aprovechamiento de subproductos, biocontrol y fertilización orgánica en el cultivo. Scientia Agropecuaria, 14(4), 479-497. https://doi.org/10.17268/sci.agropecu.2023.040

Carranza-Ortiz D., Ambrosio-Gómez M., Chávez-Portillo M.,Carreón-Hidalgo J. y Martínez-Ramos T. (2025). Extracción e Identificación de Compuestos Fenólicos de hojas de mango (Mangifera indica L.) Revista Politécnica de Aguascalientes, 6 (4) ISSN: 2954-5102

Chaichit, S., Nitthikan, N., Kiattisin, K., y Jiranusornkul, S. (2026). Composición química y potencial antienvejecimiento de fracciones de

subproductos *de Passiflora edulis*: un estudio comparativo que integra perfilado metabolómico y acoplamiento molecular. *Compuestos 6(*2), 32. https://doi.org /10.3390/compounds6020032

Chaves, J., de Souza, M., da Silva, L., Lachos-Perez, D., Torres-Mayanga, P., Machado, A., Forster-Carneiro, T., Vázquez-Espinosa, M., González-de-Peredo, A., Barbero, G., & Rostagno, M. (2020). Extraction of Flavonoids From Natural Sources Using Modern Techniques. Frontiers in chemistry, 8(507887), 1-25. https://doi.org /10.3389/fchem.2020.507887

Cuong, T., Phuong, D., Anh, N., Khanh, P., Huong, T., & Cuong, N. (2019). Chemical compositions of Passiflora edulis seed oil cultivated in Viet Nam. Vietnam Journal of Science and Technology, 57(5), 551-558. https://doi.org /10.15625/2525-2518/57/5/13801

Delovino, R., & Carlos, R. (2026). Phytochemical analysis of mango leaves (Mangifera indica L.). International Journal for Multidisciplinary Research, 8(1), 1-8.13. https://doi.org /10.36948/ijfmr.2026.v08i02.71487

Díaz-Villagómez, D., Hernández-Ramírez, R., Cruz-Cruz, D., & Villegas-Gómez, C. (2023). Análisis fitoquímico: Una visión integral de los métodos de extracción de productos naturales. Naturaleza y Tecnología, 10(1) 22-35.

Domínguez-Ruvalcaba, J., Calderón-Santoyo, M., González-Gutiérrez, K., & Ragazzo-Sánchez, J. (2025). Extracto polifenólico de hojas de mango (Mangifera indica L.): Caracterización y actividad antifúngica in vitro. Revista Internacional de Investigación e Innovación Tecnológica, 13(75), 22-38.

García-Granados, R., Cruz-Sosa, F., Alarcón-Aguilar, F., Nieto-Trujillo, A., & Gallegos-Martínez, M. (2019). Análisis fitoquímico cualitativo de los extractos acuosos de Thalassia testudinum Banks ex Köning et Sims de la localidad de Champotón, Campeche, México, durante el ciclo anual 2016-2017. Polibotánica, (48), 151-168. https://doi.org /10.18387/polibotanica.48.12

Guzmán, C., Rojas, M. A., & Aragón, M. (2021). Optimization of ultrasound-assisted emulsification of emollient nanoemulsions of seed oil of Passiflora edulis var. edulis. Cosmetics, 8(1), 1-22. https://doi.org /10.3390/cosmetics8010001

Hernández-Carranza, P., Ávila-Sosa, R., Guerrero-Beltrán, J. Á., Navarro Cruz, A. R., Corona-Jiménez, E., & Ochoa-Velasco, C. E. (2015). Optimization of Antioxidant Compounds Extraction from Fruit By Products: Apple Pomace, Orange and Banana Peel. Journal of Food Processing and Preservation, 40, 103-115. https://doi.org /10.1111/jfpp.12588

Jeszka-Skowron, M., Sentkowska, A., Pyrzyńska, K., & De Peña, M. (2016). Chlorogenic acids, caffeine content and antioxidant properties of green coffee extracts: influence of green coffee bean preparation. European Food Research and Technology, 242(9), 1403-1409. doi.org /10.1007/s00217-016-2643-y

Jorge, N., Malacrida, C., Angelo, P., Andreo, D. (2009). Composição centesimal e atividade Antioxidante do extrato de sementes de maracujá (passiflora edulis) em óleo de soja. Pesquisa Agropecuária Tropical, 39(4), 380-385.

Kassi, A., Soro, Y., Koffi, E., & Sorho, S. (2019). Physicochemical study of kernel oils from ten varieties of Mangifera indica (Anacardiaceae) cultivated in Cote d'Ivoire. African Journal of Food Science, 13(7), 135-142. https://doi.org /10.5897/AJFS2019.1827

Kaur, J., Kaushik, D., Kumar, M., Babagil, G., Amarowicz, R., Proestos, C., Oz, E., Oz, F., Esatbeyoglu, T., & Bordiga, M. (2025). Comprehensive Analysis and Characterization of Mangifera indica L. Leaf Powder. Food science & nutrition, 13(6). 1-13. https://doi.org/10.1002/fsn3.70083

Krambeck, K., Oliveira, A., Santos, D., Pintado, M. M., Silva, J. B., Sousa Lobo, J. M., & Amaral, M. (2020). Identification and quantification of stilbenes (piceatannol and resveratrol) in Passiflora edulis by-products. Pharmaceuticals, 13(4), 1-9. https://doi.org/10.3390/ph13040073

Kulkarni, V., & Rathod, V. (2018). Exploring the potential of Mangifera indica leaves extract versus mangiferin for therapeutic application. Agriculture and Natural Resources, 52(2), 155-161. doi.org /10.1016/j.anres.2018.07.001

Kumar, A., Kumar, J., Tomer, V., Oz, E., Proestos, C., Zeng, M., Elobeid, T., & Oz, F. (2023). Major Phytochemicals: Recent Advances in Health Benefits and Extraction Method. Molecules, 28(2), 1-41. https://doi.org /10.3390/molecules28020887

Kumar, M., Saurabh, V., Tomar, M., Hasan, M., Changan, S., Sasi, M., Maheshwari, C., Prajapati, U., Singh, S., Prajapat, R. K., Dhumal, S., Punia, S., Amarowicz, R., & Mekhemar, M. (2021). Mango (Mangifera indica L.) Leaves: Nutritional Composition, Phytochemical Profile, and Health-Promoting Bioactivities. Antioxidants (Basel, Switzerland), 10(2), 1-23. https://doi.org /10.3390/antiox10020299

Malacrida, C., & Jorge, N. (2012). Yellow passion fruit seed oil (Passiflora edulis f. flavicarpa): Physical and chemical characteristics. Brazilian Archives of Biology and Technology, 55(1), 127-134. https://doi.org /10.1590/S1516-91320120001000016

Medina-Saavedra, G., Ramírez-Rivera, E., Herrera-Corredor, J., Sánchez-Valera, O., & Ramón-Canul, L. (2020). Evaluación de diversas actividades biológicas in vitro en las hojas de Mangifera indica L. Journal CIM, 8(1), 1421-1428.

Medina-Saavedra, G. Y., Herrera-Corredor, J. A., Vargas-Rivera, Y., Sánchez-Valera, O. V., Cabal-Prieto, A., Prinyawiwatkul, W. & Ramón Canul, L. G. (2021). Mango (Mangifera indica L.) leaf extracts as ingredient for the formulation of functional beverages with biological activity. International Journal of Food Science & Technology, 56(7), 3322-3332. https://doi.org /10.1111/ijfs.14910.

Mehmood, H., Mehmood, J., & Zulfiqar, N. (2024). Exploring the phytochemistry and pharmacology of Mangifera indica L. (Mango) leaves: A review. International Journal of Plant Based Pharmaceuticals, 4(1), 9-18, https://doi.org /10.29228/ijpbp.38.

Mirza, B., Croley, R., Ahmad, M., Pumarol, J., Das, N., Sethi, G., y Bishayee, A. (2021). Mango (Mangifera indica L.): a magnificent plant with cancer preventive and anticancer thera-peutic potential. Critical Reviews in Food Science and Nutrition. 61(13), 2125–2151. https://doi.org /10.1080/10408398.2020.1771678

Minniti, G., Laurindo, L. F., Machado, N. M., Duarte, L. G., Guiguer, E. L., Araujo, A. C., Dias, J. A., Lamas, C. B., Nunes, Y. C., Bechara, M. D., Baldi Júnior, E., Gimenes, F. B., & Barbalho, S. M. (2023). Mangifera indica L., By-Products, and Mangiferin on Cardio-Metabolic and Other Health Conditions: A Systematic Review. Life, 13(12), 1-18. https://doi.org /10.3390/life13122270

Morais, C. A., de Rosso, V. V., Estadella, D., & Pisani, L. P. (2016). Anthocyanins as inflammatory modulators and the role of the gut microbiota. *Journal of Nutritional Biochemistry*, *33*, 1-7. h https://doi.org /10.1016/j.jnutbio.2015.11.008

Nadeem, M., & Imran, M. (2016). Promising features of mango (Mangifera indica L.) kernel oil: a review. Journal of Food Science and Technology, 53(5), 2185-2195. https://doi.org/10.1007/s13197-015-2166-8

Noguera-Machado, N., Ojeda, L., Jiménez, M., Kremisisky, M., Velásquez, I., & Pacheco, F. (2019). Evaluación del extracto hidroalcohólico de las semillas de Passiflora edulis y su efecto sobre el crecimiento de Escherichia coli (ATCC 25922). Saber, 31, 248-255.

Pacheco-Coello, F., Peraza-Matrero, M., Orosco-Vargas, C., Ramirez-Azuaje, D., & Pinto-Catari, I. (2020). Determination of total phenolic compounds and evaluation of the antioxidant activity of commercial and artisanal green tea traded in Maracay, Venezuela. Revista Boliviana de Química, 37(1), 28-33. doi: 10.34098/2078-3949.37.1.4

Pantoja-Chamorro, A., Hurtado-Benavides, A., & Martinez-Correa, H. (2017). Caracterización de aceite de semillas de maracuyá (Passiflora edulis Sims.) procedentes de residuos agroindustriales obtenido con CO2 supercrítico. Acta Agronómica, 66(2), 178-85. https://doi.org/10.15446/acag.v66n2.57786

Patel, S., Soni, H., Mishra, K., & Singhai , A. (2011). Recent updates on the genus Passiflora: A review. International Journal of Research in Phytochemistry and Pharmacology, 1(1), 1-16.

Peron, R., Abu, A., Zainudin, M., Abdul, A., Nik, N., Md Sarip, M., & Mohd, N. (2025). Optimization of Harumanis mango leaves extract for enhanced pharmacognostic profile using response surface methodology approaches. Pertanika Journal of Tropical Agricultural Science, 48(5), 1419-1439.

Rajakumar, G., Rahuman, A., Roopan, S., Chung, I.-M., Anbarasan, K., & Karthikeyan, V. (2014). Efficacy of larvicidal activity of green synthesized titanium dioxide nanoparticles using Mangifera indica extract against blood-feeding parasites. Parasitology Research, 114, 571-581. https://doi.org/10.1007/s00436-014-4232-1

Rizwana, H., Al Otibi, F., & Al-malki, N. (2019). Chemical composition, FTIR studies and antibacterial activity of Passiflora edulis f. edulis (Fruit). Journal of Pure and Applied Microbiology, 13(4), 2489-2498. https://doi.org/10.22207/JPAM.13.4.64

Rosário, R., Soares, S., Martins, M., Nascimento, F., Silva, J., Teixeira-Costa, B., Figueira, M., & Santos, O. (2022). Bioactive, technological-functional potential and morphological structures of passion fruit albedo (Passiflora edulis). Food Science and Technology, 42, 1-10.

Santana, F., Torres, L., Shinagawa, F., Silva, A., Yoshime, L., Melo, I., Marcellini, P., & Mancini-Filho, J. (2017). Optimization of the antioxidant polyphenolic compounds extraction of yellow passion fruit seeds (Passiflora edulis Sims) by response surface methodology. Journal of Food Science and Technology, 54(11), 3552-3561. https://doi.org/10.1007/s13197-017-2813-3

Santos, O., Vieira, E., Soares, S., Conceição, L., Nascimento, F., & Teixeira-Costa, B. E. (2020). Utilization of agroindustrial residue from passion fruit (Passiflora edulis) seeds as a source of fatty acids and bioactive substances. Food Science and Technology, 41(Suppl. 1), 218-225. https://doi.org/10.1590/fst.16220

Scotti, E., Velásquez, I., Ojeda, L., Pacheco, F. y Noguera-Machado, N. (2020). Caracterización e incorporación de un extracto de semillas de parchita (Passiflora edulis) en un hidrogel. Revista Ingeniería UC, 27(3), 273-281.

Shaikh, J., & Patil, M. (2020). Qualitative tests for preliminary phytochemical screening: An overview. International Journal of Chemical Studies, 8(2), 603-608. https://doi.org/10.22271/chemi.2020.v8.i2i.8834

Silva, J., Maciel, P., Silva, E., Macedo, R., Santiago, A.,

Pereira, D., Lima, M., & Ferreira, M. (2023). Extração, caracterização e avaliação do potencial antioxidante do óleo fixo de semente de maracujá amarelo (Passiflora edulis f. flavicarpa). Research, Society and Development, 12(3), 1-19. http://dx.doi.org/10.33448/rsd-v12i3.40606.

Verde-Star, M., García-González, S., & Rivas-Morales, C. (2016). Metodología científica para el estudio de plantas medicinales. En Rivas-Morales, C., Oranday-Cárdenas, M. & Verde-Star, M. (Eds.), Investigación en plantas de importancia médica, OmniaScience, 1-40. http://dx.doi.org/10.3926/oms.313

Villada, J., Aguillón, J., Restrepo, B., Loango, N., & Maldonado, M. (2023). Identification of potential bioactive compounds of Passiflora edulis leaf extract against colon adenocarcinoma cells. Biochemistry and biophysics reports, 34,(101453). 1-7. https://doi.org/10.1016/j.bbrep.2023.101453

Wang, X., Cao Y.,Chen S., Lin J.,Huang D. (2021). Anti-Inflammation Activity of Flavones and Their Structure−Activity Relationship. J.Agric. Food Chem.69,7285−7302. doi.org/10.1021/acs.jafc.1c02015

Wink, M. (2015). Modes of Action of Herbal Medicines and Plant Secondary Metabolites. Medicines. 2(3), 251-286. https://doi.org/10.3390/medicines2030251

Wu, L., Wu, W., Cai, Y., Li, C., & Wang, L. (2020). HPLC fingerprinting based multivariate analysis of phenolic compounds in mango leaves varieties: Correlation to their antioxidant activity and in silico α glucoidase inhibitory ability. Journal of pharmaceutical and biomedical analysis, 191, 113616. https://doi.org/10.1016/j.jpba.2020.113616.

Yuan T. Z., Kao C. L., Li W. J., Li H. T., Chen C. Y. (2017). Constituyentes químicos de las hojas de *Passiflora edulis*. Química Nacional. Compd. 53, 1165–1166. https://doi.org/10.1007/s10600-017-2227-5

Zomer, A., Rodrigues, C., & Maldaner, L. (2022). Piceatannol: a natural stilbene with a broad spectrum of biological activities. Research, Society and Development, 11(9), 1-10. https://doi.org/10.33448/rsd-v11i9.32221

Zahoor, S., Anwar, F., Qadir, R., Soufan, W., & Sakran, M. (2023). Physicochemical attributes and antioxidant potential of kernel oils from selected mango varieties. ACS Omega, 8(25), 22613-22622. https://doi.org/10.1021/acsomega.3c01155

***Received:*** *April 07,2026*

***Accepted:*** *July 05,2026*

***Jiménez-Ruiz, Rudy****: PhD candidate in Technological Chemistry. Soil and Environmental Research and Technology Laboratory. University of Carabobo, Valencia, Venezuela.*
**https://orcid.org/0000-0002-7454-8904**

***Velásquez, Ingrid*****:** *Doctor of Engineering, Chemical Area, Soil and Environmental Research and Technology Laboratory, and Chemical Research Center. University of Carabobo, Valencia, Venezuela. Email: ivvelasquez@uc.edu.ve*
**https://orcid.org/0000-0002-5522-0161**